Quasi-positive families of flux continuous finite volumes schemes in two and three dimensions.

Zheng, Hongwen

Zheng, Hongwen (2010) *Quasi-positive families of flux continuous finite volumes schemes in two and three dimensions..* thesis, Swansea University.
http://cronfa.swan.ac.uk/Record/cronfa42405

Swansea University
Prifysgol Abertawe

Quasi-Positive Families of Flux Continuous Finite Volumes Schemes in Two and Three Dimensions

Hongwen Zheng

Submitted to the University of Wales in fulfilment of the requirements for the
Doctor of Philosophy

April 5th 2010

Civil and Computational Engineering Centre
School of Engineering
Swansea University
Singleton Park, Swansea SA2 8PP
Wales, United Kingdom

DECLARATION

This work has not previously been accepted in substance for any degree and is not being concurrently submitted in candidature for any degree.

Signature (candidate)

Date 15 April 2010

STATEMENT 1

This dissertation is being submitted in partial fulfilment of the requirements for the degree of a PhD in the School of Engineering.

Signature (candidate)

Date 15 April 2010

STATEMENT 2

This dissertation is the result of my own independent work/investigation, except where otherwise stated. Other sources are acknowledged by footnotes giving explicit references. A bibliography is appended.

Signature (candidate)

Date 15 April 2010

STATEMENT 3

I hereby give consent for my dissertation, if accepted, to be available for photocopying and for inter-library loan, and for the title and summary to be made available to outside organisations.

Signature (candidate)

Date 15 April 2010

Quasi-Positive Families of Flux Continuous Finite Volumes Schemes in Two and Three Dimensions

by

Hongwen Zheng

Contents

Acknowledgments

First of All I would like to thank my supervisor Prof Michael G. Edwards for his support, encouragement and guidance during all stages of my PhD research. His deep insight into the research issue and high standard towards research quality are always an impetus and incentive for my progress.

I wish to thank all my friends in the department whose company has been very valuable in making my stay at Swansea a very pleasant one. I will specially like to thank my friends Derek, Mayur, Sadok, Maziar, Chenfeng and Zhun for giving me company during late hours of my PhD work. The staff at the School of Engineering has been fabulous. They have always been there to assist me with all administrative matter. I am also thankful to Exxon-Mobil for the financial support for my research.

Finally, My deepest gratitude goes to all my family for their help and moral support during my studies. It is the love of my wife, Zhe which had made it possible, Zhe has been very supportive through the difficult and enjoyable days we both have gone through. Thankyou for being there for me in times of need and advice, thankyou also for sharing with me in times of joy and celebration.

Summary

In this thesis, new families of full pressure support flux-continuous, locally conservative, finite-volume schemes are presented for solving the general geometry-permeability tensor pressure equation on structured and unstructured grids in two and three dimensions. The families of flux-continuous schemes have also been referred to in the literature as Multi-point Flux Approximation or MPFA schemes. The schemes are applicable to the general tensor pressure equation with discontinuous coefficients and remove the $O(1)$ errors introduced by standard reservoir simulation (two-point flux) schemes when applied to full, anisotropic and asymmetric permeability tensor flow approximation. Such tensors may arise when fine scale permeability distributions are upscaled to obtain gridblock-scale permeability distributions. In contrast to the previous MPFA schemes which assume point-wise pressure and flux continuity locally, the new families of schemes presented in the work recover full pressure continuity across the interface between neighboring subcells.

The M-matrix conditions [1, 2] define the upper limits for ensuring a local maximum principle is obtained for full-tensor fields. A key condition is that the modulus of the off-diagonal tensor coefficients are bounded by the minimum of the diagonal coefficients. For higher anisotropic ratios, when the resulting discrete matrices violate these bounds these schemes can violate the maximum principle (as with more standard methods) and the numerical pressure solutions can consequently exhibit spurious oscillations.

The new family of schemes yield improved performance for challenging problems where earlier flux-continuous schemes exhibit strong spurious oscillations. The M-matrix analysis leads to an optimal quadrature range for these methods. The degree of freedom within the family of full pressure continuity schemes presented is shown to maximise the quadrature range of the flux-continuous schemes. For strongly anisotropic full-tensor cases where M-matrix conditions are violated, it is shown that the earlier families of schemes cannot avoid decoupling of the solution which leads to severe spurious oscillations in the discrete solution. The full quadrature range of the new schemes permits use of quadrature points that were previously out of range for the earlier methods, and that the resulting schemes minimize spurious oscillations in discrete pressure solutions. The new formulation leads to a more robust quasi-positive family of flux-continuous schemes applicable to general discontinuous full-tensor fields.

This work also extends the single parameter family of FPS schemes to double families of schemes with general flexibility in quadrature that allow different quadrature points to be used on different control-volume subfaces. The new schemes minimize spurious oscillations in discrete pressure solutions. The new formulation leads to more robust quasi-positive families of flux-continuous schemes applicable to general discontinuous full-tensor fields.

The full pressure support flux continuous schemes also extend to 3D on structured and unstructured grids. Surface auxiliary control volume and volume auxiliary control volume are introduced to handle extra degrees of freedom which are required for full pressure continuity over neighboring subcell surface. The new schemes are shown to be beneficial in high anisotropic test cases while remaining comparable with previous tetrahedral pressure support (TPS) schemes in terms of convergence rate.

Multi-family schemes in 3D are also presented in this work. This is the extension of 2D double family to 3D. Compared to single family FPS schemes, multi-family schemes are shown to be able to maximize the quadrature and have incomparable flexibility over previous schemes, leading to improved solutions.

List of Figures

List of Tables

Chapter 1

Introduction and Background

1.1 General Background

Reservoir simulation is the process to infer the behavior of a hydrocarbon reservoir from the behavior of a mathematical model which describes it [3]. It is a powerful technique for reservoir management. However the accuracy of the numerical solution is dependent upon the numerical methods adopted. Accurate prediction of flow behavior is the key to the success of a simulation study. Due to the complexity of geology, geometry and heterogeneity, anisotropy is not uncommon in subsurface reservoir. Algorithms for solving such system require carefully selected methods to get accurate approximation.

Numerical methods are required in the reservoir simulation to obtain numerical solutions of mass and energy conservation laws. Momentum is provided by Darcy's Law, where Darcy velocity is proportional to pressure gradient. An accurate pressure solution is always required in order to obtain a reliable simulation. Traditional methods such as finite difference and finite element method have faced major challenges when heterogeneity and anisotropy are present in the domain. It is well known that the two point flux approximation leads to an $O(1)$ error when full tensors occur [2]. Full tensors can be caused by local grid distortion, structured and unstructured grids, upscaling and cross-bedding [2]. Flux continuous finite volume schemes have been introduced in the last decades [4, 5, 1, 6, 2, 7, 8, 9, 10, 11, 12, 13, 14, 15, 16, 17, 18, 19, 20, 21, 22, 23, 24] which are control volume distributed (CVD). This kind of method is also known as Multi Point Flux Approximation (MPFA) [25, 26, 27, 28, 29, 30, 31, 32]. Closely related schemes are presented in [33, 34, 35, 36] and [37]. However when the anisotropic ratio is high, the traditional MPFA methods can violate the Discrete Maximum Principle (DMP), leading to spurious non-physical oscillations. The aim of this thesis is to develop reliable and stable elliptic discretization which can minimize the spurious non-physical oscillation which can be caused by the earlier methods. The new methods are developed for the classical cell types on structured and unstructured grids in both 2D and 3D. Traditional MPFA methods assume point-wise pressure and flux continuity across the control volume interface, thus the pressure support over the subcell is in a triangle, we term it Triangular (Tetrahedral in 3D) Pressure(Potential) Support scheme (TPS).

In this work, the causes for the previous CVD (MPFA) methods violating Discrete Maximum Principal are investigated. This phenomenon is explained via a mapping between CVFE and TPS schemes. The drawback of TPS family is that they fall into a decoupled zone in terms of quadrature.

The remedy for this problem is a new formulation called full pressure support scheme (FPS). Also a further mapping between CVFE and FPS schemes shows both TPS and FPS schemes can be mapped into CVFE family. In contrast to the small quadrature range of TPS family, FPS family recovers the full quadrature range of the CVFE family.

1.2 Recent Development of Numerical Schemes

Since the limitation of standard MPFA methods has attracted a lot of attention, a number of new numerical methods have been proposed to tackle this issue. These methods can be categorized into three types: linear methods, non-linear methods and grid optimization.

1.2.1 Linear methods

(i) Anisotropy-favoring triangulation which is presented in [21] [22] and further details appear in [23]. An interesting formulation integrated with grid optimization was proposed, where anisotropy favoring shceme/grid will yield improved resolution for challenging test cases. It is believed that it is a guiding principle for scheme development and grid generation that can minimize non-physical oscillations.

(ii) Quasi Positive families and double families schemes. These schemes are discribed in this thesis and published in [17] and [38].

(iii) Enriched MPFA. This formulation [39] belongs to the family of methods developed in this thesis. This method uses 5 local unknowns to calculate the local flux continuity and assumes piece-wise linear potential distribution in local cell, which are similar to the treatment of [33]. This method is equivalent to the special case of $\eta = \frac{1}{4}$ of the single family method developed in this work.

(iv) L-methods. An algorithm based on the continuity of local flux is proposed by Aavatsmark and his coauthors [32]. This approach has been extended to 3D. This method seeks to use decreased support to approximate local flux while still maintaining the essential flux continuity condition. It should be noted that the general algorithm for this approach is quite complex and dealing with boundary condition needs special care, e.g. in [40] the authors prove that L-method needs to combine with other approach to handle Dirichlet Boundary condition to keep the convergence property.

1.2.2 Non-Linear methods

(i) Flux splitting technique. This was first proposed in [8]. The idea of this technique is to split the operator into two parts, then solve the system via iteration. This strategy can be applied in matrix level or flux level. A local discrete maximum principle (DMP) can be achieved by special treatment of the iteration procedure [21, 22].

(ii) Positivity-preserving non-linear method. An interesting nonlinear method was proposed by Lipnikov et al to handle the high anisotropic case [41]. This method is designed to ensure that the solution remains positive for positive data, i.e. it has a monotone matrix.

1.2.3 Grid optimization

(i) Grid optimization techniques have been proposed for improving stability of the discrete system for variable anisotropy [42]. Improved resolution in case of high anisotropic ratio has been observed.

1.3 Scope of Work and Research Contribution

The main contributions of this research work are summarized as follows:

(i) Novel families of flux continuous control volume distributed finite volume schemes have been implemented in 2D and 3D on structured and unstructured grids comprised all basic cell types. These new schemes are locally conservative flux continuous with full pressure continuity on all control volume sub-interfaces. Extra local degree of freedom are introduced per primal cell in order to impose full pressure continuity and lead to full pressure support (FPS). The new FPS methods have an extended quadrature range that matches that of CVFE in the constant coefficient case. The previous methods are a subset of the new methods. The new methods also possess the important property of being quasi-positive, i.e. the resulting discrete solutions only have at worst small or negligible spurious non physical oscillations in contrast to the earlier TPS methods. When implementing these new methods, a zero divergence condition is employed for determining the additional degree(s) of freedom.

(ii) In this thesis Discrete Maximum Principle (DMP) of traditional CVD (MPFA) method (TPS) is investigated, the limitation of traditional MPFA is discussed. A new theory of quasi-positive M-Matrices is proposed to aid analysis in cases where the schemes do not have M-Matrices or monotone matrices.

(iii) The term *Positivity* is used here in reference to schemes that possess an M-Matrix and thus a local Discrete Maximum Principle (DMP). For CVD (MPFA) methods, M-matrix analysis is presented in 2D by Edwards and Rogers in [2]. A similar theory about monotone matrix condition is developed by Nordbotten et al [43]. In this thesis, three-dimensional M-matrix conditions are also presented.

A list of publications resulting from this work is given in the bibliography.

1.4 Organization of the Thesis

The structure of this thesis is organized as follows:

General introduction has been given in chapter 1. Scope of the thesis and technical contribution are also discuss within.

The single and multi-phase flow mass conservation equations for fluid flow in porous media are presented in Chapter 2. Description of the problem to be solved with specified boundary conditions is also presented in this chapter.

Chapter 3 discusses numerical discretization methods, desirable properties and various methods used in reservoir simulation.

Chapter 4 is the main contribution of this thesis, new families of locally conservative flux continuous finite volume schemes are developed and analysis is presented. In contrast to the previous point-wise pressure continuity along the control volume surface, the new formulation provide full pressure continuity over the whole control volume sub-surface between neighboring subcells. In addition the new methods improve performance for high anisotropy ratio problems.

In Chapter 5 double families of flux continuous finite volume schemes are presented. The new double-family formulation is shown to expand on the current single-parameter range of existing schemes that have M-matrices. While it is shown that a double family formulation does not lead to an unconditional M-matrix scheme, a quasi-positive QM-matrix analysis is presented that classifies the behaviour of the new schemes with respect to double-family quadrature. The extension to double family quadrature is shown to be beneficial with reduced sensitivity in results at high anisotropy ratio.

Chapter 6 provides a summary of the development of a new family of three dimensional flux-continuous finite volume methods for solving the pressure equation resulting from Darcy's law. Key physical constraints of continuity in normal flux and *full* pressure continuity are imposed at control-volume interfaces. This chapter continues with the derivation of algebraic flux continuity conditions for full-tensor discretization operators and extends the family of flux-continuous full-pressure continuity schemes of [17] into three dimensions, for general structured and unstructured grids.

In Chapter 7 new multi-family flux-continuous finite volume methods are presented on grids comprised of any cell type in three dimensions. The methods continue to retain the standard number of reservoir simulation degrees of freedom in the approximation while maintaining flux and pressure continuity, with each control-volume being assigned a single discrete pressure value. This contrasts with the mixed finite element method, which requires that an additional degree of freedom corresponding to every continuous interface condition in the grid be added to the global system matrix. The resulting quasi-positive formulation has a significant advantage over the earlier point-wise continuous schemes with an increased quadrature range that enables the new schemes to compute discrete pressure solutions for strongly anisotropic full-tensor fields that are essentially free of spurious oscillations. The multi-family formulation permits maximum flexibility in quadrature yielding improved solution resolution.

Finally, chapter 8 summarizes the novel research contributions of this work and recommendations are made for continuation of work through future research.

Chapter 2

Mathematical Model

2.1 Introduction

The flow behavior of water, oil and gas in a subsurface reservoir can be studied quantitatively via an appropriate mathematical model and suitable numerical discretization methods. This chapter introduces the fundamental equations which govern fluid flow in porous media. Physical laws of mass, energy and momentum conservation are used together with empirical Darcy's law to define the velocity field.. Flow equations of both single-phase and multi-phase are introduced and boundary conditions are discussed. Detailed discussion of this topic is given in [44]. Throughout this thesis, focus is on numerical methods for single-phase flow.

2.2 Flow Equations

2.2.1 Darcy's Law and Incompressible Single Phase Flow

Darcy's law is a phenomenologically derived constitutive equation that describes the flow of a fluid through a porous medium [45]. This law states that the rate of flow through a porous filter is inversely proportional to the length of the filter and proportional to the difference in pressure head across the medium, in a mathematical form of 2.1.

$$\mathbf{v} = -\frac{\mathbf{K}}{\mu}\nabla\phi \tag{2.1}$$

The proportionality constant **K** is called the permeability or conductivity of the medium and μ is the viscosity. When gravity is included, Darcys law for single phase flow is defined as

$$\mathbf{v} = -\frac{\mathbf{K}}{\mu}(\nabla\phi - \rho g \nabla z) \tag{2.2}$$

Here, g is the gravitational constant and z is the spatial coordinate in the downward direction. In this work for notational convenience we shall include viscosity in **K** and write 2.2 as

$$\mathbf{v} = -\mathbf{K}(\nabla\phi - \rho g \nabla z) \tag{2.3}$$

Mass conservation is another important law that is used in the development of the flow equations in porous media. For steady-state flow the equation of continuity requires that the amount of fluid flowing into the control-volume must be equal to the amount flowing out. Assuming there is only a single incompressible phase present, mass conservation together with Darcy's law for single phase flow, over the control-volume Ω leads to an equation for pressure in integral form is written as:

$$\int_{\Omega} \nabla \cdot \mathbf{v} d\tau = -\oint_{\partial_\Omega} \mathbf{K}\nabla\phi \cdot \hat{\mathbf{n}} ds = M \tag{2.4}$$

Where v (defined by equation 2.3) is the Darcy velocity, **K** is the elliptic permeability tensor in which the viscosity is implicitly assumed to be incorporated, ∂_Ω is the boundary of Ω, $\hat{\mathbf{n}}$ is the unit outward normal and ϕ is the pressure and M is a source term which is zero away from well locations. Here the gravitation term $\rho g \nabla z$ is dropped for easy notation, however, when the algorithm is established, this term can easily be incorporated.

The pressure equation is used for many early-stage and simplified flow studies. Typical usages include: identifying streamlines,flow patterns and flow directions; finding connections between producers and injectors; in flow-based upscaling; in history matching (pressure); and in other preliminary model tracer studies.

2.2.2 Multi-phase Flow

When multiple phases or components are present in porous media, Darcy's law may be extended to describe simultaneous flow of more than one phase where phases' velocity is defined by:

$$\mathbf{v_l} = -\frac{k k_{rl}}{\mu_l} \left(\nabla \phi - \rho_l g \nabla z \right) \tag{2.5}$$

where $l = (o, w, g)$ (oil,water and gas phases, respectively) and k_{rl} is the relative permeability of phase l, which is used to account for the reduced permeability of each phase due to the presence of the other phases. In petroleum reservoirs different hydrocarbon components can exist in both a gas and a fluid phase.

Two widely used models for multi-phase flow are *black-oil model*[46] and *compositional model* [47]. The *black-oil model* is usually used for simulating dry gas, water, and nonvolatile oils, while the *compositional model* is best suited for light oils, condensates, and natural gases. There are also other models used, eg. *thermal model* is also frequently used because of high fluid densities and viscosities, and the complicated physics involved when massive changes take place in reservoir temperature and calorific energy. Advanced thermal recovery methods are typically required for heavy oil, extra heavy oil, and bitumen reservoirs

The focus of this thesis is mainly on numerical disretization of single phase flow, it is noted that solution of multi-phase flow requires the discretization of the pressure equation and saturation equations (spatial and temporal discretizations). The general formulation of the pressure equation is used in the coupled solver procedure for multi-phase flow by incorporating saturation-dependent variables. A detailed discussion of the flow equations involved in multi-phase flow is given in [3, 44].

2.3 Boundary Conditions

The two most common boundary conditions used in reservoir simulators to solve the general pressure equation are as follows:

2.3.1 Dirichlet

The Dirichlet condition involves the specification of pressure for example on the domain boundaries, or in the field at wells. In reservoir simulation, this may involve specifying flowing bottom hole pressure at a well and a constant pressure at some physical boundaries of reservoir. Numerically this boundary condition is very easy to handle via specifying the known variable as a right-hand side or simply defining the known discrete variable value.

2.3.2 Neumann

The Neumann condition involves specification of flow rates or flux on domain boundaries or wells. Typical Neumann conditions are zero normal flow on solid walls and prescribed flow rates at certain wells in the field. This kind of boundary condition is very easy to implement by modifying the right vector or through the simplified global assembly procedure.

Chapter 3

Numerical Discretization Method and Previous Work

3.1 Introduction

Much of the theory of physical phenomena is described by differential and integral equations. Such equations appear not only in physical sciences, but in biology, sociology, and all scientific disciplines that attempt to understand these physical phenomena. However many of these equations have no explicit solution. Therefore to find solutions to such equations we must resort to numerical techniques. The objective of any numerical method for solving a problem involving a differential or integral equation is to generate a set of algebraic equations involving a finite number of unknowns, whereby the solution of algebraic equations characterizes an approximation of the solution of the original problem.

In view of the complexity of the permeability and geometry of petroleum reservoirs, numerical methods are necessary for discretization of reservoir simulation. Certain properties are needed for a suitable solution.

This chapter is organized as follows: Section 3.2 lists the properties of numerical methods for reservoir simulation.

Section 3.3 introduces mostly used numerical discretization methods in reservoir simulation.

Section 3.4 traces the history of Control Volume Distributed (CVD) flux continuous formulation which is also called Multi-Point Flux Approximation (MPFA) in literature. CVD concept is the foundation for this work.

3.2 Property of Numerical Solution

There are many numerical methods available in the application of reservoir simulation. It should be noted that every method has its limitation and needs to be selected carefully. In this section the desirable properties of numerical methods are studied. In most cases, it is not possible to analyze the complete method. Before a method is used, the components of the method should be analyzed to check for suitability. If not, then it is meaningless to go any further. Important properties are listed below, detailed description can be seen from [48].

3.2.1 Consistency

The truncation error is the difference between the discretized equation operating on the exact solution and the exact differential equation. A numerical method is called consistent if the truncation error tends to zero when the mesh spacing tends to zero $\Delta t \rightarrow 0$ in time and/ or $\Delta x \rightarrow 0$. Truncation errors are obtain via Taylor series expansion.

Lax equivalence theorem states that a consistent finite difference approximation for a well-posed linear initial value problem is convergent if and only if it is stable. Stability is another condition that is required and defined below.

3.2.2 Stability

A numerical method is said to be stable if the error is bounded through the process of the numerical solution procedure. An unstable algorithm can produce non-physical oscillations which can render the discrete resolution useless. Throughout this work, stability is a key property studied for numerical methods proposed.

3.2.3 Convergence

A numerical method is convergent if the error between the discretized equation solution and the exact solution of the partial differential equations tends to zero as the grid spacing tends to zero. According to the Lax equivalence theorem, for a consistent solution to an initial value problem, stability is the necessary and sufficient condition for convergence. However stability is not always easy to analyze, thus numerical convergence experiments/tests are often carried out to check for convergence rates. This is achieved by repeating the calculation on a series of refined meshes.

3.2.4 Conservation

Mathematical models are built from physical problems via conservation laws. It is natural to require that the numerical schemes satisfy conservation property locally and globally. Local conservation means the net flux leaving a control volume is equal to the net flux entering this volume in the absence of sources and sinks. Global conservation means the net fluxes entering the global domain are equal to the fluxes leaving the domain [48]. Source and sink terms should be treated such that the total source or sink in the domain is equal to the net flux through the boundaries. It is recommended to build a conservative method that respects the basic conservation laws.

3.2.5 Boundedness

All numerical solutions must be within certain bounds. For example, pressure must be within the bound of a maximum value at a source (well), sink or boundary and saturation must lie between 0% to 100%. If connate water (Water trapped in the pores of a rock during formation of the rock) or residual oil (Oil that does not move when fluids are flowed through the rock in normal conditions, for example primary and secondary recovery, and invasion) is considered, then the saturations must be even in a smaller regime. We should notice any numerical method producing unbounded solutions may have stability and convergence problems and should not be used.

3.2.6 Reliability

Physically realistic solutions must always be ensured whenever a method is used. It will be shown in this thesis that non-physical oscillations will appear if the method is not carefully selected. If strong non-physical oscillations appear, the method is unreliable and should not be used.

3.2.7 Accuracy

It is important to be aware that numerical solutions of subsurface flow problems are only *approximate solutions.* Through the stages from a real life problem to a visible numerical solution, three types of systematic solution error maybe introduced: modeling errors, discretization errors and iteration errors [48].

3.3 Numerical Discretization Methods

3.3.1 Finite Difference Method

The earliest numerical discretization method for partial differential equations is the finite difference method (FDM). Taylor series expansions are used to derive finite difference methods for approximation of derivatives in an ordinary or partial differential equation. Truncation terms are discarded which can indicate the local approximation order. This method has been used extensively in conventional reservoir simulation [49, 50, 51, 52, 53].

Since FDM methods are derived directly for derivatives making up a partial differential equation, the conservation property is not guaranteed. It is observed that classical FDM is easy to break down near the discontinuities [54]. For the general tensor equations (off-diagonal coefficients are none zero), classical FDM based on two-point pressure differences can result in an O(1) error leading to an incorrect solution [4, 2]. Irregular boundaries are difficult to handle in FDM but are common in reservoir simulation. Due to the above drawbacks, classical FDM's are not suitable for reservoir simulation.

3.3.2 Finite Element Method

A revolutionary advance in numerical methods for partial differential equations came with the innovation of finite element methods (FEM). FEM is famous for the flexibility in dealing with general mesh and arbitrary boundaries. The underlying idea for FEM is to find a approximate space (finite) to the solution, and various approaches have been proposed like Rayleigh-Ritz (based on variational formulation) and Galerkin (based on the weak formulation).

Nowadays FEM's are standard in the scientific community and very well known examples in the literature are [55, 56, 57, 58, 59, 60, 61].

FEM has been widely used in various disciplines of engineering and science. Although FEM is known to be accurate on smooth data (homogeneous permeability) [60], while applicable to quite general grids, standard FEM lacks local flux continuity which is essential in reservoir simulation due to sudden changes in rock properties. This leads to a discrete error in pressure [13, 14, 62, 63, 64, 65, 66] and undesirable smearing effect in solution being observed [62, 67]. Advantages of the flux continuous CVD(MPFA) verses CVFE are shown in [13, 14]. While other finite element methods such as Discontinuous Galerkin (DG) methods [68, 69, 70] and Mixed finite element methods (MFEM) [71] have improved resemblance of the physics of the problem and ability to handle discontinuous media they require more degrees of freedom.

3.3.3 Mixed Finite Element Method

The term mixed method was first used in the 1960's to describe finite element methods in which both stress and displacement fields are approximated as primary variables. In reservoir simulation, this means both potential and velocity are treated as primal variables [72], while in the classical finite element method only potential is primal and velocity is obtained via a post-processing procedure using an approximation of Darcy's Law.

The MFEM may have better properties due to two different approximation spaces. For example, when choosing the approximation spaces, local flux continuity is a property of the formulation which is essential in reservoir simulation. Since it is still in the frame work of finite element method, the flexibility of applying complex geometry, dealing with anisotropy, heterogeneity and discontinuity of permeability tensor can be achieved [73].

The mixed finite element method has been proposed for reservoir simulation [74, 75, 76]. The theoretical properties are easy to verify as it can be considered in the general frame work of finite element. The mixed finite element framework has also been extended to account for a control volume formulation [77, 78]. Another form of mixed finite element method was developed by Wheeler, Yotov and co-workers [79, 80]. The relationship between the mixed finite element method and flux-continuous CVD(MPFA) schemes was deduced by Edwards in [9] and recently a proof of convergence of MPFA was presented in [81], which exploits this relationship. The CVD(MPFA) and MFEM relationship is discussed further in [16]. Discontinuous Galerkin method [82, 83] and Mixed Finite element method are frequently used in reservoir simulation [73, 84], but they prove to be computationally more expensive due to the additional degrees of freedom (DOF), e.g. for a structured mesh, triple DOF in 2D and quadruple DOF in 3D.

3.3.4 Finite Volume Method

The finite volume method is a method for approximating partial differential equations as algebraic equations [54]. Similar to the finite difference method and finite element method, values (potential) are calculated at discrete places on a meshed geometry. *Finite volume* refers to the small volume surrounding each node point on a mesh. In the finite volume method, volume integrals in a partial differential equation that contain a divergence term are converted to surface integrals, using the Gauss divergence theorem. These terms are then evaluated as fluxes at the surfaces of each finite volume. Because the flux entering a given volume is identical to that leaving the adjacent volume, these methods are locally conservative. Another advantage of the finite volume method is that it is easily formulated to allow for unstructured meshes.

An important property of FVM is the introduction of control-volume average of medium property. Godunov [85] introduced this interpretation in the discretization of the gas dynamics equations by assuming piecewise constant solution representation in each control-volume with values equal to cell average. The finite volume formulation is also suitable for discontinuity capturing and is also used for hyperbolic conservations laws [86, 87, 88, 89, 54].

Local flux continuity is a desirable property in numerical modeling of flow in porous media. Various formulations of FVM are derived such that fluxes are conserved [90, 91, 92, 93] for both cell-centred and (dual grid) polygonal control-volume node based formulations. Previous numerical discretization techniques [6, 4, 1, 2, 7, 9, 10, 11, 19, 12, 20, 21, 22, 23, 15] based on flux-continuous finite volume formulation is the foundation of this work and will be discussed in more detail in the later chapters. In terms of implementation FVM is as simple as FDM, while FVM has the flexibility in dealing with complex geometries. Compared to the mixed finite element method, FVM is computationally much cheaper.

3.3.5 Finite Volume Formulation

The finite volume formulations considered in this work are termed control-volume distributed formulations [2, 9, 24] in the sense that rock properties (porosity, permeability) and flow variables are assigned to the control volume.

The 2D formulations of the flux-continuous schemes presented in this thesis involve cell-centred/control volume distributed formulation for structured quadrilateral grids and cell-vertex/control volume distributed formulation for both structured quadrilateral and unstructured triangular grids. The 3D formulation of the schemes are cell-vertex/control volume distributed. However, it should be noted that on a structured grid the cell-centred/control volume distributed formulation of the family of flux-continuous schemes can easily be converted to cell-vertex/control volume distributed formulation by translating the operations onto a grid that is essentially a dual mesh.

3.4 A Brief Overview of Flux Continuous Schemes

Currently Flux Continuous Finite Volume Scheme (CVD or MPFA) are perhaps the most popular methods in reservoir simulation. These methods are locally conservative with essential local flux continuity imposed across control volume interfaces.

Other methods including MFEM and MHFE are more expensive in terms of computational cost since they introduce more variables in global matrix assembly.

An investigation of the Mixed Hybrid Finite Element Method (MHFE) and TPS schemes (earlier MPFA) was carried out in [94]. Superiority of TPS over MHFE in terms of accuracy and efficiency is demonstrated via numerical experiment. Both methods yielded solutions with non-physical oscillations.

When applying these schemes to the elliptic pressure equation with a strongly anisotropic full-tensor field they can fail to satisfy the maximum principle (as with other FEM and finite-volume methods) and result in spurious oscillations in the numerical pressure solution. The question of stability in this situation has drawn substantial attention and is also one of the central themes of this thesis.

Chapter 4

A Quasi-Positive family of Continuous Darcy-Flux Finite Volume Schemes with Full Pressure Support on Quadrilateral and Triangular Grids

4.1 Introduction

In this chapter Darcy flux approximations are formulated for quadrilateral and triangular meshes. When formulating a finite-volume pressure equation scheme, continuous normal flux and pressure are key physical constraints that must be imposed at control-volume interfaces, across which strong discontinuities in permeability can occur. Rapid variation in permeability with strong anisotropy are common features in subsurface reservoirs.

The derivation of algebraic flux continuity conditions for full tensor discretization operators has lead to families of efficient locally conservative flux-continuous control volume distributed (CVD) finite-volume schemes for determining the discrete pressure and velocity fields in subsurface reservoirs [4, 2, 9, 10, 11, 8, 16, 19, 21, 22], these schemes are classified by the quadrature parameterization $0 < q \leq 1$. Schemes of this type are also called multi-point flux approximation schemes or MPFA [27, 30] where focus has been on a scheme that belongs to the above mentioned family with $(q = 1)$. Further schemes of this type are presented in [33, 34, 35, 36] and [37] via a novel mixed method. All of these schemes are applicable to the diagonal and full tensor pressure equation with generally discontinuous coefficients and remove the O(1) error introduced by standard reservoir simulation schemes when applied to full tensor flow approximation. Coupling of the flux-continuous schemes with higher order convective flux approximations are presented on mixed quadrilateral-triangle grids [13] and on tetrahedra-hexahedra grids with a pyramid interface in [14] respectively. Other schemes that preserve flux continuity have been developed from variational frameworks, using the mixed finite element method (MFE) e.g. [72, 73, 95, 96, 74, 97] and related work [98] and discontinuous galerkin methods [82, 83], however these schemes require additional degrees of freedom.

When applying these schemes to the elliptic pressure equation with a strongly anisotropic full-tensor field they can fail to satisfy the maximum principle (as with other FEM and finite-volume methods) and result in spurious oscillations in the numerical pressure solution. M-matrix conditions were first derived in [4, 1, 2], monotone matrix conditions are presented in [99, 43]. Grid optimization techniques have also been used to improve stability of the discrete system [42]. Discretization schemes aimed at improving stability are presented in [100], [23] and [101]. Non-linear methods have also been proposed, [21, 22] (flux-splitting) and [41] (positivity preserving) both of which have been shown to yield numerical pressure solutions that are free of spurious oscillations.

The M-matrix conditions [1, 2, 17] define bounds on the tensor coefficients for ensuring that a local discrete maximum principle is obtained for full-tensor fields. A key condition is that the modulus of the off-diagonal tensor coefficients are bounded by the minimum of the diagonal coefficients. For higher anisotropic ratios, when the resulting discrete matrices violate these bounds these schemes can violate the maximum principle (as with more standard methods) and the numerical pressure solutions can consequently exhibit spurious oscillations.

In this chapter a new family of flux-continuous, locally conservative, finite-volume schemes is presented for solving the general tensor pressure equation of subsurface flow in porous media. The new schemes have full pressure continuity imposed across control-volume faces, in contrast to the earlier families of flux-continuous schemes with point-wise continuity in pressure and flux. A full pressure continuity scheme that has helped to motivate this formulation was introduced in [33]. However, the formulation of [33] is derived from linear basis functions and consequently does not extend to a family of schemes. A brief description of the schemes presented here was first given in [2] and initial test results are given in [102].

The new family of schemes yield improved performance for challenging problems where earlier flux-continuous schemes exhibit strong spurious oscillations. The M-matrix analysis leads to an optimal quadrature range for these methods [17]. The degree of freedom within the family of full pressure continuity schemes presented is shown to maximise the quadrature range of the flux-continuous schemes. For strongly anisotropic full-tensor cases where M-matrix conditions are violated, it is shown that the earlier families of schemes cannot avoid decoupling of the solution which leads to severe spurious oscillations in the discrete solution. The full quadrature range of the new schemes permits use of quadrature points that were previously out of range for the earlier methods, and that the resulting schemes minimize spurious oscillations in discrete pressure solutions. The new formulation leads to a more robust quasi-positive family of flux-continuous schemes applicable to general discontinuous full-tensor fields.

This chapter is organized as follows: Section 4.2 gives a description of the single phase flow problem encountered in reservoir simulation with respect to the general tensor pressure equation. In Section 4.3 the formulation of the point-wise continuous triangle-pressure-support (TPS) flux-continuous finite volume schemes with discretization in *physical* space is presented. A general CVFE family formulation [1] is presented in section 4.4 which motivates the basis functions for the new full-pressure support scheme and comparisons between schemes. The family of Full-Pressure Support (FPS) schemes is introduced in section 4.5. Positivity conditions are presented in section 4.6. The relationships between TPS, FPS and CVFE are presented in section 4.7 for a spatially constant tensor together with M-matrix properties of the schemes. The TPS, FPS quadrature ranges are compared in section 4.8, where the crucial advantages of FPS over TPS are given. In section 4.9 the TPS schemes are shown to belong to the upper quadrature limit which leads to decoupled solutions, and helps to explain the sensitivity of TPS at high anisotropy ratio. Quasi-positive QM-matrices which are outside of the formal M-matrix limits are presented in section 4.10. Numerical examples are presented in section 4.11, that illustrate benefits and features of the schemes in terms of QM-matrix properties. Summaries follow in section 4.12.

4.2 Flow Equation and Problem Description

4.2.1 Cartesian tensor

The problem is to find the pressure ϕ satisfying

$$-\int_{\Omega} \nabla \bullet \mathbf{K}(x,y)\nabla\phi d\tau = \int_{\Omega} q d\tau = \mathbf{M} \tag{4.1}$$

over an arbitrary domain Ω, subjected to suitable (Neumann/Dirichlet) boundary conditions on boundary $\partial\Omega$, where $\mathbf{V} = -\mathbf{K}\nabla\phi$ is the Darcy velocity. The right hand side term $\mathbf{M}$ represents a specified flow rate and $\nabla = (\partial_x, \partial_y)$. Matrix $\mathbf{K}$ can be a diagonal or full cartesian tensor with general form

$$\mathbf{K} = \begin{pmatrix} K_{11} & K_{12} \\ K_{12} & K_{22} \end{pmatrix} \tag{4.2}$$

The full tensor pressure equation is assumed to be *elliptic* such that

$$K_{12}^2 \leq K_{11}K_{22} \tag{4.3}$$

The tensor can be discontinuous across internal boundaries of Ω. The boundary conditions imposed here are Dirichlet and Neumann. For incompressible flow pressure is specified at atleast one point in the domain. For reservoir simulation, Neumann boundary conditions on $\partial\Omega$ requires zero flux on solid walls such that $(K\nabla\phi)\cdot\hat{n} = 0$, where $\hat{n}$ is the outward normal vector to $\partial\Omega$.

4.2.2 General tensor equation

The pressure equation is defined above with respect to the *physical* tensor in the initial classical Cartesian coordinate system. Now we proceed to a general curvilinear coordinate system that is defined with respect to a uniform dimensionless transform space with a (ξ, η) coordinate system. Choosing Ω_p to represent an arbitrary control volume comprised of surfaces that are tangential to constant (ξ, η) respectively, equation 4.1 is integrated over Ω_p via the Gauss divergence theorem to yield

$$-\oint_{\partial\Omega_p} (\mathbf{K}\nabla\phi)\cdot\hat{\mathbf{n}}ds = \mathbf{M} \tag{4.4}$$

where $\partial\Omega_p$ is the boundary of Ω_p and $\hat{n}$ is the unit outward normal. Spatial derivatives are computed using

$$\phi_x = J(\phi, y)/J(x, y), \phi_y = J(x, \phi)/J(x, y), \tag{4.5}$$

where $J(x,y) = x_\xi y_\eta - x_\eta y_\xi$ is the Jacobian. Resolving the x,y components of velocity along the unit normals to the curvilinear coordinates (ξ,η), e.g., for ξ = constant, $\hat{\mathbf{n}}ds = (y_\eta, -x_\eta)d\eta$ gives rise to the general tensor flux components

$$F = -\int (T_{11}\phi_\xi + T_{12}\phi_\eta)d\eta, \quad G = -\int (T_{12}\phi_\xi + T_{22}\phi_\eta)d\xi, \tag{4.6}$$

where general (Piola) tensor $\mathbf{T}$ has elements defined by

$$\begin{aligned} T_{11} &= (K_{11}y_\eta^2 + K_{22}x_\eta^2 - 2K_{12}x_\eta y_\eta)/J, \\ T_{22} &= (K_{11}y_\xi^2 + K_{22}x_\xi^2 - 2K_{12}x_\xi y_\xi)/J, \\ T_{12} &= (K_{12}(x_\xi y_\eta + x_\eta y_\xi) - (K_{11}y_\eta y_\xi + K_{22}x_\eta x_\xi))/J \end{aligned} \tag{4.7}$$

and the closed integral can be written as

$$\int\int_{\Omega_p} \frac{(\partial_\xi \tilde{F} + \partial_\eta \tilde{G})}{J} J d\xi d\eta = \triangle_\xi F + \triangle_\eta G = m \tag{4.8}$$

where e.g. $\triangle_\xi F$ is the difference in net flux with respect to ξ and $\tilde{F} = -(T_{11}\phi_\xi + T_{12}\phi_\eta)$, $\tilde{G} = -(T_{12}\phi_\xi + T_{22}\phi_\eta)$. Thus any scheme applicable to a full tensor also applies to non-K-Orthogonal grids. Note that $T_{11}, T_{22} \geq 0$ and ellipticity of $\mathbf{T}$ follows from equations 4.3 and 4.7. Full tensors can arise from upscaling, unstructured grids and local orientation of the grid and permeability field. For example by equation 4.7, a diagonal anisotropic Cartesian tensor leads to a full tensor on a curvilinear *orthogonal* grid.

4.3 Family of Flux-Continuous Finite Volume Schemes

Families of flux-continuous locally conservative control-volume distributed (CVD) finite volume schemes presented in[2, 9, 10, 11, 8, 16, 19] have been developed for different grid types including cell vertex and cell centred structured and unstructured formulations in physical space and transform space. Numerical convergence rates for a range of quadrature rules in physical space are presented in[19]. We present a sum-

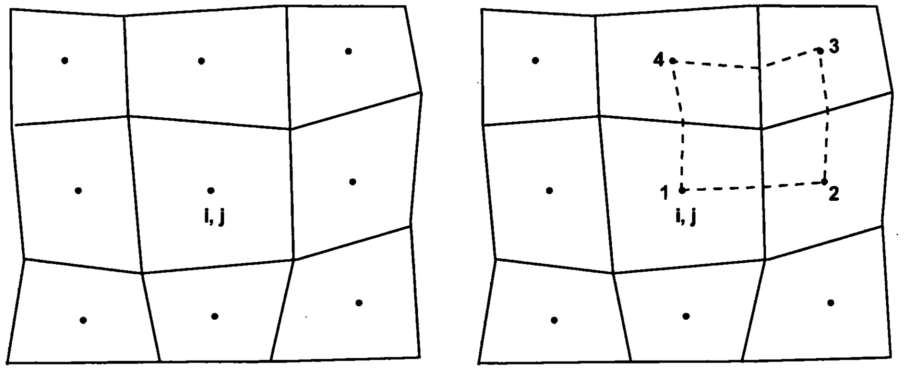

(a) (b)

Figure 4.1: (a) Nine-node Support, Cell centered Control-volume i, j (b) Dual-cell Dashed line

mary of the formulation here for the structured cell-centred quadrilateral formulation. (The formulation has also been developed for cell-vertex structured and unstructured grids e.g. [9, 19]). The nine node support of the cell-centred scheme centred on i, j is indicated in Fig. 4.1(a)). The scheme has cell centred flow and rock variables, so that the approximation points (or nodes) are at the centres of the primal grid cells and the primal grid cells are also the control-volumes over which permeability is defined to be piecewise constant, i.e. in this case control-volume distributed CVD with respect to the primal grid cells. Each group of four cell-centred nodes forms a *dual-cell* Fig. 4.2, and four triangles are then defined in the *dual-cell* as drawn in Fig. 4.3 e.g. at (a),(b), the position depending on the quadrature point defined below. The *dual-cell* perimeter is defined by joining cell centres with cell edge mid-points as indicated by the dashed contour in Fig. 4.2(b). The dual cells partition the primal cells (or control-volumes) into subcells. Two faces of each subcell also coincide with *sub faces* of the parent control-volume e.g. faces (S, V_3), (V_3, W) are faces of the subcell defined by corner points $(i, j), S, V_3, W$ Fig 4.2 (b).

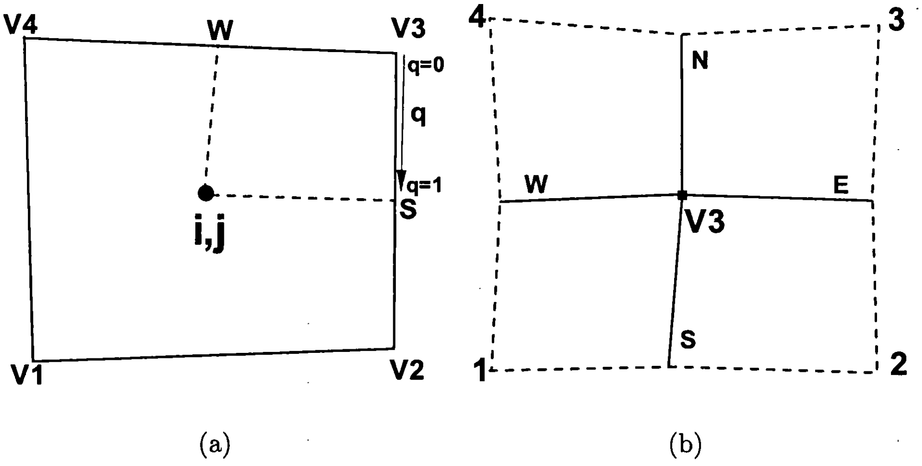

Figure 4.2: (a) Cell centre node i, j and 4 vertices $V1, ...V4$ of Primal cell. (b)Dual cell centered on $V3$, subcells and local node numbering over dual cell

Family of Flux-Continuous Schemes - Quadrature Parameterization

Families of flux continuous schemes are formed when imposing normal flux and pressure continuity conditions on the *sub-faces* where the four shaded triangles meet, at the four positions (N, S, E, W). These points lie on the faces of the subcells that are within the perimeter of the dual cell shown with dashed line in Fig. 4.2(a)). On each *sub-face* the point of continuity is parameterized with respect to the subcell face by the variable q where referring to Fig. 4.2(a) the range of q is given by $(0 < q \leq 1]$ with $q = 1$ corresponding to the point of intersection between the subfaces and the dual-cell perimeter. Hence for a given subcell, the points of continuity can lie anywhere in the interval $(0 < q \leq 1]$ on the two faces of each subcell inside a dual cell, that coincide with the control-volume *sub-faces*, and the value of q defines the local quadrature point and hence the family of flux-continuous finite-volume schemes. Cell face pressures $\phi_N, \phi_S, \phi_E, \phi_W$ are introduced at N, S, E, W locations. Pressure sub-triangles are then defined with local triangular support imposed within each quarter (sub-cell) of the *dual-cell* as shown (shaded triangles) in Fig. 4.3. Pressure ϕ, in local cell coordinates, then assumes a piecewise linear variation over each shaded

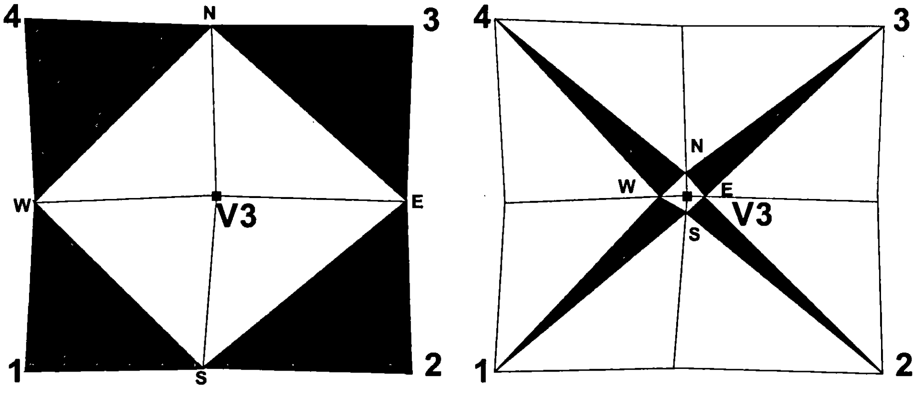

(a) (b)

Figure 4.3: (a) Standard quadrature,q=1 (b) Example quadrature q=0.1, triangle pressure support

triangle, with triangular pressure support (TPS).

The parametric variation in q is illustrated further using the sub-cell example of Fig.4.2, with sub-cell containing shaded sub-triangle $(1, S, W)$. Let $\mathbf{r}_1 = (x_1, y_1)$ denote the coordinates of the cell-centre and $\mathbf{r}_S = (x_S, y_S)$,$\mathbf{r}_W = (x_W, y_W)$ denote the local continuity coordinates. Then it is understood that the continuity position is a function of q with $\mathbf{r}_S(q)$ and $\mathbf{r}_W(q)$.

Piecewise constant Darcy fluxes are now constructed on each of the pressure sub-triangles belonging to the sub-cells of the *dual-cell.* The local linear pressure ϕ, is expanded in sub-triangle coordinates. The Darcy flux approximation for sub-triangle $(1, S, W)$ is given below.

$$\begin{pmatrix} \phi_\xi \\ \phi_\eta \end{pmatrix} = \begin{pmatrix} \phi_S - \phi_1 \\ \phi_W - \phi_1 \end{pmatrix} \tag{4.9}$$

and

$$\begin{pmatrix} x_\xi(q) \\ x_\eta(q) \end{pmatrix} = \begin{pmatrix} x_S(q) - x_1 \\ x_W(q) - x_1 \end{pmatrix}, \begin{pmatrix} y_\xi(q) \\ y_\eta(q) \end{pmatrix} = \begin{pmatrix} y_S(q) - y_1 \\ y_W(q) - y_1 \end{pmatrix} \tag{4.10}$$

Using equations 4.9,4.10 the discrete Darcy velocity is defined as

$$v_h = -\mathbf{K}^1 \nabla \phi_h = -\mathbf{K}^1 \mathbf{G}(q) \begin{pmatrix} \phi_\xi \\ \phi_\eta \end{pmatrix} \tag{4.11}$$

Where $\mathbf{K}^1$ is the local permeability tensor of cell 1 and dependency of $\nabla\phi_h$ on quadrature point arises through

$$\mathbf{G}(q) \begin{pmatrix} \phi_\xi \\ \phi_\eta \end{pmatrix} = \begin{pmatrix} y_\eta(q) & -y_\xi(q) \\ -x_\eta(q) & x_\xi(q) \end{pmatrix} \frac{1}{J(q)} \begin{pmatrix} \phi_S - \phi_1 \\ \phi_W - \phi_1 \end{pmatrix} \tag{4.12}$$

where approximate $\mathbf{r}_\xi(q)$ and $\mathbf{r}_\eta(q)$are defined by Eq. 4.10. The normal flux at the left hand side of S(Fig.4.2) is resolved along the outward normal vector $dL_S = \frac{1}{2}((y_{v3} - y_{v2}), -(x_{v3} - x_{v2}))$ and is expressed in terms of the general tensor $T = T(q)$ as

$$F_S^1 = v_h \cdot dL_S = -(T_{11}^1 \phi_\xi + T_{12}^1 \phi_\eta)|_S^1 \tag{4.13}$$

where it is understood that the resulting coefficients of $-(\phi_\xi, \phi_\eta)|_S^1$ denoted by $T_{11}|_S^1$ and $T_{12}|_S^2$ are sub-cell (physical-space) approximations of the general tensor components (Eq. 4.29) at the left hand face at S, and are functions of q. A similar expression for flux is obtained at the right hand side of S from cell 2 (Fig.4.2(b)). Similarly sub-cell fluxes are resolved on the two sides of the other faces at E,W and N. Flux continuity is then imposed across the four cell interfaces at the four positions N,S,E and W (Fig.4.3) which are specified according to quadrature point q.

The *physical* space flux-continuity conditions for cells 1 to 4, sharing a common grid vertex inside the dual-cell are then expressed as

$$\begin{aligned} F_N &= -(T_{11}\phi_\xi + T_{12}\phi_\eta)|_N^3 = -(T_{11}\phi_\xi + T_{12}\phi_\eta)|_N^4, \\ F_S &= -(T_{11}\phi_\xi + T_{12}\phi_\eta)|_S^1 = -(T_{11}\phi_\xi + T_{12}\phi_\eta)|_S^2, \\ F_E &= -(T_{12}\phi_\xi + T_{22}\phi_\eta)|_E^2 = -(T_{12}\phi_\xi + T_{22}\phi_\eta)|_E^3, \\ F_W &= -(T_{12}\phi_\xi + T_{22}\phi_\eta)|_W^1 = -(T_{12}\phi_\xi + T_{22}\phi_\eta)|_W^4 \end{aligned} \tag{4.14}$$

The above system of equations (4.14) is then wriiten as the linear system

$$F = A_L\Phi_f + B_L\Phi_v = A_R\Phi_f + B_R\Phi_v \tag{4.15}$$

where $F = (F_N, F_S, F_E, F_W)^T$ are the fluxes defined in the dual-cell and $\Phi_f = (\phi_N, \phi_S, \phi_E, \phi_W)^T$ are the interface pressures. Similarly $\Phi_v = (\phi_1, \phi_2, \phi_3, \phi_4)^T$ are the cell centered pressures. Thus the four interface pressures are expressed in terms of the four cell centered pressures. Using equation 4.15, Φ_f is now expressed in terms of Φ_v to obtain the dual-cell flux and coefficient matrix

$$F = (A_L(A_L - A_R)^{-1}(B_R - B_L) + B_L)\Phi_v \tag{4.16}$$

Thus the cell-face pressures are eliminated from the flux by being determined locally in terms of the cell centered pressures in a preprocessing step, avoiding introduction of the interface pressure equations into the assembled discretization matrix. The equation 4.16 can also be written as

$$\mathrm{A}F = -\Delta\Phi_v \tag{4.17}$$

where the entries of matrix A are accumulated inverse tensor elements and $\Delta\Phi_v = (\phi_{21}, \phi_{32}, \phi_{34}, \phi_{41})^T$ are the differences of cell-centred pressures. Consistency of the formulation follows from Eq. 4.17 which shows that flux is zero for constant potential.

The relationship between CVD(MPFA) and the mixed method, first presented in [9] for $q = 1$ (and used in a convergence proof [103]) hinges on Eq. 4.17. A novel mixed method with similar properties and proven convergence is presented in [37]. The above system of Eq. 4.17 also represents the generalisation of the standard flux with harmonic coefficients to general elements with families of schemes defined by quadrature point q, see [9, 16] for details. Although the physical space families do not posses symmetric discretization matrices for arbitrary quadrilaterals they are positive definite subject to discrete ellipticity of the symmetric part of the tensor [16].

However transform space (cell and sub-cell) formulations that are symmetric positive definite are presented in [2, 10, 11, 16]. Flux continuity in the case of a general-tensor is obtained while maintaining the standard *single* degree of freedom per cell. Since the continuity equations depend on both ϕ_ξ and ϕ_η(unless a diagonal tensor is assumed with cell-face midpoint quadrature resulting in a 2-point flux), the interface pressures $\Phi_f = (\phi_N, \phi_S, \phi_E, \phi_W)^T$ are locally coupled and each group of four interface pressures is determined simultaneously in terms of the group of four cell centered pressures whose union contains the continuity positions. Finally for a structured grid the scheme is defined by

$$F_{i+1/2,j} - F_{i-1/2,j} + F_{i,j+1/2} - F_{i,j-1/2} = M \tag{4.18}$$

where i, j are the integer coordinates of the central quadrilateral cell, Fig. 4.1) and

$$\begin{aligned} F_{i+1/2,j} &= F_{S_{i+1/2,j+1/2}} + F_{N_{i+1/2,j-1/2}}, \\ F_{i,j+1/2} &= F_{E_{i-1/2,j+1/2}} + F_{W_{i+1/2,j+1/2}} \end{aligned} \tag{4.19}$$

where $i + 1/2, j + 1/2$ denote the "integer" coordinates of the top right hand side dual-cell centred on vertex V_3, Fig. 4.3. The unstructured formulation is presented in e.g. [9].

In later sections results from an M-matrix analysis will be presented for a spatially *constant* full-tensor field. The discrete family scheme coefficients for the point-wise continuous triangle pressure support (TPS) schemes are presented in table 4.1 below for a *spatially constant* full-tensor field where the numbering of coefficients is indicated in Fig.4.4.

Where it is understood that $\alpha_T = \frac{(1-q)}{2(2-q)}$, $\beta_T = \frac{1}{2(2-q)}$ and $E = \frac{T_{12}^2}{T_{11}T_{22}}$. Here E is a measure of ellipticity and it follows that $E \leq 1$.

For a spatially constant tensor the above family of schemes can be related to a simpler family of CVFE schemes given below. This will prove useful in unwrapping some of the underlying properties of the above schemes.

integer coords	Coeff'ts	Full Tensor
i,j	M_{11}	$2(T_{11}+T_{22})-2(T_{11}+T_{22})(\alpha_T+\beta_T E)$
i+1,j	M_{12}	$-T_{11}+(T_{11}+T_{22})(\alpha_T+\beta_T E)$
i+1,j+1	M_{13}	$-\frac{1}{2}(T_{11}+T_{22})(\alpha_T+\beta_T E)-\frac{T_{12}}{2}$
i,j+1	M_{14}	$-T_{22}+(T_{11}+T_{22})(\alpha_T+\beta_T E)$
i-1,j+1	M_{15}	$-\frac{1}{2}(T_{11}+T_{22})(\alpha_T+\beta_T E)+\frac{T_{12}}{2}$
i-1,j	M_{16}	$-T_{11}+(T_{11}+T_{22})(\alpha_T+\beta_T E)$
i-1,j-1	M_{17}	$-\frac{1}{2}(T_{11}+T_{22})(\alpha_T+\beta_T E)-\frac{T_{12}}{2}$
i,j-1	M_{18}	$-T_{22}+(T_{11}+T_{22})(\alpha_T+\beta_T E)$
i+1,j-1	M_{19}	$-\frac{1}{2}(T_{11}+T_{22})(\alpha_T+\beta_T E)+\frac{T_{12}}{2}$

Table 4.1: *q-Family (TPS) Coefficients For Constant Tensor Field*

4.4 CVFE

The purpose of this section is to introduce an approximation framework that is highly influential within the development of the new full pressure continuity family of schemes. The family of symmetric positive definite control-volume finite element (CVFE) full-tensor schemes was first presented in [1], with further properties in [7]. A comparative formalism of the control-volume distributed CVD(MPFA) point-wise continuous family and the CVFE family is also included in [8]. The CVFE framework is quite transparent for spatially constant permeability coefficients and includes all possible single parameter locally conservative constant coefficient nine-point diagonal and full-tensor schemes. For constant coefficients the flux-continuous schemes can be mapped onto the more transparent control-volume finite element CVFE nine-point framework. Such a mapping was demonstrated in [2] for the family of general tensor schemes as a function $\eta = \eta(q)$, where η is a CVFE family basis function parameterization and q is the flux-continuous quadrature parameterization. A diagram illustrating the variations of q and η is given in Fig.4.8. The mapping facilitated the M-matrix analysis of the CVD(MPFA) methods [4, 2, 17] and links to the cell-wise CVFE M-matrix analysis in [1]. This approach is expanded upon here in performing

5	4	3
6	1	2
7	8	9

Figure 4.4: Numbering of approximation support nodes (stencil)

an M-matrix analysis of the new full pressure continuity schemes.

The family of quadrilateral CVFE fluxes is defined over a primal grid cell if a cell-vertex formulation is employed and is defined over the primal dual-cell if a cell-centred formulation is employed. The CVFE fluxes are derived from a bilinear approximation of pressure and position vector over the cell with

$$\phi = (1-\xi)(1-\eta)\phi_1 + \xi(1-\eta)\phi_2 + \xi\eta\phi_3 + (1-\xi)\eta\phi_4 \tag{4.20}$$

$$\mathbf{r} = (1-\xi)(1-\eta)\mathbf{r}_1 + \xi(1-\eta)\mathbf{r}_2 + \xi\eta\mathbf{r}_3 + (1-\xi)\eta\mathbf{r}_4 \tag{4.21}$$

where $0 \leq \xi, \eta \leq 1$. The resulting fluxes are given by

$$\begin{aligned}
F_N &= -\tfrac{1}{2}(T_{11}((\phi_2-\phi_1)(1-\eta)+(\phi_3-\phi_4)\eta)+T_{12}((\phi_4-\phi_1)(1-\xi)+(\phi_3-\phi_2)\xi) \\
F_S &= -\tfrac{1}{2}(T_{11}((\phi_2-\phi_1)(1-\eta)+(\phi_3-\phi_4)\eta)+T_{12}((\phi_4-\phi_1)(1-\xi)+(\phi_3-\phi_2)\xi) \\
F_E &= -\tfrac{1}{2}(T_{12}((\phi_2-\phi_1)(1-\eta)+(\phi_3-\phi_4)\eta)+T_{22}((\phi_4-\phi_1)(1-\xi)+(\phi_3-\phi_2)\xi) \\
F_W &= -\tfrac{1}{2}(T_{12}((\phi_2-\phi_1)(1-\eta)+(\phi_3-\phi_4)\eta)+T_{22}((\phi_4-\phi_1)(1-\xi)+(\phi_3-\phi_2)\xi)
\end{aligned} \tag{4.22}$$

where it is understood that each flux can have its own local coordinates, e.g. $F_S = F_S(\xi_S, \eta_S)$. The range over which each flux is defined is given in table 4.2 below.

Flux	ξ	η
F_N	$\frac{1}{2}$	$\frac{1}{2} < \eta \leq 1$
F_S	$\frac{1}{2}$	$0 \leq \eta < \frac{1}{2}$
F_E	$\frac{1}{2} < \xi \leq 1$	$\frac{1}{2}$
F_W	$0 \leq \xi < \frac{1}{2}$	$\frac{1}{2}$

Table 4.2: **CVFE Fluxes**

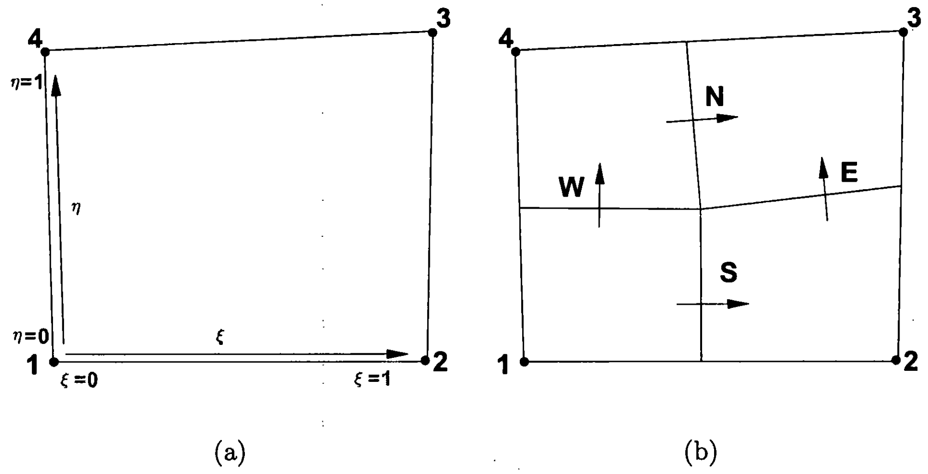

Figure 4.5: (a) local CVFE coordinate system (b) local CVFE fluxes

In this chapter we focus on a single parametric family of schemes. For constant coefficients, the correspondence between the flux-continuous CVD schemes and CVFE schemes is understood through $\xi = \eta = \eta(q)$. The N, S, E, W fluxes correspond with the parametric definition of the 4 control-volume subfaces that are inside the cell. For example, F_S is defined at a point on the subcell control-volume subface Fig. 4.5, where $\xi_S = 1/2$. Similarly F_E is defined on the adjoining control-volume subface Fig.4.5, where $\eta_E = 1/2$ so that

$$\begin{aligned} F_S &= -\tfrac{1}{2}(T_{11}((\phi_2 - \phi_1)(1 - \eta) + (\phi_3 - \phi_4)\eta) + \tfrac{1}{2}T_{12}((\phi_4 - \phi_1) + (\phi_3 - \phi_2))) \\ F_E &= -\tfrac{1}{2}(\tfrac{1}{2}T_{12}((\phi_2 - \phi_1) + (\phi_3 - \phi_4)) + T_{22}((\phi_4 - \phi_1)(1 - \xi) + (\phi_3 - \phi_2)\xi)) \end{aligned} \tag{4.23}$$

where the parameter range is defined in table 4.2 with $\xi = \eta$, double parameter families ($\xi \neq \eta$) will be presented in the next chapter. The analysis is simplified by normalizing the flux parameter range by using the same variable η and the same parameter range ($0 \leq \eta < \frac{1}{2}$) for all fluxes and e.g. the flux pair F_S, F_E are given by

$$\begin{aligned} F_S &= -\tfrac{1}{2}(T_{11}((\phi_2 - \phi_1)(1 - \eta) + (\phi_3 - \phi_4)\eta) + \tfrac{1}{2}T_{12}((\phi_4 - \phi_1) + (\phi_3 - \phi_2)) \\ F_E &= -\tfrac{1}{2}(\tfrac{1}{2}T_{12}((\phi_2 - \phi_1) + (\phi_3 - \phi_4)) + T_{22}((\phi_4 - \phi_1)\eta + (\phi_3 - \phi_2)(1 - \eta)) \end{aligned} \tag{4.24}$$

where each flux is defined in it's own local coordinate system and the base schemes of each flux parameterization now correspond with $\eta = 0$. The nine-point scheme coefficients are listed in the CVFE table 4.3 below where the numbering of coefficients is indicated in Fig.4.4.

Flux-continuity and Local Conservation

We note that CVFE schemes are locally conservative, but not flux continuous; A flux-continuous finite-volume scheme is locally conservative however the converse is not necessarily true and CVFE is a case in point. Of course CVFE is trivially flux continuous over the control-volume faces [1], but in the CVFE formulation key flux continuity is lacking across the interior interfaces across which the permeability can

int coords	**Coefficients**	**Full Tensor**
i,j	M_{11}	$2(T_{11}+T_{22})-2\eta(T_{11}+T_{22})$
i+1,j	M_{12}	$-T_{11}+\eta(T_{11}+T_{22})$
i+1,j+1	M_{13}	$-\frac{1}{2}\eta(T_{11}+T_{22})-\frac{1}{2}T_{12}$
i,j+1	M_{14}	$-T_{22}+\eta(T_{11}+T_{22})$
i-1,j+1	M_{15}	$-\frac{1}{2}\eta(T_{11}+T_{22})+\frac{1}{2}T_{12}$
i-1,j	M_{16}	$-T_{11}+\eta(T_{11}+T_{22})$
i-1,j-1	M_{17}	$-\frac{1}{2}\eta(T_{11}+T_{22})-\frac{1}{2}T_{12}$
i,j-1	M_{18}	$-T_{22}+\eta(T_{11}+T_{22})$
i+1,j-1	M_{19}	$-\frac{1}{2}\eta(T_{11}+T_{22})+\frac{1}{2}T_{12}$

Table 4.3: **CVFE** *Family Coefficients For Constant Tensor Field*

be discontinuous in the general case. In the M-matrix analysis summary presented in this chapter, schemes are compared for the simplified case of a spatially constant full-tensor field.

4.5 Family of Flux-Continuous Schemes with Full Pressure Continuity

The family of flux-continuous schemes presented in section 4.3 fulfills a number of desirable constraints. However, these schemes are only continuous in pressure and flux in a pointwise sense. Here we introduce a new class of schemes which have continuous pressure support over the entirety of each sub-face. This is achieved by introducing a further interface pressure at the common corner of the four subcells as indicated in Fig.4.6 (a), i.e. at the common primal grid vertex if cell-centred and at the centre of gravity of the primal-cell if the formulation is cell vertex. This enables a bilinear support in pressure to be introduced over each subcell so that *full pressure continuity* is achieved over the faces of each control-volume. The bilinear support retains a degree of freedom in position of flux continuity on a subface, and is motivated in part by the generality of the CVFE framework of section 4.4, however it is emphasized here

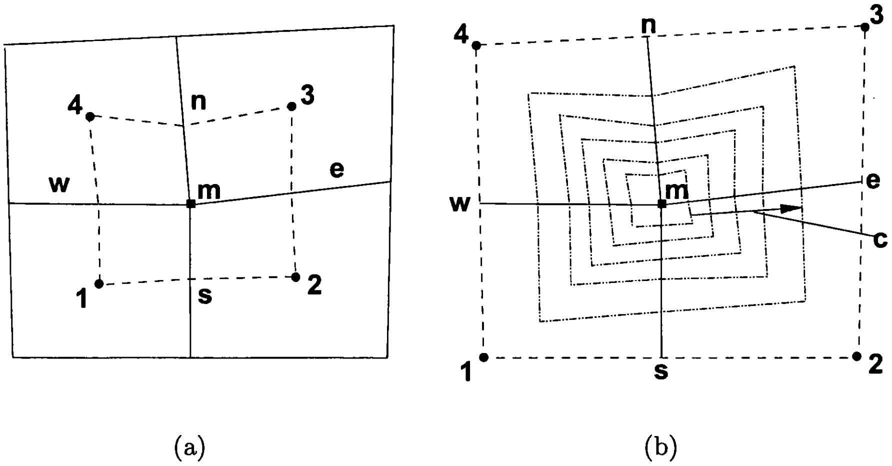

Figure 4.6: (a) FPS Dual cell (dashed) with auxiliary pressure nodes n, s, e, w, m and subcells $(1, s, m, w)$, $(s, 2, e, m)$, $(m, e, 3, n)$, $(w, m, n, 4)$ (b) Example range of auxiliary Control-volumes (dashed) centred on m

that the following schemes are designed to be flux continuous over the control-volume faces that separate the piecewise constant variation in permeability field, leading to a new family of flux-continuous schemes with full pressure support FPS.

The extra degree of freedom in pressure connecting the four subcells of the dual cell requires an additional constraint equation per dual-cell. Here we employ a similar approach to that of [33] and solve for the additional degree of freedom by imposing the discrete integral form of Eq.4.1 to hold over the dual-cell. For incompressible flow away from a source/sink this effectively ensures that the dual-cell is divergence free. In order to define the additional dual-cell divergence approximation an auxiliary control-volume surrounding the dual-cell centre is introduced as indicated with the dashed line in Fig.4.6 (b). Details for the cell centred formulation follow below.

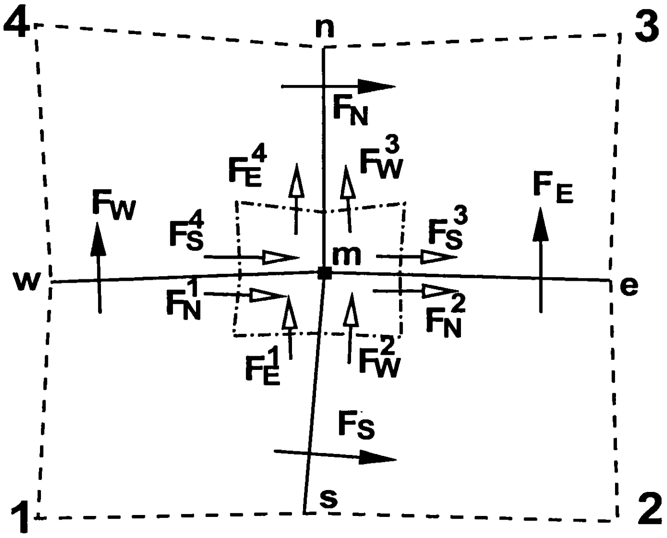

Figure 4.7: Fluxes in dual cell: Solid arrow = primal-flux, hollow arrow = auxiliary control-volume flux

4.5.1 Family of CVD(MPFA) Full Pressure Continuity Schemes - Quadrature parameterization

In this formulation the *lower-case* indices (n, s, e, w) indicate the mid-points of the primal grid cell faces, that are connected to the dual-cell mid-point m forming the interior subcell faces. After introduction of a further interface pressure at the common corner m of the four subcells (i.e. at the dual-cell centre) indicated in Fig. 4.6, 4.7, the set of local interface pressures to be determined over the dual-cell is given by $\Phi_f = (\phi_n, \phi_s, \phi_e, \phi_w, \phi_m)^T$. A subcell bilinear approximation of pressure and position vector is introduced locally over each subcell with local parametric coordinates $(0 \leq \tilde{\xi}, \tilde{\eta} \leq 1)$, from which approximate derivatives are derived over each sub-cell. For example over subcell 1 Fig. 4.6 (a), (with corners labeled anti-clockwise $(1, s, m, w)$) we obtain

$$\begin{aligned} \phi_{\tilde{\xi}} &= (1 - \tilde{\eta})(\phi_s - \phi_1) + \tilde{\eta}(\phi_m - \phi_w) \\ \phi_{\tilde{\eta}} &= (1 - \tilde{\xi})(\phi_w - \phi_1) + \tilde{\xi}(\phi_m - \phi_s) \end{aligned} \tag{4.25}$$

and

$$\begin{aligned}\mathbf{r}_{\tilde{\xi}} &= (1-\widetilde{\eta})(\mathbf{r}_s-\mathbf{r}_1)+\widetilde{\eta}(\mathbf{r}_m-\mathbf{r}_w)\\ \mathbf{r}_{\tilde{\eta}} &= (1-\widetilde{\xi})(\mathbf{r}_w-\mathbf{r}_1)+\widetilde{\xi}(\mathbf{r}_m-\mathbf{r}_s)\end{aligned} \tag{4.26}$$

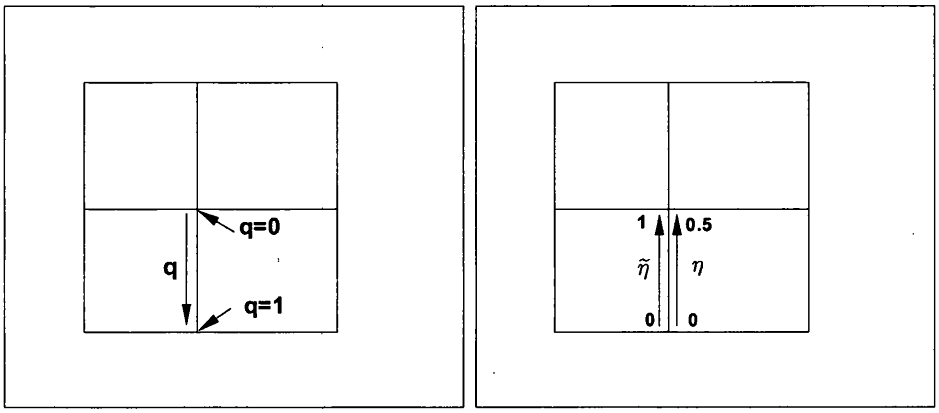

(a) (b)

Figure 4.8: (a)Variation of q for TPS (b)Variation of η for FPS and CVFE

Using equations 4.25,4.26 the discrete Darcy velocity at S is defined as

$$\mathbf{v}_h = -\mathbf{K}^1\nabla\phi_h = -\mathbf{K}^1\mathbf{G}(\widetilde{\eta})\begin{pmatrix}\phi_{\tilde{\xi}}\\ \phi_{\tilde{\eta}}\end{pmatrix} \tag{4.27}$$

where $\mathbf{K}^1$ is the local permeability tensor of vertex 1 and dependency of $\nabla\phi_h$ on quadrature point arises through

$$\nabla\phi_h = \mathbf{G}(\widetilde{\eta})\begin{pmatrix}\phi_{\tilde{\xi}}\\ \phi_{\tilde{\eta}}\end{pmatrix} = \begin{pmatrix}y_{\tilde{\eta}} & -y_{\tilde{\xi}}\\ -x_{\tilde{\eta}} & x_{\tilde{\xi}}\end{pmatrix}\frac{1}{J(x,y)}\begin{pmatrix}\phi_{\tilde{\xi}}\\ \phi_{\tilde{\eta}}\end{pmatrix} \tag{4.28}$$

Approximate $\mathbf{r}_{\tilde{\xi}}$ and $\mathbf{r}_{\tilde{\eta}}$ are defined by Eq. 4.26 and $J(x,y) = x_{\tilde{\xi}}y_{\tilde{\eta}} - x_{\tilde{\eta}}y_{\tilde{\xi}}$ over a subcell. The discrete normal Darcy flux at the left hand side of S (see Fig.4.7), is then resolved along the outward normal vector $dL_S = ((y_m - y_s), -(x_m - x_s))$ and is expressed in terms of the resulting discrete general tensor $\mathbf{T} = \mathbf{T}(\widetilde{\xi}, \widetilde{\eta})$ as

$$F_S^1 = \mathbf{v}_h \cdot dL_S = -(T_{11}^1 \phi_{\widetilde{\xi}} + T_{12}^1 \phi_{\widetilde{\eta}})|_S^1 \tag{4.29}$$

where it is understood that the coefficients of $-(\phi_{\widetilde{\xi}}, \phi_{\widetilde{\eta}})|_S^1$ denoted by $T_{11}|_S^1$ and $T_{12}|_S^2$ are sub-cell (physical-space) approximations of the general tensor components (Eq. 4.29) at the left hand face at S, which result from normal flux resolution. A similar expression for flux is obtained at the right hand side of S from subcell 2 (Fig.4.7). The south flux is a function of $\widetilde{\eta}$. Similarly sub-cell fluxes are resolved on the two sides of the other subfaces at E, W and N. Flux continuity is then imposed across the four cell interfaces at the four positions N, S, E, W (Fig.4.7) which are specified by chosen quadrature points. The N, S, E, W fluxes are defined here with respect to $\widetilde{\eta}$.

As in the TPS formulation *upper-case* N, S, E, W define the flux positions of the family of FPS schemes on the control-volume sub-faces. However, unlike the TPS formulation the FPS interface pressures $(\phi_n, \phi_s, \phi_e, \phi_w)$ remain attached to the mid-points of the primal grid cell faces. The flux continuity conditions of Eq. 4.14 are now redefined using the above approximate derivatives of ϕ and $\mathbf{r}$ given in Eq.'s 4.25-4.26 which replace that of Eq.'s 4.9, 4.10. The family of schemes is defined by a symmetric position of flux continuity parameterized by the local basis function $\widetilde{\eta}$, with respect to pairs of subcell faces. The FPS flux position is later expressed in terms of the CVFE parameter η where $\eta = \widetilde{\eta}/2$ (shown later) and with respect to the TPS parameter q, with $\eta = (1-q)/2$ so that the interval of FPS flux integration $0 \leq \eta < \frac{1}{2}$ can be readily compared with CVFE and TPS, c.f. Fig.4.8. This aids the comparison between TPS, CVFE and FPS schemes presented below. To clarify notation, for example F_S will denote a flux at a quadrature point that may either coincide with s or be between s and m, but never coincides with m, i.e. $0 \leq \widetilde{\eta} < 1$ or $1 \geq q > 0$ or equivalently $0 \leq \eta < \frac{1}{2}$. The additional discrete divergence condition for determining ϕ_m is added to the four interface continuity conditions leading to the local algebraic system

$$
\begin{aligned}
F_N &= -(T_{11}\phi_{\tilde{\xi}} + T_{12}\phi_{\tilde{\eta}})|_N^3 = -(T_{11}\phi_{\tilde{\xi}} + T_{12}\phi_{\tilde{\eta}})|_N^4, \\
F_S &= -(T_{11}\phi_{\tilde{\xi}} + T_{12}\phi_{\tilde{\eta}})|_S^1 = -(T_{11}\phi_{\tilde{\xi}} + T_{12}\phi_{\tilde{\eta}})|_S^2, \\
F_E &= -(T_{12}\phi_{\tilde{\xi}} + T_{22}\phi_{\tilde{\eta}})|_E^2 = -(T_{12}\phi_{\tilde{\xi}} + T_{22}\phi_{\tilde{\eta}})|_E^3, \\
F_W &= -(T_{12}\phi_{\tilde{\xi}} + T_{22}\phi_{\tilde{\eta}})|_W^1 = -(T_{12}\phi_{\tilde{\xi}} + T_{22}\phi_{\tilde{\eta}})|_W^4, \\
&- \textstyle\sum_{\partial\Omega_{AUX}} (\mathbf{K}\nabla\Phi)\cdot\hat{\mathbf{n}}\Delta s = 0
\end{aligned}
\tag{4.30}
$$

Here we illustrate discrete flux continuity for the second equation of Eq.4.30, at a point S between s and m with

$$
\begin{aligned}
F_S &= -(T_{11}^1((1-\widetilde{\eta})(\phi_s - \phi_1) + \widetilde{\eta}(\phi_m - \phi_w) - T_{12}^1(\phi_m - \phi_s)) \\
&= -(T_{11}^2((1-\widetilde{\eta})(\phi_2 - \phi_s) + \widetilde{\eta}(\phi_e - \phi_m) - T_{12}^2(\phi_m - \phi_s))
\end{aligned}
\tag{4.31}
$$

where for the left hand side flux, approximations of $\phi_{\tilde{\xi}}$ and $\phi_{\tilde{\eta}}$ are given by Eq.4.25. Analogous sub-cell approximations are constructed for each of the flux continuity conditions in Eq.4.30. The alternative q parameterization of flux continuity is given by

$$
\begin{aligned}
F_S &= -(T_{11}^1(q(\phi_s - \phi_1) + (1-q)(\phi_m - \phi_w) - T_{12}^1(\phi_m - \phi_s)) \\
&= -(T_{11}^2(q(\phi_2 - \phi_s) + (1-q)(\phi_e - \phi_m) - T_{12}^2(\phi_m - \phi_s))
\end{aligned}
\tag{4.32}
$$

Referring now to the auxiliary control-volume (perimeter shown dot-dashed) centred on the auxiliary node m of Fig. 4.7 the auxiliary control-volume is comprised of 4 *sub-subcells* one in each subcell. The discrete approximation of the 5^{th} equation in the set of Eq.4.30 which represents the local auxiliary divergence condition is constructed in an analogous procedure to that of the primary control-volume approximation of divergence, with eight fluxes one per subface of the auxiliary control-volume. Since the auxiliary control-volume faces lie inside the primary control-volumes where permeability is piecewise constant, the auxiliary control-volume approximation is based on the CVFE formulation. The auxiliary control-volume fluxes are parameterized with $1 \geq p > 0$, where p is a free parameter that defines the local auxiliary flux quadrature, although $p = q$ is one possibility. Note that the auxiliary control-volume can lie in or on the dual-cell, the actual size of the auxiliary control-volume is a further degree of freedom to be chosen within the scheme, and is parameterized by the variable $1 \geq c > 0$, where $c = 1$ corresponds to an auxiliary control-volume that matches the dual-cell and as $c \to 0$ the auxiliary control-volume tends to zero. The primal control-volume and auxiliary control-volume fluxes are indicated in Fig. 4.7, with solid arrows for primal fluxes and hollow arrows for auxiliary fluxes. The auxiliary fluxes have super-fixes indicating the auxiliary subcell and compass suffices indicating position relative to the primal subcell in which they are defined. For example referring again to subcell 1 (corners $1, s, m, w$), the auxiliary control-volume flux F_N^1 is defined on the top left sub-subcell face by

$$\begin{aligned} F_N^1 = c(&-T_{11}^1(c(1-p)(\phi_s - \phi_1) + (1 - c(1-p))(\phi_m - \phi_w)) \\ &-T_{12}^1(c(\phi_w - \phi_1) + (1-c)(\phi_m - \phi_s))) \end{aligned} \tag{4.33}$$

which is a function of the auxiliary quadrature and control-volume size parameters p and c respectively and the tensor here is defined with respect to the auxiliary subcell. In the general case this formulation leads to a multiple family of schemes which are functions of the main flux continuity point parameter q, the auxiliary control-volume flux parameter p and auxiliary control-volume size parameter c.

The degrees of freedom of the five equation system Eq.4.30 are the five interface pressures $\Phi_f = (\phi_n, \phi_s, \phi_e, \phi_w, \phi_m)^T$ and the four primal cell centred pressures $\Phi_c = (\phi_1, \phi_2, \phi_3, \phi_4)^T$. The system of equations is rearranged in a similar form to Eq. 4.15 viz

$$A_L^{5X5}\Phi_f + B_L^{5X4}\Phi_c = A_R^{5X5}\Phi_f + B_R^{5X4}\Phi_c \tag{4.34}$$

where A_L^{5X5}, A_R^{5X5} are 5X5 matrices and B_L^{5X4}, B_R^{5X4} 5X4 matrices. Since we only require the four fluxes, we let A_L^{4X5} denote the first four rows of matrix A_L^{5X5} and B_L^{4X4} denote the first four rows of matrix B_L^{5X4}.

The dependence on Φ_f is removed via Eq.4.34 and the continuous fluxes of the families of FPS schemes are now expressed in terms of Φ_c with

$$\mathbf{F} = (A_L^{4X5}(A_L^{5X5} - A_R^{5X5})^{-1}(B_R^{5X4} - B_L^{5X4}) + B_L^{4X4})\Phi_c$$

For a spatially constant tensor field on a logically rectangular grid the family of full pressure support (FPS) schemes reduce to nine-point schemes with coefficients given in the table 4.4 below.

integer coords	**Coeff'ts**	**Full Tensor**
i,j	M_{11}	$2(T_{11}+T_{22}) - 2(T_{11}+T_{22})(\alpha_F + \beta_F ER)$
i+1,j	M_{12}	$-T_{11} + (T_{11}+T_{22})(\alpha_F + \beta_F ER)$
i+1,j+1	M_{13}	$-\frac{1}{2}(T_{11}+T_{22})(\alpha_F + \beta_F ER) - \frac{T_{12}}{2}$
i,j+1	M_{14}	$-T_{22} + (T_{11}+T_{22})(\alpha_F + \beta_F ER)$
i-1,j+1	M_{15}	$-\frac{1}{2}(T_{11}+T_{22})(\alpha_F + \beta_F ER) + \frac{T_{12}}{2}$
i-1,j	M_{16}	$-T_{11} + (T_{11}+T_{22})(\alpha_F + \beta_F ER)$
i-1,j-1	M_{17}	$-\frac{1}{2}(T_{11}+T_{22})(\alpha_F + \beta_F ER) - \frac{T_{12}}{2}$
i,j-1	M_{18}	$-T_{22} + (T_{11}+T_{22})(\alpha_F + \beta_F ER)$
i+1,j-1	M_{19}	$-\frac{1}{2}(T_{11}+T_{22})(\alpha_F + \beta_F ER) + \frac{T_{12}}{2}$

Table 4.4: *q-Family (FPS) Coefficients For Constant Tensor Field*

Where it is understood that $\alpha_F = \frac{(1-q)}{2}$, $\beta_F = \frac{cq}{2(q+pc-c)}$, $R = \frac{H_M}{A_R}$ which is the ratio of the harmonic mean to arithmetic mean of diagonal coefficients T_{11}, T_{22} where $H_M = 2\frac{T_{11}T_{22}}{T_{11}+T_{22}}$, $A_R = \frac{T_{11}+T_{22}}{2}$ and therefore $R \leq 1$, and as before (for the TPS scheme) $E = \frac{T_{12}^2}{T_{11}T_{22}}$ is an ellipticity measure and it follows that $ER \leq 1$.

4.5.2 Triangular FPS Schemes

The generalisation of the method to triangle grids follows a similar procedure to the quadrilateral grid method. For the cell-vertex case, with primary vertex pressures $\Phi_V = (\phi_1, \phi_2, \phi_3)^T$ are defined at the triangle vertices, Fig 4.9. There are now three subcells meeting inside the triangle, so that the triangle acts as the dual-cell. An interface pressure is introduced at the mid-point of each triangle edge and one at the centre where the subcells meet so that $\Phi_f = (\phi_n, \phi_s, \phi_e, \phi_m)^T$. A local bilinear

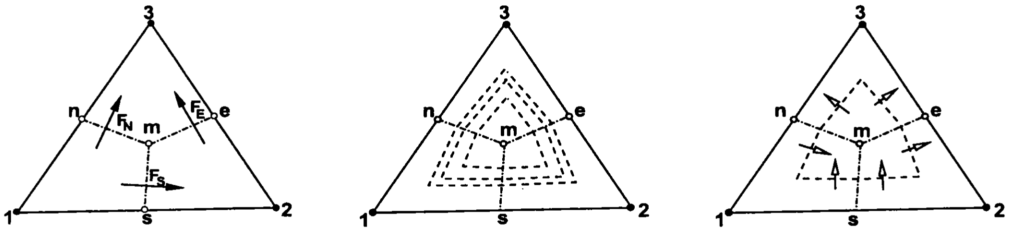

(a) (b) (c)

Figure 4.9: (a)Subcells of primary control-volumes (Primary fluxes solid arrows) (b) Example Auxiliary Control volumes (dashed lines) (c) Auxiliary fluxes on auxiliary dashed sub-faces

variation in pressure is introduced over each subcell as before. One flux continuity condition is imposed at each of the three subcell faces leading to three fluxes $\mathbf{F} = (F_N, F_S, F_E)^T$, and zero divergence is applied over a sub-control-volume surrounding the triangle centre of gravity, providing a total of four equations for the four auxiliary pressures Φ_f.

The resulting system of equations are given by

$$\begin{aligned}
F_N &= -(T_{11}\phi_{\tilde{\xi}} + T_{12}\phi_{\tilde{\eta}})|_N^3 = -(T_{11}\phi_{\tilde{\xi}} + T_{12}\phi_{\tilde{\eta}})|_N^4, \\
F_S &= -(T_{11}\phi_{\tilde{\xi}} + T_{12}\phi_{\tilde{\eta}})|_S^1 = -(T_{11}\phi_{\tilde{\xi}} + T_{12}\phi_{\tilde{\eta}})|_S^2, \\
F_E &= -(T_{12}\phi_{\tilde{\xi}} + T_{22}\phi_{\tilde{\eta}})|_E^2 = -(T_{12}\phi_{\tilde{\xi}} + T_{22}\phi_{\tilde{\eta}})|_E^3, \\
&-\textstyle\sum_{\partial\Omega_{AUX}} (\mathbf{K}\nabla\Phi)\cdot\hat{\mathbf{n}}\Delta s = 0
\end{aligned} \tag{4.35}$$

and represent the triangle equivalent of Eq. 4.30. Approximation of Eq.4.35 and subsequent elimination of the auxiliary pressures follows an analogous procedure to that of Eq's.4.33-4.34. Primal divergence is then approximated by the assembly of continuous control-volume subcell fluxes over each polygon surrounding each vertex.

4.6 Positivity and M-matrices

The families of flux-continuous schemes TPS and FPS both result in a discrete matrix which forms 5-9 row entries in 2D and 7-27 row entries in 3D on a structured grid. The discrete systems can be written as

$$\mathbf{A}\phi = b \tag{4.36}$$

Where **A** is the discrete matrix operator, ϕ is the unknown pressure and b is the source term. Ideally the discrete system of equation 4.36 should be *monotone*, and satisfy a *maximum principle* that is analogous to that of the continuous counterpart of the discrete problem and hence ensuring that the numerical solution is free from nonphysical oscillations. The discrete matrix operator **A** is *monotone* if and only if **A** is non-singular and it obeys the following condition[104]

$$\mathbf{A}^{-1} \geq \mathbf{O} \tag{4.37}$$

where **O** is a zero matrix. While a monotone discretization matrix ensures that a non-negative source and boundary data yields a non-negative pressure field, it has not been proven that a monotone discretization matrix will prevent discrete spurious local extrema occuring in the discrete solution of the general tensor pressure equation. A sufficient condition for a maximum principle (which can ensure that no spurious extrema occur in the discrete solution) is that **A** is an **M**−matrix, i.e. monotone or positive definite with $a_{i,j} \leq 0, i \neq j$.

Conditions for an M-matrix

The following set of conditions are often easier to verify;

A is an **M**−matrix if

$$\begin{aligned} a_{i,i} &> 0, \forall i \\ a_{i,j} &\leq 0, \forall i, j, i \neq j \\ \Sigma_j a_{i,j} &\geq 0, \forall i \end{aligned} \tag{4.38}$$

In addition **A** must be either strictly diagonally dominant (strict inequality in the latter of Eq. 4.38) or weakly diagonally dominant with strict inequality for at least one row, **A** must also be irreducible [104].

Use of the term monotonicity is too strong when describing multi-dimensional solutions, as the local solution can often have a saddle point in structure [17]. Here the term positivity is used as defined below.

4.6.1 Positivity

Following Edwards and Zheng [17], the term positivity is defined below.

For the i^{th} equation of Eq.4.36, away from any source or sink, it follows that

$$\phi_i = -\frac{1}{a_{ii}} \sum_{j(i \neq j)} a_{ij} \phi_j \tag{4.39}$$

If **A** is an M-matrix, by consistency for a constant potential field it follows from Eq.4.39 that each non-specified ϕ_i is a convex average of its connecting neighbours. Thus each ϕ_i is bounded between the maximum and minimum of connecting neighbours, such a condition is consistent with the absence of spurious oscillations and defines a local discrete maximum principle. When **A** is an M-matrix Eq.4.39 defines a positive scheme where the weights of ϕ_j are *positive* and sum to unity.

The first M-matrix analysis for schemes of this type is presented in [4, 1, 2, 17], where conditions for nine-node flux continuous schemes to be an M-Matrix are

$$min(T_{1,1}, T_{2,2}) \geq \eta(T_{1,1} + T_{2,2}) \geq | T_{1,2} | \tag{4.40}$$

and η is a function of quadrature point. One of the essential conditions here is that

$$\mid T_{1,2} \mid \leq min(T_{1,1}, T_{2,2}) \tag{4.41}$$

which is only *sufficient for ellipticity* [4] and therefore quite limiting on the range of tensors that are applicable. Tensors that are elliptic with

$$T_{1,2}^2 \leq T_{1,1}T_{2,2} \tag{4.42}$$

and are such that $\mid T_{1,2} \mid > min(T_{1,1}, T_{2,2})$ violate the M-Matrix criteria of Eq. 4.40 and expose the M-Matrix limit.

Numerical examples are presented in the results section where the maximum principle is violated and in these cases the methods do not possess an M-matrix or a monotone matrix. Examples are presented for both TPS and FPS flux-continuous finite volume CVD(MPFA) schemes.

4.6.2 Related Work on Stability

In many cases discrete stable solutions of second order elliptic full tensor problems that are free of spurious oscillations can be computed with schemes that do not necessarily obey the M-matrix conditions needed to ensure a maximum principle. In [43] rather than an M-matrix, a monotone matrix is pursued for monotonicity. The authors present a detailed analysis to derive the conditions that are sufficient for the matrix to be monotone. Plots of monotone matrix regions are given in the tensor coefficient plane [43] expressed in terms of the minimum diagonal tensor coefficient versus the absolute off-diagonal tensor coefficient, normalized with respect to the maximum diagonal tensor coefficient. While this is an interesting viewpoint, as discussed above, it has not been proven that a monotone matrix will ensure a discrete solution is obtained without spurious oscillations. Such a solution can be obtained if the matrix is an M-matrix. A monotone matrix is an M-matrix if the off-diagonal coefficients are not positive and thus a monotone matrix is only part of the condition required for a discrete maximum principle as discussed above. From the monotone matrix conditions together with the negative inequality conditions for off-diagonals (i.e. M-matrix conditions), [43] goes on to arrive at the same M-matrix bounds as first presented in [1, 2] (in slightly different notation). An optimal scheme is also identified which corresponds to the quadrature point defined by Eq.4.47 below, first presented in [2]. We illustrate the M-matrix conditions of the schemes presented here in the tensor coefficient plane further below.

However, the major challenge to all schemes occurs when the crucial sufficient M-matrix condition of Eq.4.41 is violated, i.e. when $(min(T_{1,1}, T_{2,2})^2 < T_{1,2}^2 \leq T_{1,1}T_{2,2})$. In this case the schemes do not have M-matrices or monotone matrices. Four types of discretization have been proposed to date to overcome this limitation; The first two involve constructing the discrete approximation based on that resulting from the optimal point defined by Eq.4.47 below, either by special case triangulation according to anisotropy angle [23] or by special case construction also according to anisotropy [101]. The second two approaches involve non-linear flux approximation, either by flux-splitting with an imposed maximum principle [21, 22] or by a local positivity preserving approximation [41]. The approach adopted here involves using the optimal point of Eq.4.47 as a quadrature point. The analysis below shows that the optimal quadrature point can be selected by the FPS and CVFE families for all elliptic tensors, but when strong full-tensor anisotropy is present the optimal point is outside the TPS quadrature range [17].

First the relationship between the new Full-Pressure Support FPS family, the original Triangle Pressure Support (TPS) family and control-volume finite element (CVFE) family is presented for the case of spatially constant full tensor coefficients.

4.7 Relationship between TPS, FPS and CVFE for a spatially constant tensor

In this section we will present a novel mapping between TPS, FPS and CVFE for a spatially constant tensor. A detailed discussion can be found in [17] by Edwards and Zheng.

A correspondence (or mapping) between the flux-continuous CVD family coefficients and the CVFE family coefficients is now established for a spatially constant general full-tensor field. By definition since the general full-tensor is assumed to be spatially constant, there is no need to take account of discontinuous coefficients (fluxes are automatically continuous) and the analysis simplifies considerably. However the construction of triangle pressure support (TPS) and full pressure support (FPS) in the case of constant tensor coefficients still yields families of schemes with distinct properties. The mapping between schemes enables us to understand important consequences of the different discretizations, basically from a single analysis which is verified by practical examples.

In this case the CVD(MPFA) flux continuous (TPS) and (FPS) schemes take same form as the family of CVFE schemes. For a spatially constant full tensor the schemes take the common form

$$\begin{aligned}
&-\Bigg(T_{11}(\phi_{i+1,j}-2\phi_{i,j}+\phi_{i-1,j})+T_{22}(\phi_{i,j+1}-2\phi_{i,j}+\phi_{i,j-1})\\
&+\tfrac{T_{12}}{2}\Big(\phi_{i+1,j+1}-\phi_{i-1,j+1}+\phi_{i-1,j-1}-\phi_{i+1,j-1}\Big)\\
&+\tfrac{\eta}{2}(T_{11}+T_{22})\Big(4\phi_{i,j}-2(\phi_{i+1,j}+\phi_{i-1,j}+\phi_{i,j+1}+\phi_{i,j-1})\\
&+\phi_{i+1,j+1}+\phi_{i-1,j+1}+\phi_{i-1,j-1}+\phi_{i+1,j-1}\Big)\Bigg)
\end{aligned} \tag{4.43}$$

where the latter difference term of Eq.4.43 multiplying $\frac{\eta}{2}(T_{11}+T_{22})$ is a mixed fourth derivative approximation. The nature of η in this term governs the actual difference between the schemes for a constant general full-tensor field. The coefficients of the respective TPS and FPS families are given in table 4.1 and table 4.4 above, for a spatially constant full-tensor field. The coefficients of the CVFE family are given in table 4.3. Inspection of Eq.4.43 and comparison between tables 4.1,4.4 and 4.3 shows that for a constant tensor the flux continuous schemes *map* on to the CVFE scheme for specific functional definitions of $\eta = \eta(q)$ as shown below. We also note that since the CVFE family is symmetric positive definite see [17], it follows from the mappings below that the TPS and FPS families of schemes are therefore symmetric positive definite for spatially constant elliptic tensor coefficients for $\eta < 1/2$.

4.7.1 Triangle Pressure Support TPS

For the TPS schemes (compare table 4.1 and 4.3) the mapping corresponds with η in the CVFE scheme defined by

$$\eta(q) = \alpha_T + \beta_T E = \frac{(1-q)}{2(2-q)} + \frac{1}{2(2-q)}E \tag{4.44}$$

where α_T, β_T and E are defined in section 3 above and from which it follows that $\alpha_T + \beta_T E \leq 1/2$.

4.7.2 Full Pressure Support FPS

For the FPS schemes (compare table 4.4 and 4.3) the mapping corresponds with η in the CVFE scheme defined by

$$\eta(q) = \alpha_F + \beta_F ER = \frac{(1-q)}{2} + \frac{cq}{2(q+pc-c)}ER \tag{4.45}$$

where α_F, β_F and ER are defined in section 5 and from which it follows that $\alpha_F + \beta_F ER \leq 1/2$. Thus both schemes are within the range of the CVFE η family. The η family embodies *all* single parameter 9-point schemes, reduced support schemes and the subordinate 7-point schemes. This is made clear below. Therefore an M-matrix analysis of the CVFE family with coefficients in table 4.3 is directly applicable to the TPS and FPS families with coefficients of table 4.1 and table 4.4 via the relationship given by Eq's. 4.44, 4.45 and is performed below.

4.7.3 Cell-wise M-matrix Conditions

An M-matrix test is easily conducted by considering cell-wise assembly of fluxes and performing a cell-wise M-matrix analysis following [1]. We refer the detailed discussion to Edwards and Zheng [17], and the crucial condition for a CVFE scheme to have an M-maxtrix is listed below:

$$| T_{12} | \leq \eta(T_{11} + T_{22}) \leq min(T_{11}, T_{22}) \tag{4.46}$$

from which it follows that the diagonal coefficient of ϕ_2 is positive since $0 \leq \eta < \frac{1}{2}$. We note that Eq. 4.46 is identical to Eq. 4.40 which also confirms the sufficient conditions for a single family of M-matrix full-tensor schemes, cf. [2]. The M-matrix conditions of Eq.4.46 can also be seen to be sufficient by inspection of table 4.3, where the left-hand inequality is sufficient for $M_{13}, M_{15}, M_{17}, M_{19}$ to each be non-positive and the right-hand inequality is sufficient for$M_{12}, M_{14}, M_{16}, M_{18}$ to each be non-positive and for $M_{11} > 0$. These conditions now establish the following theorem [17]:

Conditional M-matrix *Any single parameter η−family of consistent locally conservative schemes on or within the 9-point stencil applied to the pressure equation with a locally constant full-tensor field can only provide a conditional M-matrix subject to Eq. 4.46. Note: FPS is exact for piecewise linear and bilinear fields, since the pressure basis functions are piecewise bilinear.*

For example, the inequality of Eq.4.46 shows that if a locally constant full-tensor is present and the basic scheme is employed, i.e. $\eta = 0$ then the M-matrix condition is unconditionally violated. However, if $\eta \neq 0$, it is possible to still obtain an M-matrix provided that Eq. 4.46 is satisfied, which places clear limitations on the range of full tensor coefficients permissible. Also since $\eta = 1/3$ corresponds the Galerkin finite element method [7] it follows that the well known Galerkin method is also subject to a conditional M-matrix. Examples will be presented in the results section.

4.7.4 Variable Support Reduction and 7-point Schemes

As noted in [2], if we choose quadrature points with

$$\eta = \mid T_{12} \mid / (T_{11} + T_{22}) \tag{4.47}$$

then an M-matrix is obtained subject to a sufficient condition for ellipticity, i.e.

$$\mid T_{12} \mid \leq min(T_{11}, T_{22}) \tag{4.48}$$

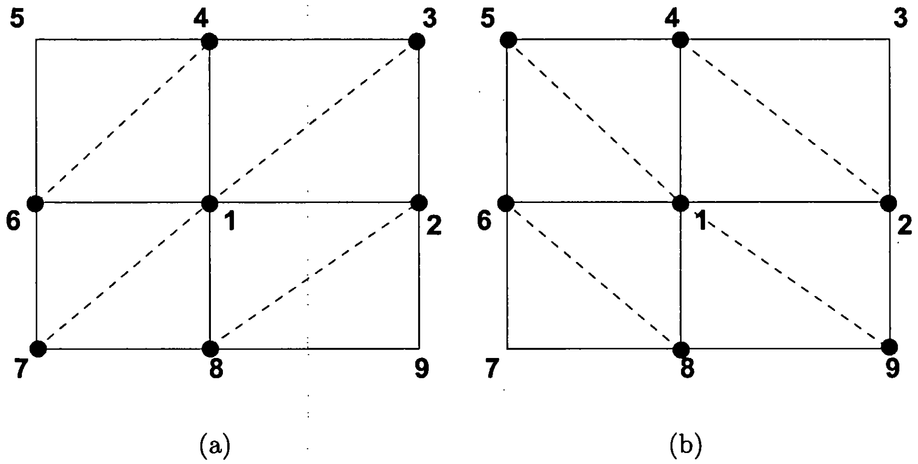

Figure 4.10: (a) T_{12} positive over all contributing dual-cells - right inclined 7 pt scheme (solid nodes) (b) T_{12} negative over all contributing dual-cells - left inclined 7 pt scheme (solid nodes)

giving the upper limit on the tensor cross-term. Upon examination of Eq. 4.24 we see that choosing the FPS (or equivalent CVFE) quadrature point of Eq.4.47

naturally reduces the coefficient of local node 4 to zero if $T_{12} > 0$, see more detailed discussion in [17]. This is also clear from the CVFE table 4.3. If the local tensor field has a positive cross-term for each contributing cell the net effect is to reduce a 9-point scheme to a 7-point (triangle) scheme with upward "+ve" support as indicated in Fig. 4.10 (a), also by CVFE table 4.3 (for a constant tensor) $M_{15} = M_{19} = 0$ while the other off-diagonals are non-positive subject to Eq.4.48. Conversely a similar analysis for the net flux contribution at node 1 reveals that if $T_{12} < 0$ a downward "-ve" triangle support" is obtained Fig. 4.10 (b), again this is also verified by inspection of the CVFE table 4.3 where in this case $M_{13} = M_{17} = 0$ when Eq.4.47 holds. We shall refer to Eq.4.47 as the *optimal support condition.* We also note that Eq.4.48 is consistent with the triangular grid M-matrix conditions presented in [10, 11], and defines the M-matrix *upper limit* for the cross coefficient $\mid T_{12} \mid$.

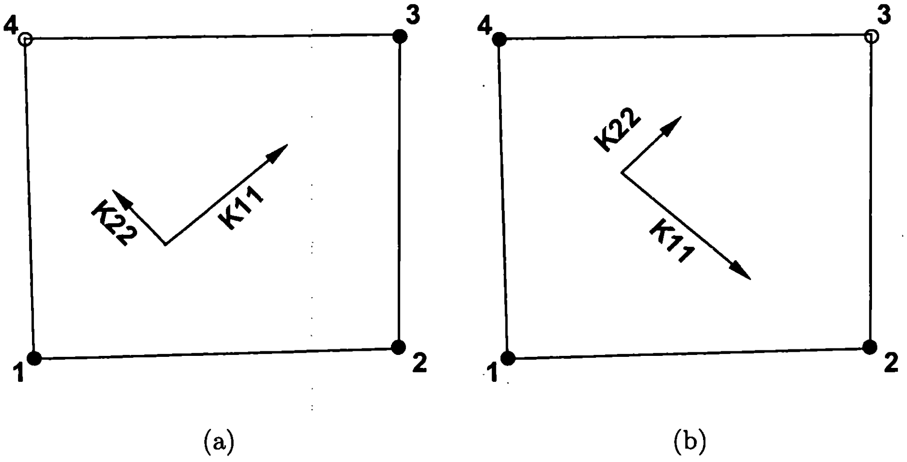

Figure 4.11: (a) Net positive T_{12} over a dual-cell: Optimal Support scheme for control-volume at 2 uses nodes $1, 2, 3$ (b) Net negative T_{12} over a dual-cell: Optimal Support scheme for control-volume at 1 uses nodes $4, 1, 2$

In general the choice of quadrature defined by Eq. 4.47 leading to (*optimal support*) yields a scheme that will select a variable support Fig. 4.11 (a),(b) that favors the local tensor anisotropy orientation (sign of the cross-terms) and can vary between a nine point scheme to a seven point scheme (on a structured grid) and maintain an M-matrix provided Eq. 4.48 holds. The general condition for nine-point schemes to reduce their support (seven point schemes of this type only result if cross terms are of the same sign for all contributing cells) depends upon η being chosen such that Eq.4.47 holds. The resulting scheme with quadrature defined by Eq.4.47 leading to *optimal support* is given in table 4.5 below for a spatially constant full tensor coefficient field.

integer coords	**Coeff'ts**	**Full Tensor**
i,j	M_{11}	$2(T_{11}+T_{22})-2\mid T_{12}\mid)$
i+1,j	M_{12}	$-T_{11}+\mid T_{12}\mid$
i+1,j+1	M_{13}	$-\frac{1}{2}(\mid T_{12}\mid +T_{12})$
i,j+1	M_{14}	$-T_{22}+\mid T_{12}\mid$
i-1,j+1	M_{15}	$-\frac{1}{2}(\mid T_{12}\mid -T_{12})$
i-1,j	M_{16}	$-T_{11}+\mid T_{12}\mid$
i-1,j-1	M_{17}	$-\frac{1}{2}(\mid T_{12}\mid +T_{12})$
i,j-1	M_{18}	$-T_{22}+\mid T_{12}\mid$
i+1,j-1	M_{19}	$-\frac{1}{2}(\mid T_{12}\mid -T_{12})$

Table 4.5: Optimal Support $\eta =\mid T_{12}\mid /(T_{11}+T_{22})$ *(FPS) Coefficients For Constant Tensor Field*

As can be seen from Table 4.5, the optimal support scheme relies upon exact algebraic cancelation for actual reduced support. Otherwise when coefficients vary over the subcells algebraic cancelation is unlikely, optimal support is then only achieved either by anisotropy angle favoring triangulation [23] or by special case construction according to anisotropy [101].

4.8 TPS versus FPS Quadrature Range

The key advantage of full pressure support (FPS) over the triangle pressure support (TPS) formulation becomes apparent when considering the range of validity of the quadrature points. The family of CVFE schemes which includes all spatially constant full-tensor 9-point schemes and their subsets are well defined for $0 \leq \eta < \frac{1}{2}$, or alternatively in terms of the common parameterization q defined above, for $1 \geq q > 0$.

4.8.1 TPS

The TPS $\eta(q)$ has a non-linear variation with respect to q, c.f. Eq. 4.44 and Table 4.1. At the ends of the $[0,1]$ q-interval for TPS

$$\begin{aligned} \eta(0) &= \tfrac{1}{4}(1+E) \\ \eta(1) &= \tfrac{1}{2}E \end{aligned} \tag{4.49}$$

which reveals that this scheme has a reduced quadrature range for the general case.

It can be shown that Eq.4.47 is outside the quadrature range when the optimal quadrature point of Eq.4.47 is less than the minimum TPS quadrature $\eta = E/2$ [17], which occurs when

$$\mid T_{12} \mid > 2T_{11}T_{22}/(T_{11}+T_{22}) \tag{4.50}$$

The latter inequality holds in three test cases presented in the results section.

4.8.2 FPS

In contrast for CVD FPS the end interval values are from Eq. 4.45 and table 4.4

$$\begin{aligned} \eta(0) &= \tfrac{1}{2} \\ \eta(1) &= \tfrac{c}{2(1+pc-c)}ER \end{aligned} \tag{4.51}$$

which recovers the upper bound of 1/2 for maximum quadrature range for a diagonal or full tensor. However from Eq.4.51 the lower bound $\eta(1)$ only tends to zero if the auxiliary control-volume size tends to zero, which occurs in the limit as $c \to 0$, showing the value of allowing the control-volume size to vary. Crucially the variation of FPS $\eta(q)$ is essentially linear in q for $1 \geq q > 0$ provided that c is sufficiently small. From Eq. 4.45 as $c \to 0$ then $\eta(q) \to (1-q)/2 = \widetilde{\eta}/2$ yielding direct correspondence between

FPS and the full family of CVFE schemes for spatially constant tensor coefficients, leading to a quadrature range that embraces all classical single parameter nine-node schemes.

We have already noted that Eq.4.47 leads to a reduced support scheme, and in particular yields a 7-point scheme if all contributing cross-terms are of the same sign. In the general case Eq.4.47 can be used to define $\eta(q)$ locally over each subcell cluster comprising a dual-cell, according to the local tensor variation. The local sign of the cross-terms over the dual cell determines the ultimate support of the FPS scheme. Thus Eq.4.47 is an example of an FPS scheme that self adapts the support, in this case such that *optimal support* is naturally selected for any tensor, by ellipticity $\mid T_{12} \mid /(T_{11} + T_{22}) \leq 1/2$. For small cross-terms, if $T_{12} \to 0$ the quadrature Eq.4.47 defaults to zero yielding the basic diagonal-tensor 5-point operator.

Other M-matrix schemes that adapt the quadrature point according to the local tensor variation can also be defined by choosing other values of $\eta(q)$ that lie in the range defined by Eq.4.46. For example choosing the right hand bound $\eta = min(T_{11}, T_{22})/(T_{11} + T_{22})$ leads to another type of reduced support scheme (H/I support discussed below and see Appendix A). Note here that the M-matrix conditions again reduce to Eq.4.48 and $\eta \to 0$ as the anisotropy and/or grid aspect ratio increases.

In the general case when the tensor varies over the dual-cell Fig. 4.2 a locally upscaled tensor is used to determine the quadrature point for the dual-cell, so that the range defined by Eq.4.46 and any consequent choice of $\eta(q)$ in the range will always be based on a locally upscaled average tensor, here local 2x2 renormalization of [6] is used to define the 2x2 subcell average tensor over the dual-cell. Consequently the optimal bound defined by Eq.4.47 can only be defined with respect to the local mean tensor of the dual-cell and will not necessarily have exact *optimal support.* If Eq.4.48 holds, then FPS may still have an M-matrix. If Eq.4.48 is violated FPS does not have an M-matrix with respect to the mean tensor, but the *mean optimal* quadrature point can still be employed. The effects and practical implications of this are considered below in the section on quasi-positive schemes.

4.8.3 M-matrix Diagrams

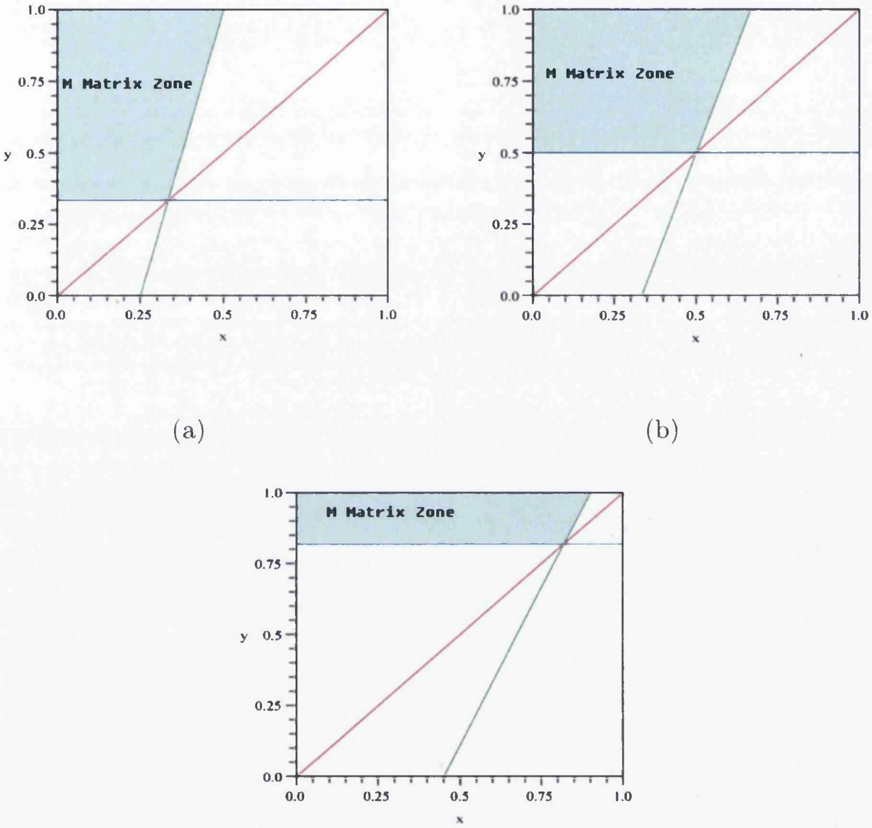

(a)

(b)

(c)

Figure 4.12: M-Matrix Zones for examples of η: (a)$\eta = \frac{1}{4}$. (b)$\eta = \frac{1}{3}$. (b)$\eta = 0.45$.

Here we present illustrative M-matrix diagrams for FPS in the (x, y) plane where we let $T_{22} = min(T_{11}, T_{22})$ and define $x = |T_{12}|/T_{11}$, $y = T_{22}/T_{11}$, so that $0 \leq x, y \leq 1$. Due to the nonlinear nature of the TPS quadrature point of Eq.4.44 with respect to x, y there is no linear correspondence between TPS and FPS in the (x, y) plane for a fixed value of q. Also, while any TPS η quadrature point belongs to FPS, the converse is not true because FPS has the larger quadrature range. FPS M-matrix diagrams are shown for $\eta = (0.25, 1/3, 0.45)$ in Fig. 4.12 and for the optimal point of Eq.4.47 where $\eta = x/(1+y)$ in Fig. 4.17a. The diagrams are composed of the bounds of the inequality conditions of Eq.4.46.

4.9 Decoupled Approximation

The cause of spurious non-physical oscillations induced by the TPS formulation when the anisotropy ratio is high is shown in [17]. The analysis is based on the decoupling behavior of CVFE as quadrature approaches $\eta = 1/2$, i.e. the dual-cell midpoint if cell-centred.

The quadrature point $\eta = 1/2$ is a critical point for the above CVFE, FPS and TPS approximations. Again as a consequence of the above relationships of Eq.'s 4.44,4.45 for a spatially constant tenor field, we need only substitute $\eta = 1/2$ in the CVFE approximation to see the effect. Referring to table 4.3 we obtain the scheme [17]

int coords	**Coefficients**	**Full Tensor**
i,j	M_{11}	$(T_{11} + T_{22})$
i+1,j	M_{12}	$\frac{1}{2}(T_{22} - T_{11})$
i+1,j+1	M_{13}	$-\frac{1}{4}(T_{11} + T_{22}) - \frac{1}{2}T_{12}$
i,j+1	M_{14}	$\frac{1}{2}(T_{11} - T_{22})$
i-1,j+1	M_{15}	$-\frac{1}{4}(T_{11} + T_{22}) + \frac{1}{2}T_{12}$
i-1,j	M_{16}	$\frac{1}{2}(T_{22} - T_{11})$
i-1,j-1	M_{17}	$-\frac{1}{4}(T_{11} + T_{22}) - \frac{1}{2}T_{12}$
i,j-1	M_{18}	$\frac{1}{2}(T_{11} - T_{22})$
i+1,j-1	M_{19}	$-\frac{1}{4}(T_{11} + T_{22}) + \frac{1}{2}T_{12}$

Table 4.6: **CVFE** *Coefficients For Constant Tensor field:* $\eta = 1/2$

and note that the resulting discretization permits the *checker board* solution as in

Fig.4.13

int coords	ϕ
i,j	C
i+1,j	$-C$
i+1,j+1	C
i,j+1	$-C$
i-1,j+1	C
i-1,j	$-C$
i-1,j-1	C
i,j-1	$-C$
i+1,j-1	C

Table 4.7: **CVFE** *decoupled solution at* $\eta = 1/2$

+c	-c	+c
-c	+c	-c
+c	-c	+c

Figure 4.13: Decoupled Solution.

where C is an arbitrary constant. The solution is strongly oscillatory and decoupled, Fig.4.13. This helps to explain the extreme sensitivity of the TPS scheme, where for a highly anisotropic full tensor, the ellipticity measure $E = T_{12}^2/(T_{11}T_{22})$ tends to unity, for the example (below) $E = 0.99776$, by Eq. 4.49 it follows that $\eta(TPS) \rightarrow 1/2$ for any value of q, resulting in an oscillatory decoupled solution. Therefore for a highly anisotropic full-tensor violating the M-matrix condition, we may regard the TPS family as belonging to the interval

$$1/2 - \epsilon_{TPS} < \eta \leq 1/2 \tag{4.52}$$

where $\eta_{DC} = 1/2 - \epsilon_{TPS}$ defines a cut-off limit above which decoupling takes place (suffix DC denotes decoupled). The precise cut-off limit is at present undetermined, but a first estimate is obtained from the minimum of the TPS range with $1/2 - \epsilon_{TPS} \sim E/2$.

4.10 Quasi-Positive QM-matrices

The practical effects of this comparison in terms of benefit and validity of quadrature is seen in the results section. As we can see from the analysis, an M-matrix is no longer available for a general high-anisotropy permeability tensor. In our study we observe that even in the situation where an M-matrix does not exist, the FPS formulation permits solutions that are essentially free of spurious oscillations.

First we return to the case of a spatially constant tensor. Following [17], if the optimal quadrature point of Eq.4.47 is chosen when the system has no M-matrix (and the matrix is not monotone), i.e. when $\mid T_{1,2} \mid > min(T_{1,1}, T_{2,2})$, then inspection of table 4.5 shows that the matrix coefficients $M_{13}, M_{15}, M_{17}, M_{19}$ still remain non-positive. For ellipticity we must have $\mid T_{12} \mid \leq max(T_{11}, T_{22})$ so that either M_{12} and M_{16} or M_{14} and M_{18} are non-positive. Without loss of generality, suppose that $T_{11} = max(T_{11}, T_{22})$, then under the assumption of violation of Eq.4.48 M_{12} and M_{16} will be non-positive and M_{14} and M_{18} will be positive. Therefore in this case, only two off-diagonal coefficients violate the M-matrix conditions, which by symmetry of the matrix is the least number possible.

Next we present other quadrature points that lead to matrices with the minimum of only one unique positive off-diagonal coefficient that violates the M-matrix conditions. Note; in this case there are two offending off-diagonal coefficients by symmetry. We shall refer to the resulting matrices as Quasi-Positive M-matrices or QM-matrices, (the name is also motivated in part by the essentially non-oscillatory solutions obtained with the schemes) [17]. By symmetry we only have to consider the four coefficients $M_{12}, M_{13}, M_{14}, M_{15}$.

QM-matrices where only 2 coefficients violate the M-matrix conditions are defined over the two intervals

$$\begin{gathered} 0 \leq \eta \leq T_{22}/(T_{11}+T_{22}) \\ \mid T_{1,2} \mid /(T_{11}+T_{22}) \leq \eta < 1/2 - \epsilon_{TPS} \end{gathered} \tag{4.53}$$

and where solutions are essentially free of spurious oscillations. The upper bound of $1/2 - \epsilon_{TPS}$ in the second interval ensures that η never enters the decoupled zone of Eq. 4.52, where the method can produce decoupled oscillatory solutions as shown above. We note by inspection of M_{14} and M_{15} in table 4.3, referring to the respective intervals of Eq.4.53, as η decreases over the first interval and as η increases over the second interval the offending positive coefficient increases in size in each case. This shows that the schemes defined by the quadrature points

$$\eta = min(T_{11}, T_{22})/(T_{11}+T_{22}) \tag{4.54}$$

$$\eta = \mid T_{1,2} \mid /(T_{11}+T_{22}) \tag{4.55}$$

are both optimal over their respective intervals in the sense that they lead to matrices that are both the closest matrices to M-matrices in pattern, with the minimum number (two due to symmetry) of off-diagonal coefficients that violate the M-matrix conditions, and that the violating coefficients are minimized in magnitude at these points, subject to the constraint that only one of the four unique off-diagonal coefficients is positive.

We denote the optimal quadrature points of Eq's.4.54, 4.55 by η_{HI} and η_{OS} respectively. The case $\eta_{HI} = min(T_{11}, T_{22})/(T_{11}+T_{22})$ leads to a reduced support scheme with H support when $T_{22} = min(T_{11}, T_{22})$ (with coefficients given in Appendix A) as indicated in Fig.4.14a and alternatively if $T_{11} = min(T_{11}, T_{22})$ we obtain a scheme

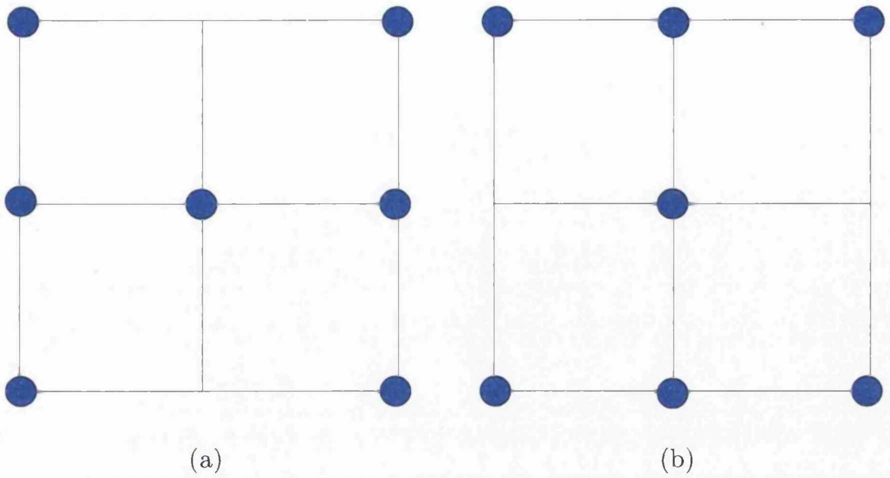

Figure 4.14: Stencil of H/I scheme. (a)H scheme (b)I scheme

with I support as shown in Fig.4.14 (b), hence the general index HI. The optimal support (OS) point $\eta_{OS} = \mid T_{1,2} \mid / (T_{11} + T_{22})$ is more attractive since this leads to optimal support that favours the anisotropy of the problem [17], and is found to yield improved results, as presented below.

Returning to the case where $T_{22} = min(T_{11}, T_{22})$, the interval

$$T_{22}/(T_{11} + T_{22}) < \eta < T_{12}/(T_{11} + T_{22}) \tag{4.56}$$

connects the above minimum positive coefficient intervals of Eq. 4.53. In this case two unique off-diagonal coefficients M_{14} and M_{15} are found to be positive. It is interesting to note that this interval is precisely the reverse of the M-matrix interval of Eq.4.46 and now contains the maximum number of offending coefficients, i.e. four by symmetry. However the four positive coefficients are always bounded above by the maximum of the coefficients at the optimal points.

We next plot the coefficients $M_{12}, M_{13}, M_{14}, M_{15}$ against η in Fig.4.15, for an example where $T_{11} = max(T_{11}, T_{22})$ and $T_{12} > 0$. In this example

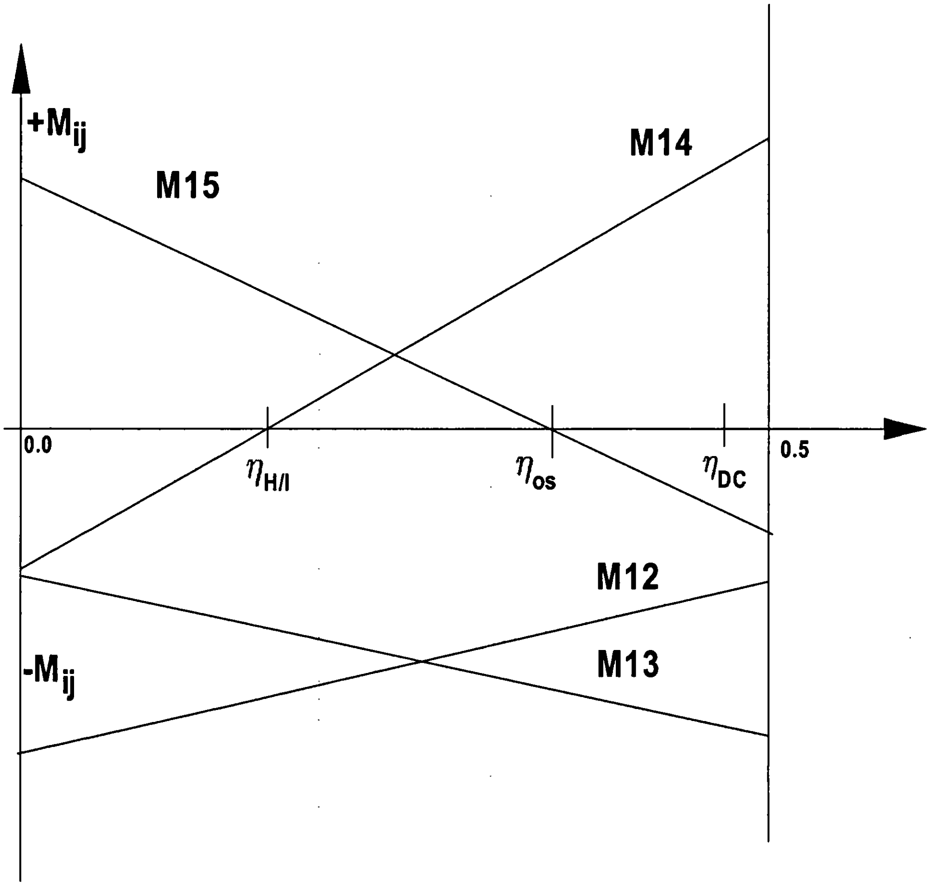

Figure 4.15: QM-matrix: Unique coefficients $M_{12}, M_{13}, M_{14}, M_{15}$ versus η (quadrature range)

$$\mathbf{K} = \begin{pmatrix} 2464.360020 & 1148.683643 \\ 1148.683643 & 536.6399794 \end{pmatrix}$$

The intervals in Fig.4.15 are (a) the first of Eq. 4.53 i.e. $[0, \eta_{HI}]$, (b) Eq. 4.56 i.e. $[\eta_{HI}, \eta_{OS}]$, (c) second of Eq. 4.53 i.e. $[\eta_{OS}, \eta_{DC}]$, (d) the decoupled (TPS) interval $[\eta_{DC}, 1/2]$. The QM-matrices complement the M-matrices so that the entire elliptic region is covered as indicated in Fig.4.17 (b).

A further consequence of this analysis is that for η belonging to the above intervals

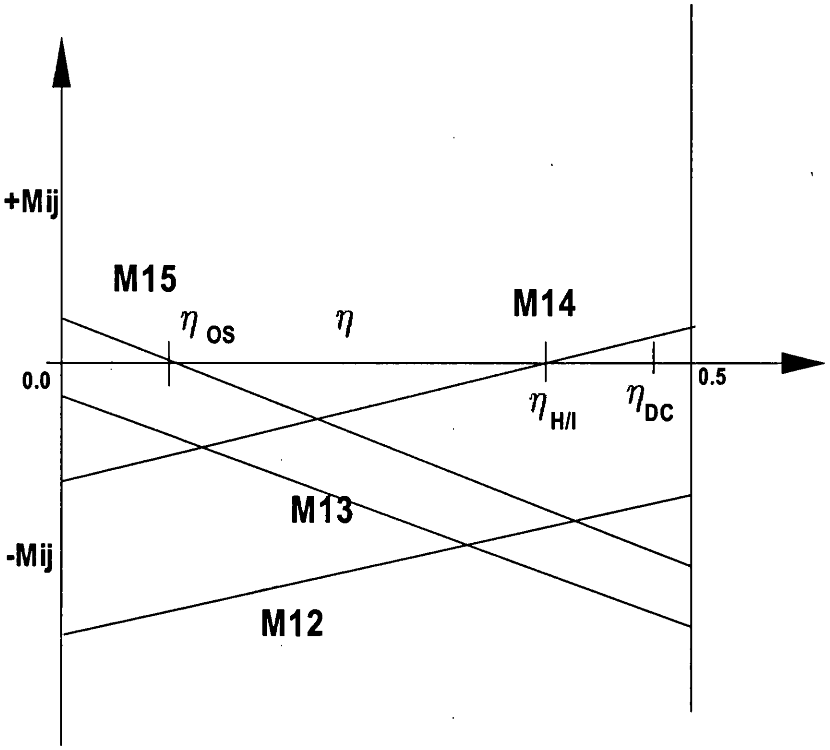

Figure 4.16: M-matrix: Unique coefficients $M_{12}, M_{13}, M_{14}, M_{15}$ versus η (quadrature range)

(a)-(c) (and always away from the singular point), when not equal to one of the optimal points, the QM-matrix schemes will again have up to 9-points in support. This is an important observation when applying the method to heterogeneous cases where a locally upscaled tensor is used to define the unique η optimal quadrature point over a dual-cell as discussed above. Note that the upscaled tensor is only used to define the quadrature, once the quadrature is defined, the flux continuous method is then used to solve the original problem with the original permeability field. For general permeability variation the resulting value of η is unlikely to lead to *exact* optimal

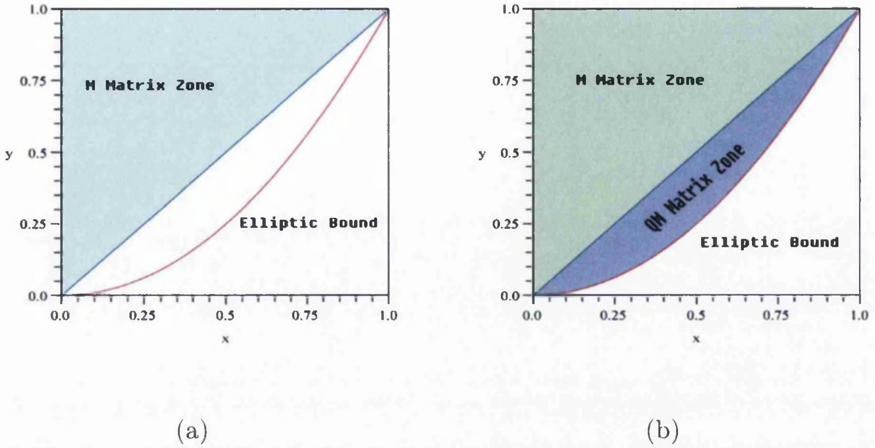

(a) (b)

Figure 4.17: M-Matrix Zone and QM-Matrix Zone for Optimal Support FPS Scheme. (a)Optimal Support M-Matrix zone (b)QM-Matrix Zone

support, but can still improve solution resolution. Numerical pressure solutions are compared for a range of quadrature points spanning the quadrature interval and show that well resolved solutions are obtained within a range of 15 percent of the optimal point.

We again emphasize that the above analysis is for constant coefficients. The discrete matrix will not necessarily be symmetric in the general case e.g. for general quadrilateral cells with a physical space formulation (where exact geometry is maintained in the finite-volume flux) and the coefficients will not take such a simple form. However, the above analysis still provides an important guide in terms of discretization effects.

Finally we make a comparison with a tensor that leads to an M-matrix [105]. In this case

$$\mathbf{K} = \begin{pmatrix} 2.500000000 & 0.8660254040 \\ 0.8660254040 & 1.500000000 \end{pmatrix}$$

and plot the resulting coefficients $M_{12}, M_{13}, M_{14}, M_{15}$ against η in Fig.4.16 for this case, where $T_{11} = max(T_{11}, T_{22})$ and $T_{12} > 0$. From the above M-matrix conditions, the region which contrasts with 4.53 and does not have an M-matrix is defined by the bounds

$$\begin{aligned} 0 \leq \eta \leq T_{1,2}/(T_{11}+T_{22}) \\ \mid T_{22} \mid /(T_{11}+T_{22}) \leq \eta < 1/2 - \epsilon_{TPS} \end{aligned} \tag{4.57}$$

while from Eq. 4.48 an M-matrix is obtained if η satisfies

$$T_{12}/(T_{11}+T_{22}) < \eta < T_{22}/(T_{11}+T_{22}) \tag{4.58}$$

which corresponds to Fig.4.17 (a).

4.11 Numerical Results

A comparison is now presented between the new full pressure support formulation and earlier triangular pressure support formulation. As with the TPS family, the new FPS family of schemes are exact for piecewise linear test cases with jumps in full-tensor permeability. However unlike TPS, the FPS formulation is also exact for piecewise bilinear pressure fields with jumps in full-tensor permeability, consistent with the FPS subcell bilinear basis functions. Convergence behaviour has been found to match that of the TPS schemes for all cases tested.

The Discrete L_2 *norm* is used to investigate pressure and velocity errors, which is defined for pressure and velocity as

$$||\phi_h - \phi||_{L_2} = \Big(\frac{\sum_i (A_i(\phi_{h,i} - \phi_i)^2)}{\sum_i A_i}\Big)^{1/2} \tag{4.59}$$

$$||f_h - f||_{L_2} = \Big(\frac{\sum_j (Q_j(f_{h,j} - f_j)^2)}{\sum_j Q_j}\Big)^{1/2} \tag{4.60}$$

Here, $f = \mathbf{v} \cdot \mathbf{n}$ (where $\mathbf{v} = -\mathbf{K}\nabla\phi$) is the edge normal flow velocity. Subscript h refers to numerical solution. Further A_i is the area of the grid cell i,and Q_j is the Area associated with edge j (where two cells are separated by edge j). The grid refinement levels used for the L_2 *norm* calculation were 16x16, 32x32, 64x64, 128x128 and 256X256 for all test cases in 2D. In each case Dirichlet boundary conditions are prescribed via the exact solutions.

The Discrete L_∞ *norm* is also used to investigate pressure and velocity errors and is defined for pressure and velocity below

$$||\phi_h - \phi||_{L_\infty} = max_{i=1}^{Nnode}||\phi_{h,i} - \phi_i|| \tag{4.61}$$

$$||f_h - f||_{L_2} = max_{j=1}^{Nedge}||f_{h,j} - f_j|| \tag{4.62}$$

Here, Nnode is the total number of nodes and Nedge is the total number of edge where flux has been assigned on.

4.11.1 Case 1: Discontinuous Bilinear Test Case

In a 2D domain $\Omega = [0,1]X[0,1]$, the permeability fields are divided by $x = \frac{1}{2}$ and the tensors are defined below.

$$K_L(x,y) = \begin{pmatrix} 1 & 0.5 \\ 0.5 & 1 \end{pmatrix} \tag{4.63}$$

$$K_R(x,y) = \begin{pmatrix} 10 & 2 \\ 2 & 100 \end{pmatrix} \tag{4.64}$$

Where $K = K_L$ when $x \leq \frac{1}{2}$ and $K = K_R$ otherwise.

Subject to Dirichlet boundary conditions, the pressure field is defined by

$$\phi = \begin{cases} 10 + 20xy, & x \leq \frac{1}{2} \\ 10.75 - 1.5x + 9y + 2xy, & x > \frac{1}{2} \end{cases}$$

This case also leads to a source term on the right hand side of the standard pressure equation which is discontinuous at the interface over which Permeability is discontinuous. The actual sources to the left and right domain are -20 and -8 respectively.

The numerical solution of FPS schemes is exact for all quadrature points tested. While for the TPS family, the observed best L^2 convergence rate is 1.01, see Fig. 4.18.

Note in this case the bilinear function leads to a source term on the right hand side of the standard pressure equation which is discontinuous at the interface over which permeability is discontinuous.

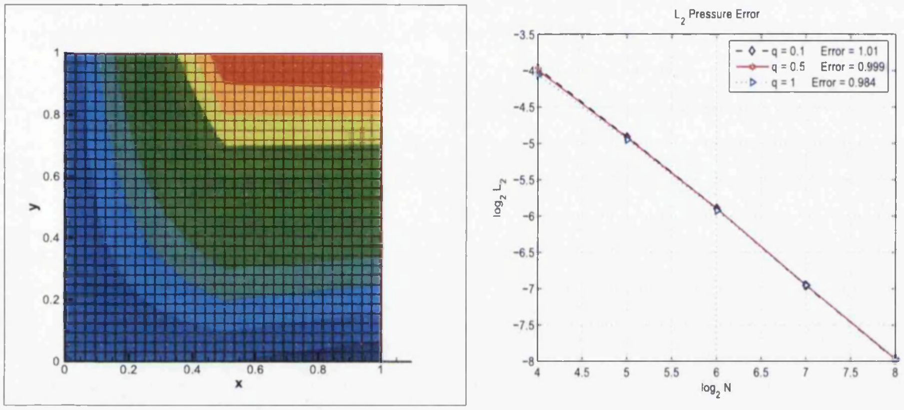

(a) Contour plot of pressure

(b) Convergence for different q for TPS schemes

Figure 4.18: Bilinear test case.

4.11.2 Case 2: Piece-wise Quadratic-Bilinear Discontinuity

This test case was previously presented in [23] in 3D. In a 2D domain $\Omega = [0,1]X[0,1]$, the permeability fields are divided by $x = \frac{1}{2}$.

$$K_L(x,y) = \begin{pmatrix} 1 & 0 \\ 0 & 1 \end{pmatrix} \tag{4.65}$$

$$K_R(x,y) = \begin{pmatrix} 5 & 4 \\ 4 & 5 \end{pmatrix} \tag{4.66}$$

Subject to the Dirichlet boundary conditions, the pressure field is defined by

$$\phi = \begin{cases} (2x-1)^2 + 5(2x-1)y, & x \leq \frac{1}{2} \\ (2x-1)^2 + (2x-1)y, & x > \frac{1}{2} \end{cases}$$

This case also leads to a source term on the right hand side of the standard pressure equation which is discontinuous at the interface over which permeability is discontinuous. The actual sources to the left and right domain are -8 and -56 respectively.

FPS schemes are exact for any suitable quadrature points.

4.11.3 CASE 3: Piecewise Quadratic Test Case: quadratic discontinuity

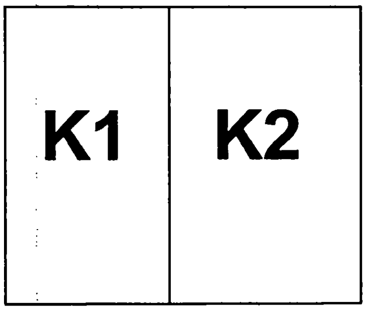

(a)

Figure 4.19: Case 3: Two sub-domains with discontinuous permeability

This case is from [2]. In this case the pressure field is varying piecewise quadratically over the domain shown in Fig.4.19. The domain discontinuity is aligned along the line $x = 1/2$, and the analytical solution is given by

$$\phi(x,y) = \begin{cases} c_l x^2 + d_l y^2, & x < 1/2, \\ a_r + b_r x + c_r x^2 + d_r y^2, & x \geq 1/2, \end{cases}$$

$$K = \begin{cases} \begin{pmatrix} 50 & 0 \\ 0 & 1 \end{pmatrix}, & x < 1/2, \\ \begin{pmatrix} 1 & 0 \\ 0 & 10 \end{pmatrix}, & x \geq 1/2, \end{cases}$$

$$\begin{aligned} \alpha &= K_{11}|_r / K_{11}|_l, \\ \beta &= K_{22}|_l / K_{22}|_l, \\ a_r &= 1, \\ f &= 4a_r/((\alpha - 2)\beta + 1), \\ b_r &= (\beta - 1)f, \\ c_r &= f, \\ d_r &= -c_r K_{11}|_r / K_{22}|_r, \\ c_l &= \alpha\beta c_r, \\ d_l &= d_r \end{aligned} \tag{4.67}$$

Dirichlet boundary conditions are imposed, permeability is discontinuous across the line $x = 1/2$. This case also leads to a source term on the right hand side of the standard pressure equation which is discontinuous at the interface over which Permeability is discontinuous. The actual sources to the left and right domain are $-100c_l - 2d_l$ and $-2c_r - 20d_r$ respectively.

Convergence rates for FPS are shown in Fig.4.20. In this case $q = 0.1667$ gives the best convergence rate.

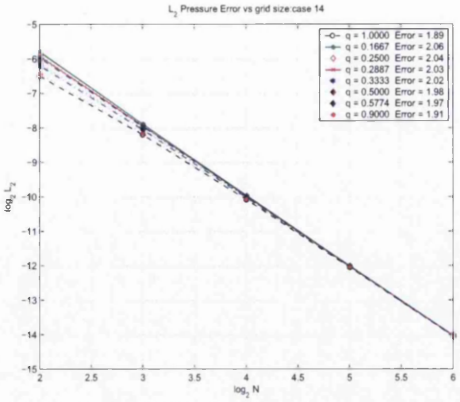

Figure 4.20: Case 3:quadratic case - for a range of q test for FPS schemes, L2 Convergence rates for pressure,

4.11.4 Case 4: Polar case with cartesian grid

The next two cases test the effect of discontinuous permeability with a corner in the field upon convergence. These following test cases (case 4-5) are taken from Eigestad *et al.*[106] and B.Riviere [82]. The problems involve a rectangular domain with discontinuous permeability variation and the exact solution in each case takes the form

$$\phi(r,\theta) = r^{\alpha}(a_i sin(\alpha\theta) + b_i cos(\alpha\theta)) \tag{4.68}$$

Difference between problems are in terms of strength of the coefficients, permeability tensor and orientation, which also determine the level of difficulty in each case.

For this case analytical pressure solution is given by equation 4.68 and the domain discontinuity shown in Fig. 4.21(a) has an internal angle $\theta = \pi/2$. The permeability tensor is given as $\mathbf{K_i} = k_i\mathbf{I}$ where k_i is a scalar, for $i = 1, ..., 4$, taking values $k_1 = 5, k_3 = k_1$ and $k_2 = 1, k_4 = k_1$. Cartesian is used to test this problem. The coefficients

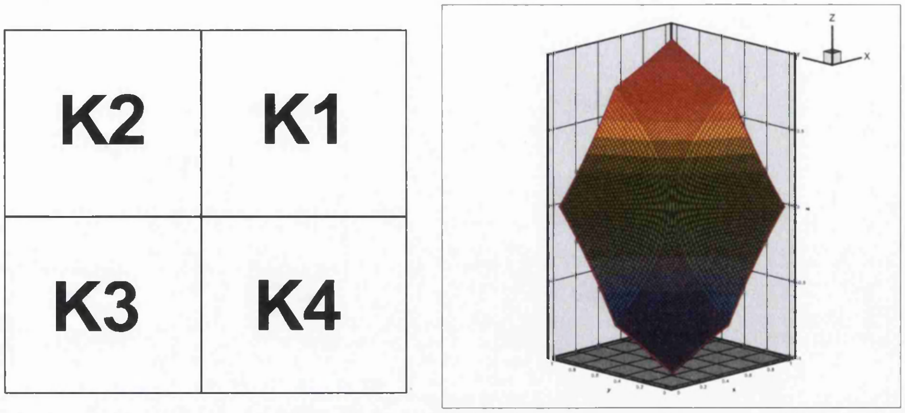

(a) (b)

Figure 4.21: Case 4 Polar case with cartesian grid. (a) Permeability domain. (b)Exact solution of 64x64 grid.

that describe the analytical solution are given by

$$\begin{aligned}
\alpha &= 0.53544095, \\
a_1 &= 0.44721360, \quad b_1 = 2.33333333, \\
a_2 &= -0.74535599, \quad b_2 = 1.0, \\
a_3 &= -0.94411759, \quad b_3 = 0.5555556, \\
a_4 &= -2.40170264, \quad b_4 = -0.481481481.
\end{aligned} \tag{4.69}$$

The exact solution is shown in Fig. 4.21(b).

The L_2 and L_∞ norms of pressure and velocity errors are shown in figure 4.22. Notice the relationship between q and η is $\eta = \frac{1-q}{2}$ for FPS scheme with $c \to 0$, the particular schemes are identified by q here. It can be inferred that the FPS schemes are comparable with TPS scheme in terms of convergence behavior.

4.11.5 Case 5: Polar case with transfinite grid

Here the analytical solution for pressure is also given by equation 4.68 and the domain discontinuity is along the line $\pi/3$ as shown in figure 4.23(a) with the perme-

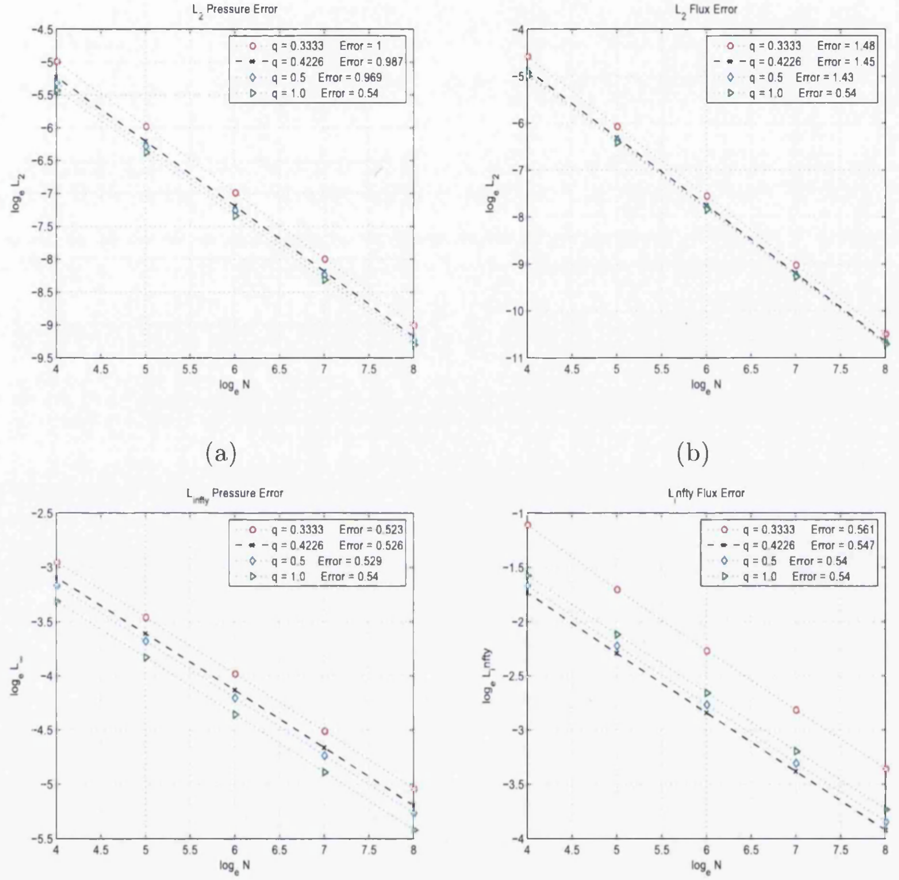

(a) (b)

(c) (d)

Figure 4.22: Case 4 Polar case convergence. Test for different q with the mapping $\eta = \frac{1-q}{2}$. (a)L_2 error norm of pressure (b)L_2 error norm of flux. (c)L_∞ error norm of pressure. (d)L_∞ error norm of flux.

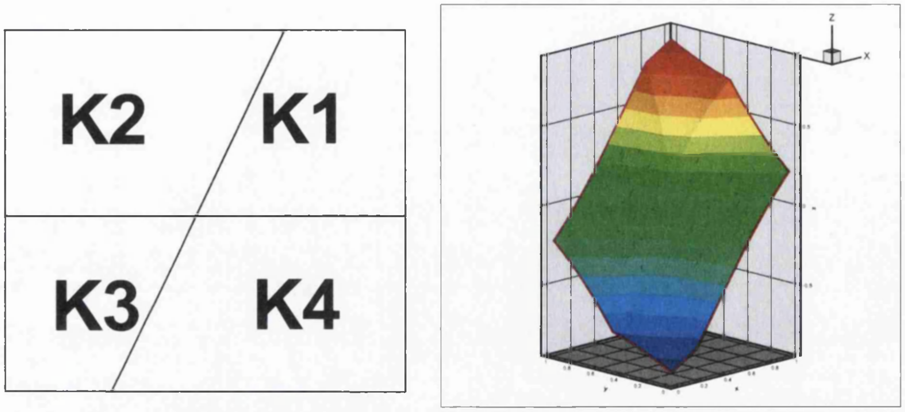

(a) (b)

Figure 4.23: Case 5 Polar case with transfinite grid. (a) Permeability domain. (b)Exact solution of 64x64 grid.

ability tensor $\mathbf{K_i} = k_i \mathbf{I}$, where k_i is a scalar, for $1, ..., 4$, taking values $k_1 = 6, k_3 = k_1$ and $k_2 = 1, k_4 = k_1$. The grids used to test this case were aligned along the discontinuity. The coefficients that describe the analytical solution are given by

$$\begin{aligned} \alpha &= 0.51671199, & & \\ a_1 &= 1.0, & b_1 &= 0.27735010, \\ a_2 &= 1.71428571, & b_2 &= -0.91129318, \\ a_3 &= 0.32944606, & b_3 &= -0.98406726, \\ a_4 &= -0.820074971, & b_4 &= -1.75974652. \end{aligned} \tag{4.70}$$

The L_2 and L_∞ convergence rates of pressure and flux are shown in Fig 4.24 The L_2 pressure convergence for this test case with the grid aligned along the discontinuity was of the order of $h^{1.06}$ for quadrature $q = 1$ ($\eta = 0$ for $c = 0$) and the L_2 velocity convergence was found to be of the order of $h^{1.42}$. The L_∞ convergence is of the order $h^{0.644}$ on $q = 1$ for pressure and $h^{0.518}$ for flux on $q = 0.5$ respectively. Generally L_∞ convergence rate is lower than L_2 convergence rate for the quadrature points tested.

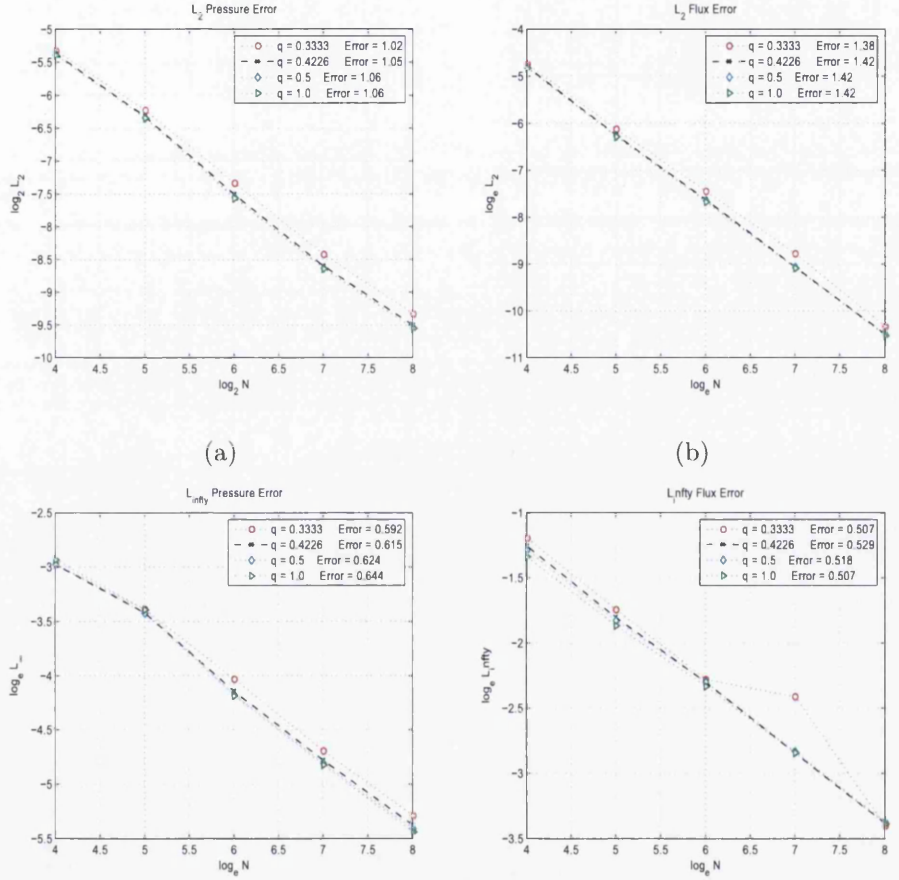

(a) (b)

(c) (d)

Figure 4.24: Case 4 Polar case convergence. (a)L_2 error norm of pressure (b)L_2 error norm of flux. (c)L_∞ error norm of pressure. (d)L_∞ error norm of flux.

4.11.6 CASE 6: PLANAR FULL-TENSOR FIELD

The second case involves a uniform anisotropic domain with a Green's function (point source) in the middle of the domain and with Dirichlet boundary pressure data defined by the Green's function.

The full-tensor is given by

$$\mathbf{K} = \begin{pmatrix} 2464.360020 & 1148.683643 \\ 1148.683643 & 536.6399794 \end{pmatrix} \tag{4.71}$$

with high anisotropy ratio 3000:1 and grid *non-aligned* with the principal axes, which are oriented at an angle of 25 degrees to the computational grid, leading to a full-tensor. The full-tensor field violates the inequality of Eq.4.48 so that no 9-point scheme or subset scheme can possess an M-matrix in this case.

The first result involves using the TPS 9-point scheme with $q = 1$ on a 64×64 grid. The TPS numerical pressure solution is shown in Fig's. 4.25(a), 4.26(a) with visible strong spurious oscillations. We note that the condition of Eq. 4.47 could not be satisfied by the TPS scheme due to the limited quadrature range.

The family of FPS schemes are investigated here. The quadrature points that have been tested are given below

$$\eta = [0, 1/6, \eta_{H/I}, 1/4, 1/3, \eta_{OS} - \varepsilon, \eta_{OS}, \eta_{OS} + \varepsilon, 0.45] \tag{4.72}$$

where $\eta_{H/I}, \eta_{OS}$ correspond to the two optimal QM-matrix schemes, here ε is defined by 15 percent of optimal support quadrature η_{OS}.

Results are shown for a 64×64 grid in Fig's. 4.25, 4.26. The solution resolution is seen to sharpen gradually from $\eta = 0$ to $\eta = 0.45$. In this case the solution in the range $\eta_{H/I}$ is found to be of a slightly more diffuse and smoother nature. At $\eta = 0.25$ the mid-point of the quadrature range, which would correspond with the scheme of [39], the solution is of medium resolution, but also indicates the formation of a trough either side of the peak. Since the tensor is spatially constant throughout the field the FPS

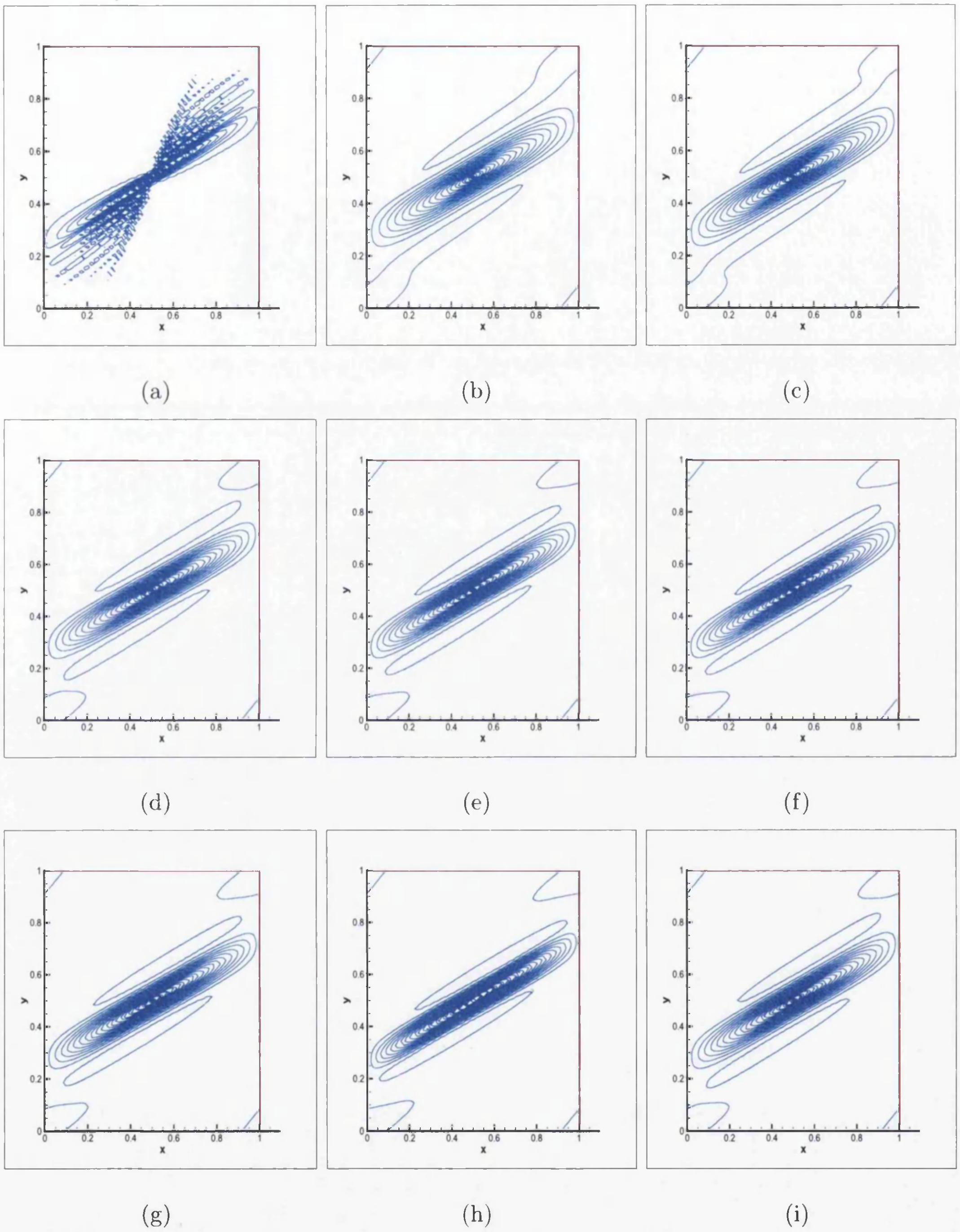

(a) (b) (c)

(d) (e) (f)

(g) (h) (i)

Figure 4.25: Cell-vertex scheme: Contours for homogeneous full-tensor case. (a)TPS q=1. (b)FPS H scheme. (c)FPS $\eta = 0.25$. (d)FPS $\eta = \frac{1}{3}$. (e)FPS $\eta = \eta_{OS} - 15\%$. (f)FPS $\eta = \eta_{OS}$. (g)FPS $\eta = \eta_{OS} + 15\%$. (h)FPS $\eta = 0.45$. (i)FPS $\eta = Gauss$

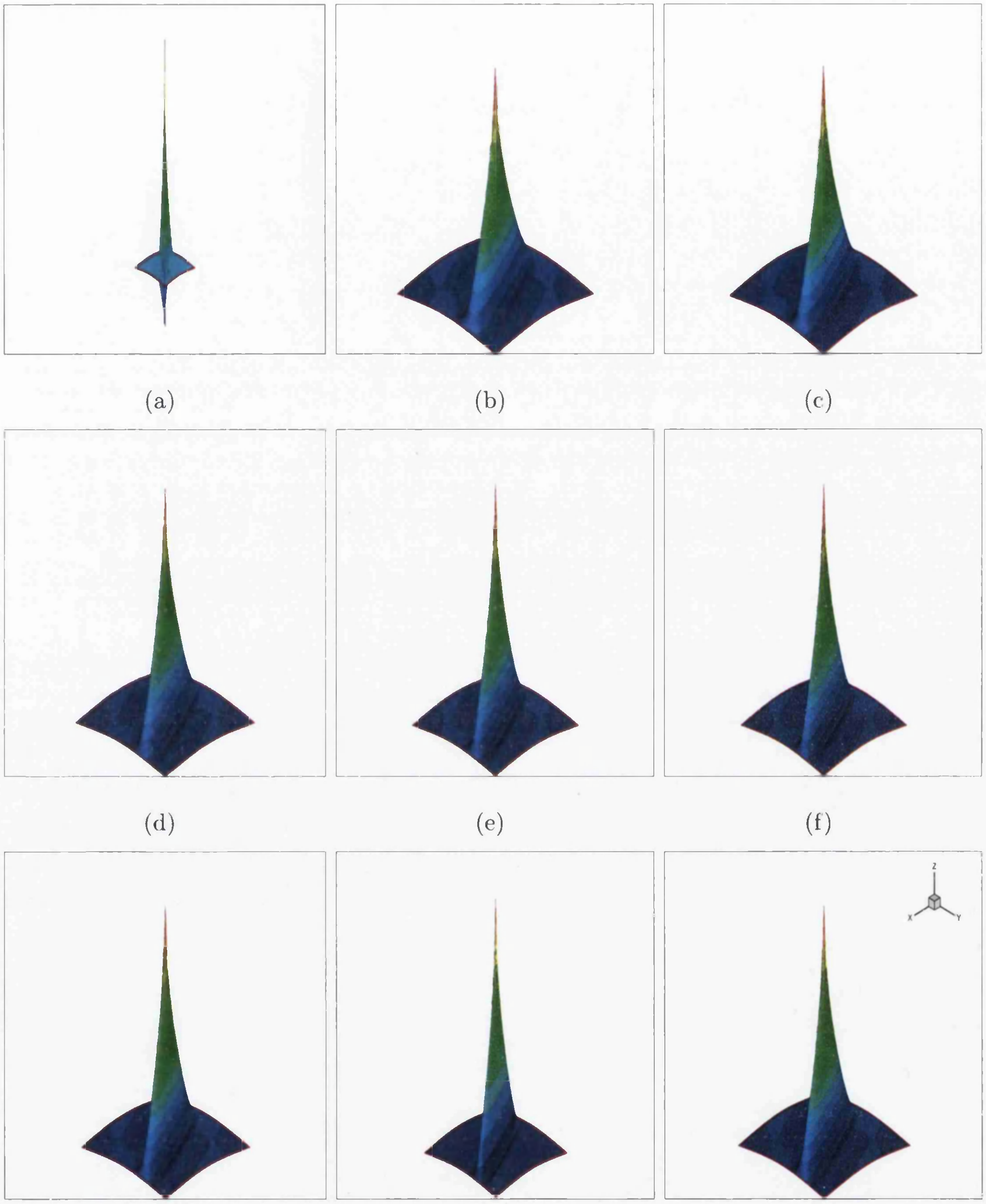

(a) (b) (c)

(d) (e) (f)

(g) (h) (i)

Figure 4.26: Cell-vertex scheme: Iso-surface plots for homogeneous full-tensor case. (a)TPS q=1. (b)FPS H scheme. (c)FPS $\eta = 0.25$. (d)FPS $\eta = \frac{1}{3}$. (e)FPS $\eta = \eta_{OS} - 15\%$. (f)FPS $\eta = \eta_{OS}$. (g)FPS $\eta = \eta_{OS} + 15\%$. (h)FPS $\eta = 0.45$.(i)FPS $\eta = Gauss$

family coincides with the CVFE family. Note in this constant coefficient case $\eta = 1/3$ corresponds to the Galerkin finite element method and $\eta = 1/6$ corresponds with the sixth-order accurate Laplacian operator when the tensor is diagonal isotropic [7]. For $\eta = \eta_{OS}$ FPS has an angled 7-point approximation according to local orientation of the full-tensor field. Although a trough now forms either side of the peak, the numerical pressure solutions of Fig's. 4.25, 4.26 from (d) to (h) are otherwise of improved resolution and practically oscillation free for the entire quadrature of Eq. 4.72. The solutions corresponding to the interval $[\eta_{OS} - \varepsilon, \eta_{OS} + \varepsilon]$ (e) to (g) are seen to have quite comparable resolution.

Numerical results for cell-centred schemes are shown in Fig's 4.27, 4.28. Similar behavior has been observed, although it is shown that Cell-centred schemes have larger decoupled zone than the cell-vertex schemes. For example, for cell-vertex scheme, $\eta = 0.45$ (Fig 4.25 (h), and Fig 4.26 (h).) can still give satisfying results though approaching singular point $\eta = 0.5$. While for cell-centred scheme $\eta = 0.425$ has already shown spurious oscillation (Fig 4.27 (i), and Fig 4.28 (i).).

4.11.7 CASE 7: STRONG DISCONTINUOUS FULL-TENSOR (ZIGZAG) FIELD

In this case the boundary conditions for the unit domain involve a constrained pressure source-sink configuration placed at diagonally opposite corners of the domain. The bottom left pressure is set to 0.0 and the top right-hand corner pressure is set to 200, together with pressure set to 100 on all boundary walls. The permeability tensor changes direction in anisotropy at one third and two thirds the way across the domain. The discontinuous full-tensor permeability field is defined in sections with sign of cross-terms varying, the tensor is assigned to the first section with

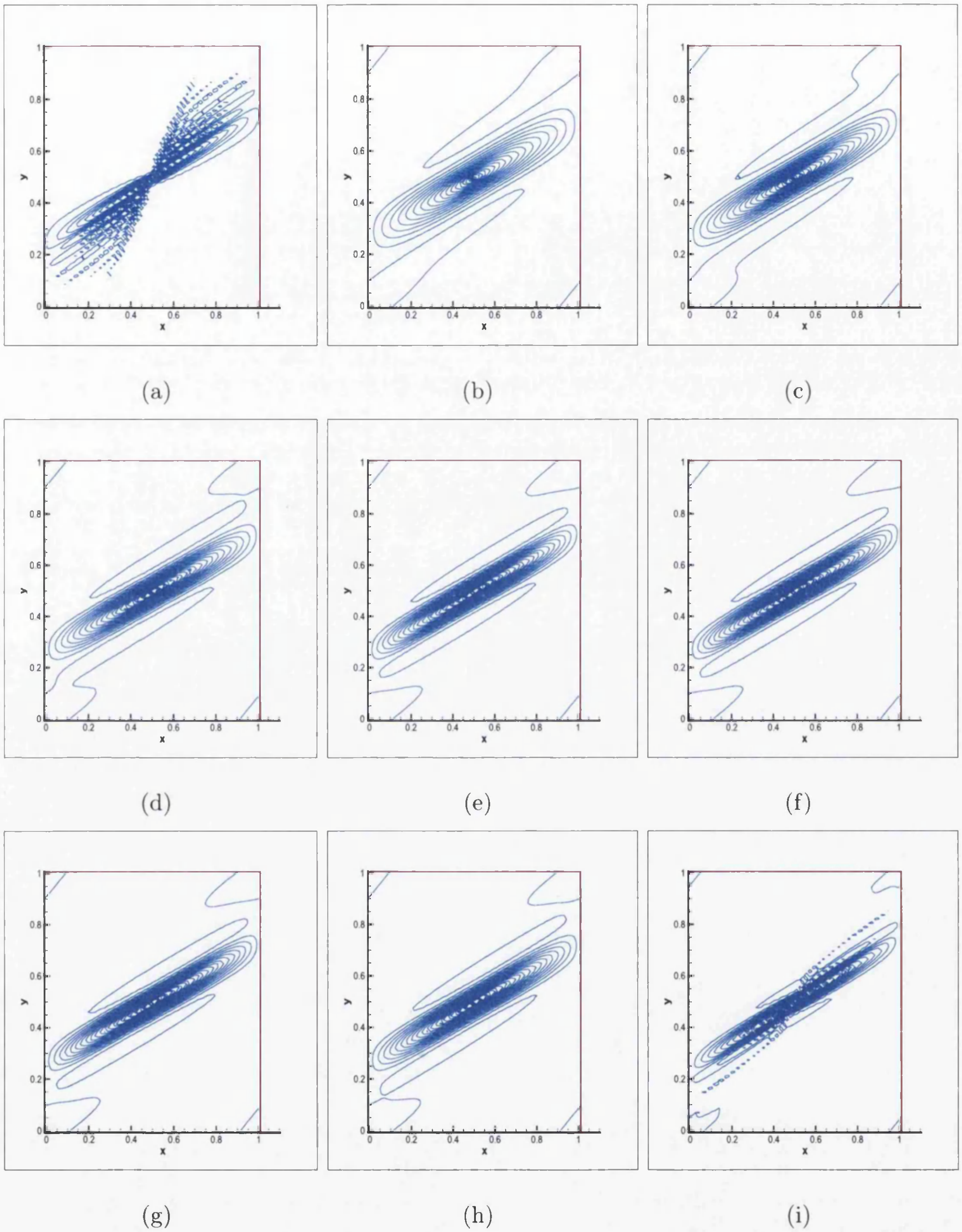

(a) (b) (c)

(d) (e) (f)

(g) (h) (i)

Figure 4.27: Cell-Centred Scheme: Contours for homogeneous full-tensor case. (a)TPS q=1. (b)FPS H scheme. (c)FPS $\eta = 0.25$. (d)FPS $\eta = \frac{1}{3}$. (e)FPS $\eta = \eta_{OS} - 15\%$. (f)FPS $\eta = \eta_{OS}$. (g)FPS $\eta = \eta_{OS} + 15\%$. (h)FPS $\eta = \mathit{Gauss}$. (i)FPS $\eta = 0.425$.

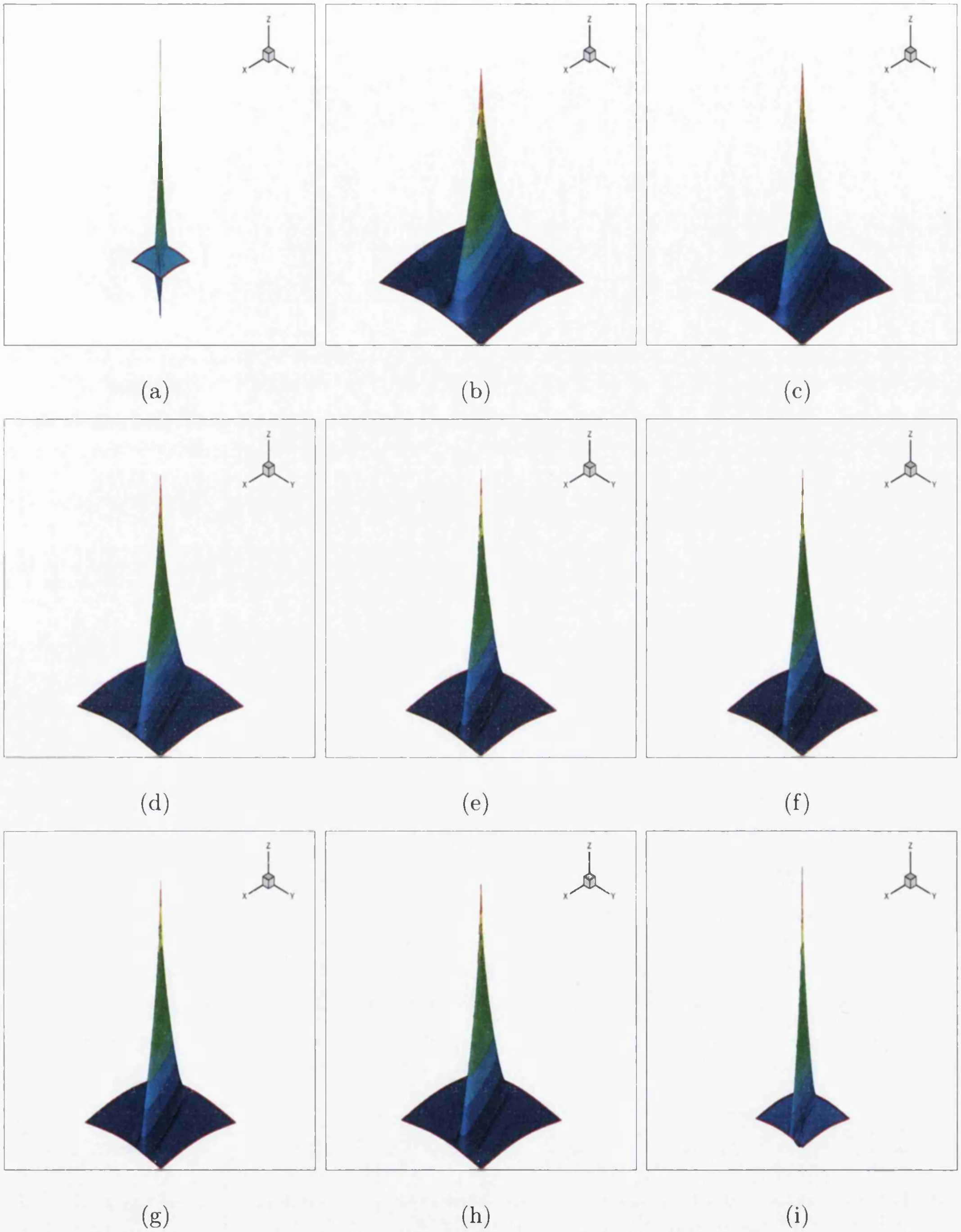

(a) (b) (c)

(d) (e) (f)

(g) (h) (i)

Figure 4.28: Cell-Centred Scheme: Iso-surface plots for homogeneous full-tensor case. (a)TPS q=1. (b)FPS H scheme. (c)FPS $\eta = 0.25$. (d)FPS $\eta = \frac{1}{3}$. (e)FPS $\eta = \eta_{OS} - 15\%$. (f)FPS $\eta = \eta_{OS}$. (g)FPS $\eta = \eta_{OS} + 15\%$. (h)FPS $\eta = Gauss$. (i)FPS $\eta = 0.425$.

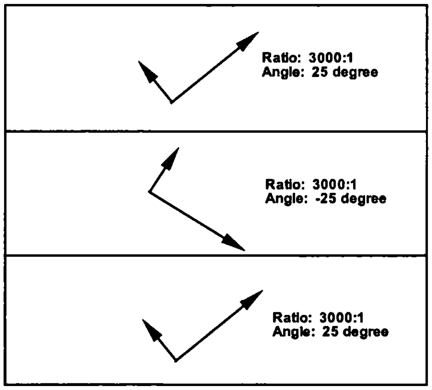

Figure 4.29: Case 7: Principal axes of permeability in Zigzag sub-domains

$$\mathbf{K} = \begin{pmatrix} 2464.360020 & +1148.683643 \\ +1148.683643 & 536.6399794 \end{pmatrix}$$

to second section with

$$\mathbf{K} = \begin{pmatrix} 2464.360020 & -1148.683643 \\ -1148.683643 & 536.6399794 \end{pmatrix}$$

and third section with

$$\mathbf{K} = \begin{pmatrix} 2464.360020 & +1148.683643 \\ +1148.683643 & 536.6399794 \end{pmatrix}$$

as indicated in Fig.4.29, at each section the principal axes are oriented at an angle of 25 degrees, (i.e. minus, plus, minus 25 degrees) to the computational grid. The tensor again has a principal anisotropy ratio of 3000:1, violating the M-matrix condition, Eq.4.48 in each section. A 64 × 64 grid is employed for the computations.

Results are presented for the TPS scheme with $q = 1$ Fig's.4.30 (a), 4.31 (a) for a 64x64 grid, again the condition of Eq. 4.47 could not be satisfied by the TPS scheme due to the smaller quadrature range (the cross-term is greater than the harmonic average of the diagonals i.e. Eq.4.50 holds in this case). There are very strong oscillations in the solution showing clear violation of the maximum principle as expected

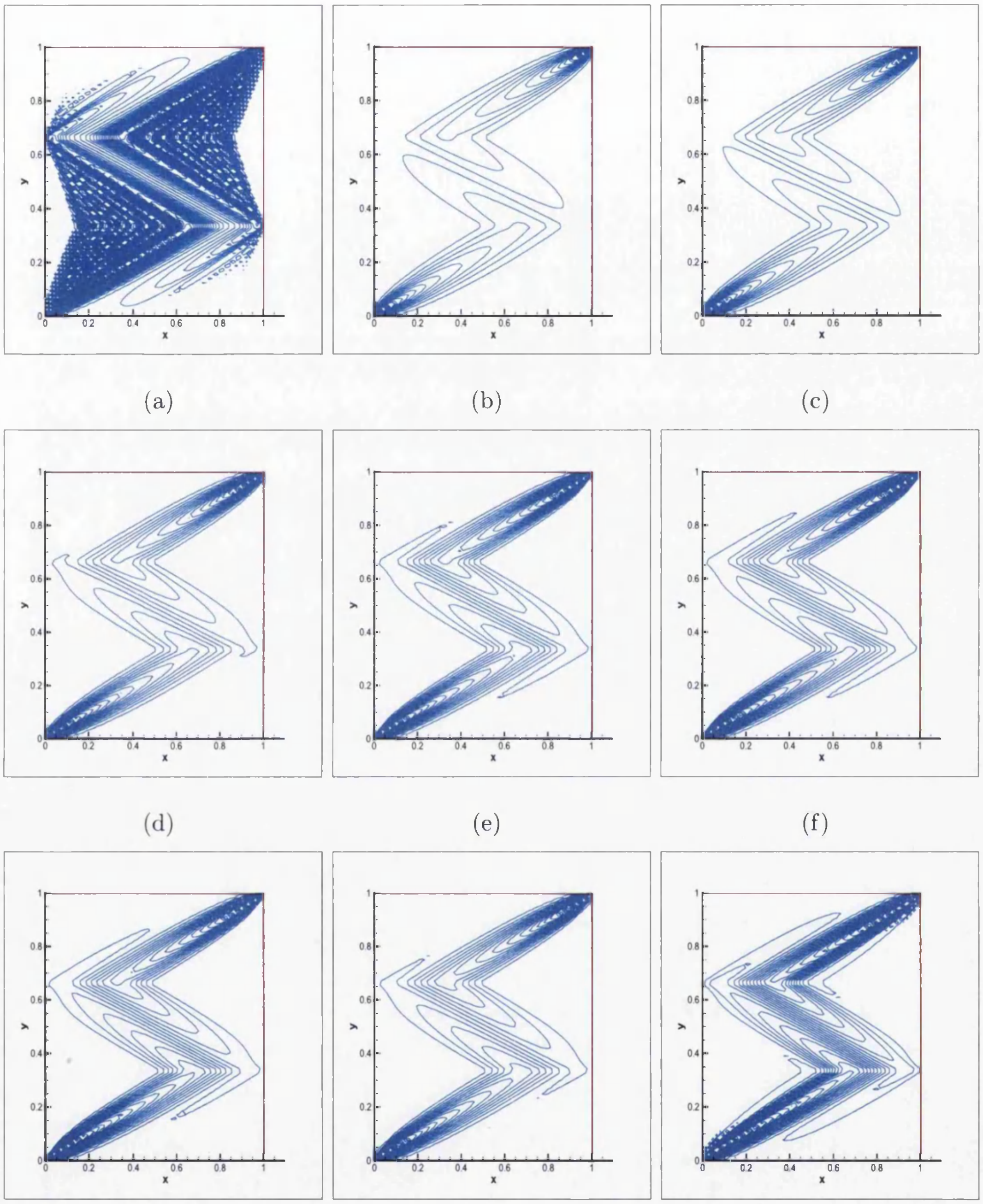

(a) (b) (c)

(d) (e) (f)

(g) (h) (i)

Figure 4.30: Case 7:Contours: 3 sub-domain case. (a)TPS q=1. (b)FPS H scheme. (c)FPS $\eta = 0.25$. (d)FPS $\eta = \frac{1}{3}$. (e)FPS $\eta = \eta_{OS} - 15\%$. (f)FPS $\eta = \eta_{OS}$. (g)FPS $\eta = \eta_{OS} + 15\%$. (h)FPS $\eta = Gauss$.(i)FPS $\eta = 0.45$

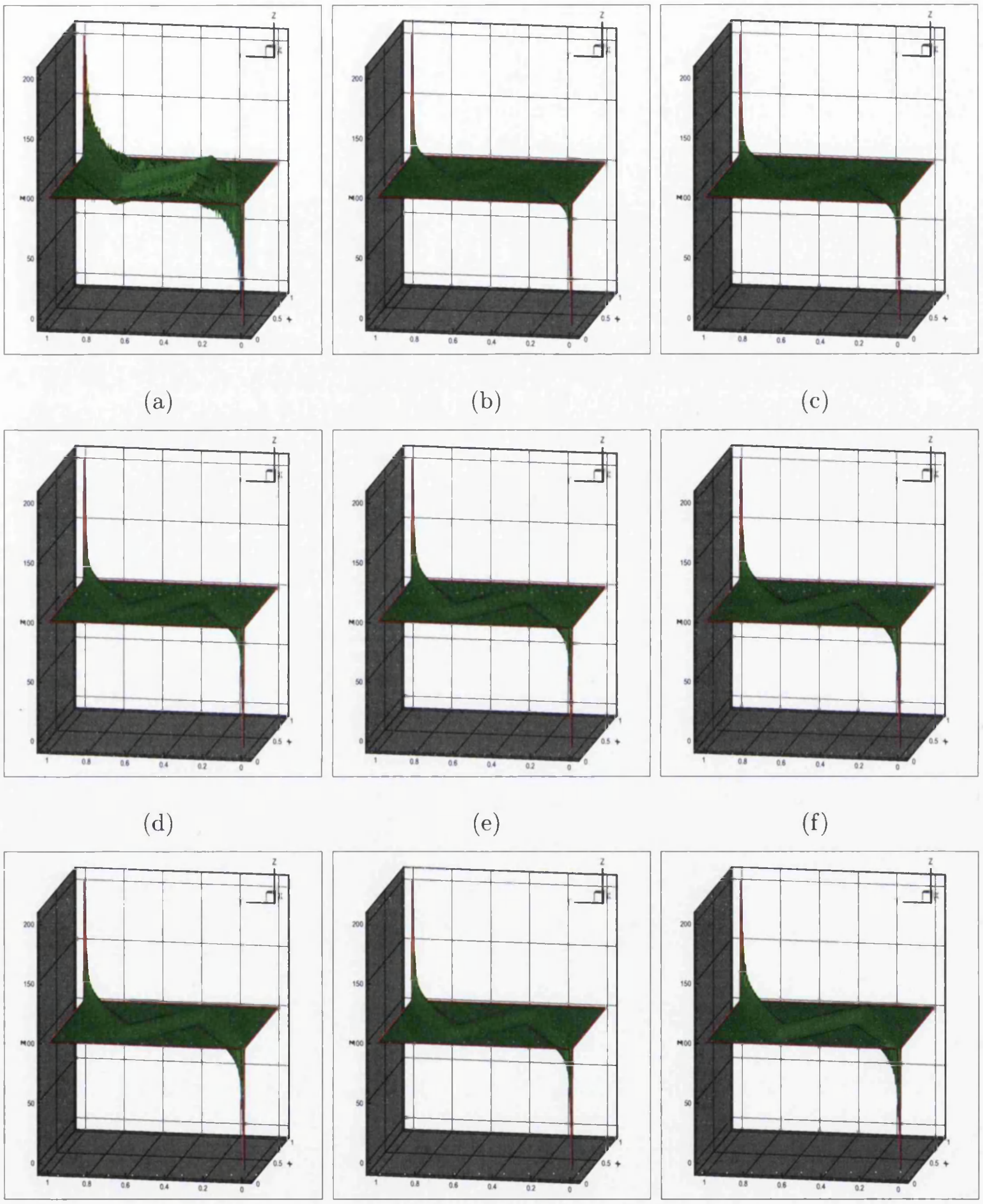

(a) (b) (c)

(d) (e) (f)

(g) (h) (i)

Figure 4.31: Case 7: Iso-surface plot, 3 sub-domains. (a)TPS q=1. (b)FPS H scheme. (c)FPS $\eta = 0.25$. (d)FPS $\eta = \frac{1}{3}$. (e)FPS $\eta = \eta_{OS} - 15\%$. (f)FPS $\eta = \eta_{OS}$. (g)FPS $\eta = \eta_{OS} + 15\%$.(h)FPS $\eta = Gauss$.(i)FPS $\eta = 0.45$

from the M-matrix analysis.

We now compare with the FPS scheme for the above range of quadrature points in case 6. A locally upscaled tensor is used to define the quadrature over the dual-cell, which yields a mean tensor for regions where permeability varies, in this case along the sub-domain boundaries where permeability is discontinuous.

We begin with the optimal scheme quadrature point defined by Eq. 4.47. In this case away from the discontinuities the support of the scheme reduces such that the scheme fulfills the *optimal support condition.* Thus away from the discontinuities this particular FPS scheme essentially leads to an angled approximation according to local orientation of the full-tensor field, the results are shown in Fig.4.30 (f), 4.31 (f). While oscillations are present for some quadrature points, they are seen to be considerably reduced compared to TPS and the solution is well resolved. Thus the FPS formulation yields almost oscillation free results for both planar and discontinuous full-tensor permeability fields.

In general, the solution resolution is seen to sharpen from $\eta = 0$ to $\eta = 0.45$, Fig's. 4.30, 4.31. Here solutions are seen to have quite comparable resolution in the interval $[1/3, \eta_{OS} + \varepsilon]$

Numerical results for cell-centred schemes are shown in Fig's 4.32, 4.33. Similar behavior to the previous case is observed, i.e. the cell-centred schemes have larger decoupled zone than the cell-vertex schemes. For example, for the cell-vertex scheme, $\eta = 0.45$ (Fig 4.30(h), and Fig 4.31(h).)yields well resolved stable results while for the cell-centred scheme $\eta = 0.425$ already shows spurious oscillation (Fig 4.32(i), and Fig 4.33(i).).

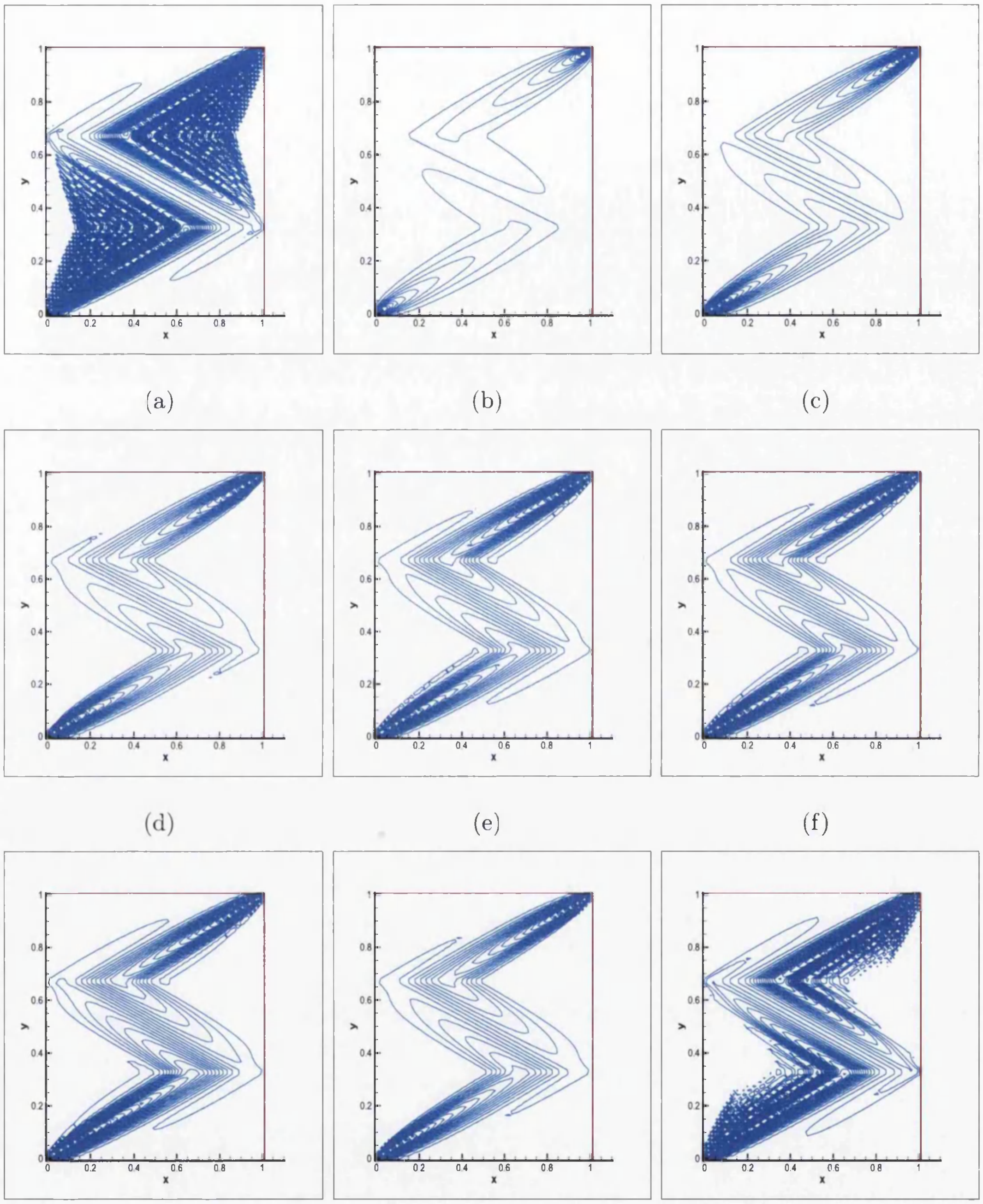

(a) (b) (c)

(d) (e) (f)

(g) (h) (i)

Figure 4.32: Cell-centred results – Contours: 3 sub-domain case. (a)TPS q=1. (b)FPS H scheme. (c)FPS $\eta = 0.25$. (d)FPS $\eta = \frac{1}{3}$. (e)FPS $\eta = \eta_{OS} - 15\%$. (f)FPS $\eta = \eta_{OS}$. (g)FPS $\eta = \eta_{OS} + 15\%$. (h)FPS $\eta = Gauss$.(i)FPS $\eta = 0.425$

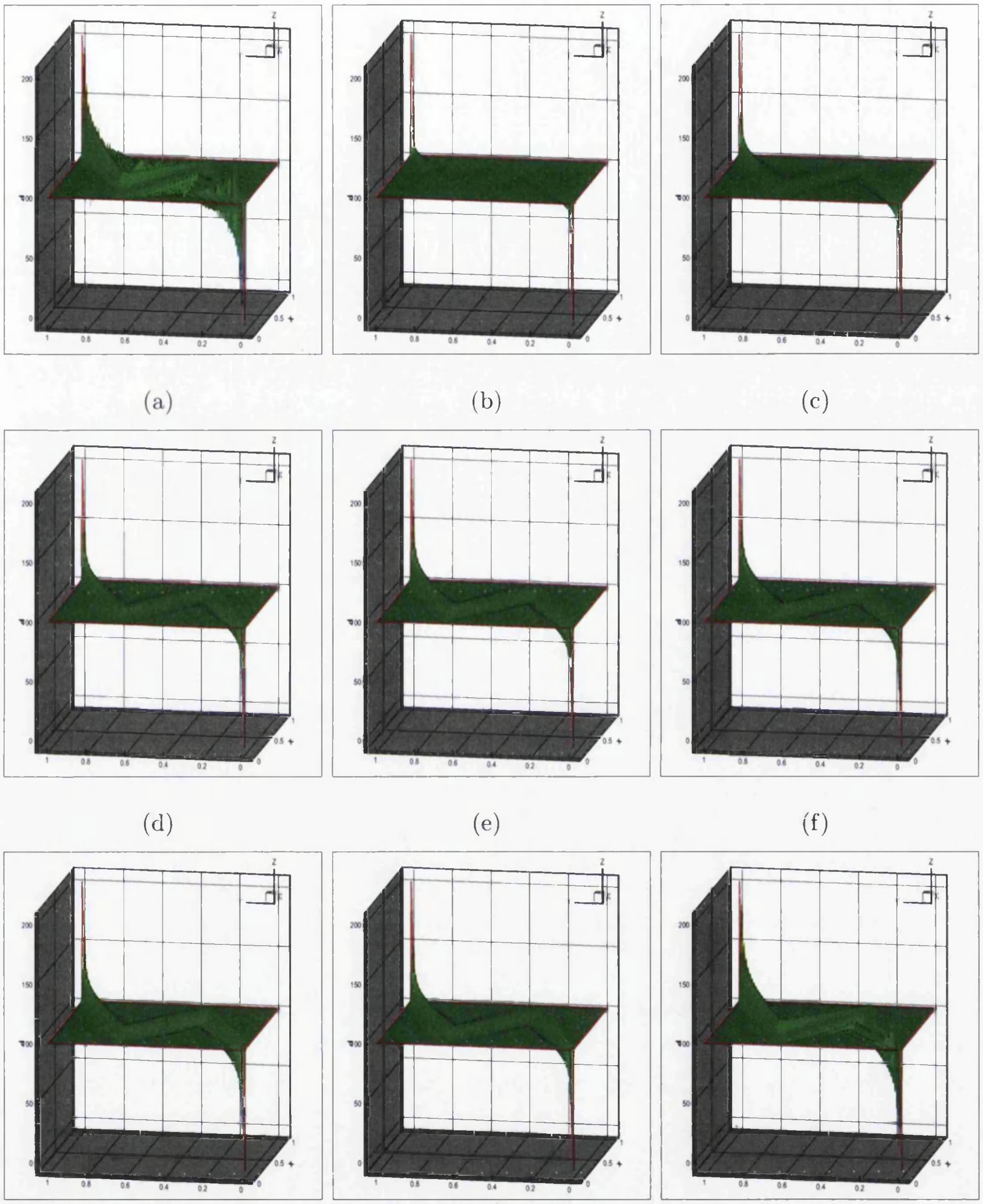

(a) (b) (c)

(d) (e) (f)

(g) (h) (i)

Figure 4.33: Cell-centred results – Iso-surface plot, 3 sub-domains. (a)TPS q=1. (b)FPS H scheme. (c)FPS $\eta = 0.25$. (d)FPS $\eta = \frac{1}{3}$. (e)FPS $\eta = \eta_{OS} - 15\%$. (f)FPS $\eta = \eta_{OS}$. (g)FPS $\eta = \eta_{OS} + 15\%$.(h)FPS $\eta = Gauss$.(i)FPS $\eta = 0.425$

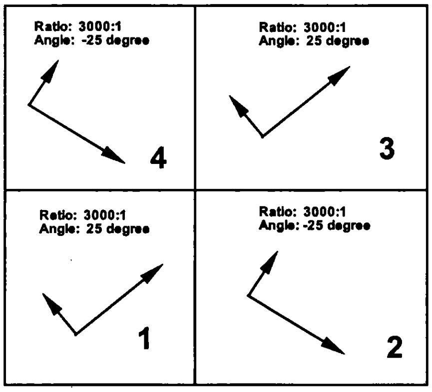

(a)

Figure 4.34: Case 8: 2X2 sub-domains with local tensor principal axes orientations

4.11.8 CASE 8: STRONG DISCONTINUOUS FULL-TENSOR 2×2 DOMAIN

In this case the boundary conditions involve a source and sink located at diagonally opposite points in the field (source lower left $\mathbf{r} = (0.25, 0.25)$ and zero pressure prescribed on the boundary walls. The permeability tensor changes direction in anisotropy over each quarter of the domain. With reference to sub-domains 1 to 4, the full-tensor field is defined by

$$\mathbf{K} = \begin{pmatrix} 2464.360020 & +1148.683643 \\ +1148.683643 & 536.6399794 \end{pmatrix}$$

in 1,

$$\mathbf{K} = \begin{pmatrix} 2464.360020 & -1148.683643 \\ -1148.683643 & 536.6399794 \end{pmatrix}$$

in 2,

$$\mathbf{K} = \begin{pmatrix} 2464.360020 & +1148.683643 \\ +1148.683643 & 536.6399794 \end{pmatrix}$$

in 3

$$\mathbf{K} = \begin{pmatrix} 2464.360020 & -1148.683643 \\ -1148.683643 & 536.6399794 \end{pmatrix}$$

in 4, as indicated in Fig.4.34. In each sub-domain the principal axes are oriented at an angle of +25 or −25 degrees, to the computational grid as indicated in Fig.4.34. As before the tensor has a principal anisotropy ratio of 3000:1, and the elliptic tensor violates the condition for an M-matrix. A 64×64 grid is employed for the comparison.

Results from the TPS scheme with $q = 1$ Fig's. 4.35 (a), 4.36 (a) for a 64x64 grid, indicate the decoupling effect due to the small quadrature range at the upper end of the quadrature interval. Again there are very strong oscillations in the solution showing clear violation of the maximum principle.

We next compare with the family of FPS schemes for the above range of quadrature points. This case leads to similar conclusions to the previous test. As in the previous case a locally upscaled tensor is used to define the quadrature over the dual-cell, which yields a mean tensor for regions where permeability varies, along the sub-domain boundaries where permeability is discontinuous.

For the optimal scheme quadrature point defined by Eq. 4.47, away from the discontinuities the support of the scheme reduces such that the scheme fulfills the *optimal support condition* with an angled approximation according to the local sign of cross-terms of the full-tensor field. The optimal quadrature point is based on a local mean tensor where permeability varies. Results are shown in Fig's. 4.35, 4.36.

In general, the solution resolution consistently sharpens from $\eta = 0$ to $\eta = 0.45$. Oscillations are not detected for some quadrature points. Here solutions are seen to have quite comparable resolution and be particularly well resolved for η in the interval $[1/3, 0.45]$, Fig's. 4.35, 4.36.

Numerical results for the cell-centred schemes are shown in Fig's 4.37, 4.38. Similar behavior is observed, although the cell-centred schemes have larger decoupled zone than the cell-vertex schemes. For example, for cell-vertex scheme, $\eta = 0.45$ (Fig

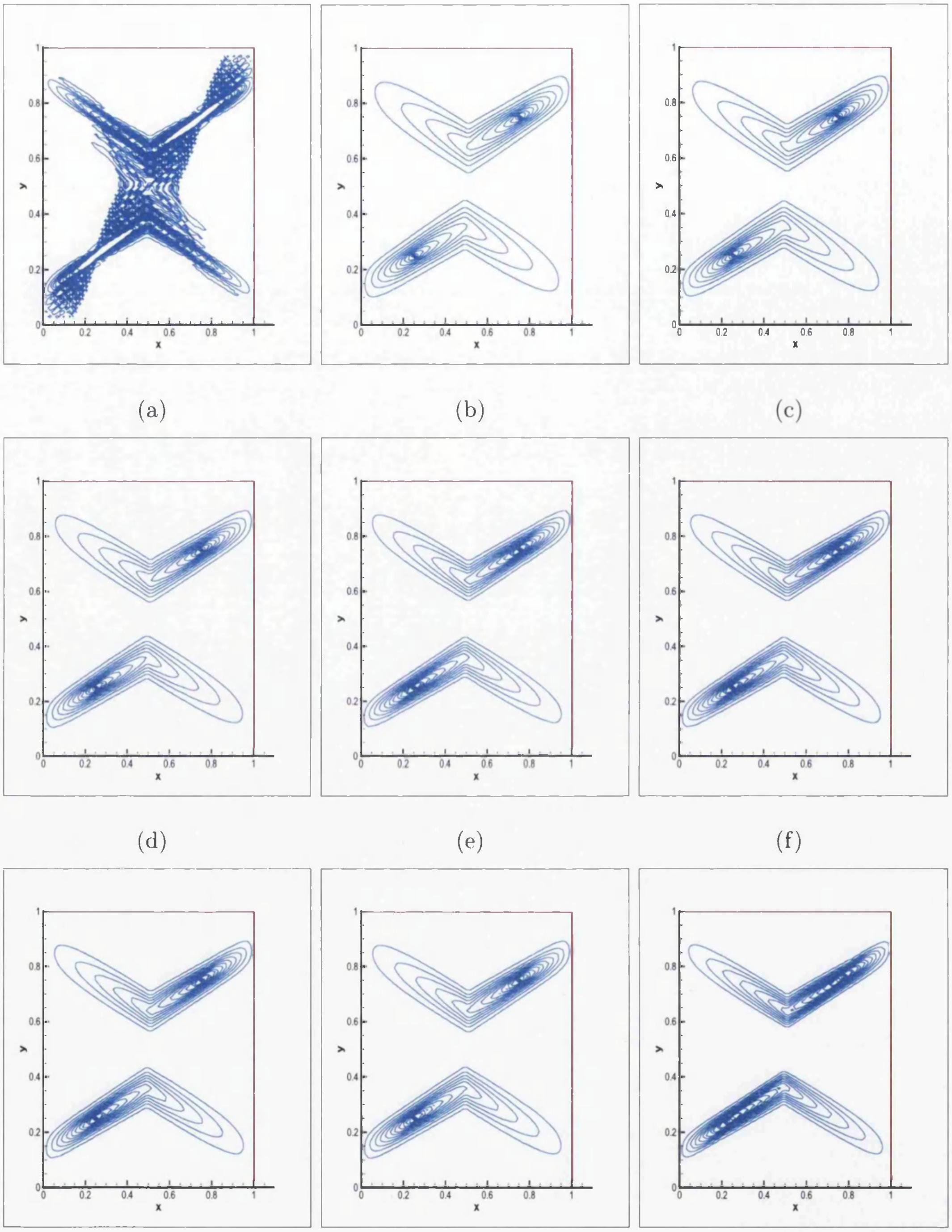

(a) (b) (c)

(d) (e) (f)

(g) (h) (i)

Figure 4.35: Case 8: Cell-vertex scheme, Contours for 2X2 domain. (a)TPS q=1. (b)FPS H scheme. (c)FPS $\eta = 0.25$. (d)FPS $\eta = \frac{1}{3}$. (e)FPS $\eta = \eta_{OS} - 15\%$. (f)FPS $\eta = \eta_{OS}$. (g)FPS $\eta = \eta_{OS} + 15\%$. (h)FPS $\eta = Gauss$. (i)FPS $\eta = 0.45$

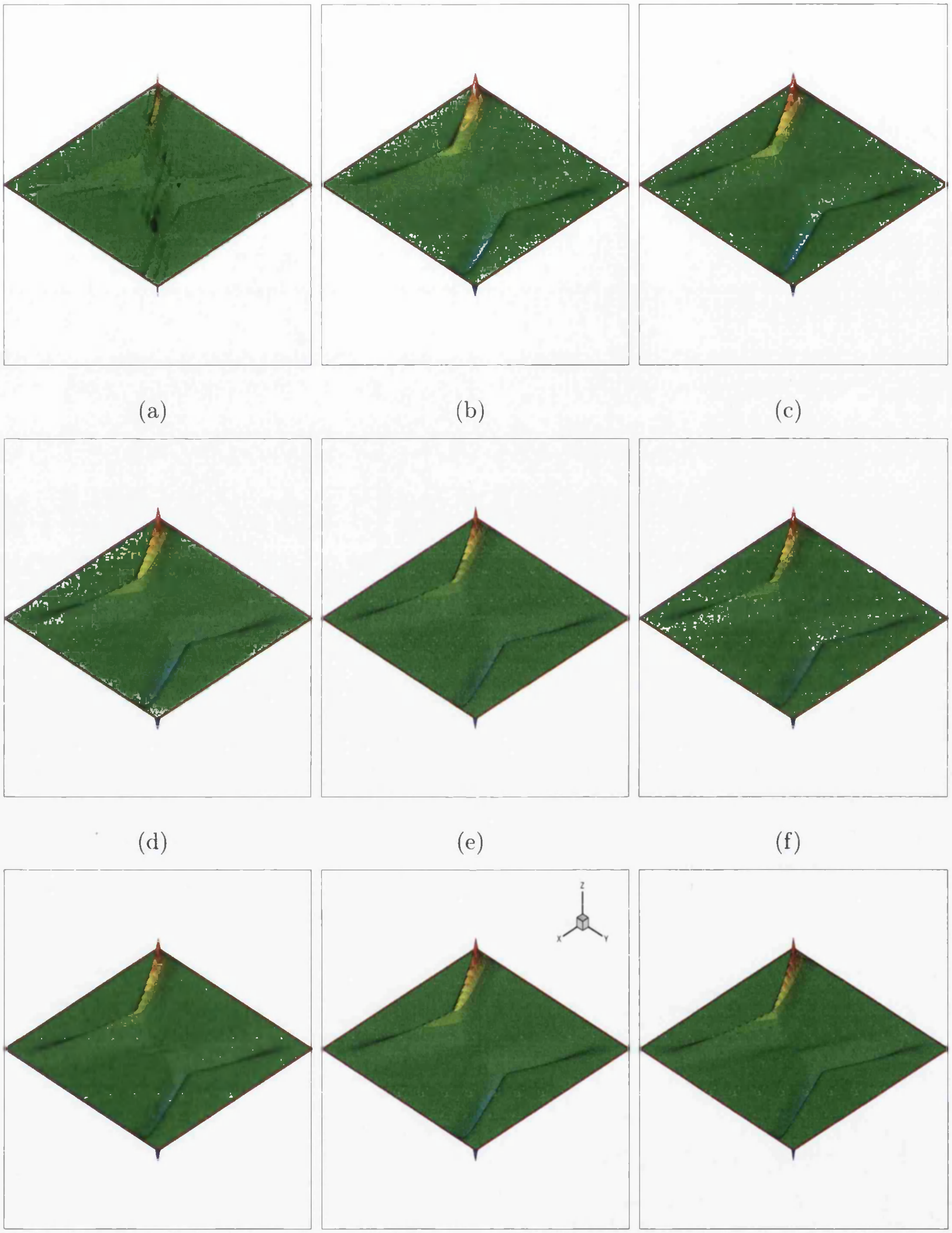

(a) (b) (c)

(d) (e) (f)

(g) (h) (i)

Figure 4.36: Case 8: Cell-vertex scheme, Iso-surface plot for 2X2 domain. (a)TPS q=1. (b)FPS H scheme. (c)FPS $\eta = 0.25$. (d)FPS $\eta = \frac{1}{3}$. (e)FPS $\eta = \eta_{OS} - 15\%$. (f)FPS $\eta = \eta_{OS}$. (g)FPS $\eta = \eta_{OS} + 15\%$.(h)FPS $\eta = Gauss$. (i)FPS $\eta = 0.45$

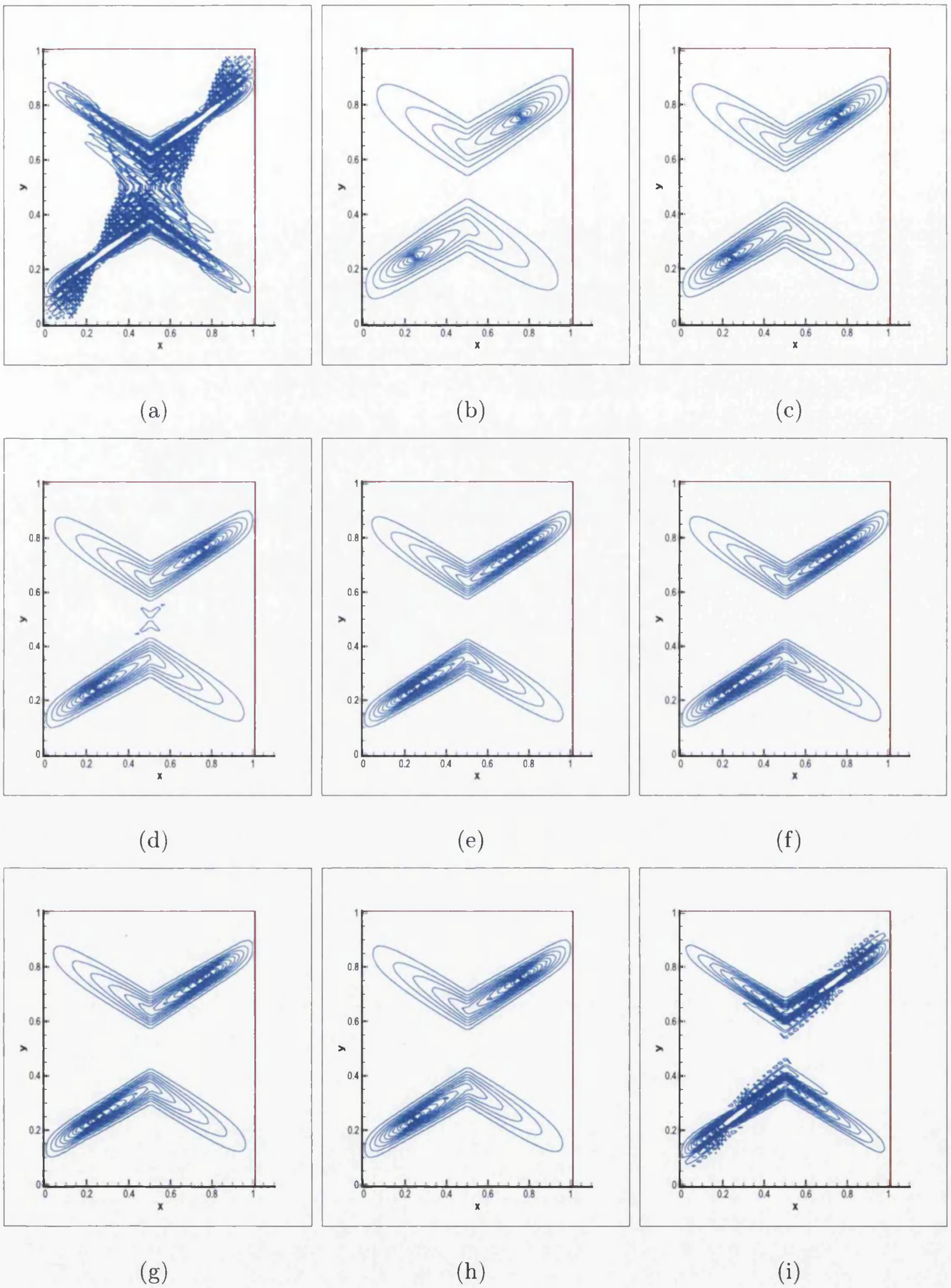

(a) (b) (c)

(d) (e) (f)

(g) (h) (i)

Figure 4.37: Case 8:Cell-centred scheme, Contours for 2X2 domain. (a)TPS q=1. (b)FPS H scheme. (c)FPS $\eta = 0.25$. (d)FPS $\eta = \frac{1}{3}$. (e)FPS $\eta = \eta_{OS} - 15\%$. (f)FPS $\eta = \eta_{OS}$. (g)FPS $\eta = \eta_{OS} + 15\%$. (h)FPS $\eta = Gauss$. (i)FPS $\eta = 0.425$

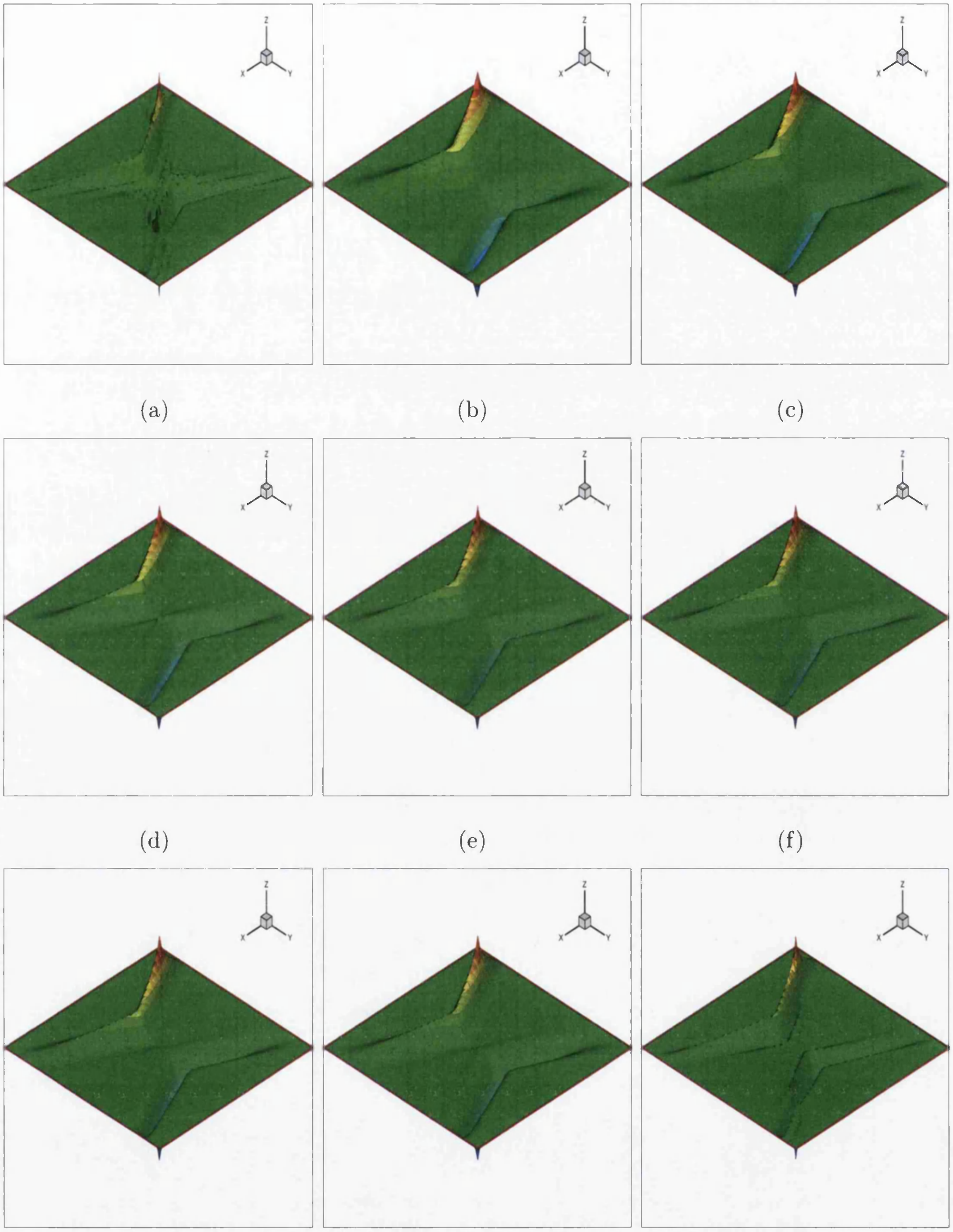

(a) (b) (c)

(d) (e) (f)

(g) (h) (i)

Figure 4.38: Case 8:Cell-centred scheme, Iso-surface plot for 2X2 domain. (a)TPS q=1. (b)FPS H scheme. (c)FPS $\eta = 0.25$. (d)FPS $\eta = \frac{1}{3}$. (e)FPS $\eta = \eta_{OS} - 15\%$. (f)FPS $\eta = \eta_{OS}$. (g)FPS $\eta = \eta_{OS} + 15\%$.(h)FPS $\eta = Gauss$. (i)FPS $\eta = 0.425$

4.35 (h), and Fig 4.36 (h).)yields satisfying stable results while for the cell-centred scheme $\eta = 0.425$ already shows spurious oscillation (Fig 4.37 (i), and Fig 4.38 (i).).

4.12 Summary

A new family of locally conservative flux-continuous, finite-volume schemes is presented for solving the general tensor pressure equation. The new family of schemes have full pressure continuity imposed across control-volume faces, in contrast to the earlier families of flux-continuous schemes, which are point-wise continuous in pressure and flux.

The new family of schemes offers maximum flexibility in range of quadrature. The permissible quadrature range of the earlier pointwise schemes is shown to be half that of the full continuity schemes for a diagonal tensor. When applying both the point-wise continuous schemes and full pressure continuity schemes to full-tensor fields with high anisotropy ratios, the schemes can fail to satisfy the maximum principle. For strong full-tensor anisotropy, the point-wise TPS schemes are shown to have quadrature points that lie within a small neighbourhood of the singular decoupled end point of the quadrature interval, leading to strong spurious oscillations in the solution.

The family of FPS schemes are shown to be symmetric positive definite for a spatially constant full elliptic tensor. Constant coefficient M-matrix bounds for the general family of full-tensor schemes define tensor-coefficient dependent quadrature interval limits for obtaining locally bounded solutions. When the governing conditions are satisfied the discrete pressure field is free of spurious oscillations. An *optimal support condition* is identified from the M-matrix conditions, via a bounding quadrature point that defines the upper limit on the tensor cross-term.

The new family of schemes are tested on a range of problems involving strong full-tensor anisotropy where both M-matrix and monotone matrix conditions are violated.

Results are presented for a range of quadrature points belonging to the new family and show that the occurrence of spurious oscillations in the discrete pressure field is minimal provided the quadrature point lies outside of the neighbourhood of the pointwise continuity schemes which are essentially decoupled in this case. A study of the non-monotone case motivates the introduction of quasi-positive QM-matrices. The optimal support quadrature point is also optimal with respect to a QM-matrix.

The new full pressure support schemes are shown to share the full CVFE quadrature range for spatially constant tensor coefficients. The optimal support quadrature point is shown to lie within the quadrature range of the full pressure support scheme for all elliptic tensors. For regions where the tensor is spatially constant, the optimal support quadrature point yields a scheme that self-adapts the discretization support locally according to the local orientation of the tensor field. The tests conducted show the optimal point yields results of sharper resolution than results corresponding to the first interval of the quadrature range.

For a spatially variable tensor field a locally upscaled tensor is used to define the local tensor dependent optimal quadrature point per dual-cell, the resulting finite volume method is then applied to the original (non-upscaled) problem. In this case the scheme will have a quadrature point that lies in the neighbourhood of the exact optimal point. Tests of quadrature points within 15 percent (or slightly more) of the optimal point are found to yield results of comparable resolution to that of the optimal point, with similar sharper resolution.

The cell-centred formulation is also developed and compared with the cell-vertex formulation. The numerical results show that the cell-centred schemes have a slightly larger decoupled zone and correspondingly smaller region of stability. Although generally the FPS cell-centred formulation also provides a much improved quadrature range that yields results with few spurious oscillations.

Chapter 5

Double family of Continuous Darcy-Flux Finite Volume Schemes with Full Pressure Support

5.1 Introduction

This chapter presents the development of new double-families of flux-continuous finite volume methods for the pressure equation resulting from Darcy's law and mass conservation. Key physical constraints of continuity in normal flux and full pressure continuity are imposed at control-volume interfaces.

In this chapter new families of flux-continuous, locally conservative, finite-volume schemes are presented for solving the general tensor pressure equation. The new schemes have full pressure continuity imposed across control-volume faces, in contrast to the earlier families of flux-continuous schemes with point-wise continuity in pressure and flux. This work extends the single parameter family of [17] to double families of schemes with general flexibility in quadrature that allow different quadrature points to be used on different control-volume subfaces [38].

For strongly anisotropic full-tensor cases where M-matrix conditions are violated, the earlier pointwise continuous families of schemes cannot avoid decoupling of the solution which leads to severe spurious oscillations in the discrete solution [17]. The new schemes minimize spurious oscillations in discrete pressure solutions. The new formulation leads to more robust quasi-positive families of flux-continuous schemes applicable to general discontinuous full-tensor fields.

5.2 Double-Families of Flux-Continuous Schemes with Full Pressure Continuity

Here we extend the single parameter method of [17] to double families of schemes which have continuous pressure support over the entirety of each control-volume subface. The double families of schemes allow different quadrature points to be used on different control-volume subfaces leading to anisotropic quadrature schemes that prove to be beneficial for anisotropic problems.

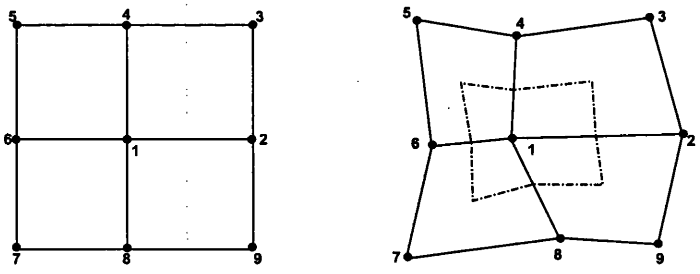

(a) (b)

Figure 5.1: (a)Numbering of scheme support nodes (stencil)(b) Nine-node Support, Control-volume i, j Dot-Dashed with Primal-cell $i + 1/2, j + 1/2$ Solid line

Cell-vertex and cell-centred formulations are developed. In this section we present the cell-vertex quadrilateral formulation. The support and numbering for the cell-vertex scheme are shown in Fig. 5.1. A dual grid of polygonal control-volumes is constructed from the primal grid by joining primal grid cell-centres to cell edge mid-points, so that each interior vertex is placed inside a control-volume Fig.5.1 (b). Discrete flow and rock variables are assigned to the grid vertices and permeability has a piecewise constant variation over the dual grid of control-volumes. Introduction of the dual-grid (dot-dashed) partitions each primal grid cell into four sub-quadrilateral cells (subcells). Each subcell of a primal cell is therefore attached to a unique vertex and is also a subcell of the corresponding vertex control-volume. The subcell faces that lie inside a primal cell are thus subfaces of the corresponding vertex control-volumes and are interfaces across which permeability may jump in variation. Consequently the physical constraints of continuity in pressure and normal flux must be imposed across the resulting subfaces. This is achieved cell-wise, four local flux continuity conditions (together with pressure continuity) are imposed over the four interior subfaces between subcells in each primal cell to handle jumps in permeability between adjacent control-volumes, details are given below.

5.2.1 Double Families of Full Pressure Continuity Schemes - Quadrature parameterization

In this primal cell-wise formulation the *lower-case* indices (n, s, e, w) indicate the mid-points of the faces of a primal cell. The mid-points are connected to the primal cell centre m, forming the four interior subcell faces, or sub-faces Fig. 5.2 (a) where subfaces are indicated with dot-dashed lines. Interface pressures are introduced at the indicated fixed positions (n, s, e, w) in Fig.5.2 (a). Full sub-cell face pressure continuity is achieved by introduction of a further interface pressure at the common corner m of the four subcells (i.e. at the primal cell centre) indicated in Fig. 5.1, 5.2. The set of local interface pressures to be determined over the primal cell is given by $\Phi_f = (\phi_n, \phi_s, \phi_e, \phi_w, \phi_m)^T$.

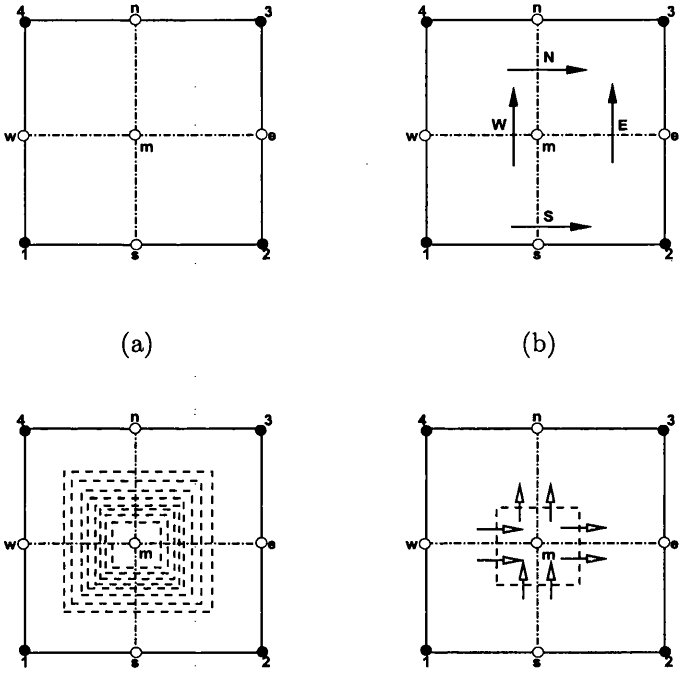

(a) (b)

(c) (d)

Figure 5.2: (a) Local nodes in a cell, control-volume sub-faces dot-dashed (b)Double-family Primary Fluxes N, S, E, W in a cell (Solid arrows). (c) auxiliary control volumes (dashed lines). (d) auxiliary fluxes in a cell (hollow arrows)

A subcell bilinear approximation of pressure and position vector is introduced locally over each subcell with local master element parametric coordinates $(0 \leq \tilde{\xi}, \tilde{\eta} \leq 1)$ where for example over subcell $(1, s, m, w)$ pressure and position vector are defined by

$$\phi = (1 - \tilde{\xi})(1 - \tilde{\eta})\phi_1 + \tilde{\xi}(1 - \tilde{\eta})\phi_s + \tilde{\xi}\tilde{\eta}\phi_m + (1 - \tilde{\xi})\tilde{\eta}\phi_w \tag{5.1}$$

$$\mathbf{r} = (1 - \tilde{\xi})(1 - \tilde{\eta})\mathbf{r}_1 + \tilde{\xi}(1 - \tilde{\eta})\mathbf{r}_s + \tilde{\xi}\tilde{\eta}\mathbf{r}_m + (1 - \tilde{\xi})\tilde{\eta}\mathbf{r}_w \tag{5.2}$$

This permits a degree of freedom in position of flux continuity on each sub-face, leading to new families of flux-continuous schemes with full pressure support. The schemes are consequently exact for any piecewise linear or bilinear pressure field provided the Darcy flux is consistently resolved in physical space as follows. Approximate derivatives are derived from the bilinear map over each sub-cell. For example over subcell 1 (with corners labeled anti-clockwise $(1, s, m, w)$) we obtain

$$\begin{aligned} \phi_{\tilde{\xi}} &= (1 - \tilde{\eta})(\phi_s - \phi_1) + \tilde{\eta}(\phi_m - \phi_w) \\ \phi_{\tilde{\eta}} &= (1 - \tilde{\xi})(\phi_w - \phi_1) + \tilde{\xi}(\phi_m - \phi_s) \end{aligned} \tag{5.3}$$

with an analogous approximation for position vector derivatives.

$$\begin{aligned} \mathbf{r}_{\tilde{\xi}} &= (1 - \tilde{\eta})(\mathbf{r}_s - \mathbf{r}_1) + \tilde{\eta}(\mathbf{r}_m - \mathbf{r}_w) \\ \mathbf{r}_{\tilde{\eta}} &= (1 - \tilde{\xi})(\mathbf{r}_w - \mathbf{r}_1) + \tilde{\xi}(\mathbf{r}_m - \mathbf{r}_s) \end{aligned} \tag{5.4}$$

Using equations 5.3,5.4 the discrete Darcy velocity at S is defined as

$$v_h = -\mathbf{K}^1 \nabla \phi_h = -\mathbf{K}^1 \mathbf{G}(\tilde{\eta}) \begin{pmatrix} \phi_{\tilde{\xi}} \\ \phi_{\tilde{\eta}} \end{pmatrix} \tag{5.5}$$

Where $\mathbf{K}^1$ is the local permeability tensor of vertex 1 and dependency of $\nabla \phi_h$ on quadrature point arises through

$$\nabla \phi_h = \mathbf{G}(\tilde{\eta}) \begin{pmatrix} \phi_{\tilde{\xi}} \\ \phi_{\tilde{\eta}} \end{pmatrix} = \begin{pmatrix} y_{\tilde{\eta}} & -y_{\tilde{\xi}} \\ -x_{\tilde{\eta}} & x_{\tilde{\xi}} \end{pmatrix} \frac{1}{J(\tilde{\xi}, \tilde{\eta})} \begin{pmatrix} \phi_{\tilde{\xi}} \\ \phi_{\tilde{\eta}} \end{pmatrix} \tag{5.6}$$

where approximate $\mathbf{r}_{\widetilde{\xi}}$ and $\mathbf{r}_{\widetilde{\eta}}$are defined by Eq. 5.4. The discrete normal Darcy flux at the left hand side of S Fig.5.2(b), is then resolved along the outward normal vector $dL_S = ((y_m - y_s), -(x_m - x_s))$ and is expressed in terms of the general tensor $\mathbf{T} = \mathbf{T}(\widetilde{\xi}, \widetilde{\eta})$ as

$$F_S^1 = v_h \cdot dL_S = -(T_{11}^1 \phi_{\widetilde{\xi}} + T_{12}^1 \phi_{\widetilde{\eta}})|_S^1 \tag{5.7}$$

where it is understood that the resulting coefficients of $-(\phi_{\widetilde{\xi}}, \phi_{\widetilde{\eta}})|_S^1$ denoted by $T_{11}|_S^1$ and $T_{12}|_S^2$ are sub-cell (physical-space) approximations of the general tensor components (Eq. 5.7) at the left hand face at S. A similar expression for flux is obtained at the right hand side of S from subcell 2 Fig.5.2(b). The south flux is a function of $\widetilde{\eta}$. Similarly sub-cell fluxes are resolved on the two sides of the other faces at E, W and N. Flux continuity is then imposed across the four cell interfaces at the four positions N, S, E, W Fig.5.2(b) which are specified by chosen quadrature points defined with respect to $\widetilde{\xi}, \widetilde{\eta}$.

Note that *upper-case* N, S, E, W define the flux positions of the family of schemes on the control-volume sub-faces, while the actual interface pressures $(\phi_n, \phi_s, \phi_e, \phi_w)$ remain attached to the mid-points of the faces of the primal grid cell. The complete vector of interface pressures $\Phi_f = (\phi_n, \phi_s, \phi_e, \phi_w, \phi_m)^T$ are determined in terms of the primal degrees of freedom $\Phi_v = (\phi_1, \phi_2, \phi_3, \phi_4)^T$ at the vertices of the primal cell, by imposing flux continuity across the four subcell faces inside the cell, together with a zero divergence condition for ϕ_m, thus enabling Φ_f to be expressed in terms of the four primal cell vertex pressures $\Phi_v = (\phi_1, \phi_2, \phi_3, \phi_4)^T$.

The primal cell divergence approximation is introduced over an auxiliary control-volume surrounding the cell centre. The location of the auxiliary control-volume is another parameter to be specified, e.g. any of the indicated dot-dashed lines in Fig's.5.2 (c),(d). The four flux continuity conditions together with the zero divergence condition lead to the local algebraic system

$$\begin{aligned}
F_N &= -(T_{11}\phi_{\tilde{\xi}} + T_{12}\phi_{\tilde{\eta}})|_N^3 = -(T_{11}\phi_{\tilde{\xi}} + T_{12}\phi_{\tilde{\eta}})|_N^4,\\
F_S &= -(T_{11}\phi_{\tilde{\xi}} + T_{12}\phi_{\tilde{\eta}})|_S^1 = -(T_{11}\phi_{\tilde{\xi}} + T_{12}\phi_{\tilde{\eta}})|_S^2,\\
F_E &= -(T_{12}\phi_{\tilde{\xi}} + T_{22}\phi_{\tilde{\eta}})|_E^2 = -(T_{12}\phi_{\tilde{\xi}} + T_{22}\phi_{\tilde{\eta}})|_E^3,\\
F_W &= -(T_{12}\phi_{\tilde{\xi}} + T_{22}\phi_{\tilde{\eta}})|_W^1 = -(T_{12}\phi_{\tilde{\xi}} + T_{22}\phi_{\tilde{\eta}})|_W^4,\\
&\quad -\textstyle\sum_{\partial\Omega_{AUX}}(\mathbf{K}\nabla\Phi)\cdot\hat{\mathbf{n}}\Delta s = 0
\end{aligned} \tag{5.8}$$

The double-family of schemes is defined by the positions of flux continuity parameterized by the local basis function $\tilde{\xi}, \tilde{\eta}$, with respect to pairs of subcell faces. The double-parameter family is distinguished from a single parameter family by allowing quadrature points that are not necessarily equal along adjoining subcell faces so that $\tilde{\xi} \neq \tilde{\eta}$. To clarify notation, for example F_S will denote a flux at a quadrature point that may either coincide with s or be between s and m, but never coincides with m, i.e. $0 \leq \tilde{\xi}, \tilde{\eta} < 1$. Here we illustrate discrete flux continuity for the second and fourth equations of Eq.5.8, which are defined by different values of $\tilde{\xi}$ and $\tilde{\eta}$ respectively. The second equation is defined at a point S between s and m with

$$\begin{aligned}
F_S &= -(T_{11}^1((1-\tilde{\eta})(\phi_s - \phi_1) + \tilde{\eta}(\phi_m - \phi_w)) + T_{12}^1(\phi_m - \phi_s))\\
&= -(T_{11}^2((1-\tilde{\eta})(\phi_2 - \phi_s) + \tilde{\eta}(\phi_e - \phi_m)) + T_{12}^2(\phi_m - \phi_s))
\end{aligned} \tag{5.9}$$

where for the left hand side flux, approximations of $\phi_{\tilde{\xi}}$ and $\phi_{\tilde{\eta}}$ are given by Eq.5.3 and F_S is a function of $\tilde{\eta}$, $F_S = F_S(\tilde{\eta})$ and the geometric tensor coefficients are calculated at S where the position is defined by the quadrature point $\tilde{\eta}$, where $\mathbf{r}|_S = (1-\tilde{\eta})\mathbf{r}_s + \tilde{\eta}\mathbf{r}_m$.

The fourth equation is defined at a point W between w and m (again never coinciding with m) with

$$\begin{aligned}
F_W &= -(T_{12}^1(\phi_m - \phi_w) + T_{22}^1((1-\tilde{\xi})(\phi_w - \phi_1) + \tilde{\xi}(\phi_m - \phi_s)))\\
&= -(T_{12}^4(\phi_m - \phi_w) + T_{22}^4((1-\tilde{\xi})(\phi_4 - \phi_w) + \tilde{\xi}(\phi_n - \phi_m)))
\end{aligned} \tag{5.10}$$

where for the left hand side flux (with respect to edge (m, w)), approximations of $\phi_{\tilde{\xi}}$ and $\phi_{\tilde{\eta}}$ are again given by Eq.5.3 and now F_W is a function of $\tilde{\xi}$, $F_W = F_W(\tilde{\xi})$ and the tensor coefficients are calculated at W where the position is defined by the quadrature point $\tilde{\xi}$, $\mathbf{r}|_W = (1-\tilde{\xi})\mathbf{r}_w + \tilde{\xi}\mathbf{r}_m$.

Analogous sub-cell approximations are constructed for each of the flux continuity conditions in Eq.5.8, leading to $F_N(\widetilde{\eta}), F_S(\widetilde{\eta}), F_E(\widetilde{\xi}), F_W(\widetilde{\xi})$ which are not necessarily symmetrically located c.f. Fig. 5.2 (b), where $\widetilde{\xi} \neq \widetilde{\eta}$ creating double families. The actual choice of quadrature points $(\widetilde{\xi}, \widetilde{\eta})$ are discussed in section 5.4.

Referring now to the discrete auxiliary divergence approximation, the 5^{th} equation of Eq.5.8, the auxiliary control-volume (perimeter shown dot-dashed) centred on the auxiliary node m of Fig. 5.2 (c),(d) is comprised of 4 *sub-subcells* one in each subcell where permeability is piecewise constant, so the auxiliary divergence approximation is based on CVFE. The auxiliary fluxes are also parameterized with respect to $\widetilde{\xi}, \widetilde{\eta}$. The auxiliary control-volume can lie in or on the dual-cell, the size is to be chosen, and parameterized by the variable $1 \geq c > 0$, where $c = 1$ corresponds to an auxiliary control-volume that overlays the primal cell and as $c \longrightarrow 0$ the auxiliary control-volume tends to zero.

The primal control-volume and auxiliary control-volume fluxes are indicated in Fig. 5.2 (b),(d), with solid arrows for primal fluxes and hollow arrows for auxiliary fluxes. The auxiliary fluxes have super-fixes indicating the auxiliary subcell and compass suffices indicating position relative to the primal subcell in which they are defined. For example referring again to subcell 1 (corners $1, s, m, w$), the auxiliary control-volume flux F_N^1 is defined on the top left sub-subcell face by

$$\begin{aligned} F_N^1 = c(&-T_{11}^1(c(1-p)(\phi_s - \phi_1) + (1 - c(1-p))(\phi_m - \phi_w)) \\ &-T_{12}^1(c(\phi_w - \phi_1) + (1-c)(\phi_m - \phi_s))) \end{aligned} \tag{5.11}$$

which is a function of the auxiliary quadrature and control-volume size parameters $p = p(\widetilde{\xi}, \widetilde{\eta})$ and c respectively. In the general case this formulation leads to a multiple family of schemes which are also functions of the primary flux quadrature parameters $\widetilde{\xi}, \widetilde{\eta}$, the auxiliary control-volume flux parameter p and auxiliary control-volume size parameter c.

The degrees of freedom of the five equation system Eq.5.8 are the five interface pressures $\Phi_f = (\phi_n, \phi_s, \phi_e, \phi_w, \phi_m)^T$ and the four cell vertex pressures $\Phi_v =$

$(\phi_1, \phi_2, \phi_3, \phi_4)^T$. The system of equations is rearranged as

$$A_L^{5X5}\Phi_f + B_L^{5X4}\Phi_v = A_R^{5X5}\Phi_f + B_R^{5X4}\Phi_v \tag{5.12}$$

where A_L^{5X5}, A_R^{5X5} are 5X5 matrices and B_L^{5X4}, B_R^{5X4} 5X4 matrices. Since we only require the four fluxes, we let A_L^{4X5} denote the first four rows of matrix A_L^{5X5} and B_L^{4X4} denote the first four rows of matrix B_L^{5X4}.

Then the continuous fluxes of the families of FPS schemes are written as:

$$\mathbf{F} = (A_L^{4X5}(A_L^{5X5} - A_R^{5X5})^{-1}(B_R^{5X4} - B_L^{5X4}) + B_L^{4X4})\Phi_v \tag{5.13}$$

where $\mathbf{F} = (F_N, F_S, F_E, F_W)^T$. Fluxes are then assembled from respective grid cells to form control-volume face flux approximations, e.g. for a structured grid the net flux across the right hand face of control-volume i, j (local node 1) $F_{i+1/2,j} = F_{S_{i+1/2,j+1/2}} + F_{N_{i+1/2,j-1/2}}$, is a linear function at the 6 vertex values 1,2,3,4,8,9, where $i + 1/2, j + 1/2$ are integer coordinates of the top right-hand grid cell in Fig.5.1 (b). The discrete divergence is then formed over each control-volume via cell-wise assembly.

5.2.2 FPS Schemes on Triangle Grids

The generalisation of the method to triangles follows a similar procedure to the above method. The primary pressure variables are located at the primal grid cell vertices as for the quadrilateral case above, with primary variable pressures locally numbered with respect to the triangle vertices viz $\Phi_v = (\phi_1, \phi_2, \phi_3)^T$ with suffix v for vertices, as indicated in Fig. 5.3. There are now three subcells meeting inside the triangle formed by joining triangle cell center to triangle edge midpoints, each one belonging to a unique vertex of the triangle. The local continuity conditions are again naturally imposed via a primal cell-wise formulation. An interface pressure is introduced at the mid-point of each triangle edge and one at the triangle centre where the subcells meet so that $\Phi_f = (\phi_n, \phi_s, \phi_e, \phi_m)^T$. A local bilinear variation in pressure

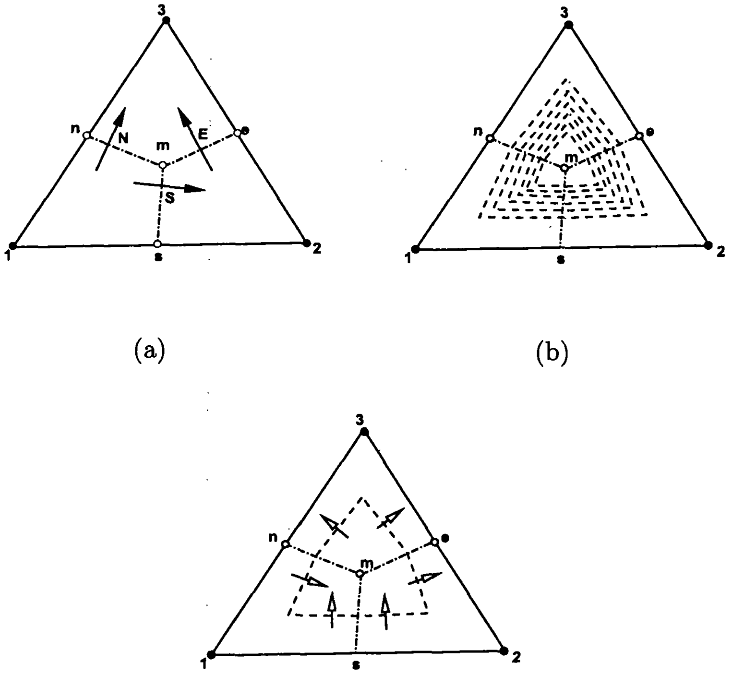

(a)

(b)

(c)

Figure 5.3: (a)Primal fluxes in triangle (solid arrows). (b) Auxiliary Control volumes in a triangle (dashed lines). (c)Auxiliary fluxes in a triangle (hollow arrows).

is introduced over each subcell as before. One flux continuity condition is imposed on each of the three subcell faces (dot-dashed subface) to determine ϕ_n, ϕ_s, ϕ_e, where a distinct quadrature can be employed on each subface, leading to double-family fluxes $\mathbf{F} = (F_N, F_S, F_E)^T$, Fig.5.3 (a). Zero divergence is applied over an auxilliary control-volume (dashed) surrounding the triangle centre of gravity Fig.5.3 (b),(c), to determine ϕ_m, providing a total of four equations for the four auxiliary pressures Φ_f. The resulting system of equations are given by

$$\begin{gathered} F_N = -(T_{11}\phi_{\tilde{\xi}} + T_{12}\phi_{\tilde{\eta}})|_N^3 = -(T_{11}\phi_{\tilde{\xi}} + T_{12}\phi_{\tilde{\eta}})|_N^4, \\ F_S = -(T_{11}\phi_{\tilde{\xi}} + T_{12}\phi_{\tilde{\eta}})|_S^1 = -(T_{11}\phi_{\tilde{\xi}} + T_{12}\phi_{\tilde{\eta}})|_S^2, \\ F_E = -(T_{12}\phi_{\tilde{\xi}} + T_{22}\phi_{\tilde{\eta}})|_E^2 = -(T_{12}\phi_{\tilde{\xi}} + T_{22}\phi_{\tilde{\eta}})|_E^3, \\ -\textstyle\sum_{\partial\Omega_{AUX}} (\mathbf{K}\nabla\Phi) \cdot \hat{\mathbf{n}}\Delta s = 0 \end{gathered} \tag{5.14}$$

and represent the triangle equivalent of Eq. 5.8. Approximation of Eq.5.14 and subsequent elimination of the auxiliary pressures follows an analogous procedure to that of Eq's.5.9-5.13. Primal divergence is then approximated by the assembly of continuous control-volume subcell fluxes over each polygon surrounding each vertex.

5.3 Double-family Relationship between FPS and CVFE for a spatially constant tensor

Flux-continuity ensures local conservation, however the converse is not necessarily true, e.g. the CVFE family is locally conservative [1], but key flux continuity is lacking across the interior interfaces where permeability can be discontinuous.

For spatially constant tensor coefficients the quadrilateral flux-continuous schemes can be mapped onto the more transparent control-volume finite element CVFE nine-point framework, see [2], and [17] for the single family FPS analysis. Here $0 \leq \xi, \eta \leq 1$ define master element coordinates over the primal cell if cell-vertex, or dual-cell if cell centred. Derivatives of bilinear expansions of $\phi, \mathbf{r}$ in ξ, η are used in defining the

CVFE double-family fluxes over the primal cell or the dual-cell, Fig.5.1 (b). The resulting fluxes at S and W contributing to control-volume 1 are given by [105]

$$\begin{aligned} F_S &= -\tfrac{1}{2}(T_{11}((\phi_2 - \phi_1)(1-\eta) + (\phi_3 - \phi_4)\eta) + \tfrac{1}{2}T_{12}((\phi_4 - \phi_1) + (\phi_3 - \phi_2)) \\ F_W &= -\tfrac{1}{2}(\tfrac{1}{2}T_{12}((\phi_2 - \phi_1) + (\phi_3 - \phi_4)) + T_{22}((\phi_4 - \phi_1)(1-\xi) + (\phi_3 - \phi_2)\xi) \end{aligned} \tag{5.15}$$

where $0 \leq \xi, \eta < 1/2$ ensuring that flux approximation remains convex over the control-volume and that the quadrature points do not both coincide with the singular point $\xi = \eta = 1/2$. Crucially here the double family schemes permit quadratures with $\xi \neq \eta$. The spatially constant tensor 9-point scheme coefficients are written as

Table 5.1: **CVFE** *Double-Family Coefficients For Constant Tensor Field*

int coords	**Coefficients**	**Full Tensor**
i,j	**M11**	$2(T11 + T22) - 2(\eta T11 + \xi T22)$
i+1,j	**M12**	$-T11 + (\eta T11 + \xi T22)$
i+1,j+1	**M13**	$-\frac{1}{2}(\eta T11 + \xi T22) - \frac{1}{2}T12$
i,j+1	**M14**	$-T22 + (\eta T11 + \xi T22)$
i-1,j+1	**M15**	$-\frac{1}{2}(\eta T11 + \xi T22) + \frac{1}{2}T12$
i-1,j	**M16**	$-T11 + (\eta T11 + \xi T22)$
i-1,j-1	**M17**	$-\frac{1}{2}(\eta T11 + \xi T22) - \frac{1}{2}T12$
i,j-1	**M18**	$-T22 + (\eta T11 + \xi T22)$
i+1,j-1	**M19**	$-\frac{1}{2}(\eta T11 + \xi T22) + \frac{1}{2}T12$

Table 5.1: *Double-Family Coefficients For Constant Tensor Field*

Note $0 \leq \xi, \eta < 1/2$ for fluxes defined in their respective control-volumes. The CVFE double-family framework is a natural extension of the single family [1] and is quite transparent and includes all possible double-parameter, consistent, locally conservative, nine-point diagonal and full-tensor schemes, for spatially constant permeability coefficients.

Symmetry of the double-family for constant coefficients is verified by inspection of the above table. The CVFE family is symmetric positive definite [17],[1] and the double-family is SPD, by a similar proof. From the mapping below it follows that the FPS families of schemes are therefore SPD for spatially constant elliptic tensor coefficients for $0 \leq \xi, \eta < 1/2$.

5.3.1 Full Pressure Support FPS and CVFE Mapping

For a spatially constant tensor the FPS schemes can also be expressed in the form of table 5.1 with ξ, η in the CVFE scheme defined by

$$\begin{aligned} \xi &= \tfrac{1}{2}(\tilde{\xi} + t(\tilde{\xi}, \tilde{\eta})ER) \\ \eta &= \tfrac{1}{2}(\tilde{\eta} + t(\tilde{\xi}, \tilde{\eta})ER) \end{aligned} \tag{5.16}$$

where

$$t(\tilde{\xi}, \tilde{\eta}) = \frac{c(2 - \tilde{\xi} - \tilde{\eta})(T_{11} + T_{22})}{(1 + c)((1 - \tilde{\eta})T_{11} + (1 - \tilde{\xi})T_{22}) + c(T_{11} + T_{22}))} \tag{5.17}$$

where $R = \frac{4T11T22}{(T_{11}+T_{22})^2}$ (harmonic/arithmetic means), and $E = \frac{T12^2}{T11T22}$ (ellipticity measure) where $R, E \leq 1$, and $0 \leq \eta < 1/2$, with maximum quadrature bounded above by 1/2. The lower bounds of ξ, η only tend to zero if the auxiliary control-volume size tends to zero, which occurs in the limit with $c \rightarrow 0$, and from Eq.5.16 it follows that $\xi = \tilde{\xi}/2, \eta = \tilde{\eta}/2$ and the FPS flux integration intervals map onto the CVFE intervals with $0 \leq \xi, \eta < \frac{1}{2}$. Therefore an M-matrix analysis of the CVFE double-family with coefficients in table 5.1 is applicable to the FPS double-family [38].

5.3.2 Triangular Pressure Support TPS and CVFE Mapping

The original point-wise continuous schemes with triangle pressure support (TPS) also extend to a double family with mapping

$$\xi = \frac{(pE + q - pq)}{2(p + q - pq)}, \quad \eta = \frac{(p + qE - pq)}{2(p + q - pq)} \tag{5.18}$$

where E is defined above and $0 < p, q \leq 1$ are local quadrature coordinates measured from the dual-cell centre to the cell-face mid-points [2], which also shows that an

Coefficients	**Full Tensor**
M11	$2(T11+T22)-((\alpha T11+\beta T22)+(\tilde{q}T11+\tilde{p}T22)E)$
M12	$-T11+\frac{1}{2}((\alpha T11+\beta T22)+(\tilde{q}T11+\tilde{p}T22)E)$
M13	$-\frac{1}{4}((\alpha T11+\beta T22)+(\tilde{q}T11+\tilde{p}T22)E)-\frac{T12}{2}$
M14	$-T22+\frac{1}{2}((\alpha T11+\beta T22)+(\tilde{q}T11+\tilde{p}T22)E)$
M15	$-\frac{1}{4}((\alpha T11+\beta T22)+(\tilde{q}T11+\tilde{p}T22)E)+\frac{T12}{2}$
M16	$-T11+\frac{1}{2}((\alpha T11+\beta T22)+(\tilde{q}T11+\tilde{p}T22)E)$
M17	$-\frac{1}{4}((\alpha T11+\beta T22)+(\tilde{q}T11+\tilde{p}T22)E)-\frac{T12}{2}$
M18	$-T22+\frac{1}{2}((\alpha T11+\beta T22)+(\tilde{q}T11+\tilde{p}T22)E)$
M19	$-\frac{1}{4}((\alpha T11+\beta T22)+(\tilde{q}T11+\tilde{p}T22)E)+\frac{T12}{2}$

Table 5.2: *Double-Family (TPS) Coefficients For Constant Tensor Field, Where* $\alpha = \frac{p(1-q)}{\sigma}$, $\beta = \frac{q(1-p)}{\sigma}$, $\tilde{q} = \frac{q}{\sigma}$, $\tilde{p} = \frac{p}{\sigma}$, $E = \frac{T12^2}{T11T22}$, $\sigma = p + q - pq$

M-matrix analysis of the CVFE double-family applies to the TPS double-family. However as for the original family, for high full-tensor anisotropy ratio when $E \approx 1$ the schemes are decoupled.

5.4 Positivity: Conditions for an M-matrix

As discussed in chapter 4, the term monotonicity is too strong when describing multi-dimensional solutions, as the local solution can often have a saddle point in structure [17]. As before we use the term positivity as defined in [17], [38] and given in chapter 4. Well known conditions for an M-matrix are also given in Chapter 4. The positivity condition is consistent with the absence of spurious oscillations and defines a local discrete maximum principle (DMP).

5.4.1 Quadrilateral M-matrix Conditions and Cell-wise Analysis

An M-matrix analysis is conducted by considering cell-wise assembly of fluxes for the cell-vertex formulation and dual-cell assembly of fluxes for the cell-centred formulation [2, 1], [17, 38].

A primal cell-wise M-matrix test for the double family is performed in [38], and leads to the following conditions:

$$\mid T_{12} \mid \leq (\eta T_{11} + \xi T_{22}) \leq min(T_{11}, T_{22}) \tag{5.19}$$

Here ξ, η can be defined independently leading to a wide range of double-family flux quadrature points. We note that M-matrix conditions for the single family of schemes are recovered for $\xi = \eta$ in Eq. 5.19 [2], [17].

The double-family nine-node M-matrix conditions of Eq.5.19 can also be verified by inspection of Table 5.1. One of the essential conditions here is that

$$\mid T_{12} \mid \leq min(T_{11}, T_{22}) \tag{5.20}$$

which is only *sufficient for ellipticity* ($T_{12}^2 \leq T_{11}T_{22}$) as for single family schemes [17]. Thus elliptic tensors with $\mid T_{12} \mid > min(T_{11}, T_{22})$ violate the M-Matrix criteria of Eq. 5.19 and expose the upper M-Matrix limit. These conditions now establish the following *Conditional M-matrix* theorem [38]: *Any double parameter family of consistent locally conservative schemes on or within the 9-point stencil applied to a constant full-tensor field can only provide a conditional M-matrix subject to Eq. 5.19.*

Note: FPS fluxes are exact for piece-wise linear and bilinear fields since the pressure basis functions are piecewise bilinear.

5.4.2 Anisotropic Optimal Support and 7-point Schemes

If we choose quadrature points ξ, η such that

$$\eta T_{11} + \xi T_{22} = \mid T_{12} \mid \tag{5.21}$$

then an M-matrix is obtained subject to the sufficient condition for ellipticity of Eq. 5.20, giving the upper limit on the tensor cross-term. Thus Eq.5.21 generalises the result of [2] where $\xi = \eta = \mid T_{12} \mid / (T_{11} + T_{22})$. Choosing FPS (or equivalent

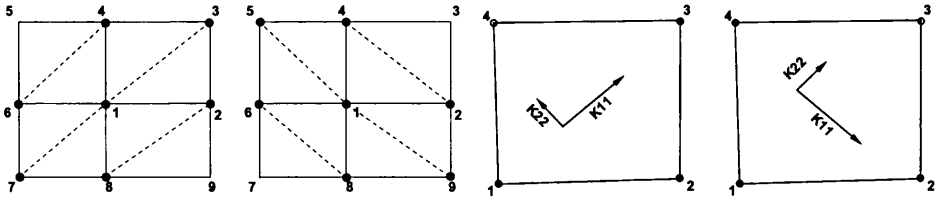

(a) (b) (c) (d)

Figure 5.4: (a) positive T_{12} over all contributing dual-cells - right inclined 7 pt scheme (b) negative T_{12} over all contributing dual-cells - left inclined 7 pt scheme (c) positive T_{12} over a dual-cell (d) negative T_{12} over a dual-cell

CVFE) quadrature points defined via Eq.5.21, it follows from Table 5.1 that if the local tensor field has a positive cross-term $T_{12} > 0$ for each cell the 9-point scheme reduces to a 7-point (triangle) scheme with diagonally upward positive-angle support as indicated in Fig. 5.4 (a), by Table 5.1 $M_{15} = M_{19} = 0$ while the other off-diagonals are non-positive subject to Eq.5.20. Conversely if $T_{12} < 0$ a diagonally downward negative-angle triangle support is obtained Fig. 5.4 (b), in this case $M_{13} = M_{17} = 0$. We note that Eq.5.20 is consistent with the triangle grid scheme M-matrix conditions presented in the next section. We shall refer to Eq.5.21 as the double-family *optimal support condition.* We also note that this leads to the *upper M-matrix limit* for the cross coefficient $\mid T_{12} \mid$. However the condition of Eq.5.21 gives a family of optimal support schemes independently of the M-matrix conditions [38].

In general, the choice of quadrature defined by Eq. 5.21 for double-families leading to (*optimal support*) yields families of schemes that will select a variable support depending upon the local tensor and orientation (sign of the cross-terms). Optimal support relies on exact algebraic cancelation for reduced support. If coefficients vary over subcells, while exact algebraic cancelation is unlikely, optimal support can still be achieved by anisotropy angle favoring triangulation [23] or by special case construction [101]. For a spatially varying tensor approximate optimal support schemes can be defined by using a locally upscaled tensor in Eq. 5.21. These observations lead to a generalisation of the single family [17].

Anisotropic Quadrature

M-matrices are obtained if Eq.5.19 is satisfied. If cross-terms vanish the quadrature Eq.5.21 defaults to zero yielding the basic diagonal-tensor 5-point operator. Other M-matrix schemes that adapt quadrature according to the local tensor variation can also be defined provided other values of ξ, η can be found that lie in the range defined by Eq.5.19.

We now consider highly anisotropic full-tensor fields where the M-matrix conditions are violated with $\mid T_{12} \mid > min(T_{11}, T_{22})$. We note that families of optimal schemes are still defined via Eq.5.21. We will denote optimal support (OS) quadrature points defining families of schemes via Eq.5.21 by $\xi = \xi_{OS}, \eta = \eta_{OS}$. We may either choose a quadrature point with $\xi = \xi_Q$ such as a Gauss point and determine η_{OS} through Eq.5.21, or choose $\eta = \eta_Q$ and determine ξ_{OS} through Eq.5.21.

Following [38], the optimal support quadrature parameter determined by Eq.5.21 is that which multiplies the $max(T_{11}, T_{22})$, while the specified value multiplies the $min(T_{11}, T_{22})$, i.e. if $T_{11} = max(T_{11}, T_{22})$ then specify ξ_Q and determine η_{OS}. Similarly if $T_{22} = max(T_{11}, T_{22})$ then specify η_Q and determine ξ_{OS}. In the first case it follows from Eq.5.21 that

$$\eta_{OS} = (\mid T_{12} \mid - \xi_Q T_{22})/T_{11} \tag{5.22}$$

which corresponds to quadratures ξ_Q, η_{OS} with ξ_Q specified and η_{OS} determined by

$$\eta_{OS} = (\mid T_{12} \mid - \xi_Q min(T_{11}, T_{22}))/max(T_{11}, T_{22}) \tag{5.23}$$

In this way the double family is determined according to field anisotropy. The advantages here are that an optimal or approximately optimal scheme can be determined using specified quadrature points such as Gauss points that are away from the singular point, while the approximate optimal point remains stable. The effect of different quadrature values is presented in the results section.

Extreme Anisotropic Quadrature

An alternative anisotropic quadrature to that of the optimal point is also presented in [38], and motivated by the above observations. We define extreme anisotropic quadrature where for $T_{11} = max(T_{11}, T_{22})$ we set $\xi = 0, \eta \rightarrow 1/2$ and for $T_{22} = max(T_{11}, T_{22})$ set $\xi \rightarrow 1/2, \eta = 0$. Setting the quadrature multiplying the minimum diagonal to zero and maximising the second quadrature exploits anisotropy while ensuring that the decoupled neighborhood where both $\xi \rightarrow 1/2, \eta \rightarrow 1/2$ is avoided. This offers an alternative quadrature that does not depend on the precise tensor coefficients, which are not uniquely defined if permeability has a spatial variation. A further option is that this quadrature can be employed locally as a bound for the optimal point if $\eta_{OS} > 1/2$, ensuring that the quadrature will remain in range. The effects of using extreme quadrature that favors the anisotropy are presented in the results section.

5.5 M-matrix Conditions for Triangle Grid Schemes

A cell-wise M-matrix analysis is performed for the triangle grid scheme in [38]. Discrete cell-vertex fluxes on a triangle with interior discontinuous coefficients can always be expressed as a linear combination of edge differences with $AF = -\Delta\Phi_v$ [9] and discrete flux components for the flux with respect to vertex 1 can be written as

$$F_i = -\big(T_{i1}(\phi_2 - \phi_1) + T_{i2}(\phi_3 - \phi_1)\big) \tag{5.24}$$

for $i = 1, 2$ where T_{ij} are local control-volume tensor coefficients derived from flux continuity conditions.

M-Matrix conditions are deduced from a cell-wise M-Matrix analysis [38] where if

$$\mid T_{21} \mid < T_{11}, \quad \mid T_{12} \mid < T_{22} \tag{5.25}$$

then the method has an M-Matrix on a triangular grid. Here symmetry may be lost in physical space. For a symmetric tensor it follows directly from Eq.5.25 that

$$\mid T_{12} \mid < min(T_{11}, T_{22}) \tag{5.26}$$

This key result of [10], is consistent with the quadrilateral optimal support M-matrix analysis c.f. Eq.5.20 above.

5.6 Decoupled Approximation

The quadrature point $\xi = \eta = 1/2$ is a singular point for the above CVFE, FPS and earlier TPS approximations, the resulting discretization permits a *checker board* solution that is strongly oscillatory and decoupled, [17, 38] varying with $\phi_{i,j} = +1$ together with diagonally connected neighbors where $\phi_{i\pm1,j\pm1} = +1$, while $\phi_{i\pm1,j} = -1$ and $\phi_{i,j\pm1} = -1$. For highly anisotropic full tensors the TPS double and single families are contained in the small end-interval (Eq.5.18) where $(\xi, \eta) \rightarrow (1/2, 1/2)$ leading to decoupling [17]. As discussed below in the next section the FPS double family approximation is constructed to avoid this region.

5.6.1 Corollary: A Monotone Discretization Matrix Avoids Decoupling

An obvious feature of a decoupled solution is the oscillation between positive and negative values. Thus we may conclude that while a scheme with a monotone discretization matrix may not be able to guarantee that resulting numerical solutions are free of spurious oscillations, the monotone property is sufficient to prevent decoupling, since a monotone matrix ensures that any problem with non-negative boundary data yields a positive solution [38]. This observation motivates the idea of constructing a monotone matrix scheme for high full-tensor anisotropy ratios. This property can be built into the approximation via a non-linear construction where scheme coefficients are functions of the solution as presented in [41, 107]. The schemes presented here are linear with respect to the solution vector and while they are not monotone for the test cases considered, they are quasi-positive as defined below and prove to be beneficial.

5.7 Quasi-Positive QM-matrices

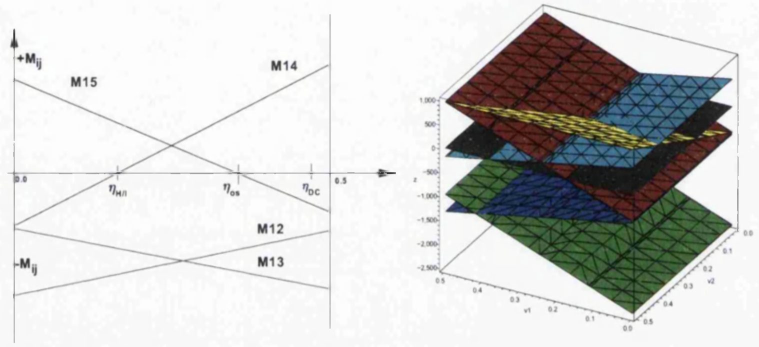

(a) $M_{1j}(\eta, \eta)$

(b) $M_{1j}(\xi, \eta)$ planes: Zero plane is black

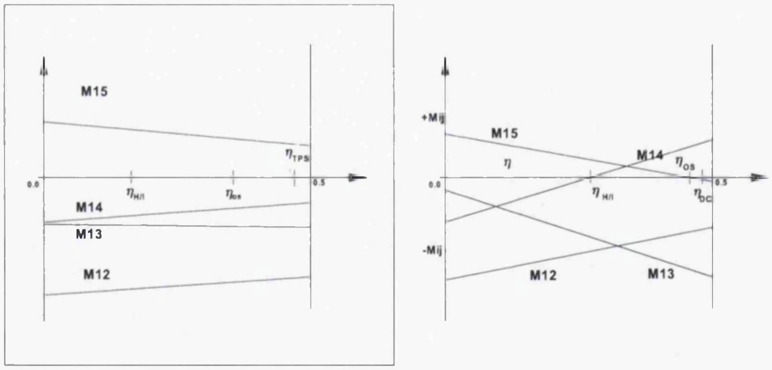

(c) $M_{1j}(\xi, 0)$

(d) $M_{1j}(0, \eta)$

Figure 5.5: Unique coefficients M12, M13, M14, M15 (quadrature ranges) (a) Single family $\xi = \eta$, (b) double-family planes, (c) double-family ξ,with $\eta = 0$. (d) double-family η with $\xi = 0$

We define a Quasi-M-matrix or QM-matrix as a matrix with the minimum of only one unique positive off-diagonal coefficient that violates the M-matrix conditions, [17, 38]. The fundamental M-matrix (and monotone) conditions are violated when $\mid T_{1,2} \mid > min(T_{1,1}, T_{2,2})$. For a spatially constant tensor Table 5.1 reveals that there are certain intervals for which there is one unique offending *positive* off-diagonal coefficient, by matrix symmetry c.f. Table 5.1, we only need to consider the signs of $M_{12}, M_{13}, M_{14}, M_{15}$. The range of positive coefficient intervals is presented in [17] for the single family and illustrated in Fig.5.5 (a). The double family permits an entire quadrature field of QM-matrices Fig. 5.5b. Note that there is always at least one unique positive off-diagonal coefficient visible in Fig's. 5.5 (a),(b),(c), which verifies violation of the M-matrix conditions. Comparing Fig. 5.5(a) for the single family and (b) for the range of double families shows that the double-families yield a wider class of QM-matrices than the single parameter family, e.g. for $\eta = 0$ in Table 5.1, then $M_{15} > 0$ for all $0 \leq \xi < 1/2$, is the only unique positive off-diagonal, while the others remain negative, Fig. 5.5 (c) which does not occur for a single family. The single family is also compared directly with the double family by including the single family matrix coefficient $M_{14}(\eta, \eta)$ in the double family diagram of planes of unique matrix coefficients Fig. 5.5 (b). The $M_{14}(\eta, \eta)$ coefficient is an extrapolated single family plane cutting through the double-family planes in Fig. 5.5 (b), indicating regions where double-families yield improved QM-matrices compared to a single family e.g. for $0 \leq M_{14}(\xi, \eta) \leq M_{14}(\eta, \eta)$. From Eq.5.21, the *optimal* support quadrature is non-unique for the double family, and yields a larger quadrature range than the single family. Optimal support points are also optimal with respect to a QM-matrix, e.g. for a single family the unique coefficient $M_{14} \geq 0$ is minimised at η_{OS}, Fig.5.5 (a). While the optimal points yield well resolved fields, consistently good resolution is also obtained for distinctly different ξ and η chosen near extremes of the quadrature range, according to the dominant anisotropic coefficient. For example if $T_{11} > T_{22}$ then $\eta \rightarrow 1/2$ while $\xi \rightarrow 0$, the matrix coefficients in this case are illustrated in Fig.5.5 (d). This strategy is unique to the double-family formulation in 2-D and has proven to be highly effective. While the leading quadrature parameter is chosen according to

strength of anisotropy, crucially the values of quadrature are independent of the tensor coefficients when chosen in this way. For a spatially varying tensor field extreme quadrature provides an important advantage and simplification when compared to using tensor dependent optimal quadrature points that are approximate particularly for discontinuous tensor coefficients.

5.7.1 QM-matrices on Triangles

The above analysis also shows that a triangulation of a quadrilateral grid that favors the anisotropy will also lead to an optimal QM-matrix for a double-family since the same optimal support is obtained.

5.8 Numerical Results

Comparisons are presented between the new full pressure support double-family formulation and earlier point-wise continuous TPS formulation for domains with full-tensors with strong cross-terms that violate the M-matrix conditions. As with the TPS family, the new FPS families of schemes are exact for piecewise linear test cases with jumps in full-tensor permeability. However unlike TPS, the FPS formulation is also exact for piecewise bilinear test cases with jumps in full-tensor permeability, consistent with the FPS subcell bilinear basis functions. Convergence behaviour has been found to match that of the TPS schemes for lower anisotropy ranges. Cases 1 and 2 demonstrate the advantages of the method in terms of quasi-positivity.

5.8.1 CASE 1: PLANAR FULL-TENSOR FIELD

The first case presented involves a uniform anisotropic medium with a point source in the middle of a square domain. Dirichlet zero pressure boundary data is applied over the entire boundary. The full-tensor is given by

$$\mathbf{K} = \begin{pmatrix} 2464.360020 & 1148.683643 \\ 1148.683643 & 536.6399794 \end{pmatrix} \tag{5.27}$$

with high anisotropy ratio 3000:1 and grid *non-aligned* with the principal axes, which are oriented at an angle of 25 degrees to the computational grid, leading to a full-tensor. The full-tensor field violates the M-matrix condition. First a quadrilateral scheme is used in each case, with a $65X65$ grid resolution.

The first result is computed using the point-wise continuous TPS double-family scheme with $p = 1, q \to 0$. The TPS numerical pressure solution is shown in Fig's. 5.6(a),5.7(a) with visible strong spurious oscillations. We note that the condition of Eq. 5.21 could not be satisfied by the TPS scheme due to the limited quadrature range.

Scheme	No. of Violation	Max	Min
TPS $p = q = 1$	162	5.5240	-1.5937
FPS OS	20	1.9350	-0.0466
FPS ($\xi = 0, \eta = 0.49$)	20	2.0232	-0.0486
FPS ($\xi = 0.49, \eta = 0$)	4	1.3518	-0.0311

Table 5.3: *Test on Discrete Maximum Principle*

Next we present the new FPS double-family results for an example optimal scheme (b), where an example optional point, using the Gauss point $\widetilde{\xi} = 1/\sqrt{3}$ is selected and where η_{OS} is defined via Eq.5.21 leading to quadratures ξ_{Gauss}, η_{OS} yielding a well resolved solution, Figs. 5.6(b),5.7(b). Next in (c) counter extreme anisotropic quadrature is employed with $\xi = 0.49, \eta = 0$, i.e. against anisotropy, resulting in Fig's. 5.6(c),5.7(c). Finally (d) extreme anisotropic quadrature favoring the anisotropy with $\xi = 0, \eta = 0.49$, yielding results shown in Fig's. 5.6(d),5.7(d) respectively. Results (b), (c) and (d) each correspond to QM-matrices and no spurious oscillations are seen in this case. As expected (c) yields the smoother solution. Result (b) uses an optimal

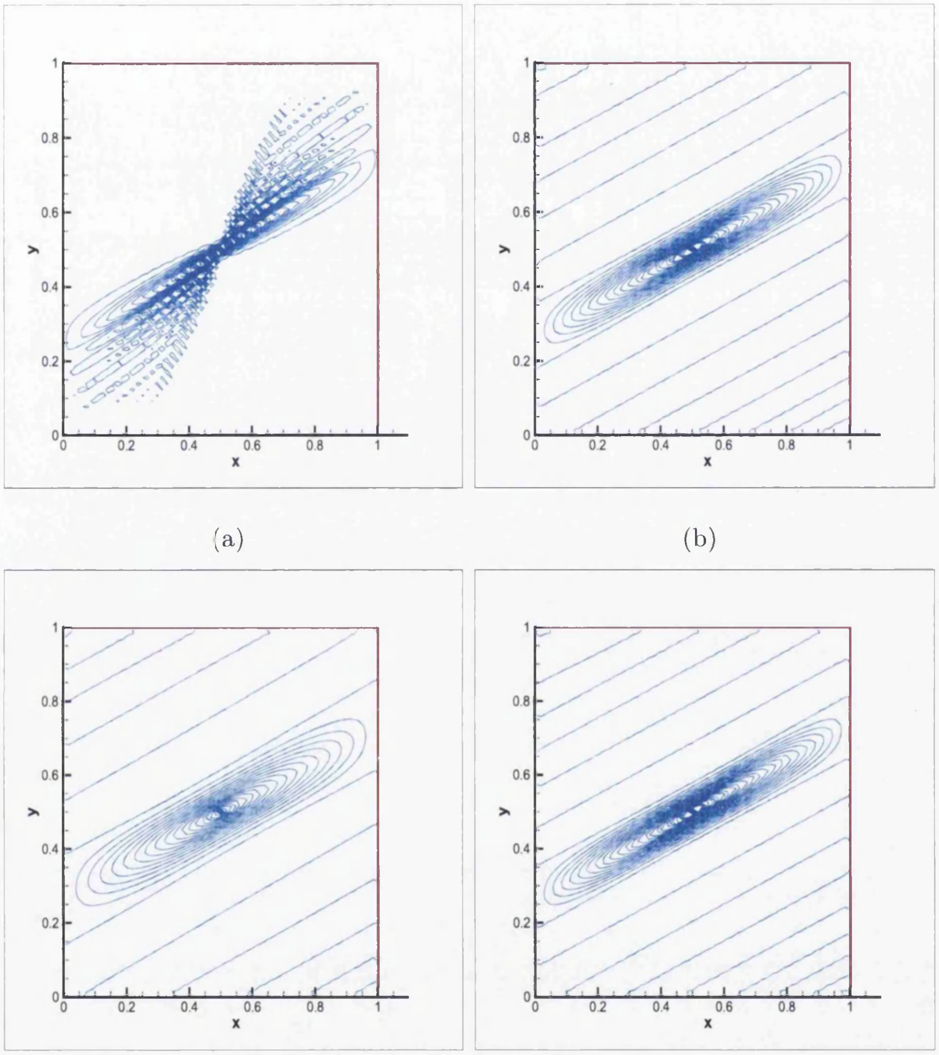

(a) (b)

(c) (d)

Figure 5.6: Homogeneous test case. (a)TPS p=1,q=0.0001 (b) FPS optimal ξ_{Gauss}, η_{OS} (c) FPS extreme counter-anisotropy $\xi = 0.49, \eta = 0$. (d) FPS extreme-anisotropy $\xi = 0, \eta = 0.49$.

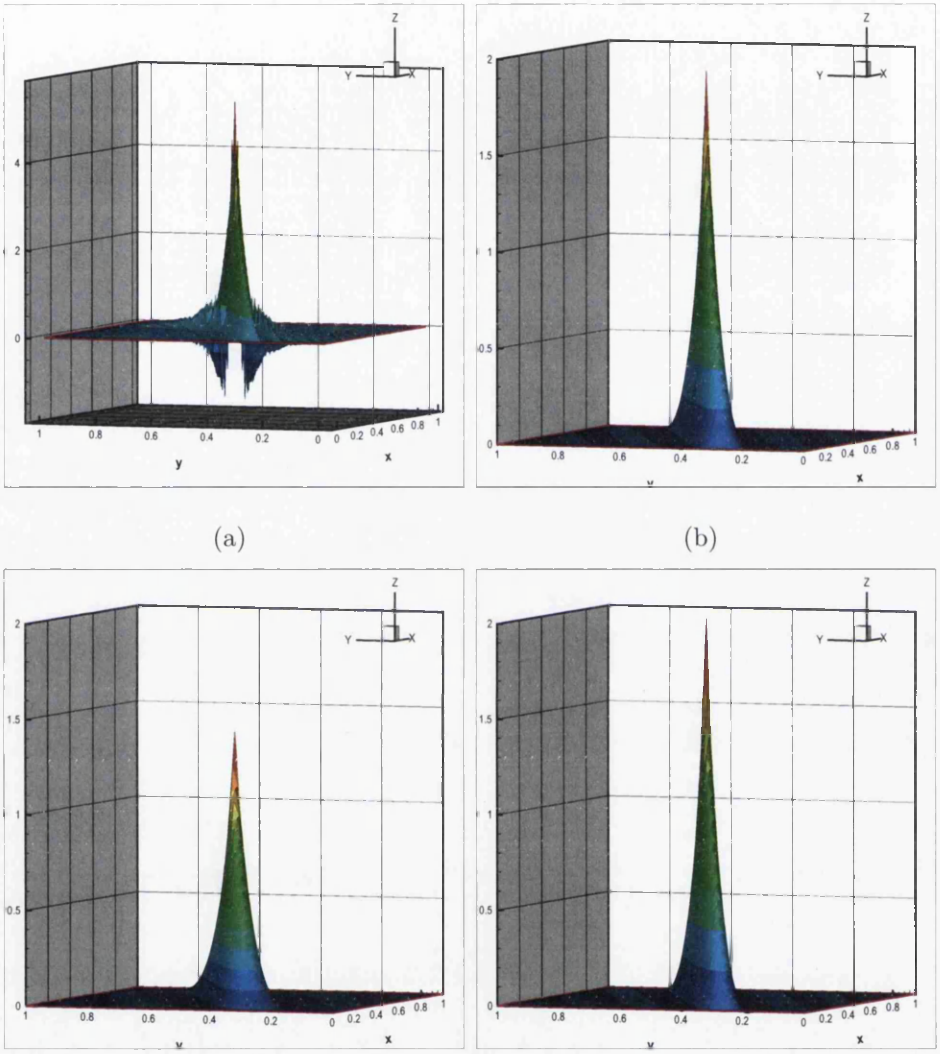

(a) (b)

(c) (d)

Figure 5.7: Homogeneous test case. (a)TPS p=1,q=0.0001 (b) FPS optimal ξ_{Gauss}, η_{OS} (c) FPS extreme counter-anisotropy $\xi = 0.49, \eta = 0$. (d) FPS extreme-anisotropy $\xi = 0, \eta = 0.49$.

point with reduced support favoring anisotropy. The solution is well resolved by (b) and (d). Note that anisotropy motivated extreme quadrature (d) yields sharper resolution than the optimal point scheme (b).

We present a comparative analysis of discrete maximum principle violation in Table 5.3. The criterion for violation is if $\phi_i > \phi_{imax}$ or $\phi_i < \phi_{imin}$, where ϕ_{imax} and ϕ_{imin} are the respective maximum and minimum values of pressure at the neighbouring nodes belonging to the support of node i. The global maximum and minimum values of pressure are also listed. The test detects violations in the fourth decimal place. A scheme that eliminates DMP violations is presented in [22].

Case 1: planar field, using perturbed quadrilateral grid

The same case is tested using a perturbed quadrilateral grid, the results are shown in Figs. 5.8(contours) and 5.9(isosurfaces), the grid is shown in Fig. 5.8(e). Again the pointwise continuous TPS scheme suffers from strong oscillations, while both the optimal point (Figs. 5.8(b) and 5.9(b)) and favorable extreme anisotropic quadrature schemes (Figs. 5.8(d) and 5.9(d)) yield similar sharp results demonstrating that their properties also apply to grids with distorted cells comprised of more general geometry.

Case 1: planar field, using triangular grids

Next we consider the triangle cell-vertex scheme. Results are compared for two $65X65$ grids, with triangulations illustrated by Fig. 5.10(a) and (b). For the grid with triangulation in the counter direction to anisotropy the solution is smoother Fig. 5.11(a) and (b), while for the grid with triangulation favoring anisotropy the solution is well resolved Fig. 5.11(c) and (d), consistent with the optimal support favoring anisotropy. We note that there is an analogous improvement in solution resolution when using anisotropy favoring quadrature and anisotropy favoring triangulation. A range of Delaunay Triangulations have also been used for the same test case. A 1283 node grid and contours are shown in Fig. 5.12(a) and (b), the solution is well resolved

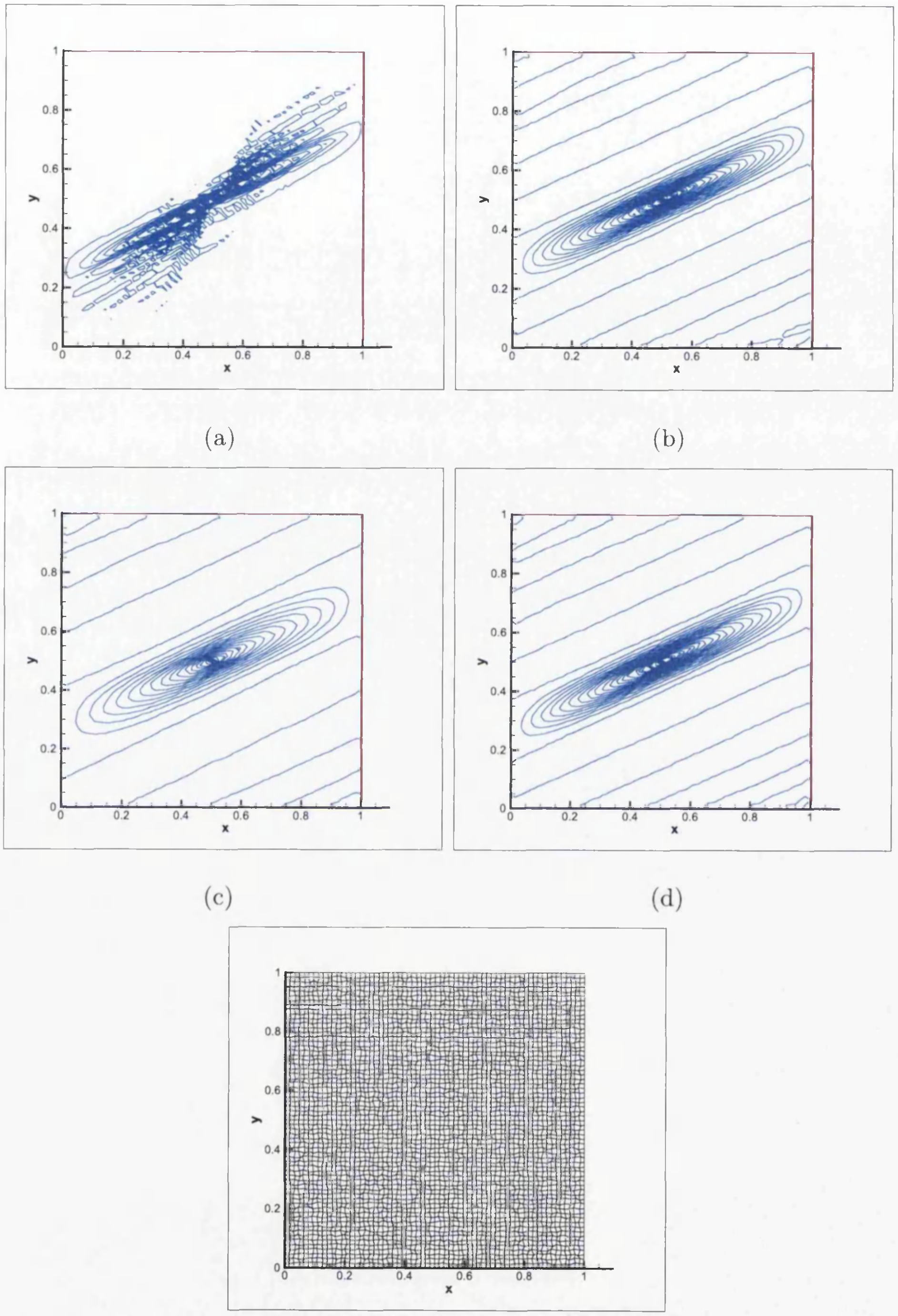

(a) (b)

(c) (d)

(e)

Figure 5.8: Test on perturbed cartesian quadrilateral grid, homogeneous tensor, contour plot: (a) TPS p=1,q=0.0001 (b)FPS optimal ξ_{Gauss}, η_{OS} (c) FPS extreme counter-anisotropy $\xi = 0.49, \eta = 0$. (d) FPS extreme favoring-anisotropy $\xi = 0, \eta = 0.49$ (e) quadrilateral perturbed mesh

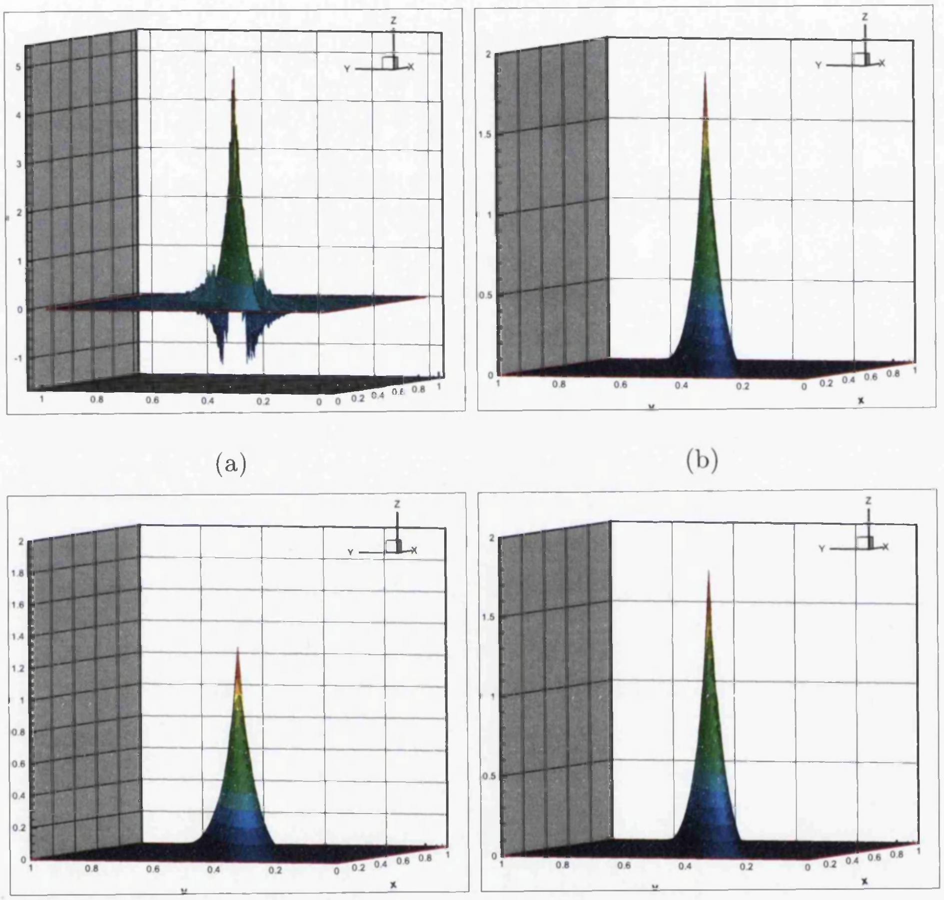

(a) (b)

(c) (d)

Figure 5.9: Test on perturbed cartesian quadrilateral grid, homogeneous tensor, isosurface plot: (a) TPS p=1,q=0.0001 (b)FPS optimal ξ_{Gauss}, η_{OS} (c) FPS extreme counter-anisotropy $\xi = 0.49, \eta = 0$. (d) FPS extreme favoring-anisotropy $\xi = 0, \eta = 0.49$

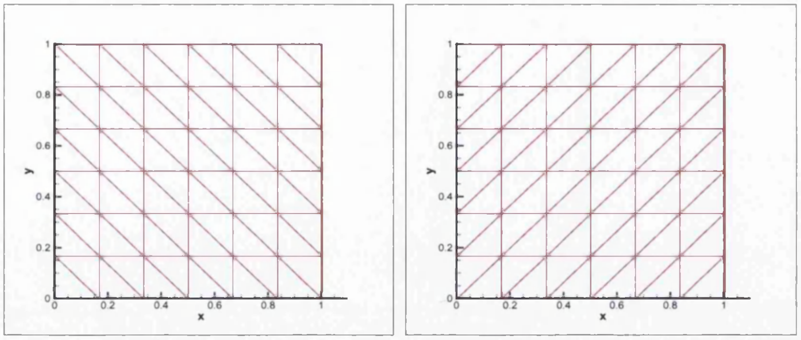

(a) (b)

Figure 5.10: FPS scheme on illustrative triangular grid. (a)Triangulation against anisotropy. (b) Triangulation favors anisotropy

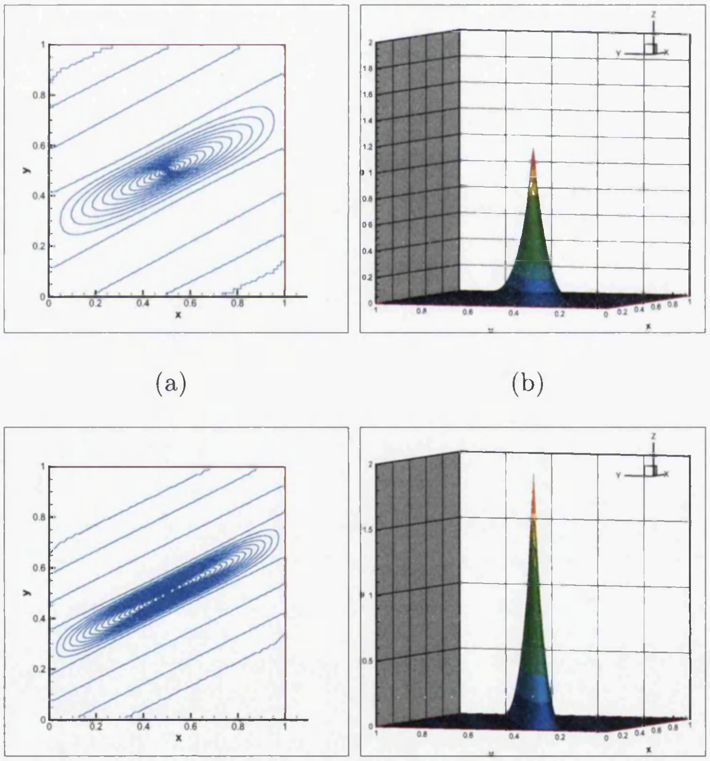

(a) (b)

(c) (d)

Figure 5.11: FPS scheme on triangular grid. (a)Triangulation against anisotropy - contours. (b) against anisotropy - isoplot. (c) Triangulation favoring anisotropy - contours. (d) favoring anisotropy - isoplot.

on the finer 2378 node grid Fig. 5.12(c) and (d). Comparison plots of Iso-surface plots are in Fig. 5.12 (e) and (f). The results indicate that the cell vertex FPS method is quite robust with respect to triangulation.

5.8.2 CASE 2: STRONG DISCONTINUOUS FULL-TENSOR (ZIGZAG) FIELD

In this case the boundary conditions for the unit domain involve a constrained pressure source-sink configuration placed at diagonally opposite corners of the domain. The bottom left pressure is set to 0.0 and the top right-hand corner pressure is set to 200, together with pressure set to 100 on all boundary walls. The permeability tensor changes direction in anisotropy at one third and two thirds the way across the domain. The discontinuous full-tensor permeability field is defined in sections with sign of cross-terms varying, the tensor of Eq. 5.27 is assigned to the first and third sections and with

$$\mathbf{K} = \begin{pmatrix} 2464.360020 & -1148.683643 \\ -1148.683643 & 536.6399794 \end{pmatrix} \tag{5.28}$$

in the second section. At each section the principal axes are oriented at an angle of 25 degrees, (i.e. plus, minus, plus 25 degrees) to the computational grid. The tensor again has a principal anisotropy ratio of 3000:1, violating the M-matrix condition in each section. Quadrilateral scheme results are presented in Figs. 16 and 17. The grid has $65X65$ resolution with control-volume boundary alignment on the interfaces between jumps in the permeability tensor.

Results are presented for the TPS scheme in Fig. 5.13(a) and 5.14(a), the condition of Eq. 5.21 is not satisfied by the TPS scheme due to the smaller quadrature range. There are very strong oscillations in the TPS solution (which remains positive) showing clear violation of the maximum principle as expected from the M-matrix and decoupling analysis.

We now compare with the FPS double-family schemes. A locally upscaled tensor is used to define the quadrature over the dual-cell (with resulting optimal scheme applied to the original permeability field), which yields a mean tensor for regions where permeability varies, in this case along the sub-domain boundaries where permeability is discontinuous. The exact tensor is otherwise obtained where the field is spatially constant over the cell.

An optimal scheme quadrature point $(\xi_{Gauss}, \eta_{OS})$is defined via Eq. 5.21. In this case away from the discontinuities the support of the scheme reduces such that the scheme has *optimal support* that favors anisotropy. Thus away from the discontinuities the FPS schemes essentially lead to angled approximations according to local orientation of the full-tensor field. The solution is well resolved and essentially free of spurious oscillations, Fig's.5.13 (b),5.14 (b).

Next in (c) FPS employs extreme counter-anisotropic quadrature with $\xi = 0.49, \eta = 0$ (i.e. against anisotropy), resulting in Fig's. 5.13(c),5.14(c), leading to a diffused solution. Finally (d) FPS extreme anisotropic quadrature favoring the anisotropy with $\xi = 0, \eta = 0.49$, yields the results in Fig's. 5.13(d),5.14(d) respectively. While a small number of oscillations are visible, the extreme quadrature scheme result (d) shows that the method consistently yields slightly sharper resolution than the optimal point scheme. As before the FPS methods yield results that are almost free of spurious oscillations with quasi-positive solutions for both planar and discontinuous full-tensor permeability fields. Both optimal point and extreme quadratures are found to be beneficial.

Case 2: Strong full-tensor (Zigzag) field, using a triangular grid

Next we test the triangular grid FPS scheme using a triangulation favoring the anisotropy. The grid has the same resolution as the previous case. An illustrative coarse grid is shown in Fig. 5.15(a). A boundary aligned grid (BAG) is employed where control-volume faces are aligned with interior boundaries across which permeability jumps and is discontinuous, the grid is illustrated in Fig. 5.15(b). This grid naturally yields an optimal support scheme due to the anisotropy favoring triangulation discussed above. The triangular grid results Fig. 5.15(c) and (d) are in very good agreement with the optimal point quadrilateral grid results Fig. 5.13(b) and 5.14(b).

5.9 Summary

A new double-family of locally conservative flux-continuous, finite-volume schemes is presented for solving the general tensor pressure equation on quadrilateral and triangular grids. The new families of schemes have full pressure continuity imposed across control-volume faces, in contrast to the earlier families of schemes which are point-wise continuous in pressure and flux.

The new families of schemes offer maximum flexibility in range of quadrature and the quadrilateral schemes are exact for piecewise bilinear pressure fields. The double-family of FPS schemes are SPD for a spatially constant full elliptic tensor.

When applying double (and single)family point-wise continuous schemes to full-tensor fields with high anisotropy ratios, the schemes can fail to satisfy the maximum principle, their limited quadrature range lies within a small neighbourhood of the singular decoupled end point of the quadrature interval, leading to strong spurious oscillations in the solution.

Tensor-coefficient dependent double-family M-matrix limits are presented for locally bounded solutions free of spurious oscillations. The bounds also show that a consistent locally conservative scheme cannot yield unconditional M-matrices for all tensors. An *optimal support condition* is identified from the M-matrix bounds, via a bounding quadrature point that defines the upper limit on the tensor cross-term. M-matrix bounds of the triangle scheme are analogous and consistent with optimal support on quadrilateral grids.

The new double-family FPS schemes are tested on problems involving strong full-tensor anisotropy where both M-matrix and monotone matrix conditions are violated. Results for the resulting extended range of quadrature points show that the occurrence of spurious oscillations in the discrete pressure field is minimal. The quadrature points are outside of the neighbourhood of the decoupled zone corresponding to the pointwise continuous schemes. Quasi-positive QM-matrices are defined. The optimal support quadrature points are also shown to be optimal with respect to a QM-matrix.

The FPS schemes map on to the CVFE quadrature range for constant tensor coefficients. When the tensor is spatially constant, the optimal support points yield schemes that self-adapt the discretization support locally according to the local orientation of the tensor field. Results show that optimal points yield well resolved solutions that are essentially free of spurious oscillations.

For a variable tensor field a locally upscaled tensor is used to define the tensor dependent optimal quadrature points which are therefore approximate. However, a precise optimal point may not be essential since the double family results show consistently improved solutions for extreme quadrature points that favor anisotropy. Alternatively an optimal support scheme can be obtained by anisotropy favoring triangulation.

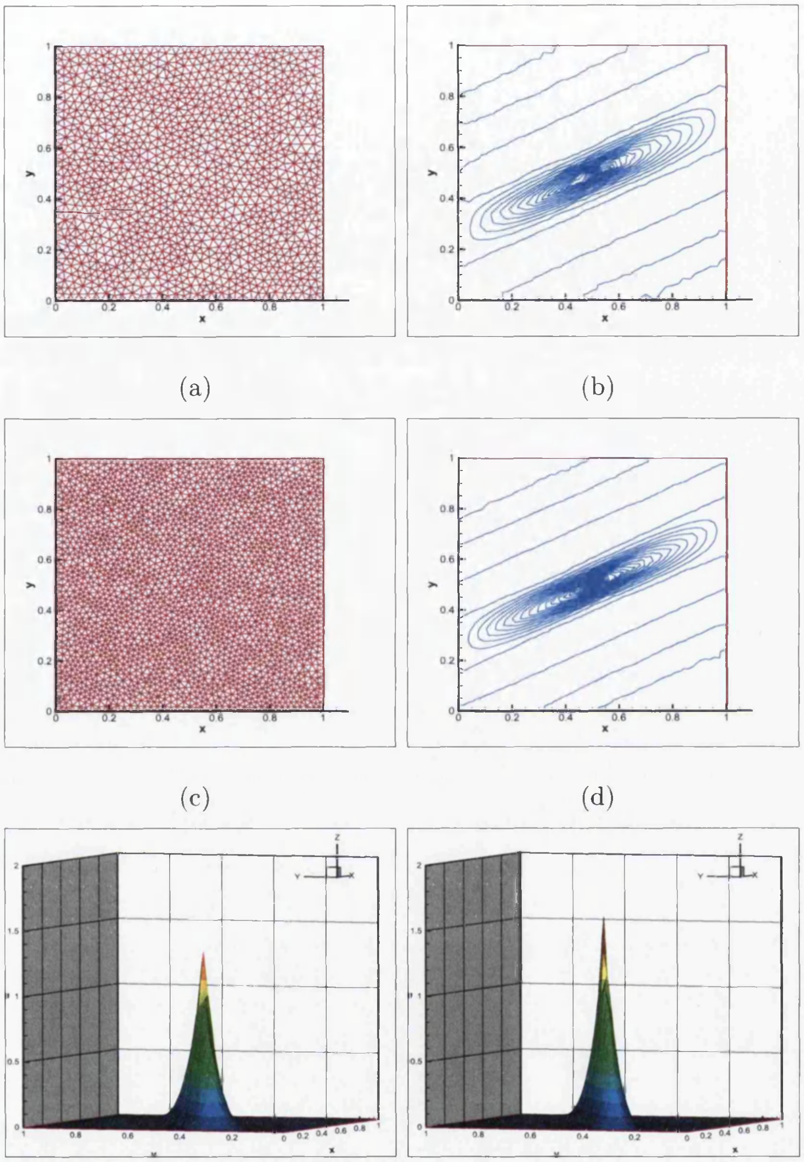

(a) (b)

(c) (d)

(e) (f)

Figure 5.12: Test for FPS Triple scheme on Coarse Triangle (a) Delaunay mesh with 1283 nodes (b) Contour plot of FPS on 1283 nodes. (c) Delaunay mesh with 2378 nodes(d) Contour plot of FPS on 2378-node-delaunay. (e) Iso-surface plot of 1283-node FPS. (f) Iso-surface plot of 2378-node FPS.

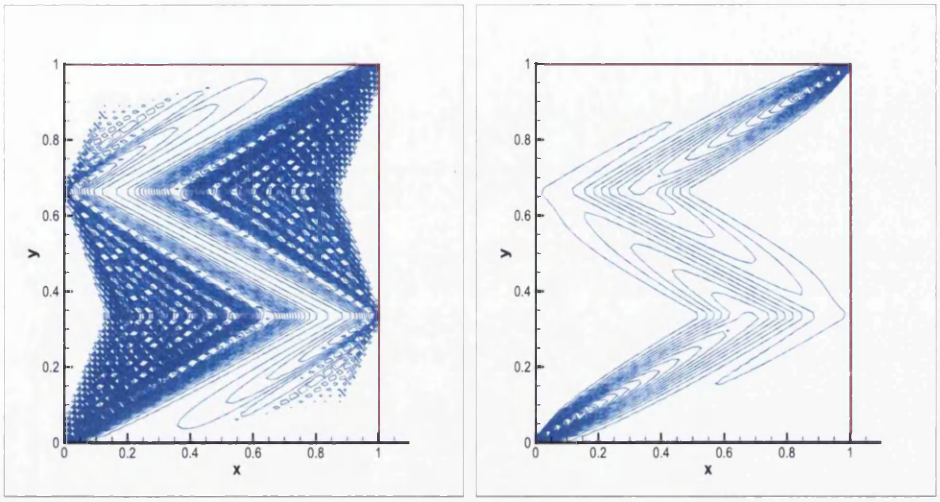

(a) TPS

(b) FPS ξ_{Gauss}, η_{OS}

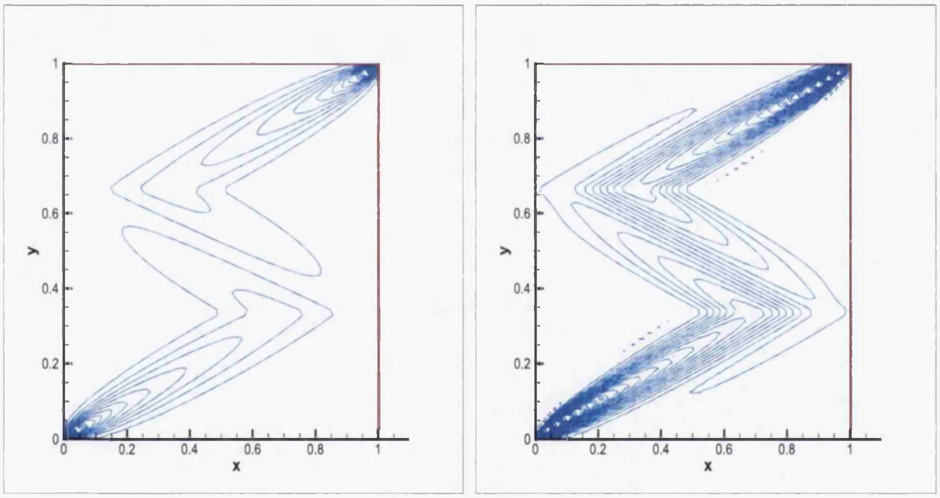

(c) FPS $\xi = 0.49, \eta = 0$

(d) FPS $\xi = 0, \eta = 0.49$

Figure 5.13: (a) TPS-quadrilateral, (b) FPS-quadrilateral: ξ_{Gauss}, η_{OS} (c) FPS-quad counter-anisotropic extreme: $\xi = 0.49, \eta = 0$ (d) FPS-quad extreme anisotropy: $\xi = 0, \eta = 0.49$

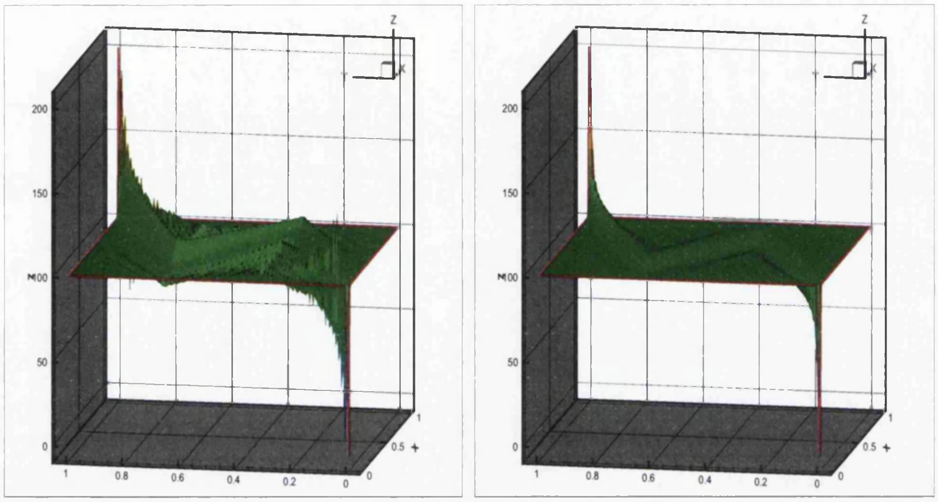

(a) TPS (b) FPS ξ_{Gauss}, η_{OS}

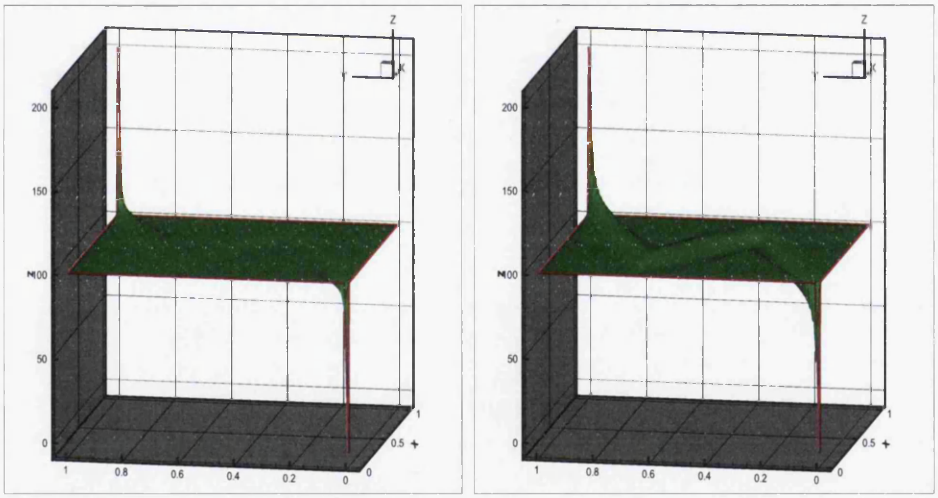

(c) FPS $\xi = 0.49, \eta = 0$ (d) FPS $\xi = 0, \eta = 0.49$

Figure 5.14: (a) TPS-quadrilateral, (b) FPS-quadrilateral: ξ_{Gauss}, η_{OS} (c) FPS-quad counter-anisotropic extreme: $\xi = 0.49, \eta = 0$ (d) FPS-quad extreme anisotropy: $\xi = 0, \eta = 0.49$

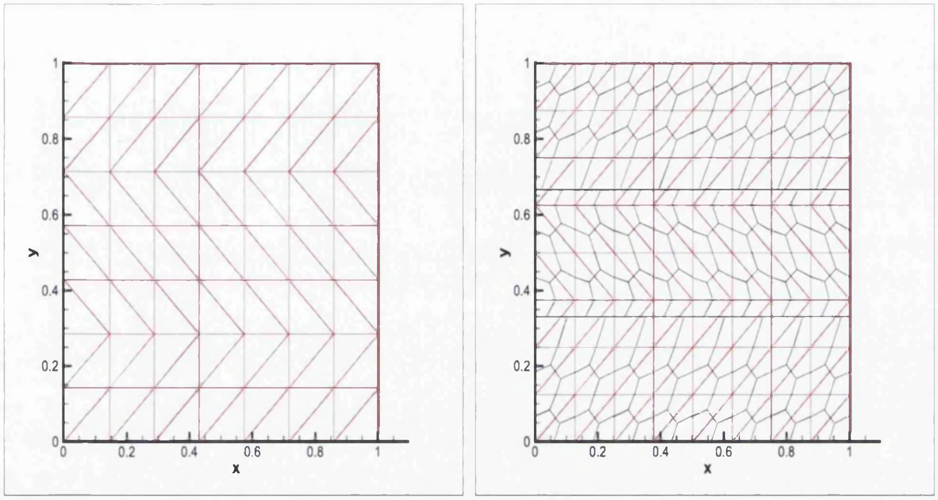

(a) Triangle Grid

(b) Control-volume Grid

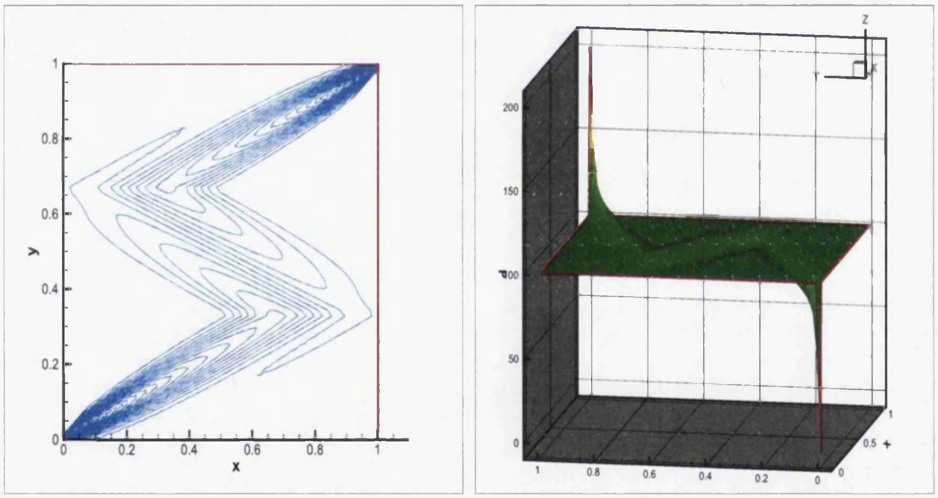

(c) FPS Triangles

(d) FPS Triangles

Figure 5.15: (a) triangle grid favoring anisotropy (b) BAG Grid control-vol subfaces aligned with jumps in perm field (c) Optimal FPS Triangle scheme contours (d) Optimal FPS Triangle scheme isoplot

Chapter 6

Families of Flux Continuous Finite Volume Schemes with Full Pressure Support on Structured and Unstructured Grids in 3D

6.1 Introduction

This chapter presents the development of a new family of three dimensional flux-continuous finite volume methods for solving the pressure equation resulting from Darcy's law. Key physical constraints of continuity in normal flux and *full* pressure continuity are imposed at control-volume interfaces.

Previous families of efficient locally conservative point-wise flux-continuous control volume distributed (CVD) finite-volume schemes for determining the discrete pressure and velocity fields are presented in e.g. [2, 9, 14, 19, 23], these schemes are classified by the quadrature parameterization $0 < q \leq 1$. Schemes of this type are also called multi-point flux approximation schemes or MPFA [30] where focus has been on a scheme that belongs to the above mentioned family with ($q = 1$). Further schemes of this type are presented in [35, 36] and [37] via a novel mixed method.

Other schemes that preserve flux continuity have been developed from variational frameworks, using the mixed finite element method (MFE) e.g. [72, 73, 95, 96, 74, 97] and related work [98] and discontinuous galerkin methods [82, 83], however these schemes require additional degrees of freedom.

This work continues with the derivation of algebraic flux continuity conditions for full-tensor discretization operators and extends the family of flux-continuous full-pressure continuity schemes of [17] into three dimensions, for general structured and unstructured grids.

6.2 Problem Description in 3D and General Tensor Equation

The problem is to find the pressure ϕ satisfying

$$-\int_{\Omega} \partial_{\xi_i}(T_{i,j}\partial_{\xi_j}\phi)d\Gamma = \mathbf{M} \tag{6.1}$$

over an arbitrary volume Ω, where the general tensor $\mathbf{T} =\mid J \mid \mathbf{J}^{-1}\mathbf{K}\mathbf{J}^{-T}$ has elements $T_{i,j}$ and is defined via the Piola transformation. Here the summation convention over repeated indices $i = 1, ...3, j = 1, ...3$ applies. Eq.6.1 is solved subject to suitable (Neumann/Dirichlet) boundary conditions on boundary $\partial\Omega$. The right hand side term $\mathbf{M}$ represents a specified flow rate. Matrix $\mathbf{K}$ is a diagonal or full symmetric elliptic cartesian permeability tensor with elements $K_{i,j}$. The tensor can be discontinuous across internal boundaries of Ω. For incompressible flow pressure is specified at at least one point in the domain. For reservoir simulation, Neumann boundary conditions on $\partial\Omega$ requires zero flux on solid walls such that $(K\nabla\phi) \cdot \hat{n} = 0$, where $\hat{n}$ is the outward normal vector to $\partial\Omega$.

6.3 Grid Definition

The primal grid considered here can be a hybrid composed of tetrahedra, prisms, pyramids and hexahedra elements in 3-D [14, 23]. In principle the only restriction on grid structure is that tetrahedra can only be joined to hexahedra through a pyramid interface [14]. The approximation is vertex centered. A polyhedral control-volume is built around each grid vertex, generating a primal-dual grid. Starting in a primal grid cell, the cell centre is joined to cell face mid-points, cell face mid-points are joined to cell edge mid-points. For tetrahedron that is Delaunay is with circum center inside the tetrahedra, the circum center can also be used in place of the cell center. As a result the primal grid cells are decomposed into subcells which are mainly sub-hexahedra cells, four for a tetrahedra, six for a prism, eight for a hexahedra, the pyramid is the special case and is decomposed into four sub-hexahedra and one octahedra corresponding to the summit node [23]. In each case the number of subcells corresponds to the number of vertices defining the primal cell, and each subcell belongs to the control-volume of the unique vertex to which it is attached. Cell vertex control-volumes are defined by a local assembly at each primal grid vertex of all subcells attached to the vertex. The resulting set of polyhedral control-volumes define a dual grid relative to the primal grid called the primal-dual. Rock permeability and porosity are assumed to be piece-wise constant over each polyhedral control-volume and flow variables belong to the control-volumes and are vertex centred. Fig's. 6.1 and 6.2. Therefore discontinuities in rock properties occur over the control-volume faces.

6.4 Flux-Continuous Schemes with Full Pressure Continuity

We illustrate the procedure with a primary hexahedral cell with local vertices numbered $1, ..., 8$, Fig 6.1. First interface pressures are introduced at the edge, cell-face and cell-centre mid-points respectively. These will be expressed algebraically in terms of the primary cell vertex pressures in a preprocessing step, through the following set of equations imposed over the primary cell. The pressure ϕ and position vector $\mathbf{r} = (x, y, z)$ assume a trilinear variation over each subcell,

$$\begin{aligned}\phi = \ & (1-\tilde{\xi})(1-\tilde{\eta})(1-\tilde{\zeta})\phi_1 + \tilde{\xi}(1-\tilde{\eta})(1-\tilde{\zeta})\phi_2 + \tilde{\xi}\tilde{\eta}(1-\tilde{\zeta})\phi_3 \\ & +(1-\tilde{\xi})\tilde{\eta}(1-\tilde{\zeta})\phi_4 + (1-\tilde{\xi})(1-\tilde{\eta})\tilde{\zeta}\phi_5 + \tilde{\xi}(1-\tilde{\eta})\tilde{\zeta}\phi_6 \\ & +\tilde{\xi}\tilde{\eta}\tilde{\zeta}\phi_7 + (1-\tilde{\xi})\tilde{\eta}\,\tilde{\zeta}\phi_8\end{aligned} \tag{6.2}$$

$$\begin{aligned}\mathbf{r} = \ & (1-\tilde{\xi})(1-\tilde{\eta})(1-\tilde{\zeta})\mathbf{r}_1 + \tilde{\xi}(1-\tilde{\eta})(1-\tilde{\zeta})\mathbf{r}_2 + \tilde{\xi}\tilde{\eta}(1-\tilde{\zeta})\mathbf{r}_3 \\ & +(1-\tilde{\xi})\tilde{\eta}(1-\tilde{\zeta})\mathbf{r}_4 + (1-\tilde{\xi})(1-\tilde{\eta})\tilde{\zeta}\mathbf{r}_5 + \tilde{\xi}(1-\tilde{\eta})\tilde{\zeta}\mathbf{r}_6 \\ & +\tilde{\xi}\tilde{\eta}\tilde{\zeta}\mathbf{r}_7 + (1-\tilde{\xi})\tilde{\eta}\,\tilde{\zeta}\mathbf{r}_8\end{aligned} \tag{6.3}$$

where $\tilde{\xi}, \tilde{\eta}, \tilde{\zeta}$ are subcell master element coordinates defined over the unit square $0 \le \tilde{\xi}, \tilde{\eta}, \tilde{\zeta} \le 1$. Subcell Darcy fluxes are defined by resolving Darcy velocity along surface area outward normal vectors with $\mathbf{F} = -\mathbf{K}\nabla\phi \bullet \Delta S$, and approximated using subcell approximations of the form illustrated by Eq.7.1 for subcell 1. The interface pressures are continuous across the respective interfaces by construction, and as a consequence of the subcell approximation, pressure is bilinear and continuous over the entire face of each subcell with *full pressure support* FPS. A local flux continuity condition is imposed for each edge-centred pressure, a surface zero divergence condition is imposed for each auxiliary cell-face pressure and zero divergence is imposed in each primal cell sub-volume, to determine to the auxiliary pressure at the cell-centre. The earlier *tetrahedral pressure support* (TPS) schemes only require one interface pressure corresponding to each edge flux and are consequently only point-wise continuous, however they require the minimum number of auxiliary equations. The bilinear FPS subcell surface support also retains a degree of freedom in position of flux continuity on a sub-face, but leads to new 3-D families of flux-continuous schemes with full pressure support with larger quadrature range.

6.4.1 Flux Continuity Conditions

Primal fluxes are defined over the hexahedral subcell faces that are inside the primal cell, by resolving the discrete Darcy flux along each normal surface area vector. Interior subcell fluxes are constructed for each subcell face belonging to a primary grid cell. As a result, a left and right flux will be defined with respect to each interior subcell face, Fig6.1. Flux continuity is achieved by equating subcell fluxes at common faces leading to

$$F_i = -(T_{i1}\phi_{\tilde{\xi}} + T_{i2}\phi_{\tilde{\eta}} + T_{i3}\phi_{\tilde{\zeta}})|_{\sigma}^{L} = -(T_{i1}\phi_{\tilde{\xi}} + T_{i2}\phi_{\tilde{\eta}} + T_{i3}\phi_{\tilde{\zeta}})|_{\sigma}^{R} \tag{6.4}$$

where suffix i indicates the local subcell coordinate, suffix $\sigma = \sigma(\tilde{\eta})$ indicates the chosen flux continuity position on an interface and thus defines the family of schemes.

For example with respect to face $b0, b1, m1, m0$ of Fig.6.3

$$\begin{aligned} F_{b1} &= -(T^1_{11}((1-\tilde{\eta})^2(\phi_{b1}-\phi_1) + \tilde{\eta}(1-\tilde{\eta})(\phi_{b0}-\phi_{b4}) + \tilde{\eta}(1-\tilde{\eta})(\phi_{m1}-\phi_{e1}) \\ &\quad +\tilde{\eta}^2(\phi_{m0}-\phi_{m4})) + T^1_{12}((1-\tilde{\eta})(\phi_{b0}-\phi_{b1}) + \tilde{\eta}(\phi_{m0}-\phi_{m1})) \\ &\quad +T^1_{13}((1-\tilde{\eta})(\phi_{m1}-\phi_{b1}) + \tilde{\eta}(\phi_{m0}-\phi_{b0}))) \\ &= -(T^2_{11}((1-\tilde{\eta})^2(\phi_2-\phi_{b1}) + \tilde{\eta}(1-\tilde{\eta})(\phi_{b2}-\phi_{b0}) + \tilde{\eta}(1-\tilde{\eta})(\phi_{e2}-\phi_{m1}) \\ &\quad +\tilde{\eta}^2(\phi_{m2}-\phi_{m0})) + T^2_{12}((1-\tilde{\eta})(\phi_{b0}-\phi_{b1}) + \tilde{\eta}(\phi_{m0}-\phi_{m1})) \\ &\quad +T^2_{13}((1-\tilde{\eta})(\phi_{m1}-\phi_{b1}) + \tilde{\eta}(\phi_{m0}-\phi_{b0}))) \end{aligned} \tag{6.5}$$

6.4.2 Auxiliary Control Volume Divergence Free Conditions

Full (bilinear) pressure continuity over the control-volume subcell faces is achieved by the introduction of further auxiliary pressures at cell centres and cell-face centres (in addition to edge interface pressures). Additional zero divergence equations are imposed to solve for the additional local degrees of freedom, as in 2D [17] with

$$-\sum_{\partial\Omega_{AUX}} (\mathbf{K}\nabla\Phi)\cdot\hat{\mathbf{n}}\Delta s = 0 \tag{6.6}$$

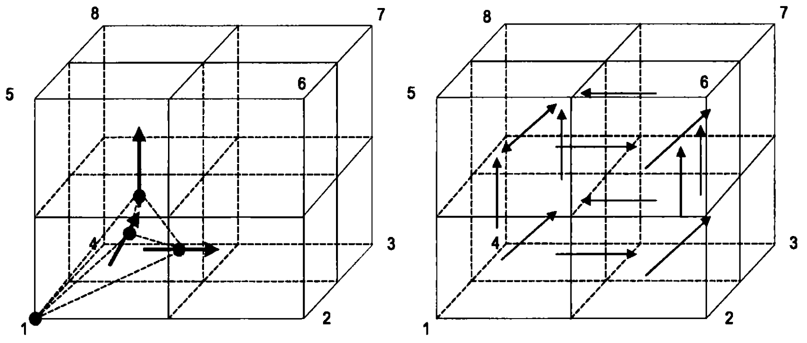

(a) (b)

Figure 6.1: Local subcell fluxes and supporting nodes: Local primal cell-vertex numbers indicate primary nodes (d.o.f), all other nodes are (auxiliary) interface nodes (a) TPS scheme. (b) FPS scheme.

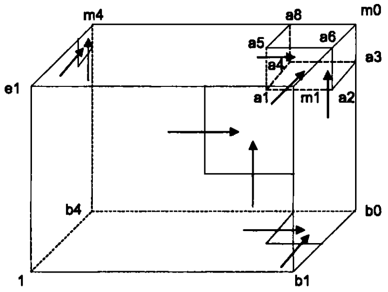

Figure 6.2: Auxiliary fluxes in a subcell. Red arrow: surface flux. Green arrow: volume flux

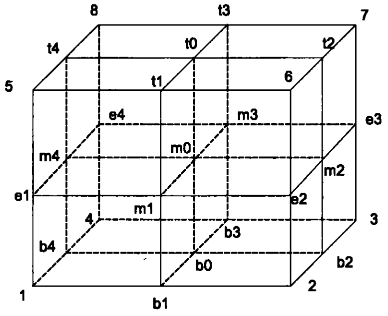

Figure 6.3: Primal hexahedral element: integer vertices are primary variables : other are auxiliary variables

This involves construction of two types of Auxiliary Control Volume (ACV) approximation for 3D FPS schemes: A surface ACV surrounding each cell-face centre and a sub-volume ACV surrounding the center of the primal cell. Auxiliary fluxes are then defined over the faces of the resulting sub-subcells, i.e. subcells of the subvolume Fig.6.2, top right corner $m0$ is primal cell centre, Fig.6.3. Since permeability is piecewise constant over the sub-subcells CVFE is employed for the auxiliary divergence approximations.

Local Flux and Divergence Conditions

The local auxiliary pressures for each cell are expressed as a total vector of edge-interface pressures $(\Phi_F)^T$ and cell-face/volume pressures $(\Phi_D)^T$ where $\Phi_A = (\Phi_F, \Phi_D)^T$ with dimension $N_A = N_F + N_D$. The primal cell-vertex pressures are $\Phi_V = (\phi_1, \phi_2, ..., \phi_{N_V})^T$, with dimension N_V. The system of equations is written as

$$A_L\Phi_A + B_L\Phi_V = A_R\Phi_A + B_R\Phi_V$$

where A_L, A_R are $N_A X N_A$ matrices and B_L, B_R are $N_A X N_V$ matrices.

The continuous fluxes of the families of FPS schemes are defined by the first N_F rows of

$$F = (A_L(A_L - A_R)^{-1}(B_R - B_L) + B_L)\Phi_V$$

The primal divergence equations are then assembled as the sum of outward normal fluxes of all subcell interfaces that comprise the net polyhedral control-volume surface. Four equation sets are described below according to the element (or cell) type.

Full Pressure Support: Hexahedral Element

The hexahedral element is divided into 8 sub-hexahedra corresponding to each primal cell vertex. Each sub-hexahedra has three interior faces that form part of the respective vertex control-volume. There are a total of twelve interior interfaces, one per cell edge. Consequently twelve local flux continuity conditions are imposed in order to determine the the twelve edge interface pressures. Seven zero divergence conditions are imposed, six on the cell faces for the six surface auxiliary pressures and one sub-volume condition for the cell-centre auxiliary pressure. $N_F = 12, N_D = 7, N_V = 8$.

Full Pressure Support: Prism Element

The prism element is divided into 6 sub-hexahedra corresponding to each primal cell vertex. The prism has nine edges, consequently nine local flux continuity conditions are imposed. In this case FPS requires six zero divergence conditions are imposed, five on the cell faces for the five surface auxiliary pressures and one sub-volume condition for the cell-centre auxiliary pressure. $N_F = 9, N_D = 6, N_V = 6$

Full Pressure Support: Tetrahedral Element

The tetrahedral element is divided into 4 sub-hexahedra corresponding to each primal cell vertex. The tetrahedra has six edges, consequently six local flux continuity conditions are imposed. In this case FPS requires five zero divergence conditions, four on the cell faces for the four surface auxiliary pressures and one sub-volume condition for the cell-centre auxiliary pressure. $N_F = 6, N_D = 5, N_V = 4$

Full Pressure Support: Pyramid Element

Special treatment is required for the pyramid cell. The pyramid element is divided into 5 subcells corresponding to each primal cell vertex. The five subcells are comprised of four sub-hexahedra corresponding to the base nodes and an octahedral subcell corresponding to the summit node [23]. The octahedral subcell has four interior interfaces inside the pyramid. The continuity conditions are treated naturally by the sub-bilinear formulation. The pyramid has eight edges and eight local flux continuity conditions are imposed. In this case FPS requires six zero divergence conditions, five on the cell faces for the five surface auxiliary pressures and one sub-volume condition for the cell-centre auxiliary pressure. The degrees of freedom of the five equation system Eq.6.6 are the five interface pressures. $N_F = 8, N_D = 6, N_V = 5$

6.5 Tetrahedral M-matrix Conditions

Cell-wise M-matrix conditions are derived in [108] and [109] for tetrahedra and hexahedra. Discrete cell-vertex fluxes for a tetrahedra with discontinuous coefficients can always be expressed as a linear combination of edge differences with $\mathrm{A}F = -\Delta\Phi_v$ [14] and thus discrete edge flux components can be written as

$$F_i = -\big(T_{i1}(\phi_1 - \phi_0) + T_{i2}(\phi_2 - \phi_0) + T_{i3}(\phi_3 - \phi_0)\big) \tag{6.7}$$

where T_{ij} are approximate tensor coefficients derived from flux continuity conditions. Cell-wise M-marix conditions are obtained [109] if

$$\begin{aligned} \mid T_{21} + T_{31} \mid &< T_{11} \\ \mid T_{12} + T_{32} \mid &< T_{22} \\ \mid T_{13} + T_{23} \mid &< T_{33} \end{aligned} \tag{6.8}$$

where symmetry may be lost in physical space. If the left hand side of Eq.6.8 is replaced with the moduli of cross-terms and symmetry is assumed, then Eq.6.8 is satisfied if

$$\mid T_{12} \mid + \mid T_{13} \mid < T_{11}, \ \mid T_{12} \mid + \mid T_{23} \mid < T_{22}, \ \mid T_{13} \mid + \mid T_{23} \mid < T_{33} \tag{6.9}$$

taken together this leads to

$$\mid T_{12} \mid + \mid T_{23} \mid + \mid T_{13} \mid < \frac{1}{2}(T_{11} + T_{22} + T_{33}) \tag{6.10}$$

A weaker inequality from Eq.6.10 is that $max(\mid T_{12} \mid, \mid T_{23} \mid, \mid T_{13} \mid) \leq \frac{1}{2} min(T_{11}, T_{22}, T_{33})$ The above sets of conditions also hold for a 3-D "7-point" scheme, i.e. a 13-point scheme.

Alternate Tetrahedral M-matrix Conditions

A second set of conditions is obtained [109] from Eq.6.7 by bounding w.r.t halves of the diagonal coefficients with

$$\mid T_{12} \mid < \frac{1}{2}T_{11},\ \mid T_{13} \mid < \frac{1}{2}T_{11},\ \mid T_{12} \mid < \frac{1}{2}T_{22},\ \mid T_{23} \mid < \frac{1}{2}T_{22},\ \mid T_{13} \mid < \frac{1}{2}T_{33},\ \mid T_{23} \mid < \frac{1}{2}T_{33}$$

leading to the conditions

$$\mid T_{12} \mid < \frac{1}{2}min(T_{11}, T_{22}) \quad \mid T_{13} \mid < \tfrac{1}{2}min(T_{11}, T_{33}) \quad \mid T_{23} \mid < \tfrac{1}{2}min(T_{22}, T_{33}) \tag{6.11}$$

while these bounds are not optimal, they demonstrate consistency with planar scheme conditions below.

6.5.1 Hexahedral M-matrix Conditions

The hexahedral-scheme yields a 27-point operator in 3-D on a structured grid. The 2-D analysis for a constant tensor field [17] shows that as the auxilliary control-volume tends to zero, the family of FPS schemes can be expressed in terms of a CVFE family. This is also shown for double parameter families [18, 38]. Our analysis suggests the same is true in 3-D [109] and is verified for a particular scheme below. Here we present the single parameter family of 3-D CVFE schemes, as a representation of FPS for constant coefficients, where ξ, η, ζ are master element (primal hexahedra) parametric coordinates defined over the unit square $0 \leq \xi, \eta, \zeta \leq 1$, symmetry is seen by inspection of the table. For a single parameter family parameterised by η, the mapping between FPS and CVFE is $\eta = \widetilde{\eta}/2$ (as in 2-D). Therefore $0 \leq \eta < 1/2$ for flux approximations inside their respective control-volumes. The coefficients are listed in the Table 6.5.1, Table 6.5.1, and Table 6.5.1. A summary of M-matrix analysis given in [108, 109] follows below

Entries M_2, M_4, M_{10} (leading to a right-hand inequality) and $M_{12}, M_{14}, M_{16}, M_{18}$ (leading to a left-hand inequality in Eq.6.12 for which Eq.6.10 is an upper bound) are

int coords	Coef	Full Tensor
i,j,k	M_1	$2(1-\eta)^2(T_{11}+T_{22}+T_{33})$
i+1,j,k	M_2	$(1-\eta)((T_{11}+T_{22}+T_{33})\eta-T_{11})$
i+1,j+1,k	M_3	$-\frac{1}{2}\eta(1-\eta)(T_{11}+T_{22})+\frac{1}{2}\eta^2T_{33}-\frac{1}{2}(1-\eta)T_{12}$
i,j+1,k	M_4	$(1-\eta)((T_{11}+T_{22}+T_{33})\eta-T_{22})$
i-1,j+1,k	M_5	$-\frac{1}{2}\eta(1-\eta)(T_{11}+T_{22})+\frac{1}{2}\eta^2T_{33}+\frac{1}{2}(1-\eta)T_{12}$
i-1,j,k	$M_6=M_2$	$(1-\eta)((T_{11}+T_{22}+T_{33})\eta-T_{11})$
i-1,j-1,k	$M_7=M_3$	$-\frac{1}{2}\eta(1-\eta)(T_{11}+T_{22})+\frac{1}{2}\eta^2T_{33}-\frac{1}{2}(1-\eta)T_{12}$
i,j-1,k	$M_8=M_4$	$(1-\eta)((T_{11}+T_{22}+T_{33})\eta-T_{22})$
i+1,j-1,k	$M_9=M_5$	$-\frac{1}{2}\eta(1-\eta)(T_{11}+T_{22})+\frac{1}{2}\eta^2T_{33}+\frac{1}{2}(1-\eta)T_{12}$

Table 6.1: 27-point family: The middle layer

int coords	Coef	Full Tensor
i,j,k+1	M_{10}	$(1-\eta)((T_{11}+T_{22}+T_{33})\eta-T_{33})$
i+1,j,k+1	M_{11}	$-\frac{1}{2}\eta(1-\eta)(T_{11}+T_{33})+\frac{1}{2}\eta^2T_{22}-\frac{1}{2}(1-\eta)T_{13}$
i+1,j+1,k+1	M_{12}	$-\frac{1}{4}\eta^2(T_{11}+T_{22}+T_{33})-\frac{1}{4}\eta(T_{12}+T_{13}+T_{23})$
i,j+1,k+1	M_{13}	$-\frac{1}{2}\eta(1-\eta)(T_{22}+T_{33})+\frac{1}{2}\eta^2T_{11}-\frac{1}{2}(1-\eta)T_{23}$
i-1,j+1,k+1	M_{14}	$-\frac{1}{4}\eta^2(T_{11}+T_{22}+T_{33})-\frac{1}{4}\eta(-T_{12}-T_{13}+T_{23})$
i-1,j,k+1	M_{15}	$-\frac{1}{2}\eta(1-\eta)(T_{11}+T_{33})+\frac{1}{2}\eta^2T_{22}+\frac{1}{2}(1-\eta)T_{13}$
i-1,j-1,k+1	M_{16}	$-\frac{1}{4}\eta^2(T_{11}+T_{22}+T_{33})-\frac{1}{4}\eta(T_{12}-T_{13}-T_{23})$
i,j-1,k+1	M_{17}	$-\frac{1}{2}\eta(1-\eta)(T_{22}+T_{33})+\frac{1}{2}\eta^2T_{11}+\frac{1}{2}(1-\eta)T_{23}$
i+1,j-1,k+1	M_{18}	$-\frac{1}{4}\eta^2(T_{11}+T_{22}+T_{33})-\frac{1}{4}\eta(-T_{12}+T_{13}-T_{23})$

Table 6.2: 27-point family: The top layer

int coords	Coef	Full Tensor
i,j,k-1	$M_{19}=M_{10}$	$(1-\eta)((T_{11}+T_{22}+T_{33})\eta-T_{33})$
i+1,j,k-1	$M_{20}=M_{15}$	$-\frac{1}{2}\eta(1-\eta)(T_{11}+T_{33})+\frac{1}{2}\eta^2T_{22}+\frac{1}{2}(1-\eta)T_{13}$
i+1,j+1,k-1	$M_{21}=M_{16}$	$-\frac{1}{4}\eta^2(T_{11}+T_{22}+T_{33})-\frac{1}{4}\eta(T_{12}-T_{13}-T_{23})$
i,j+1,k-1	$M_{22}=M_{17}$	$-\frac{1}{2}\eta(1-\eta)(T_{22}+T_{33})+\frac{1}{2}\eta^2T_{11}+\frac{1}{2}(1-\eta)T_{23}$
i-1,j+1,k-1	$M_{23}=M_{18}$	$-\frac{1}{4}\eta^2(T_{11}+T_{22}+T_{33})-\frac{1}{4}\eta(-T_{12}+T_{13}-T_{23})$
i-1,j,k-1	$M_{24}=M_{11}$	$-\frac{1}{2}\eta(1-\eta)(T_{11}+T_{33})+\frac{1}{2}\eta^2T_{22}-\frac{1}{2}(1-\eta)T_{13}$
i-1,j-1,k-1	$M_{25}=M_{12}$	$-\frac{1}{4}\eta^2(T_{11}+T_{22}+T_{33})-\frac{1}{4}\eta(T_{12}+T_{13}+T_{23})$
i,j-1,k-1	$M_{26}=M_{13}$	$-\frac{1}{2}\eta(1-\eta)(T_{22}+T_{33})+\frac{1}{2}\eta^2T_{11}-\frac{1}{2}(1-\eta)T_{23}$
i+1,j-1,k-1	$M_{27}=M_{14}$	$-\frac{1}{4}\eta^2(T_{11}+T_{22}+T_{33})-\frac{1}{4}\eta(-T_{12}-T_{13}+T_{23})$

Table 6.3: 27-point family: The bottom layer

non-positive if

$$| T_{12} | + | T_{23} | + | T_{13} | \leq \eta(T_{11} + T_{22} + T_{33}) \leq min(T_{11}, T_{22}, T_{33}) \tag{6.12}$$

Entries (M_3, M_5) and M_{11}, M_{15} and M_{13}, M_{17} are respectively non-positive if the three inequalities hold

$$\begin{aligned} -\tfrac{1}{2}\eta(1-\eta)(T_{11}+T_{22}) + \tfrac{1}{2}\eta^2 T_{33} + \tfrac{1}{2}(1-\eta) \mid T_{12} \mid\leq 0 \\ -\tfrac{1}{2}\eta(1-\eta)(T_{11}+T_{33}) + \tfrac{1}{2}\eta^2 T_{22} + \tfrac{1}{2}(1-\eta) \mid T_{13} \mid\leq 0 \\ -\tfrac{1}{2}\eta(1-\eta)(T_{22}+T_{33}) + \tfrac{1}{2}\eta^2 T_{11} + \tfrac{1}{2}(1-\eta) \mid T_{23} \mid\leq 0 \end{aligned} \tag{6.13}$$

The two-dimensional inequalities are recovered in each plane from Eq's.6.12,6.13. Also the inequality resulting from summation of Eq. 6.13 is satisfied by the l.h.s inequality of Eq.6.12.

Reduced Support Case 1 Reduced support may be deduced from both of Eq.'s 6.12,6.13,and the table scheme coefficients with e.g.

$$\eta = (| T_{12} | + | T_{23} | + | T_{13} |)/(T_{11} + T_{22} + T_{33}) \tag{6.14}$$

However, optimal support in 3-D requires the introduction of multiple families, which are beyond the scope of this chapter, though here we present a summary.

M-matrix and Optimal Support 19 to 13 Point Schemes

The FPS mapping onto CVFE for planar 19 point schemes, defined by collapsing quadratures to the three cross-intersecting planes, is established directly from correspondence with the 2-D analysis [18], and it also follows that the planar families are SPD for a constant elliptic tensor. The M-matrix conditions for families of 19 point schemes are given by [109]

$$\begin{aligned} 2 \mid T_{12} \mid\leq \zeta(T_{11} + T_{22}) \leq min(T_{11}, T_{22}) \\ 2 \mid T_{13} \mid\leq \eta(T_{11} + T_{33}) \leq min(T_{11}, T_{33}) \\ 2 \mid T_{23} \mid\leq \xi(T_{22} + T_{33}) \leq min(T_{22}, T_{33}) \end{aligned} \tag{6.15}$$

where $0 \leq \xi, \eta, \zeta < 1/2$. The optimal point per plane that reduces each planar 9-point scheme to a 7-point scheme, resulting in the net 19 point scheme reducing to a net 13-point scheme are defined by the left limit of Eq.6.15 where

$$\zeta = \frac{2 \mid T_{12} \mid}{(T_{11} + T_{22})},\ \eta = 2\frac{\mid T_{13} \mid}{(T_{11} + T_{33})},\ \xi = 2\frac{\mid T_{23} \mid}{(T_{22} + T_{33})} \tag{6.16}$$

We note that substitution of Eq. 6.16 in Eq. 6.15 leads to recovery of the same M-matrix conditions as for the tetrahedron in Eq.6.11. This provides a 3-D generalisation of the reduction of 9-point schemes to 7-point schemes via quadrature, with analogous conditions to M-matrices on quadrilaterals and triangles [17]. For constant coefficients the scheme will self-adapt the discretization support locally according to the local orientation of the tensor field.

However, we note that Eq.6.11 places a stronger limit on the size of the cross-terms than in 2-D. While the limits of Eq's.6.11,6.15 are sufficient they are not optimal as implied by Eq.6.9, where e.g. if $T_{13} \simeq 0, T_{23} \simeq 0$, then the 2-D limit is only recovered by Eq.6.9. We note that the optimal quadrature coordinates of Eq.6.16 reduces a 19-point scheme to an optimal 13-point scheme with M-matrix conditions given by Eq.6.9 [108]. Alternative optimal scheme developments in 3-D are presented in [23, 32].

6.6 Quasi-Positive QM-matrices

We have defined a Quasi-M-matrix or QM-matrix as a matrix with the minimum of only one unique positive off-diagonal coefficient that violates the M-matrix conditions [17] (provided the quadrature is below the decoupled zone). FPS schemes are shown to possess a range of QM-matrices when the fundamental M-matrix (and monotone) condition is violated in 2-D, when $\mid T_{1,2} \mid > min(T_{1,1}, T_{2,2})$ [17]. The fundamental M-matrix (and monotone) violation occurs in 3-D when Eq.6.8 is violated. The QM-matrix definition is extended in 3-D to matrices with up to three unique positive off-diagonal coefficients that violate the M-matrix conditions, where each plane can permit one contribution [108]. E.g. $\eta = 0$ has a QM-matrix in 2-D, from table 1, the 3-D scheme will have a unique violation from each plane if the three cross-terms are non-zero and has a QM-matrix. The scheme resulting from Eq.6.16 appears optimal with respect to a QM-matrix.

6.7 Numerical Results

A number of numerical tests have been performed to test the new methods for various grids. Here we present the results for two test cases.

In this section convergence study results are presented for the family of schemes for a range of quadrature points $(0 < q \leq 1)$. Convergence tests were presented for the 3-D TPS formulation of the family of schemes by Pal and Edwards in [23]. The convergence rates are measured by discrete L_2 norms for both pressures and normal velocities,

$$\begin{aligned} \| \phi_h - \phi \| &= \left(\sum_i V_i (\phi_{h,i} - \phi_i)^2 \right)^{1/2} \qquad (6.17) \\ \| f_h - f \| &= \left(\sum_j \frac{(V_{j+} + V_{j-})}{4} (f_{h,j} - f_j)^2) \right)^{1/2} \end{aligned}$$

Here f_h is the discrete flux and ϕ_h refers to the discrete solution. V_i is the volume of the cell i and $V_{\pm}$ are the volumes of the cell separated by edge j. The simulation domain is [0,1]x[0,1]x[0,1] and hence the total volume of simulated domain in all the test cases is unity.

6.7.1 Quadratic test case

The first case involves a hexahedral domain with a planar discontinuity at x = 0.5, dividing the medium into two subdomains. The analytical solution for pressure in the two subdomains is given by:

$$\begin{aligned} \phi_L &= (2x-1)^2 + 5(2x-1)y + 5(2x-1)z && 0.0 \leq x < 0.5 \quad (6.18) \\ \phi_R &= (2x-1)^2 + (2x-1)y + (2x-1)z && 0.5 \leq x \leq 1.0 \end{aligned}$$

The permeability tensor is given as:

$$\begin{aligned} K_L &= \begin{pmatrix} 1 & 0 & 0 \\ 0 & 1 & 0 \\ 0 & 0 & 1 \end{pmatrix} && 0.0 \leq x < 0.5 \quad (6.19) \\ K_R &= \begin{pmatrix} 5 & 4 & 4 \\ 4 & 5 & 4 \\ 4 & 4 & 5 \end{pmatrix} && 0.5 \leq x \leq 1.0 \end{aligned}$$

This case also leads to a source term on the right hand side of the standard pressure equation which is discontinuous at the interface over which permeability is discontinuous. The actual sources to the left and right domain are -8 and -72 respectively.

The TPS scheme was tested in [23], where a convergence rate of 1.2 is obtained on a boundary aligned hexahedral grid. The boundary aligned hexahedral FPS schemes are exact for piecewise trilinear fields due to exact matching with the basis functions. For a non-boundary aligned grid (where control-volume faces are close to, but not aligned with the discontinuity, the convergence rates for pressure on pyramid, tetrahedra and prism elements are given in Fig. 6.4. The test is on a sequence of grids with the Degree of Freedom (DOF) of [125,729,4913,35937, 68921].

6.7.2 Homogeneous High Anisotropy

The second case is defined by a homogeneous domain with high anisotropic permeability at an angle of 30 degrees and point source at the domain centre. The

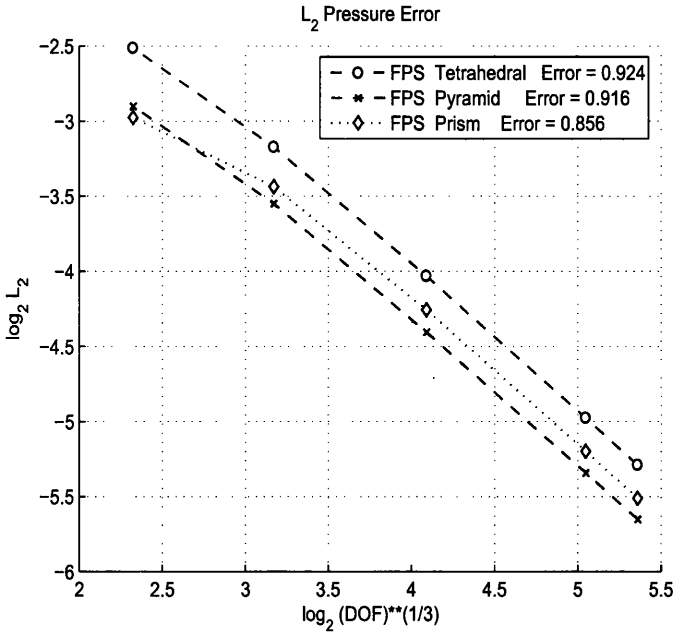

Figure 6.4: 3-D Discontinuous quadratic case: Pressure Convergence on pyramid, tetrahedra and prism elements - Non-Boundary Aligned Grids.

anisotropic ratio is 1000:1, and Dirichlet boundary condition of constant pressure is specified. The permeability tensor is:

$$K = \begin{pmatrix} 750.25 & 432.58 & 0 \\ 432.58 & 250.75 & 0 \\ 0 & 0 & 1 \end{pmatrix} \tag{6.20}$$

Tests are on grid resolution of 16X16X16 for hexahedron, and the same for prisms.

Hexahedral element

The earlier TPS scheme is contrasted with the new FPS scheme on hexahedral elements. The TPS result is shown in Fig.6.5 and clearly shows spurious oscillations consistent with the 2-D TPS results. The new FPS scheme result is shown in fig.6.6, for $\eta = 0$. The FPS scheme yields a smooth pressure solution almost free of spurious oscillations. For higher values of η the decoupling effect [17] can start to occur.

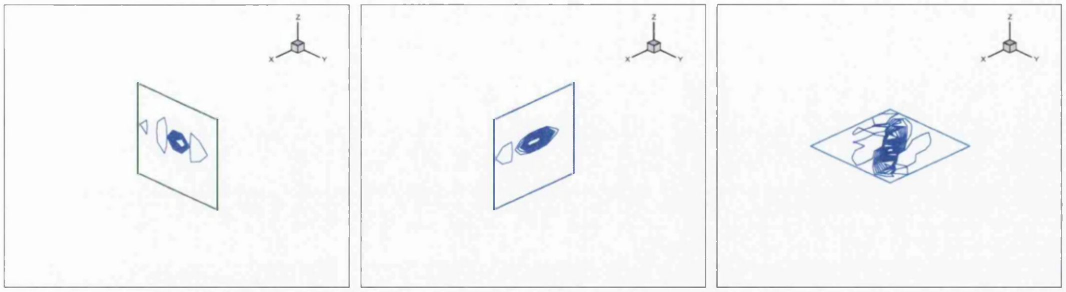

(a) (b) (c)

Figure 6.5: Plot of High anisotropic case with Hexahedral element for TPS scheme q=1. (a) Contour cut in plane x=0.5 (b) Contour cut in plane y=0.5 (c) Contour cut in plane z=0.5

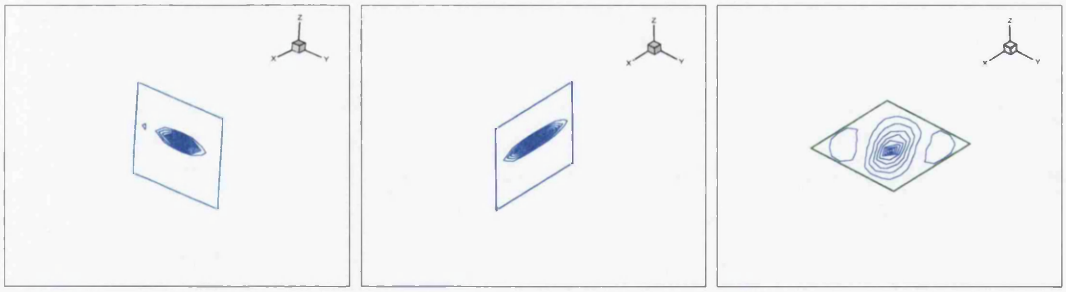

(a) (b) (c)

Figure 6.6: Plot of High anisotropic case with Hexahedral element for FPS scheme eta=0. (a) Contour cut in plane x=0.5 (b) Contour cut in plane y=0.5 (c) Contour cut in plane z=0.5

Prism element

Here we show two examples of prism elements generated from a hexahedral element in Fig.7.9. For the above test case the first prism (A) is aligned against the angle of anisotropy, while the second prism (B) favors the angle of anisotropy.

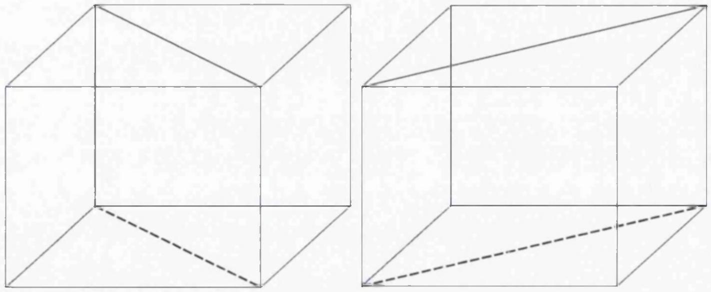

(a) (b)

Figure 6.7: Plot of Prism from hex element. (A) in Z direction, negative angle. (B) in Z direction, positive angle.

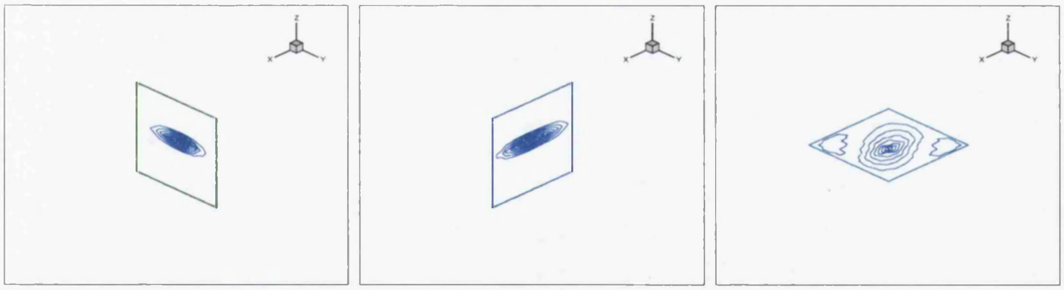

(a) (b) (c)

Figure 6.8: Plot of High anisotropic case with Prism (A) against anisotropy. (a) Contour cut in plane x=0.5 (b) Contour cut in plane y=0.5 (c) Contour cut in plane z=0.5

Prism (A) causes the solution to be relatively diffused due to the planar triangulation against the angle of anisotropy, Fig.6.8. Prism (B) yields sharp resolution with planar triangulation now favoring the angle of anisotropy (consistent with 2-D results), Fig.6.9, again spurious oscillations are reduced. This approximation is an optimal support scheme.

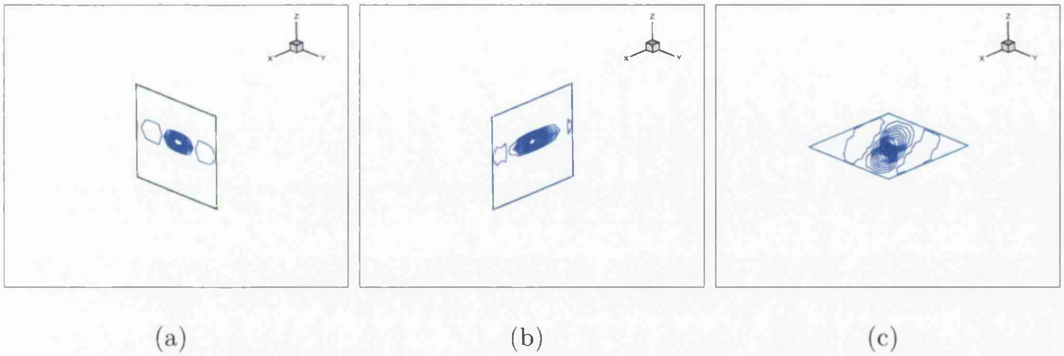

Figure 6.9: Plot of High anisotropic case with Prism (B) favors anisotropy. (a) Contour cut in plane x=0.5 (b) Contour cut in plane y=0.5 (c) Contour cut in plane z=0.5

6.8 Summary

New families of locally conservative flux-continuous, finite-volume schemes are presented for solving the general tensor pressure equation on tetrahedra, prisms, pyramids and hexahedra elements in 3-D. The new families of schemes have full pressure continuity imposed across control-volume faces, in contrast to the earlier point-wise continuous schemes.

The new families of schemes offer improved flexibility in range of quadrature and the hexahedral scheme fluxes are exact for piecewise trilinear pressure fields in 3-D, bilinear in 2-D and the families are SPD for a constant elliptic tensor.

When applying point-wise continuous schemes to full-tensor fields with high anisotropy ratios, the schemes violate the maximum principle, with a limited quadrature range that causes decoupling leading to strong spurious oscillations in the solution.

Tensor-coefficient dependent family M-matrix limits are presented for locally bounded solutions free of spurious oscillations. *Optimal support* conditions are identified from M-matrix bounds, via a bounding quadrature point that defines the upper limit on the tensor cross-terms. Planar self-adapting optimal support schemes are also defined together with M-matrix conditions. M-matrix conditions of the tetrahedra scheme yields equivalent limiting conditions consistent with optimal support.

The new families of schemes are tested on problems involving strong full-tensor anisotropy where both M-matrix and monotone matrix conditions are violated. Results show that spurious oscillations in the discrete pressure field are significantly reduced when using quadrature points outside of the decoupled zone. Quasi-positive QM-matrices are defined. The FPS schemes are shown to have QM-matrices and an optimal support QM-matrix scheme is obtained by anisotropy favoring triangulation.

Chapter 7

Multi-family Schemes in 3D

7.1 Introduction

New multi-family flux-continuous finite volume methods are next presented for solving the pressure equation on grids comprised of any cell type in three dimensions. Key physical constraints of continuity in normal flux and *full* pressure continuity are imposed at control-volume interfaces as the method discussed in Chapter 6. However there are important distinctions in formulation from the previous chapter.

This work continues with the derivation of local algebraic flux continuity conditions for full-tensor discretization operators and extends the families of flux-continuous full-pressure continuity schemes of [17, 108, 18] into three dimensions with multi-family formulations for general structured and unstructured grids. The methods retain the standard number of reservoir simulation degrees of freedom in the approximation while maintaining flux and pressure continuity, with each control-volume being assigned a single discrete pressure value. This contrasts with the mixed finite element method, which requires that an additional degree of freedom corresponding to every continuous interface condition in the grid be added to the global system matrix. The resulting quasi-positive formulation has a significant advantage over the earlier point-wise continuous schemes with an increased quadrature range that enables the new schemes to compute discrete pressure solutions for strongly anisotropic full-tensor fields that are essentially free of spurious oscillations. The results presented demonstrate the benefits of the schemes on structured and unstructured grids in three dimensions.

7.2 Flux-Continuous Schemes with Full Pressure Continuity for Multi-family schemes

We illustrate the procedure with a primary hexahedral cell with local vertices numbered $1, ..., 8$, Fig 6.1. First interface pressures are introduced at the edge, cell-face and cell-centre mid-points respectively. These will be expressed algebraically in terms of the primary cell vertex pressures in a preprocessing step, through the following set of equations imposed over the primary cell. The pressure ϕ and position vector $\mathbf{r} = (x, y, z)$ assume a trilinear variation over each subcell, as in the previous chapter,

$$\begin{aligned}\phi = \; & (1-\tilde{\xi})(1-\tilde{\eta})(1-\tilde{\zeta})\phi_1 + \tilde{\xi}(1-\tilde{\eta})(1-\tilde{\zeta})\phi_2 + \tilde{\xi}\tilde{\eta}(1-\tilde{\zeta})\phi_3 \\ & +(1-\tilde{\xi})\tilde{\eta}(1-\tilde{\zeta})\phi_4 + (1-\tilde{\xi})(1-\tilde{\eta})\tilde{\zeta}\phi_5 + \tilde{\xi}(1-\tilde{\eta})\tilde{\zeta}\phi_6 \\ & +\tilde{\xi}\tilde{\eta}\tilde{\zeta}\phi_7 + (1-\tilde{\xi})\tilde{\eta}\,\tilde{\zeta}\phi_8\end{aligned} \tag{7.1}$$

$$\begin{aligned}\mathbf{r} = \; & (1-\tilde{\xi})(1-\tilde{\eta})(1-\tilde{\zeta})\mathbf{r}_1 + \tilde{\xi}(1-\tilde{\eta})(1-\tilde{\zeta})\mathbf{r}_2 + \tilde{\xi}\tilde{\eta}(1-\tilde{\zeta})\mathbf{r}_3 \\ & +(1-\tilde{\xi})\tilde{\eta}(1-\tilde{\zeta})\mathbf{r}_4 + (1-\tilde{\xi})(1-\tilde{\eta})\tilde{\zeta}\mathbf{r}_5 + \tilde{\xi}(1-\tilde{\eta})\tilde{\zeta}\mathbf{r}_6 \\ & +\tilde{\xi}\tilde{\eta}\tilde{\zeta}\mathbf{r}_7 + (1-\tilde{\xi})\tilde{\eta}\,\tilde{\zeta}\mathbf{r}_8\end{aligned} \tag{7.2}$$

where $\tilde{\xi}, \tilde{\eta}, \tilde{\zeta}$ are subcell master element coordinates defined over the unit square $0 \leq \tilde{\xi}, \tilde{\eta}, \tilde{\zeta} \leq 1$. As before subcell Darcy fluxes are defined by resolving Darcy velocity along surface area outward normal vectors with $\mathbf{F} = -\mathbf{K}\nabla\phi \bullet \Delta S$, and approximated using subcell approximations of the form illustrated by Eq.7.1 for subcell 1. The interface pressures are continuous across the respective interfaces by construction, and as a consequence of the subcell approximation, pressure is bilinear and continuous over the entire face of each subcell with *full pressure support* FPS. A local flux continuity condition is imposed for each edge-centred pressure, a surface zero divergence condition is imposed for each auxiliary cell-face pressure and zero divergence is imposed in each primal cell sub-volume, to determine the auxiliary pressure at the cell-centre. In this formulation the bilinear FPS subcell surface support also retains two degrees of freedom in position of flux continuity on a sub-face. This formulation extends that presented in [108] to permit maximum flexibility in quadrature, which is achieved by allowing the coordinates of flux quadrature to vary with unequal values in general [109]. For example referring to face $b0, b1, m1, m0$ of Fig.6.3, then we can choose $\widetilde{\eta} \neq \widetilde{\zeta}$ and crucially different values can be chosen for each interface of a given control-volume Fig.7.1(a). Such a formulation has already proven beneficial in 2-D [18]. This formulation leads to new multiple families of 3-D flux-continuous schemes with full pressure support together with the maximum quadrature range.

7.2.1 Flux Continuity Conditions

Once quadrature points are selected flux continuity is imposed using the formulation of Chapter 6. Primal fluxes are defined over the hexahedral subcell faces that are inside the primal cell, by resolving the discrete Darcy flux along each normal surface area vector. Interior subcell fluxes are constructed for each subcell face belonging to a primary grid cell. As a result, a left and right flux will be defined with respect to each interior subcell face, Fig6.1. Flux continuity is achieved by equating subcell fluxes at common faces leading to

$$F_i = -(T_{i1}\phi_{\widetilde{\xi}} + T_{i2}\phi_{\widetilde{\eta}} + T_{i3}\phi_{\widetilde{\zeta}})|_{\sigma}^{L} = -(T_{i1}\phi_{\widetilde{\xi}} + T_{i2}\phi_{\widetilde{\eta}} + T_{i3}\phi_{\widetilde{\zeta}})|_{\sigma}^{R} \tag{7.3}$$

where suffix i indicates the local subcell coordinate, suffix $\sigma = \sigma(\widetilde{\eta}, \widetilde{\zeta})$ indicates the chosen flux continuity position on an interface and the coordinates in $(\widetilde{\eta}, \widetilde{\zeta})$ thus define a multiple family of schemes with different flux quadrature points on each of the three

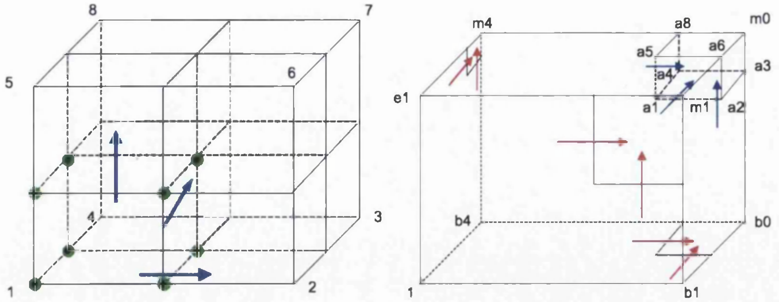

Figure 7.1: (a) Multi-family fluxes on subcell with non-symmetric positions of quadrature (b) Auxiliary fluxes in a subcell. Red arrow: surface flux. Green arrow: volume flux

sub-hexahedra surfaces.

For example with respect to face $b0, b1, m1, m0$ of Fig.6.3

$$\begin{aligned}
F_{b1} &= -(T^1_{11}((1-\widetilde{\eta})(1-\widetilde{\zeta})(\phi_{b1}-\phi_1)+\widetilde{\eta}(1-\widetilde{\zeta})(\phi_{b0}-\phi_{b4})+\widetilde{\zeta}(1-\widetilde{\eta})(\phi_{m1}-\phi_{e1}) \\
&\quad +\widetilde{\eta}\widetilde{\zeta}(\phi_{m0}-\phi_{m4}))+T^1_{12}((1-\widetilde{\zeta})(\phi_{b0}-\phi_{b1})+\widetilde{\zeta}(\phi_{m0}-\phi_{m1})) \\
&\quad +T^1_{13}((1-\widetilde{\eta})(\phi_{m1}-\phi_{b1})+\widetilde{\eta}(\phi_{m0}-\phi_{b0}))) \\
&= -(T^2_{11}((1-\widetilde{\eta})(1-\widetilde{\zeta})(\phi_2-\phi_{b1})+\widetilde{\eta}(1-\widetilde{\zeta})(\phi_{b2}-\phi_{b0})+\widetilde{\zeta}(1-\widetilde{\eta})(\phi_{e2}-\phi_{m1}) \\
&\quad +\widetilde{\eta}\widetilde{\zeta}(\phi_{m2}-\phi_{m0}))+T^2_{12}((1-\widetilde{\zeta})(\phi_{b0}-\phi_{b1})+\widetilde{\zeta}(\phi_{m0}-\phi_{m1})) \\
&\quad +T^2_{13}((1-\widetilde{\eta})(\phi_{m1}-\phi_{b1})+\widetilde{\eta}(\phi_{m0}-\phi_{b0})))
\end{aligned} \tag{7.4}$$

The non-symmetric positions of quadrature are illustrated in Fig.7.1(a).

7.2.2 Auxiliary Control Volume Divergence Free Conditions

Full (bilinear) pressure continuity over the control-volume subcell faces is achieved by the introduction of further auxiliary pressures at cell centres and cell-face centres (in addition to edge interface pressures). Additional zero divergence equations are imposed to solve for the additional local degrees of freedom, as in [108] with

$$-\sum_{\partial\Omega_{AUX}} (\mathbf{K}\nabla\Phi)\cdot\hat{\mathbf{n}}\Delta s = 0 \tag{7.5}$$

This involves construction of two types of Auxiliary Control Volume (ACV) approximation for 3D FPS schemes: A surface ACV surrounding each cell-face centre and a sub-volume ACV surrounding the center of the primal cell. Auxiliary fluxes are then defined over the faces of the resulting sub-subcells, i.e. subcells of the subvolume Fig.7.1(b), top right corner $m0$ is primal cell centre, Fig.6.3. Since permeability is piecewise constant over the sub-subcells CVFE is employed for the auxiliary divergence approximations. The formulation has also been developed for prisms, tetrahedra and pyramid elements. The corresponding elements, control-volumes and sub-faces are illustrated in chapter 6. The multi-family of schemes permits different flux quadrature points on each of the three sub-hexahedra surfaces for each element.

7.3 M-matrix Conditions and Optimal Support 19 to 13 Point Schemes

This section continues the discussion of seeking an optimal scheme via quadrature selection. The multi-family FPS schemes considered in this section maximizes the range of schemes that are possible.

The FPS mapping onto CVFE for planar 19 point schemes, defined by collapsing quadratures to the three cross-intersecting planes, is established directly from correspondence with the 2-D analysis [18], and it also follows that the planar families are symmetric positive definite (SPD in short) for a constant elliptic tensor. The M-matrix conditions for families of 19 point schemes are given by [109]

$$\begin{aligned} 2 \mid T_{12} \mid &\leq (\zeta_2 T_{11} + \zeta_1 T_{22}) \leq min(T_{11}, T_{22}) \\ 2 \mid T_{13} \mid &\leq (\eta_2 T_{11} + \eta_1 T_{33}) \leq min(T_{11}, T_{33}) \\ 2 \mid T_{23} \mid &\leq (\xi_2 T_{22} + \xi_1 T_{33}) \leq min(T_{22}, T_{33}) \end{aligned} \tag{7.6}$$

where $0 \leq \xi_1, \xi_2, \eta_1, \eta_2, \zeta_1, \zeta_2 < 1/2$. The optimal quadrature points per plane that reduces each planar 9-point scheme to a 7-point scheme, resulting in the net 19 point scheme reducing to a net 13-point scheme are defined by the left limit of Eq.7.6 where

$$\begin{aligned}(\zeta_2 T_{11} + \zeta_1 T_{22}) &= 2 \mid T_{12} \mid, \\ (\eta_2 T_{11} + \eta_1 T_{33}) &= 2 \mid T_{13} \mid, \\ (\xi_2 T_{22} + \xi_1 T_{33}) &= 2 \mid T_{23} \mid \end{aligned} \tag{7.7}$$

We note that there is a degree of freedom in choice of quadrature in each plane, leading to families of optimal schemes in contrast to the single optimal point defined in chapter 6. We also note that substitution of Eq. 7.7 in Eq. 7.6 leads to recovery of the same M-matrix conditions as for the tetrahedron in Eq.6.11. This provides a 3-D generalisation of the reduction of 9-point schemes to 7-point schemes via quadrature, with analogous conditions to M-matrices on quadrilaterals and triangles [17]. For constant coefficients the scheme will self-adapt the discretization support locally according to the local orientation of the tensor field. This formulation generalizes the single family formulation of chapter 6.

7.4 Decoupled Solution

As in two dimensions the 3-D schemes are decoupled if $\xi_1 = \xi_2 = \eta_1 = \eta_2 = \zeta_1 = \zeta_2 = 1/2$ [109]. The 27-point schemes also permit the decoupled solution when all quadratures are set equal to a 1/2. There is a strong analogy with the 2-D schemes, both in terms of the respective mappings between CVFE and the triangular pressure support TPS schemes and between CVFE and full pressure support FPS schemes [17, 18]. The TPS formulation has a quadrature that lies in the neighborhood of the singular point of the finite-volume framework leading to a decoupled solution as in 2-D. The extended support of the 3-D FPS schemes enables this neighborhood to be avoided.

7.4.1 Corollary: A Monotone Discretization Matrix Avoids Decoupling

We have already observed that a monotone discretization matrix is sufficient to prevent decoupling in 2-D, c.f. chapter 5. Since the above 3-D decoupled solution also involves oscillations between positive and negative values, we draw the same conclusion with respect to 3-D solutions [38].

7.5 Quasi-Positive QM-matrices

As for the single family of chapter 6, the schemes presented here do not have M-matrices or monotone matrices for higher full-tensor anisotropy ratios that exceed the corresponding M-matrix bounds. However, for quadrature points outside the decoupled zone the schemes yield results with relatively few spurious oscillations and are categorized in terms of a Quasi-M-matrix. The fundamental M-matrix (and monotone matrix) violation occurs in 3-D when Eq.6.8 is violated. The QM-matrix definition extends to 3-D with matrices having up to three unique positive off-diagonal coefficients that violate the M-matrix conditions, each plane making up to one contribution [108, 109]. The schemes resulting from Eq.7.7 appear optimal with respect to a QM-matrix.

7.5.1 Multi-Family Anisotropic Quadrature

When applying the methods to general heterogeneous cases a locally upscaled tensor can be used to define the unique ξ, η, ζ quadrature points over a dual-cell. Note the locally upscaled tensor is only used to define the quadrature, once the quadrature is defined, the flux continuous method is then used to solve the original fine scale problem (with the original permeability field). However, we can only expect to obtain an approximate optimal quadrature point and therefore the full support of the scheme will be retained in such cases.

For a single family formulation a bound is required on the upper quadrature limit in order to avoid the decoupled zone. The multi-family formulation offers further advantages over the single family schemes. First the reduction from 27 to 19 nodes in the planes can be achieved directly via quadratures in the planes. Secondly the multi-family enables maximum flexibility in the definition of quadrature. For example referring to Eq.7.7, instead of a single optimal quadrature point, there are multiple families of optimal schemes. E.g. we may choose ζ_1 to be a Gauss point and define ζ_2 such that optimal quadrature is obtained. However, we have observed that solution resolution is also sharpened by increasing the quadrature value multiplying the larger diagonal tensor coefficient. This motivates the selection of *extreme* quadrature values for the family parameters multiplying the larger diagonal tensor coefficients and reduced quadrature for the accompanying family parameters, leading to anisotropic quadrature which is outside of the decoupled zone. For example if $T_{11} > T_{22}$ then $\zeta_2 \rightarrow 1/2$ while $\zeta_1 \rightarrow 0$. This strategy is unique to the multi-family formulation and has proven to be highly effective. While the leading quadrature parameter is chosen according to strength of anisotropy, crucially the values of quadrature are independent of the tensor coefficients. For a spatially varying tensor field this is an important advantage and simplification when compared to the tensor dependent optimal quadrature points.

7.6 Numerical Results

A number of numerical tests have been performed to test the new methods for various grids. Here we present results for three test cases.

7.6.1 Piecewise Quadratic Test Case

Results for a piecewise quadratic case involving a jump in the full tensor is reported in [108] for the single family FPS schemes. Here we note that the exact solution is also obtained on a boundary aligned hexahedral grid for the multi-family schemes. The TPS scheme was tested in [23], where a convergence rate of 1.2 is obtained on a boundary aligned hexahedral grid. The boundary aligned hexahedral FPS schemes are exact for piecewise trilinear fields due exact matching with the basis functions.

7.6.2 Case 1: Perturbed Rhombohedron Grid

In this case we consider a perturbed grid aligned with a rhombohedron or three dimensional parallelogram. A similar test was proposed in [32]. The reference solution of Laplace's equation Eq.7.8, is used to define the boundary conditions and Laplace's equation is solved over the domain.

$$\phi = sin(\sqrt{2}\pi x/10)sinh(\pi y/10)sinh(\pi z/10) \tag{7.8}$$

The medium is assumed to be isotropic. The grids have an underlying full tensor due to the angle of the parallelogram, Fig. 7.2. The schemes are tested for convergence against the reference solution. The test is on the sequence of grids with degree of freedom (DOF) of [125,729,4913,35937,274625].

In this case the prismatic FPS scheme with prisms favoring the angle of anisotropy is optimal with a QM-matrix. Comparing convergence rates of the 27 and 19-point FPS schemes (with extremes in anisotropic quadrature) with the prism scheme rates indicates that the hexahedral schemes provide encouraging results, Fig.7.3, 7.4, 7.5.

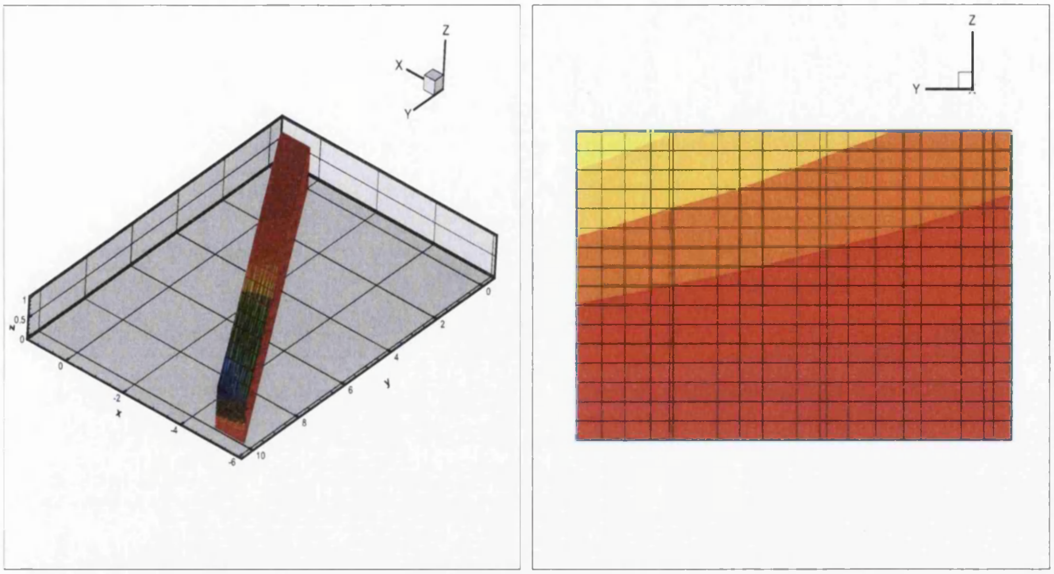

(a) (b)

Figure 7.2: Perturbed Rhombohedron Grid: (a)The approximate solution (b)Slice X=-2.5

7.6.3 Case 2a: Homogeneous Highly Anisotropic Planar Full-Tensor

The second case is defined by a homogeneous domain with planar high anisotropic permeability tensor at an angle of 30 degrees and point source at the domain centre and Dirichlet boundary conditions specified with zero pressure on the boundary surfaces. The permeability tensor is:

$$K = \begin{pmatrix} 750.25 & 432.58 & 0 \\ 432.58 & 250.75 & 0 \\ 0 & 0 & 1 \end{pmatrix} \qquad (7.9)$$

Tests are on grid resolution of 16X16X16 for hexahedron, and the same for prisms.

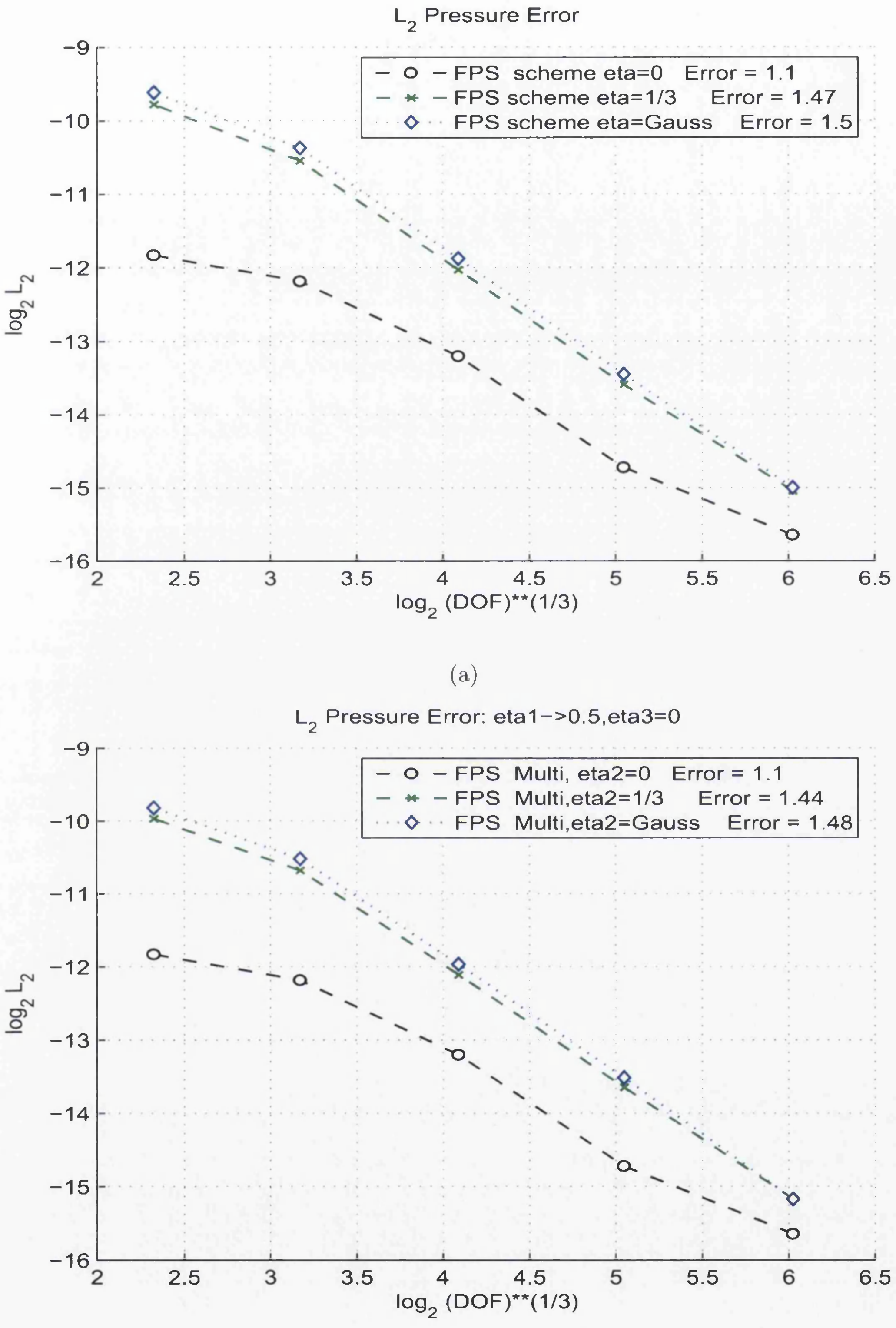

(a)

(b)

Figure 7.3: Numerical convergence of FPS schemes on perturbed parallelogram grid in 3D. (a)FPS single family (b)FPS Multi-family with $\eta_1 \rightarrow 0.5, \eta_3 = 0$

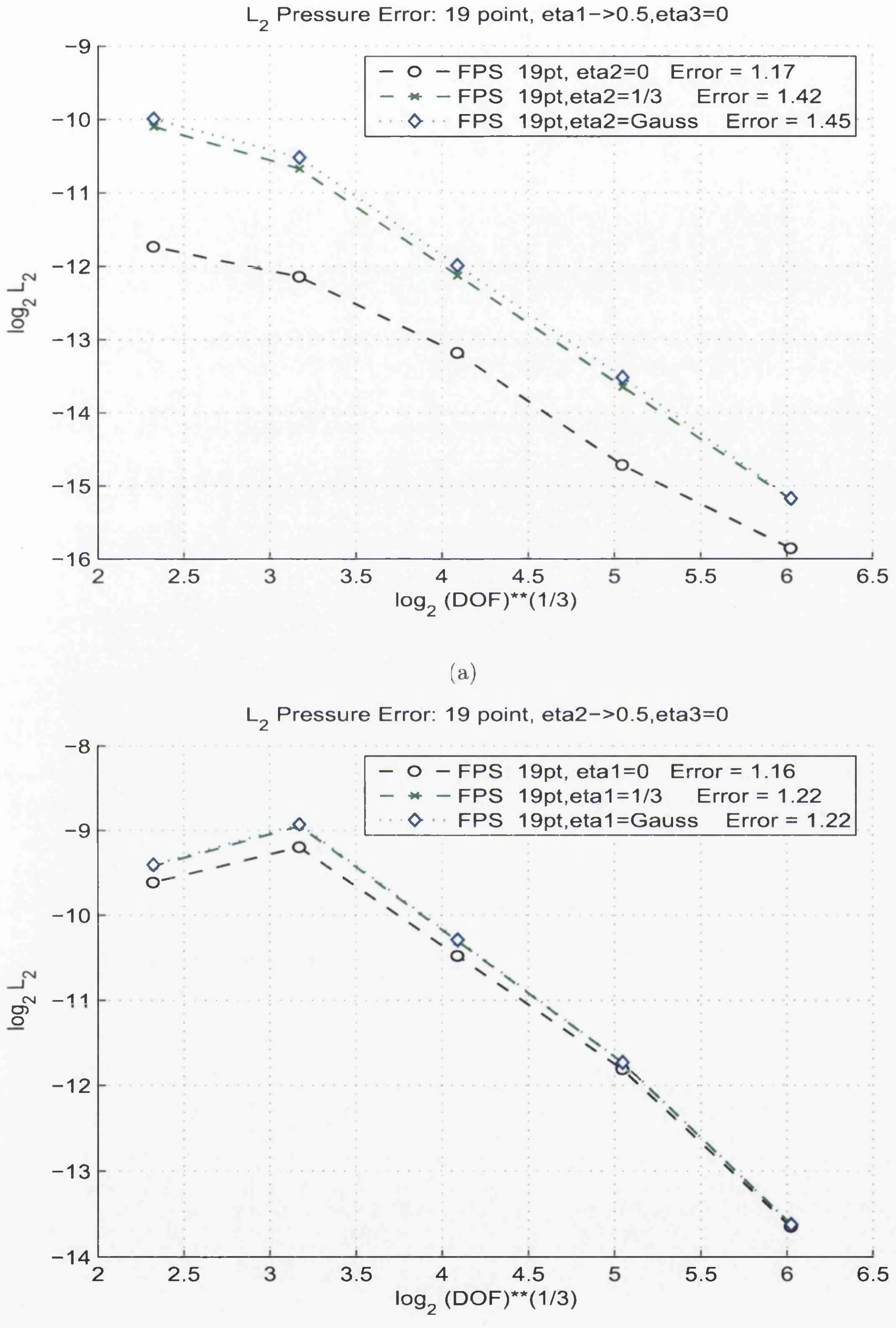

(a)

(b)

Figure 7.4: Numerical convergence of FPS 19 point schemes on perturbed parallelogram grid. (a)eta1= 0.4999,eta3 =0 (b)eta2 = 0.4999,eta3=0

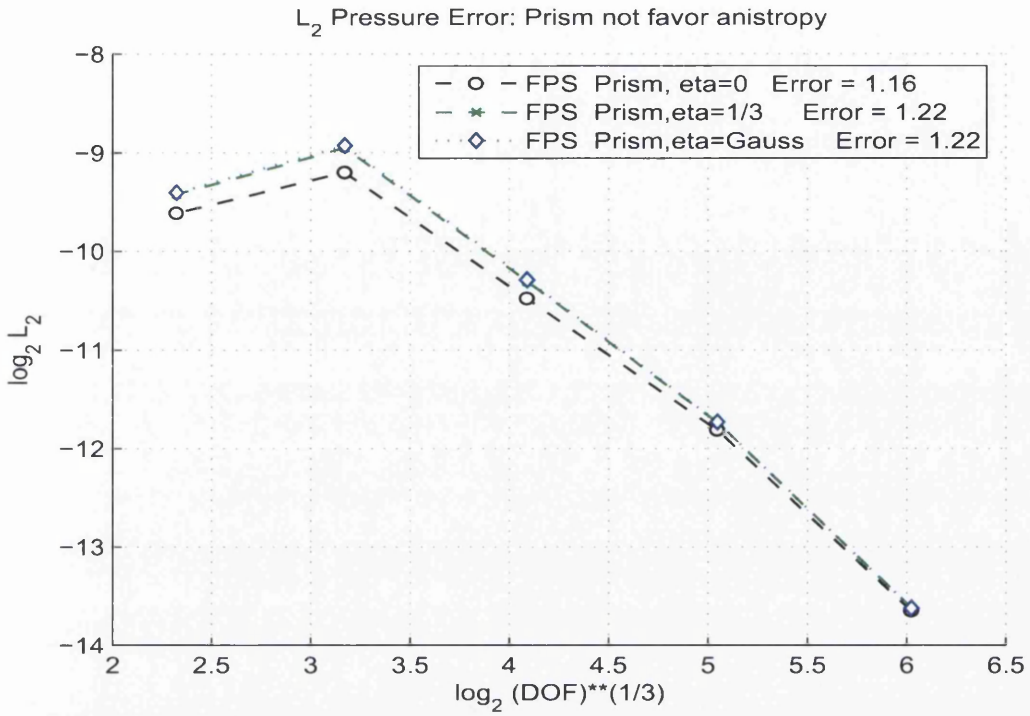

(a)

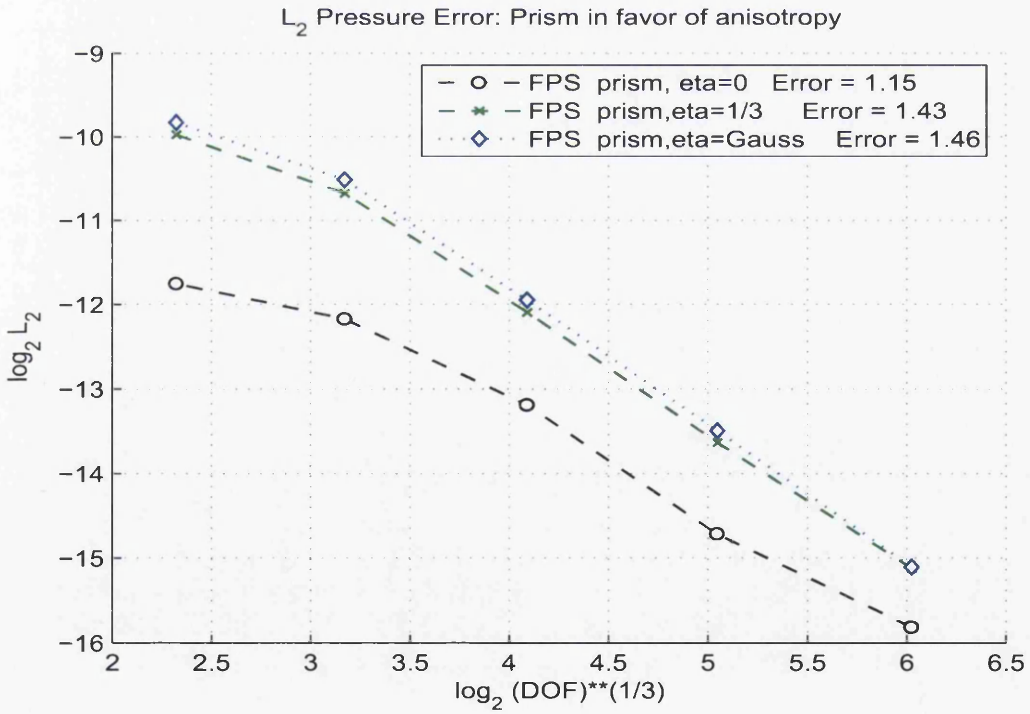

(b)

Figure 7.5: Numerical convergence of FPS schemes on perturbed Prism grid in 3D. (a)prism not in favour of anistropy (b)prism in favour of anisotropy.

Hexahedral Element

The earlier TPS scheme is contrasted with the new FPS scheme on hexahedral elements. The TPS result is shown in Fig.7.6 and clearly shows spurious oscillations consistent with the 2-D TPS results. The single-family 27-point FPS scheme result is shown in fig.7.7, for $\eta = 0$. The FPS scheme yields a smooth pressure solution relatively free of spurious oscillations. The multi-family 19 and 27-point FPS schemes yield similar results for this case, the 27-point result is shown in Fig.7.8. Extremes in anisotropic quadrature are employed for these results and give improved resolution.

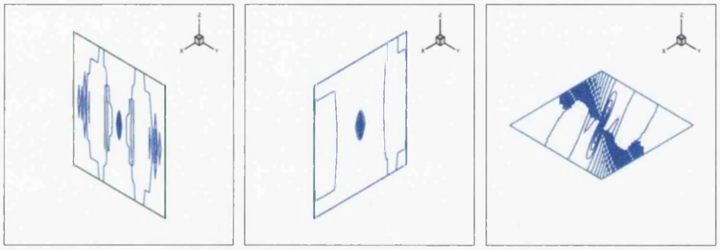

(a) (b) (c)

Figure 7.6: Case 2a: TPS Scheme with eta=0. (a)Iso-surface plot. (b)A slice of X = 0.5. (c) A slice of Y = 0.5. (d) A slice of Z =0.5.

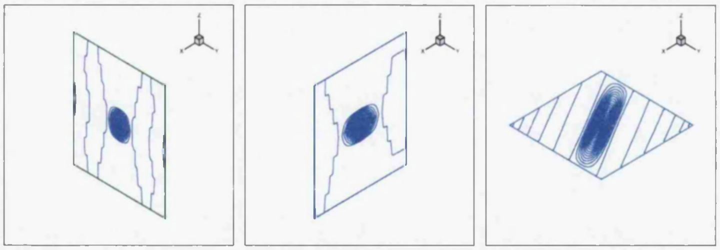

(a) (b) (c)

Figure 7.7: Case 2a: FPS 27-point scheme, single family with eta=0. (a)Iso-surface plot. (b)A slice of X = 0.5. (c) A slice of Y = 0.5. (d) A slice of Z =0.5.

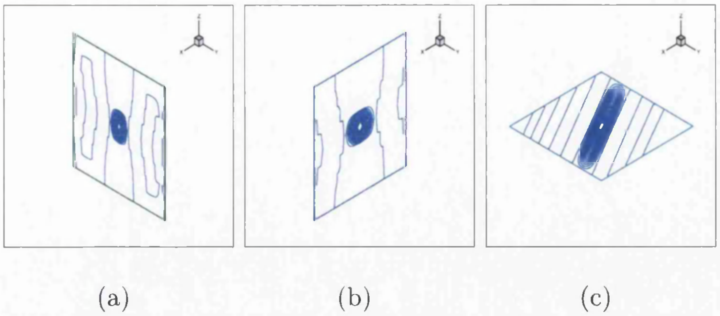

Figure 7.8: Case 2a: FPS 27-point multi-family scheme, with eta1=0,eta2=0.4999,eta3=0. (a)Iso-surface plot. (b)A slice of X = 0.5. (c) A slice of Y = 0.5. (d) A slice of Z =0.5.

Prism element

Here we show two examples of prism elements generated from a hexahedral element in Fig.7.9. For the above test case the first prism (A) is aligned against the angle of anisotropy, while the second prism (B) favors the angle of anisotropy.

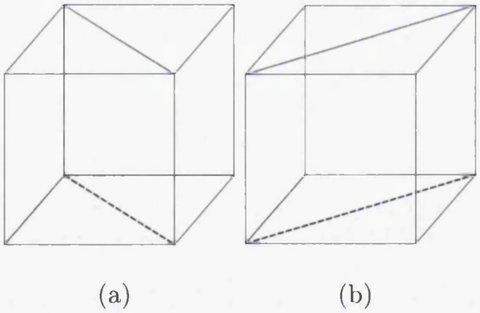

Figure 7.9: Plot of Prism from hex element. (A) unfavorable negative angle. (B) positive angle favors tensor.

Prism (A) causes the solution to be relatively diffused due to the planar triangulation against the angle of anisotropy, fig.7.10. Prism (B) yields sharp resolution with planar triangulation now favoring the angle of anisotropy (consistent with 2-D results), Fig.7.11, again spurious oscillations are reduced. This approximation is an optimal support scheme. We note that the 27-point scheme with anisotropic quadrature Fig.7.8 yields a comparable result to the optimal scheme.

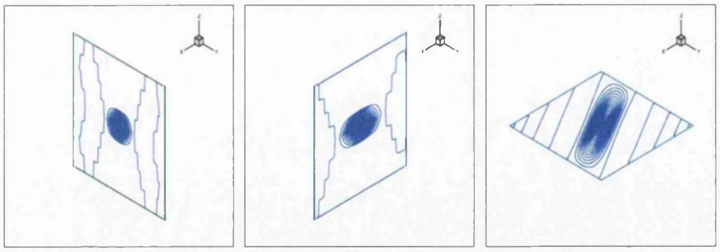
(a) (b) (c)

Figure 7.10: Case 2a: FPS on unfavorable Prism single family eta=0. (a)Iso-surface plot. (b)A slice of X = 0.5. (c) A slice of Y = 0.5. (d) A slice of Z =0.5.

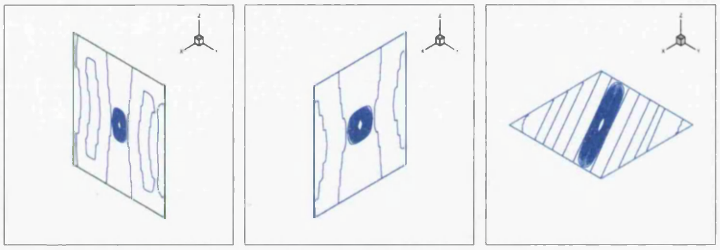
(a) (b) (c)

Figure 7.11: Case 2a: FPS on favorable Prism single family eta=0. (a)Iso-surface plot. (b)A slice of X = 0.5. (c) A slice of Y = 0.5. (d) A slice of Z =0.5.

7.6.4 Case 2b: Homogeneous Highly Anisotropic Full-Tensor

The case 2b is defined by a homogeneous domain with high anisotropic permeability at an angle of 25 degrees and point source at the domain centre and Dirichlet boundary conditions specified with zero pressure on the boundary surfaces. The permeability tensor is defined by:

$$\mathbf{K} = \begin{pmatrix} 2464.36 & 1148.68 & 50.0 \\ 1148.68 & 536.64 & 0 \\ 50.0 & 0 & 536.64 \end{pmatrix} \tag{7.10}$$

which has non-trivial cross terms in two planes together with a stronger K_{33} diagonal coefficient. The earlier TPS scheme is contrasted with the new FPS schemes on hexahedral and prism elements. The TPS result is shown in Fig.7.12 and clearly showing the expected spurious oscillations consistent with decoupling. The single-family 27-point FPS scheme result is shown in Fig.7.13, for $\eta = 0$. The base FPS scheme yields a smooth pressure solution almost free of spurious oscillations. While the multi-family 19 and 27-point FPS schemes yield similar results Fig's.7.14, 7.15 respectively, the 27-point scheme indicates improved detection of the effect of K_{13}. Extremes in anisotropic quadrature are again employed for these results and give improved resolution. The favorable prism result is shown in Fig.7.16. This method is in the optimal class of schemes. We note as in case2a, that the optimal result is comparable with the hexahedral schemes with anisotropic quadrature, again demonstrating the advantage of the multi-family formulation.

Tests are on grid resolution of 16X16X16 for both hexahedron and prisms.

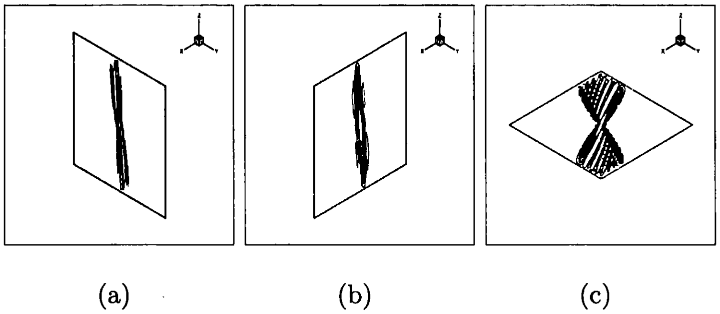
(a) (b) (c)

Figure 7.12: Case 2b: Full tensor case: TPS q=1. (a)Iso-surface plot. (b)A slice of X = 0.5. (c) A slice of Y = 0.5. (d) A slice of Z =0.5.

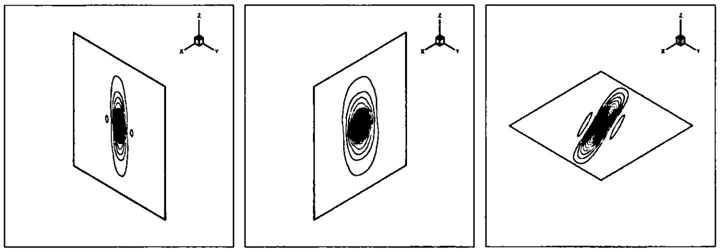

(a) (b) (c)

Figure 7.13: Case 2b: FPS 27-point scheme, single family eta =0. (a)Iso-surface plot. (b)A slice of X = 0.5. (c) A slice of Y = 0.5. (d) A slice of Z =0.5.

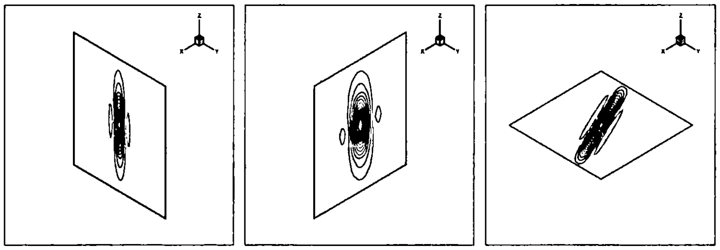

(a) (b) (c)

Figure 7.14: Case 2b: FPS 19-point Multi-family with eta2 =0.4999. (a)Iso-surface plot. (b)A slice of X = 0.5. (c) A slice of Y = 0.5. (d) A slice of Z =0.5.

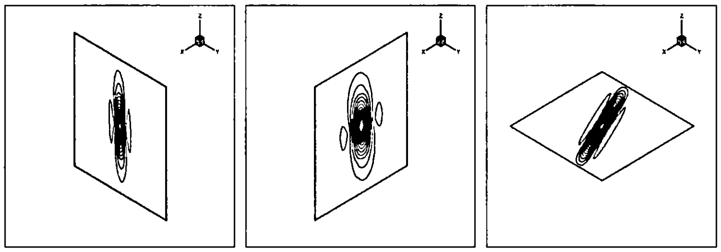

(a) (b) (c)

Figure 7.15: Case 2b: FPS 27-point Multi-family with eta2 =0.4999. (a)Iso-surface plot. (b)A slice of X = 0.5. (c) A slice of Y = 0.5. (d) A slice of Z =0.5.

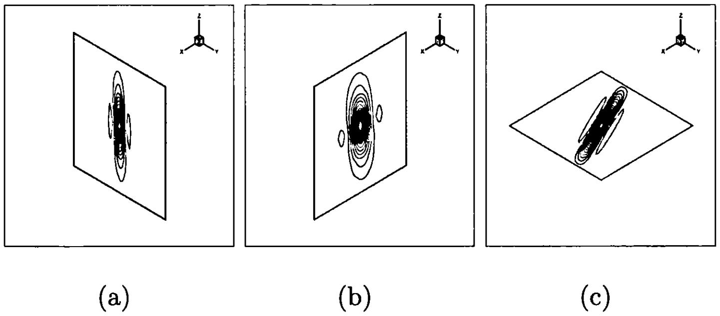

Figure 7.16: Case 2b: Full tensor case on favourable prism: FPS eta =0. (a)Iso-surface plot. (b)A slice of X = 0.5. (c) A slice of Y = 0.5. (d) A slice of Z =0.5.

7.6.5 Case 3a: Highly Anisotropic Discontinuous Full-Tensor - Zigzag

In this case the permeability field is planar in three slabs, with first and third slab defined by

$$\mathbf{K} = \begin{pmatrix} 2464.36 & 0 & 1148.68 \\ 0 & 536.64 & 0 \\ 1148.68 & 0 & 536.64 \end{pmatrix} \tag{7.11}$$

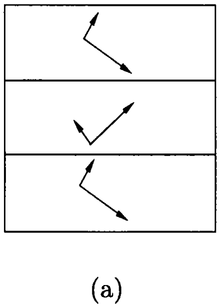

Figure 7.17: Case 3: slabs are shown in cross-section in the $x - z$ plane

and the middle slab has the same tensor in magnitude with negative cross-terms $K_{13} = -1148.68$. The slabs are shown in cross-section in the $x - z$ plane in Fig.7.17, where principal axes are indicated. Two sources are placed at (0.25,0.25,0.25) and

(0.25,0.75,0.25) and one sink at (0.75,0.5,0.75). The permeability has discontinuities at $z = 0.375$ and $z = 0.625$. As in the previous examples, the earlier TPS scheme is contrasted with the new FPS schemes on hexahedral elements. The TPS result is shown in Fig.7.18, clearly showing the expected spurious oscillations consistent with decoupling. The single-family 27-point FPS scheme result is shown in Fig.7.19, for $\eta = 0$. The base FPS scheme yields a smooth pressure solution almost free of spurious oscillations. The multi-family 19 and 27-point FPS schemes results are shown in Fig's.7.20, 7.21 respectively, the 27-point scheme yields sharper solution resolution than both the single family 27-point scheme and the 19-point multi-family scheme. Extremes in anisotropic quadrature are again employed, the 27-point FPS anisotropic scheme (result in Fig. 7.21) consistently improves resolution compared to the base scheme in all cases.

Tests are on grid resolution of 64X8X64 for both hexahedron and prisms.

7.6.6 Case 3b: Highly Anisotropic Discontinuous Full-Tensor - Zigzag - Hybrid Grid

In this case the grid is comprised of anisotropy favoring prisms together a hexahedral layer at each interface of the zigzag domain. The anisotropy favoring prism scheme belongs to the class of optimal schemes. The hexahedral layers maintain a boundary aligned grid with control-volume faces lying on the interfaces coinciding with the discontinuity in permeability tensor. Anisotropic quadrature is employed in the hexahedral elements. The results are comparable with the 27-point multi-family scheme using anisotropic extreme quadrature.

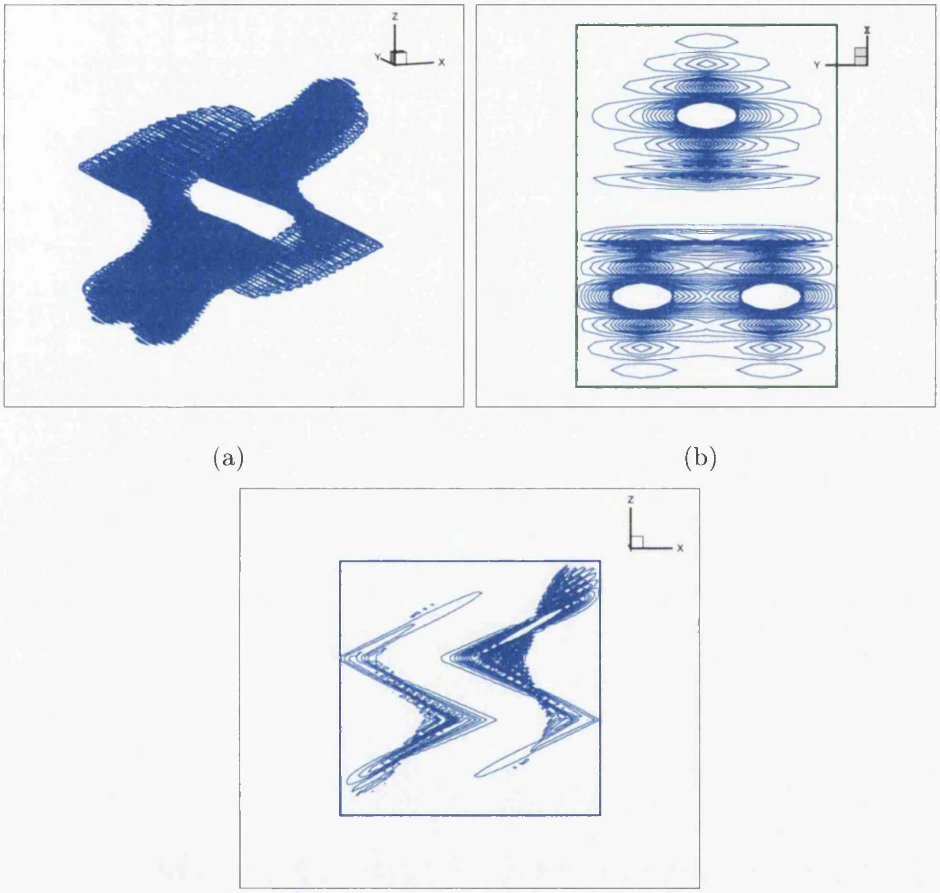

(a) (b)

(c)

Figure 7.18: TPS scheme with q=1. (a)Iso surface plot (b)A slice from cross-section. (c) Y=0.5

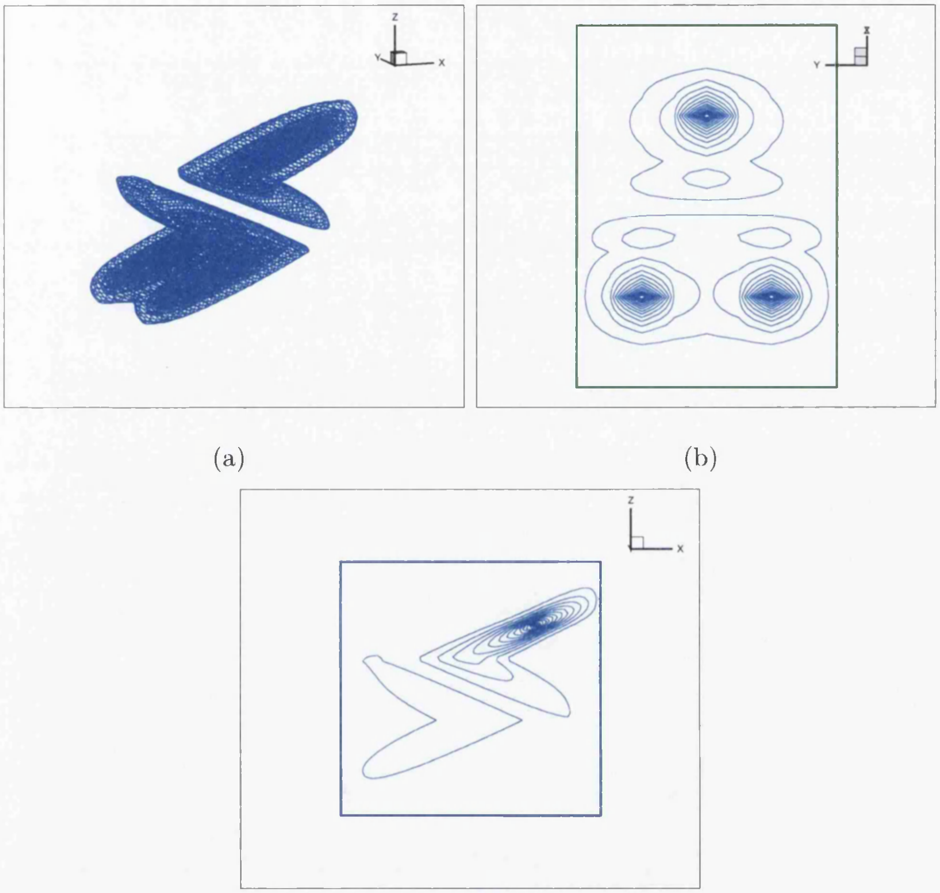

(a)

(b)

(c)

Figure 7.19: FPS single-family scheme with eta=0. (a)Iso surface plot (b)A slice from cross-section. (c) Y=0.5

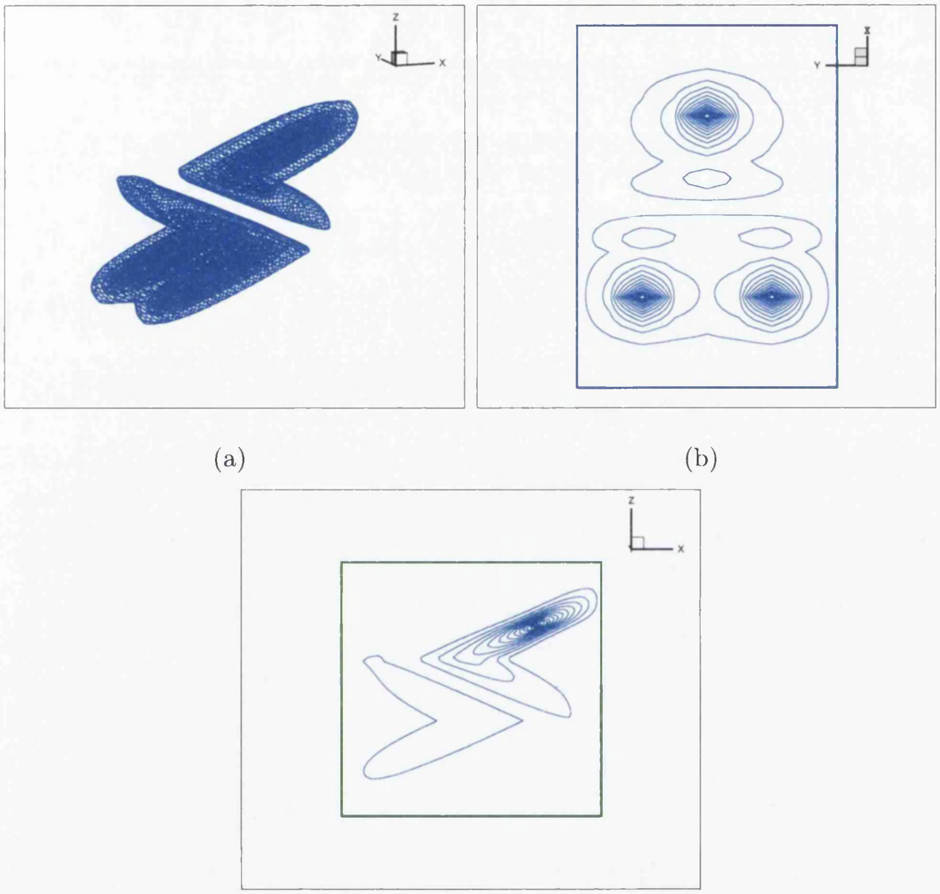

(a)

(b)

(c)

Figure 7.20: FPS 19-point multi-family with eta3=0.5 (a)Iso surface plot (b)A slice from cross-section. (c) Y=0.5

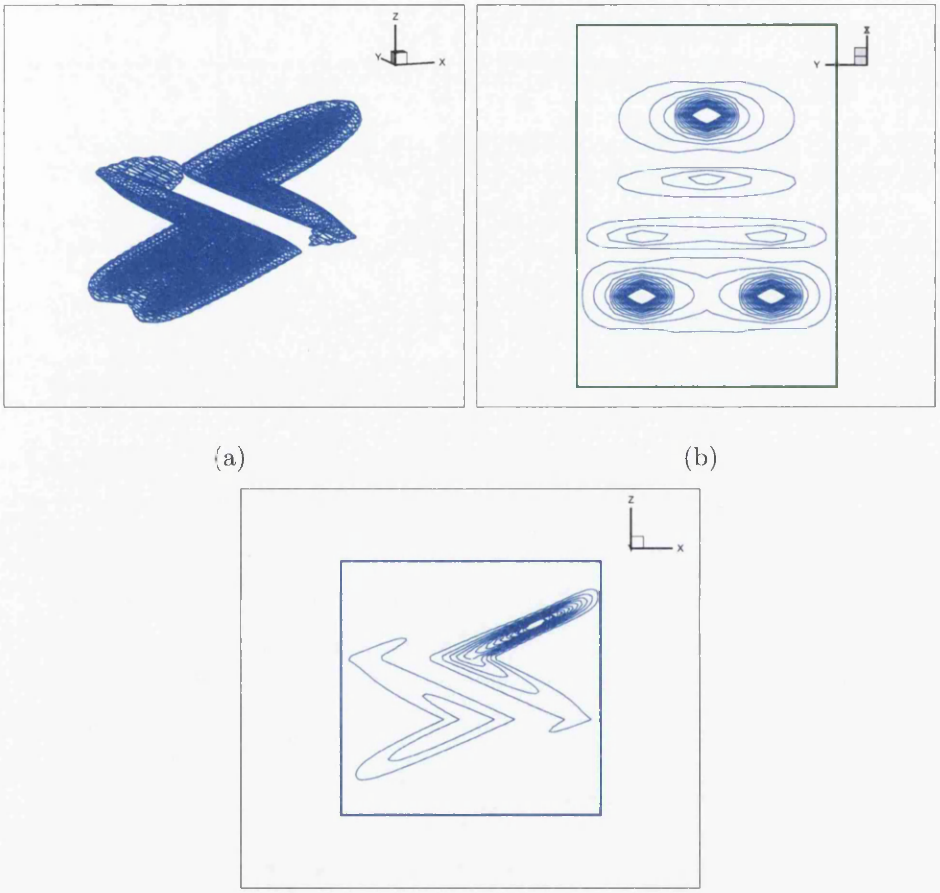

(a) (b)

(c)

Figure 7.21: FPS 27-point multi-family with eta3=0.5 (a)Iso surface plot (b)A slice from cross-section. (c) Y=0.5

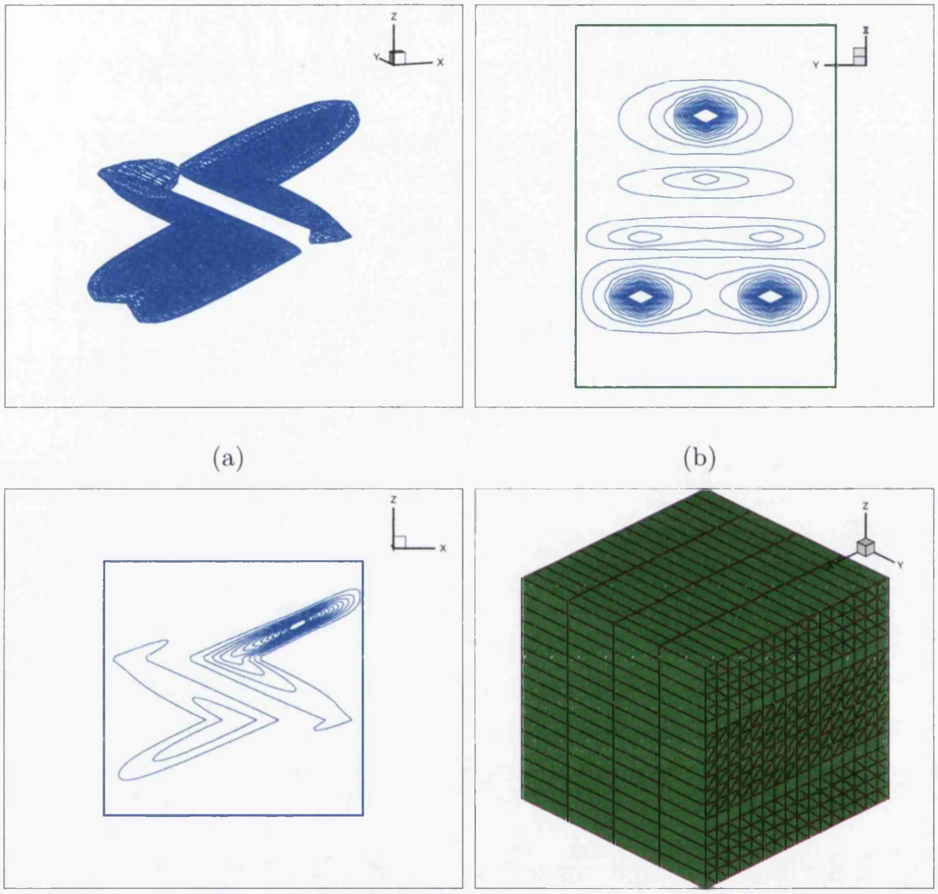

(a) (b)

(c) (d)

Figure 7.22: Hybrid grid with Hex-Multi-family eta3=0.4999, Prism eta=0. (a)Iso surface plot (b)A slice from cross-section. (c)Y=0.5. (d)Illustration of Hybrid grid

7.7 Summary

New multi-families of locally conservative flux-continuous, finite-volume schemes are presented for solving the general tensor pressure equation on tetrahedra, prisms, pyramids and hexahedra elements in 3-D. The new families of schemes have full pressure continuity imposed across control-volume faces, in contrast to the earlier point-wise continuous schemes.

The new families of schemes offer maximum flexibility in range of quadrature. The hexahedral schemes have exact fluxes for piecewise trilinear pressure fields in 3-D, bilinear in 2-D and the families are SPD for a constant elliptic tensor.

When applying the earlier point-wise continuous schemes to full-tensor fields with high anisotropy ratios, the schemes violate the maximum principle, and have a limited quadrature range that causes decoupling leading to strong spurious oscillations in the solution. Three dimensional decoupling is shown to occur at the singular end point of the quadrature range. The earlier point-wise schemes are confined to the neighborhood of the decoupled zone.

Tensor-coefficient dependent family M-matrix limits are presented for locally bounded solutions free of spurious oscillations. *Optimal support* conditions are identified from the M-matrix bounds, via bounding quadrature points that define the upper limits on the tensor cross-terms. Planar self-adapting optimal support schemes are also defined together with M-matrix conditions. M-matrix conditions of the tetrahedra scheme yields equivalent limiting conditions consistent with optimal support.

The new families of schemes are tested on problems involving strong full-tensor anisotropy where both M-matrix and monotone matrix conditions are violated. Quasi-positive QM-matrices are defined. In this case the FPS schemes have QM-matrices and optimal support QM-matrix schemes are identified. Optimal support is also obtained by anisotropy favoring prism grids. The multi-family formulation permits extreme anisotropic quadratures to be chosen that lead to improved solution resolution comparable with that of the optimal schemes. The anisotropic quadrature points remain outside of the decoupled zone enhancing robustness of the FPS formulation.

Results show that spurious oscillations in the discrete pressure field are significantly reduced by the new schemes. In particular, the optimal schemes, including anisotropy favoring prism grids and extreme anisotropic quadrature on hexahedral grids both yield pressure fields with very well resolved solutions.

Chapter 8

Conclusions and Recommendations

8.1 Conclusions

New families of locally conservative flux-continuous, finite-volume schemes are presented for solving the general tensor pressure equation on structured and unstructured grids in two and three dimensions. The schemes are developed generally for quadrilateral and triangle grid cells in 2-D, for hexahedra, tetrahedra, prisms and pyramids in 3-D. The new families of schemes have full pressure continuity imposed across control-volume faces, in contrast to the earlier families of flux-continuous schemes, which are point-wise continuous in pressure and flux.

The new family of schemes offers maximum flexibility in range of quadrature. The permissible quadrature range of the earlier pointwise schemes is shown to be half that of the full continuity schemes for a diagonal tensor. When applying both the point-wise continuous schemes and full pressure continuity schemes to full-tensor fields with high anisotropy ratios, the schemes can fail to satisfy the maximum principle. For strong full-tensor anisotropy, the point-wise TPS schemes are shown to have quadrature points that lie within a small neighbourhood of the singular decoupled end point of the quadrature interval, leading to strong spurious oscillations in the solution.

The FPS schemes are symmetric positive definite for a spatially constant full elliptic tensor. Constant coefficient M-matrix bounds for the general family of full-tensor schemes define tensor-coefficient dependent quadrature interval limits for obtaining locally bounded solutions. When the governing conditions are satisfied the discrete pressure field is free of spurious oscillations. An *optimal support condition* is identified from the M-matrix bounds, via a bounding quadrature point that defines the upper limit on the tensor cross-term.

The new family of schemes are tested on a range of problems involving strong full-tensor anisotropy where both M-matrix and monotone matrix conditions are violated. Results are presented for a range of quadrature points belonging to the new family and show that the occurrence of spurious oscillations in the discrete pressure field is minimal provided the quadrature point lies outside of the neighbourhood of the point-wise continuity schemes which are essentially decoupled in this case. Analysis of the non-monotone case leads to the introduction of quasi-positive QM-matrices. Optimal support quadrature points are also found to be optimal with respect to a QM-matrix.

The new full pressure support schemes are shown to share the full CVFE quadrature range for spatially constant tensor coefficients. The optimal support quadrature point is shown to lie within the quadrature range of the full pressure support scheme for all elliptic tensors. For regions where the tensor is spatially constant, the optimal support quadrature point yields a scheme that self-adapts the discretization support locally according to the local orientation of the tensor field. The tests conducted show the optimal point yields results of sharper resolution compared to other points in a single parameter family quadrature range.

New double-families (in 2-D) and multi-families (in 3-D) of locally conservative flux-continuous, finite-volume schemes are also presented for solving the general tensor pressure equation on all of the classical cell-types in 2-D and 3-D. These schemes also have full pressure continuity imposed across control-volume faces, in contrast to the earlier families of schemes which are point-wise continuous in pressure and flux.

The multi-families of schemes offer maximum flexibility in range of quadrature. The quadrilateral scheme fluxes are exact for piecewise bilinear pressure fields and the hexahedral fluxes are exact for piecewise trilinear pressure fields.

As with the orignal single family of pointwise schemes, when applying the multi-family point-wise continuous schemes to full-tensor fields with high anisotropy ratios, the schemes can fail to satisfy the maximum principle, their limited quadrature range lies within a small neighbourhood of the singular decoupled end point of the quadrature interval, leading to strong spurious oscillations in the solution.

Tensor-coefficient dependent double-family M-matrix limits are presented for locally bounded solutions free of spurious oscillations. The bounds also show that a consistent locally conservative scheme cannot yield unconditional M-matrices for all tensors. An *optimal support condition* is identified from the M-matrix bounds, defining a bounding quadrature point that defines the upper limit on the tensor cross-term. The triangle grid scheme has analogous M-matrix conditions consistent with optimal support.

The schemes are tested on a range of cases and the results generally indicate the benefits of the new FPS formulations. For highly anisotropic full-tensor cases the spurious oscillations induced by the earlier point-wise schemes are significantly reduced or removed. The optimal schemes including anisotropy favoring triangulation (and prisms) and multi-family extreme quadrature schemes, each yield well resolved solutions for challenging cases including highly anisotropic discontinuous full-tensors in 2-D and 3-D.

8.2 Recommendations for Future Work

The work presented in this thesis describes the development of new families of control-volume distributed flux-continuous (CVD(MPFA) multi-family) FPS schemes.

This work has laid the foundation for numerous further investigations, which will hopefully give an even greater insight into optimal approximation for subsurface reservoir simulation. Further possible research routes are suggested here:

(i) The strategy for solving faulted layer problems in this thesis is by node-splitting technique. Non-matching grid may also be used in some reservoir simulation studies. It would be interesting to see how FPS algorithm performs with a non-matching grid.

(ii) When applying double family concept to triangle grids, a triple family scheme can be achieved. How the triple family performs under different geometry-permeability conditions would be interesting to investigate.

(iii) Flux-splitting technique has been introduced to improve the stability of the numerical solution. Although the algorithm developed in this work have a quasi-positive matrix, it is generally not an M-Matrix. Further work are required to carry out the combination of FPS chemes and flux-splitting technique to achieve a Positivity guaranteed scheme.

List of Symbols

Table 1. Upper-Case Roman

$\mathbf{A}$	Jacobian matrix of 9-point flux-continuous system of equations
A_L	Matrix of assembled flux-coefficients operating on interface pressures (L-Left)
A_R	Matrix of assembled flux-coefficients operating on vertex pressures (R-Right)
$\mathbf{B}$	Jacobian matrix of 2-point flux-continuous system of equations
B_L	Matrix of assembled flux-coefficients operating on interface pressures (L-Left)
B_R	Matrix of assembled flux-coefficients operating on vertex pressures (R-Right)
$C_{i,j}$	Coarse scale cell (i-row, j-col)
E	Ellipticity of tensor ($E \leq 1$)
E	East direction
F	Flux in x-coordinate direction
G	Flux in y-coordinate direction
$\mathbf{G}$	Gradient operator
$\mathbf{I}$	Identity matrix
J	Jacobian matrix
$\mathbf{K}$	Permeability tensor (2x2 - 2D, 3x3 - 3D)
L_x	Face length along x-coordinate direction
L_y	Face length along y-coordinate direction
L_2	Error norm
M	Specified source or sink term
M_G	A positive definite matrix of size (nxn)
N	North direction
$\mathbf{O}$	Zero-matrix, matrix with all entries equal zero
Q	Source term
R	Real Space
R^d	d-dimension Real Space
S	South direction
$\mathbf{S}$	Surface of domain Ω
$\mathbf{T}$	Transmissibility tensor (2x2 - 2D, 3x3 - 3D)
$\tilde{\mathbf{T}}$	Transformed tensor (2x2 - 2D, 3x3 - 3D)
$\mathbf{U_h}$	Function space in U
$\mathbf{V_h}$	Function space in V
W	West direction
X	X-coordinate direction
Y	Y-coordinate direction
Z	Z-coordinate direction

Table 2. Lower-Case Roman

$a_{i,j}$	Element entries of matrix **A** (i-row, j-col)
$c_{i,j}$	Fine scale cell (i-row, j-col)
e_i	Edge mid-point index
e_h	Solution error $\phi - \phi_h$
f	One dimensional scalar flux
f_h	Discrete flux
f_{h_x}	Discrete flux in x-direction
f_{h_y}	Discrete flux in y-direction
f	Subscript used to represent interface of left and right cells
h	Small increment in x or y direction
i	No of cells in x-direction
j	No of cells in y-direction
k	One dimensional permeability
l	Different phases (oil, water, gas)
l	Subscript used to represent left cell
m	Source or sink in 1D
n	Iteration level
$\mathbf{n}$	Outward normal vector
$\hat{\mathbf{n}}$	Outward unit normal vector
$\vec{n_N}$	Outward normal vector at interface N
$\vec{n_S}$	Outward normal vector at interface S
$\vec{n_E}$	Outward normal vector at interface E
$\vec{n_W}$	Outward normal vector at interface W
p	Quadrature value corresponding to q_1
q	Quadrature parametrization
$\mathbf{q}$	Col-vector with values (q_1, q_2) in 2D and (q_1, q_2, q_3) in 3D
$\mathbf{r}$	Parametric variation in x and y coordinate direction
r	Subscript used to represent right cell
t	Superscript used to represent transpose of a matrix
$\mathbf{u}$	Flux in x-direction
$\mathbf{v}$	Flux in y-coordinate direction
x	x-coordinate direction
y	y-coordinate direction
z	z-coordinate direction

Table 3. Upper-case Greek

Γ	Boundary of domain Ω
Δ_i	Quantity between two different levels of i
Δ_j	Quantity between two different levels of j
$\Delta_\xi F$	Quantity between two different levels of F in ξ-coordinate
$\Delta_\eta G$	Quantity between two different levels of G in ηcoordinate
$\Delta_\phi F$	Quantity between two different levels of ϕ
$\nabla\phi$	Gradient of pressure ϕ
∇v	Gradient of velocity $\mathbf{v}$
∇z	Gradient of depth $\mathbf{z}$
Φ	Vector of pressure ϕ
Φ_F	Vector of interface pressure ϕ_f
Φ_V	Vector of vertex pressure ϕ_v
Ω	Any problem domain

Table 4. Lower-case Greek

ϕ	Discrete pressure values
ϕ_x	Derivative of pressure in x-coordinate direction
ϕ_y	Derivative of pressure in y-coordinate direction
ϕ_z	Derivative of pressure in z-coordinate direction
ϕ_l	Discrete pressure value in left cell
ϕ_r	Discrete pressure value in right cell
ϕ_f	Discrete interface pressure value
(ξ, η)	Transformed coordinates $0 \leq (\xi, \eta) \leq 1$
θ	Angle in degrees
ψ	Test function in L_2 space
φ	Test function in $H(div)$ space
(α, β)	Area coordinates
σ	Value which is function of (p,q)
μ	Viscosity of fluid
Π	pi with value in degrees = 180 degrees

Table 5. Symbols

aux	Auxiliary
min	Minimum
max	Maximum
Physical	Physical Space
Transform	Transform Space
∂_i	Partial derivative with respect to *i*,*j*,..
∇	Gradient operator
∇^T	Divergence operator
∇^2	Laplacian operator

Table 6. Abbreviations

ACV	Auxiliary Control Volume
CVD	Control Volume Distributed
DG	Discontinuous Galerkin
FDM	Finite Difference Method
FEM	Finite Element Method
FVM	Finite Volume Method
MFEM	Mixed Finite Element Method
MPFA	Multi Point Flux Approximation
NP	Nine Point
SPD	Symmetric Positive Definite
SPE	Society of Petroleum Engineers
TPFA	Two Point Flux Approximation
TP	Two Point
TPS	Triangular (Tetrahedral in 3D) Pressure Support
FPS	Full Pressure Support

Bibliography

[1] Edwards M.G. Symmetric, flux-continuous positive definite approximation of elliptic full tensor pressure equation in local conservation form. *SPE 291471, 13th SPE Reservoir Simulation Symposium, San Antonio, Texas, USA*, pages 553–562, 1995.

[2] Edwards M.G. and Rogers C.F. Finite volume discretization with imposed flux continuity for the general tensor pressure equation. *Comput. Geo.*, (2):259–290, 1998.

[3] Aziz K. and Settari A. *Petroleum Reservoir Simulation.* Applied Science Publishers, London, 1979.

[4] Edwards M.G. and Rogers C.F. A flux continuous scheme for the full tensor pressure equation. *Proceedings: 4th European Conference on the Mathematics of Oil Recovery, Norway,* 1994.

[5] Ware A.F., Parrott A.K., and Rogers C.F. A finite volume discretization for porous media flows governed by non-diagonal permeability tensors. *Proceedings of CFD 96, Eds: P.A.Thibault and D.M.Bergeron, Banff, Canada.*, pages 357–364, 1995.

[6] Edwards M.G. Superconvergent renormalization and tensor approximation. 5th *European Conference on Mathematics of Oil Recovery,Leoben-Austria*, pages 445–454, 1996.

[7] Edwards M.G. Cross flow tensor and finite volume approximation with by deferred correction. *Comput. Methods. Appl. Mech. Engrg.*, (151):143–161, 1998.

[8] Edwards M.G. M-matrix flux splitting for general full tensor discretization operator on structured and unstructured grids. *J. Comput. Phys.*, (160):1–28, 2000.

[9] Edwards M.G. Unstructured, control-volume distributed, full tensor finite volume schemes with flow based grids. *Comput. Geo.*, (6):433–452, 2002.

[10] Edwards M.G. Symmetric positive definite general tensor discretization operator on unstructured and flow based grids. 8^{th} *European Conference on Mathematics of Oil Recovery,Freiberg,Germany*, (ISBN: 90-73781-24-8):22–32, 2002.

[11] Edwards M.G. Control-volume distributed sub-cell flux schemes for unstructured and flow based grids. *SPE Reservoir Simulation Symposium, Houston, Texas,USA*, (DOI 10.2118/79710-MS):12, 2003.

[12] Edwards M.G. and Pal M. Symmetric positive definite general tensor discretization: A family of sub-cell flux continuous schemes on cell centred quadrilateral grids. *In Proceedings of the 10th European Conference on the Mathematics of Oil Recovery,Amesterdam, The Netherlands*, 2006.

[13] Edwards M.G. Higher-resolution hyperbolic-coupled-elliptic flux continuous cvd schemes on structured and unstructured grids in 2-d. *International Journal of Numerical Methods in Fluids*, (51):1059–1077, 2006.

[14] Edwards M.G. Higher-resolution hyperbolic-coupled-elliptic flux continuous cvd schemes on structured and unstructured grids in 3-d. *International Journal of Numerical Methods in Fluids*, (51):1079–1095, 2006.

[15] Edwards M.G. Pal M. and Zheng H. Quasi-montonic variable support (q1,q2)

families of continuous darcy-flux cvd(mpfa) finite volume schemes. *Preprint*, 2006.

[16] Edwards M.G. and Pal M. Positive definite q-families of continuous subcell darcy-flux cvd(mpfa) finite volume schemes and the mixed finite element method. *Int. J. Numer Meth, Fluids*, 57:355–387, 2008.

[17] Edwards M.G. and Zheng H. A quasi-positive family of continuous darcy-flux finite volume schemes with full pressure support. *Journal of Computational Physics*, 227:9333–9364, 2008.

[18] Edwards M.G. and Zheng H. Double families of quasi-positive flux-continuous finite volume schemes on structured and unstructured grids. *11th European Conference on the Mathematics of Oil Recovery (ECMOR XI),Bergen Norway, 7-11, Sep. 2008.*, 2008.

[19] Pal M., Edwards M.G., and Lamb A.R. Convergence study of a family of flux continuous, finite volume schemes for the general tensor pressure equation. *Int.J.Numer.Methods in Fluids*, 51:1177–1203, 2006.

[20] Pal M. and Edwards M.G. Effective upscaling using a family of flux-continuous, finite-volume schemes for the pressure equation. *In Proceedings, ACME 06 Conference, Queens University Belfast,Northern Ireland-UK*, pages 127–130, 2006.

[21] Pal M. and Edwards M.G. Family of flux-continuous finite-volume schemes with improved monotonicity. *Proceedings of the 10th European Conference on the Mathematics of Oil Recovery,Amesterdam, The Netherlands*, 2006.

[22] Pal M. and Edwards M.G. Flux-splitting schemes for improved montonicity of discrete solution of elliptic equation with highly anisotropic coefficients. *In*

Proceedings, ECOMASS CFD-2006 Conference, Egmond aan Zee, The Netherlands, Egmond aan Zee, The Netherlands:ISBN:90–9020970–0, 2006.

[23] Pal M. and Edwards M.G. Quasi-monotonic continuous darcy-flux approximation for general 3-d grids of any element type. *SPE Reservoir Simulation Symposium, Houston, Texas-USA*, 2007.

[24] Pal M. *Families of Control-volume Distributed (CVD MPFA) Finite Volume Approximation for the Porous Media Pressure Equation on Structured and Unstructured Grids.* PhD thesis, Swansea University, 2007.

[25] Aavatsmark I. Barkve T. Bøe Ø. and Mannseth T. Discretization on non-orthogonal, curvilinear grids for multiphase flow. *Proceedings of* 4th *European Conference on the Mathematics of Oil Recovery, Norway*, 1994.

[26] Aavatsmark I. Barkve T. Bøe Ø. and Mannseth T. Method for discretization on triangular grids for general media. *Third SIAM Conference on Mathematical and Computational Issues in the Geosciences, San Antonio, Feb 8-10*, 1995.

[27] Aavatsmark I., Barkve T. Bøe Ø., and Mannseth T. Discretization on non-orthogonal, quadrilateral grids for inhomogeneous, anisotropic media. *J.Comput.Phys.*, 127:2–14, 1996.

[28] Aavatsmark I. Barkve T. Bøe Ø. and Mannseth T. Discretization on unstructured grids for inhomogeneous, anisotropic media. part i: Derivation of the methods. *SIAM J.Sci.Comput.*, 19:1700–1716, 1998.

[29] Aavatsmark I. Barkve T. Bøe Ø. and Mannseth T. Discretization on unstructured grids for inhomogeneous, anisotropic media. part ii: Discussion and numerical results. *SIAM J.Sci.Comput.*, 19:1717–1736, 1998.

[30] Aavatsmark I. Introduction to multipoint flux approximation for quadrilateral grids. *Comput.Geo*, 6:405–432, 2002.

[31] Aavatsmark I. and Eigestad G.T. Numerical convergence of mpfa-o and u methods on general quadrilateral grids. *International Journal of Numerical Methods in fluids*, 51:939–961, 2006.

[32] I. Aavatsmark, G.T. Eigestad, B.T. Mallison, and J.M. Nordbotten. A new finite volume approach to efficient discretization on challenging grids. In *SPE Reservoir Simulation Symposium*, page paper SPE 106435, Houston, Texas, USA, 2007.

[33] Crumpton P.I., Shaw G.J., and Ware A.F. Discretization and multigrid solution of elliptic equations with mixed derivative terms and strongly discontinuous coefficients. *Journal of Computational Physics*, 116:343–358, 1995.

[34] Lee S. H., Tchelepi H., and DeChant L. J. Implementation of a flux continuous finite difference method for stratigraphic hexahedron grids. *SPE J*, 3:267–277, 2002.

[35] Lee S.H., Jenny P., and Tchelepi H. A finite volume method with hexahedral multiblock grids for modeling flow in porous media. *Comput.Geo*, 6:353–379, 2002.

[36] Verma S. Flexible grids for reservoir simulation. *PhD thesis- Stanford University*, 1996.

[37] Wheeler M.F. and Yotov I. A multipoint flux mixed finite element method. *SIAM J. Num Anal.*, 44:2082–2106, 2006.

[38] Edwards M.G. and Zheng H. Double-families of quasi-positive darcy-flux approximations with highly anisotropic tensors on structured and unstructured grids. *Journal of Computational Physics*, 229:594–625, 2010.

[39] Chen Q., Wan J., Yang Y., and Mifflin R. Enriched multi-point flux approximation for general grids. *Journal of Computational Physics*, 227:1701–1721, 2008.

[40] Cao Y., Helmig R., and Wohlmuth B. Geometrical interpretation of the multipoint flux approximation l-method. *Int. J. Numer. Meth. Fluids*, 60:1173–1199, 2008.

[41] Lipnikov K., Shashkov M., Svyatskiy D., and Vassilevski Yu. Monotone finite volume schemes for diffusion equations on unstructured triangular and shape-regular polygonal meshes. *J. Comput. Phys*, 227:492–512, 2008.

[42] Mlacnik M.J. and Durlofsky L.J. Unstructured grid optimization for improved monotonocity of discrete solutions of elliptic equation with highly anisotropic coefficients. *J. Comput. Phys*, 216:337–361, 2006.

[43] Nordbotten J.M., Aavatsmark I., and Eigestad G.T. Monotonicity of control volume methods. *Numerische Mathematik*, 106:255–288, 2007.

[44] Jacob Bear. *Dynamics of Fluids in Porous Media.* Courier Dover Publications, 1989.

[45] Darcy H. Les fontaines publiques de la ville de dijon. 1856.

[46] Norman J.C. *Elements of Petroleum Reservoirs.* Henry L. Doherty Series, 1969.

[47] Arnes J.E., Gimse T., and Lie K.A. *An Introduction to The Numerics of Flow in Porous Media Using Matlab:Geometrical Modeling, Numerical Simulation, and Optimization: Industrial Mathematics at SINTEF.* Springer Verlag, 2007.

[48] Ferziger J.H. and Peric M. *Computational methods for Fluid Dynamics 3rd Edition.* Springer, 2002.

[49] Bruce G.H., Peaceman D.W., Rachford Jr. H.H., and Rice J.D. Calculation of unsteady state gas flow through porous media. *Trans AIME*, 198:79–92, 1953.

[50] Peaceman D.W. and Rachford Jr. H.H. The numerical solution of parabolic and elliptic differential equations. *SIAM J.*, 3:28–41, 1955.

[51] Douglas Jr. J., Peaceman D.W., and Rachford Jr. H.H. A method for calculating multi-dimensional immiscible displacement. *AIME*, 216:297–308, 1959.

[52] Letkeman J.P. and Ridings R.L. A numerical coning model. *Trans AIME Soc.Petr.Eng.J.*, (10):418–424, 1970.

[53] Price H.S. and Coats K.H. Direct methods in reservoir simulation. *SPE Preprint No. 4278*, 1973.

[54] Leveque R.J. *Finite Volume Methods for Hyperbolic Problems.* Cambridge University Press-London, 2002.

[55] Zienkiewicz O.C. Origins, milestones and directions of the finite element method - personal view. *Handbook of Numerical Analysis, P.G. Ciarlet and J.L Lions (eds), Elsevier*, (4):7–67, 1996.

[56] Oden J.T. *Finite Elements: an introduction. Handbook of Numerical Analysis, P.G.Ciarlet and J.L.Lions (eds.).* Elsevier, 1996.

[57] Gupta K.K. and Meek J.L. A brief history of the beginning of the finite element method. *Handbook of Numerical Analysis, P.G. Ciarlet and J.L Lions (eds), Elsevier*, (39):3761–3774, 1996.

[58] Zienkiewicz O.C. and Cheung YK. Finite elements in the solution of field problems. *Engineer*, (200):507–510, 1965.

[59] Zienkiewicz O.C. with Cheung Y.K. *The Finite Element Method in Continuum and Structural Mechanics.* McGraw Hill, 1967.

[60] Strang G. and Fix GJ. *An Analysis of The Finite Element Method.* Prentice Hall, 1973.

[61] Zienkiewicz O.C. and Morgan K. *Finite Elements and Approximation.* Wiley, 1st edition, 1982.

[62] Klausen R.A. On locally conservative numerical methods for elliptic problems; application to reservoir simulation. *PhD Thesis ,Centre for Integrated Petroleum Research CIPR, University of Bergen.*, 2003.

[63] Hughes T.J.R., Franca L.P., Harari I., Mallet M., Shakib F., and Spelce T.E. Finite element methods for high-speed: Consistent calculation of boundary flux. *AIAA* 25th *Aerospace Science Meeting, Reno, Nevada, AIAA-87-0556*, 1987.

[64] Hansbo P. Aspects of conservation in finite element flow computations. *Comput. Methods Appl. Mech. Engrg.*, (117):423–437, 1994.

[65] Berger R.C. and Howington S.E. Discrete fluxes and mass balance in finite elements. *Journal of Hydraulic Engineering*, 128-1:87–92, 2002.

[66] Hughes TJR. Wells GN. Conservation properties for the galerkin and stabilised forms of the advection-diffusion and incompressible navier-stokes equaions. *Computer Methods in Applied Mechanics and Engineering*, 194:1141 – 1159, 2005.

[67] Prevost M., Edwards M.G., and Blunt M.J. Spe 66347 streamlines tracing on curvilinear structured and untructured grids. *SPE RSS, Houston, Texas, Feb*, 2001.

[68] Reed W.H. and Hill T.R. Triangular mesh method for solving neutron transport equation. *Technical Report LA-UR-73-479, Los Alamos Scientific Laboratory*, 1973.

[69] La Saint and Raviart. On a finite element method for solving neutron transport equation. *Mathematical Aspects of finite element methods in partial differential equations. Etd. Carl de Boor. Proceeding of a Symposium Conducted by the Mathematic Research Centre, Uni. Wisconsin-Madison*, 1974.

[70] Cockburn B., Karniadakis G.E., and Shu C-W. (Eds.). *Lecture Notes in Computational Science and Engineering. The Development of Discontinuous Galerkin Methods. Discontinuous Galerkin Method. Theory, Computation and Applications.* Springer, Berlin, 2000.

[71] Brezzi F. and Fortin M. *Mixed and Hybrid Finite Element Methods. Computational Mathematics.* Springer-Verlag, NY, 1991.

[72] Raviart R.A. and Thomas J.M. *A Mixed Finite Element method for Second Order Problems.* Springer-Verlag New York, 1977.

[73] Russell T.F. and Wheeler M.F. Finite element and finite difference methods for continuous flows in porous media. *Chapter 2, in the Mathematics of Reservoir Simulation, R.E. Ewing ed, Frontiers in Applied Mathematics SIAM*, pages 35 –106, 1983.

[74] Arbogast T., Wheeler M. F., and Yotov I. Mixed finite elements for elliptic problems with tensor coefficients as cell centered finite differences. *SIAM J. Numer. Anal.*, 34-2:828, 1997.

[75] Douglas Jr. J., Ewing R.E., and Wheeler M.F. The approximation of the pressure by mixed method in the simulation of miscible discplacement. *A.A.I.R.O Analyse Numerique*, 17:17–33, 1983.

[76] Douglas Jr. J. Ewing R.E. and Wheeler M.F. The approximation of the pressure by mixed method in the simulation of miscible discplacement. *A.A.I.R.O Analyse Numerique*, 17:249–265, 1983.

[77] Cai Z. Jones J.E. McCormick S.F and Russell T.F. Control-volume mixed finite element methods. *Comput. Geo.*, (1):289–315, 1997.

[78] Russel T. F. Relationships amongs some conservative discretizations. *Lecture Notes in Physics, Chen, Ewing and Shi (eds.)*, pages 1–16, 1999.

[79] Yotov I. Mixed finite element methods for flow in porous media. *PhD Thesis, Rice University*, 1996.

[80] Wheeler J.A., Wheeler M.F., and Yotov I. Enhanced velocity mixed finite element methods for flow in multiblock domains. *TICAM Report*, pages 1–27, 2001.

[81] Klausen R.A. and Winther R. Convergence of multipoint flux approximations on quadrilateral grids. *Num. Met. for PDE*, 22-6:1438–1454, 2006.

[82] Riviere B. Discontinuous galerkin method for solving the miscible displacement problem in porous media. *Ph.D.thesis, The University of Texas at Austin*, 2000.

[83] Riviere B., Wheeler M.F., and Banas K. Discontinuous glaerkin method applied to a single phase flow in porous media. *Comput.Geo*, (49):337, 2000.

[84] Ewing R.E. Russel T.F. and Wheeler M.F. Simulation of miscible displacement using mixed methods and a modified methods of characterstics. *SPE Reservoir Simulation Symposium, San Francisco*, (SPE 12241), 1983.

[85] Godunov S.K. A finite difference method for numerical computation of discontinuous solution of the equation of fluid dynamics. *Math. Sb.*, 47:271 – 290, 1959.

[86] Lax P.D. Weak solution of nonlinear hyperbolic equations and their numerical computation. *Comm. Pure. Appl. Math.*, 7:159–193, 1954.

[87] Lax P.D. and Wendroff B. System of conservation laws. *Comm. Pure. Appl. Math.*, 13:217–237, 1960.

[88] Harten A. Higher resolution schemes for hyperbolic conservation laws. *J. Comput. Physics*, 49(3):357–393, 1983.

[89] Leveque R.J. *Numerical Methods for Conservation Laws.* Lecture in Mathematics, ETH-Zurich, Birkhauser Verlag,Basel, 2^{nd} edition, 1994.

[90] Jameson A. and Caughey D.A. A finite volume method for transonic flow calculations. *AIAA Paper*, pages 77 –635, 1977.

[91] Hyman J.M., Knapp R., and Scovel J.C. High order finite volume approximations of differential operators on nonuniform grids. *Physica D*, 60:112–138, 1992.

[92] Versteeg H. K. and Malalasekera W. *An Introduction to Computational Fluid Dynamics: The Finite Volume Method.* Reading, MA: Addison-Wesley, 1995.

[93] Barth T. and Mario O. *Finite Volume Methods: Foundation and Analysis, Encyclopdeia of Computational Mechanics. Edited by Erwin Stein, Rene' de Borst and Thomas J.R. Hughes.* John Wiley and Sons, 2004.

[94] Younes A. and Fontaine V. Efficiency of mixed hybrid finite element and multipoint flux approximation methods on quadrangular grids and highly anisotropic media. *Int. J. Numer. Meth. Engng*, (76):314–336, 2008.

[95] Farmer C.L., Heath D.E., and Moody R.O. A global optimization approach to grid generation. *SPE Reservoir Simulation Symposium, Anaheim CA, USA*, pages 341–350, 1991.

[96] Durlofsky L.J. A triangle based mixed finite element finite volume technique for modeling two phase flow through porous media. *J. Comput. Phys*, 105:252–226, 1993.

[97] Russell T.F. Relationships among some conservative discretization methods. *In: Numerical Treatment of Multiphase Flows in Porous Media, eds. Z. Chen et al., Lecture Notes in Physics*, (552):267–282, 2000.

[98] Hyman J.M., Shashkov M., and Steinberg S. The numerical solution of diffusion problems in strongly heterogeneous non-isotropic materials. *J. Comput. Phys*, 132:130 – 148, 1997.

[99] Nordbotten J.M. and Aavatsmark I. Montonicity conditions for control volume methods on uniform parallelogram grids in homogeneous media. *Compt. Geo.*, 9:61–72, 2005.

[100] Nordbotten J.M. and Eigestad G.T. Discretization on quadrilateral grids with improved montonicity properties. *J. Comput. Physics*, 203(2):744–760, 2005.

[101] Aavatsmark I., Eigestad G.T., Mallison B.T., and Nordbotten J.M. A compact multipoint flux approximation method with improved robustness. *Num. Methods Partial Diff. Eqns*, 24:1329–1360, 2008.

[102] Zheng H., Edwards M.G., and Pal M. Flux continuous finite volume schemes with full pressure continuity. *Proceeding: 15th UK conference of ACME*, pages 48–57, 2007.

[103] Klausen R. and Winther R. Convergence of multipoint flux approximations on quadrilateral grids. *Num. Methods Partial Diff. Eqns*, 22:1438–1454, 2006.

[104] Axelsson O. *Iterative Solution Methods.* Cambridge University Press, Cambridge, 1994.

[105] Edwards M.G. and Zheng H. Quasi-positive families of continuous darcy-flux finite volume schemes on structured and unstructured grids. *Journal of Computational and Applied Mathematics*, in press:DOI:10.1016/j.cam.2009.08.078, 2009.

[106] Eigestad G.T. and Klausen R.A. On the convergence of the multi-point flux approximation o-method: Numerical experiments for discontinuous permeability. *Numerical Methods for Partial Differential Equations*, (21(6)):1079–1098, 2005.

[107] Le Potier C. Schema volume finis pour des operator operateurs de diffusion fortement anisotropes sur des maillages de triangle nonstructures. *C. R., Math., Acad. Sci. Paris, Ser. I.*, 340:921–926, 2005.

[108] H. Zheng and M.G. Edwards. Continuous darcy-flux approximations with full pressure support for structured and unstructured grids in 3-d. *11th European Conference on the Mathematics of Oil Recovery (ECMOR XI)*, 2008.

[109] H. Zheng and M.G. Edwards. Quasi-positive multi-family continuous darcy-flux approximations with full pressure support for structured and unstructured grids in 3-d. *Proceedings of SPE Reservoir Simulation Symposium, paper SPE119186*, 2nd-4th Feb. 2009.

Appendix A

H-scheme coefficients

CVD(MPFA) $\eta = T_{22}/(T_{11} + T_{22})$ *(FPS) H-scheme: Constant Tensor Field*

int coords	**Coefficients**	**Full Tensor**
i,j	**M11**	$2(T11)$
i+1,j	**M12**	$-T11 + T22$
i+1,j+1	**M13**	$-\frac{1}{2}T22 - \frac{1}{2}T12$
i,j+1	**M14**	0
i-1,j+1	**M15**	$-\frac{1}{2}T22 + \frac{1}{2}T12$
i-1,j	**M16**	$-T11 + T22$
i-1,j-1	**M17**	$-\frac{1}{2}T22 - \frac{1}{2}T12$
i,j-1	**M18**	0
i+1,j-1	**M19**	$-\frac{1}{2}T22 + \frac{1}{2}T12$

Appendix B

Local Matrix of Algorithms

B.1 Full Pressure Support Scheme in 2D quadrilateral grids

For each subcell, the flux is built using the local vertex. For the first subcell (1,s,m,w), we have:

$$\begin{aligned} F_S^1 &= a_1 * \Phi_1 + a_2 * \Phi_s + a_3 * \Phi_m + a_4 * \Phi_w \\ F_W^1 &= b_1 * \Phi_1 + b_2 * \Phi_s + b_3 * \Phi_m + b_4 * \Phi_w \end{aligned} \tag{B.1}$$

$$\begin{aligned} F_e^1 &= a_5 * \Phi_1 + a_6 * \Phi_s + a_7 * \Phi_m + a_8 * \Phi_w \\ F_n^1 &= b_5 * \Phi_1 + b_6 * \Phi_s + b_7 * \Phi_m + b_8 * \Phi_w \end{aligned} \tag{B.2}$$

For the second subcell, namely (2,s,m,e), we have

$$\begin{aligned} F_S^2 &= c_1 * \Phi_2 + c_2 * \Phi_s + c_3 * \Phi_m + c_4 * \Phi_e \\ F_E^2 &= d_1 * \Phi_2 + d_2 * \Phi_s + d_3 * \Phi_m + d_4 * \Phi_e \end{aligned} \tag{B.3}$$

$$\begin{aligned} F_W^2 &= c_5 * \Phi_2 + c_6 * \Phi_s + c_7 * \Phi_m + c_8 * \Phi_e \\ F_N^2 &= d_5 * \Phi_2 + d_6 * \Phi_s + d_7 * \Phi_m + d_8 * \Phi_e \end{aligned} \tag{B.4}$$

For the third subcell (3,n,m,e), we have

$$\begin{aligned} F_E^3 &= e_1 * \Phi_3 + e_2 * \Phi_e + e_3 * \Phi_m + e_4 * \Phi_n \\ F_N^3 &= f_1 * \Phi_3 + f_2 * \Phi_e + f_3 * \Phi_m + f_4 * \Phi_n \end{aligned} \tag{B.5}$$

$$\begin{aligned} F_S^3 &= e_5 * \Phi_3 + e_6 * \Phi_e + e_7 * \Phi_m + e_8 * \Phi_n \\ F_W^3 &= f_5 * \Phi_3 + f_6 * \Phi_e + f_7 * \Phi_m + f_8 * \Phi_n \end{aligned} \tag{B.6}$$

For the fourth subcell (4,n,m,w), we have

$$\begin{aligned} F_N^4 &= g_1 * \Phi_4 + g_2 * \Phi_n + g_3 * \Phi_m + g_4 * \Phi_w \\ F_W^4 &= h_1 * \Phi_4 + h_2 * \Phi_n + h_3 * \Phi_m + h_4 * \Phi_w \end{aligned} \tag{B.7}$$

$$\begin{aligned} F_E^4 &= g_5 * \Phi_4 + g_6 * \Phi_n + g_7 * \Phi_m + g_8 * \Phi_w \\ F_S^4 &= h_5 * \Phi_4 + h_6 * \Phi_n + h_7 * \Phi_m + h_8 * \Phi_w \end{aligned} \tag{B.8}$$

Applying the flux continuity condition:

$$\begin{gathered} F_S^1 = F_S^2 \\ F_E^2 = F_E^3 \\ F_N^3 = F_N^4 \\ F_W^4 = F_W^1 \\ F_E^1 + F_W^1 + F_S^4 = F_E^4 + F_W^3 + F_S^3 \end{gathered} \tag{B.9}$$

Then we can get the local matrix:

$$A_L = \begin{pmatrix} a_2 & 0 & 0 & a_4 & a_3 \\ d_2 & d_4 & 0 & 0 & d_3 \\ 0 & f_2 & f_4 & 0 & f_3 \\ 0 & 0 & h_2 & h_4 & h_3 \\ a_6 + b_6 + c_6 & c_8 & h_6 & a_8 + b_8 + h_8 & a_7 + b_7 + c_7 + h_7 \end{pmatrix} \tag{B.10}$$

$$B_L = \begin{pmatrix} a_1 & 0 & 0 & 0 \\ 0 & d_1 & 0 & 0 \\ 0 & 0 & f_1 & 0 \\ 0 & 0 & 0 & h_1 \\ a_5 + b_5 & c_5 & 0 & h_5 \end{pmatrix} \tag{B.11}$$

For the right hand side, we have:

$$A_R = \begin{pmatrix} c_2 & c_4 & 0 & 0 & c_3 \\ 0 & e_2 & e_4 & 0 & e_3 \\ 0 & 0 & g_2 & g_4 & g_3 \\ b_2 & 0 & 0 & b_4 & b_3 \\ d_6 & d_8 + e_6 + f_6 & e_8 + f_8 + g_6 & g_8 & d_7 + e_7 + f_7 + g_7 \end{pmatrix} \tag{B.12}$$

and

$$B_R = \begin{pmatrix} 0 & c_1 & 0 & 0 \\ 0 & 0 & e_1 & 0 \\ 0 & 0 & 0 & g_1 \\ b_1 & 0 & 0 & 0 \\ 0 & d_5 & e_5 + f_5 & g_5 \end{pmatrix} \tag{B.13}$$

The degrees of freedom of the five equation system above are the five interface pressures $\Phi_f = (\phi_n, \phi_s, \phi_e, \phi_w, \phi_m)^T$ and the four primal cell centred pressures $\Phi_c = (\phi_1, \phi_2, \phi_3, \phi_4)^T$ for a cell centred scheme. For cell vertex schemes, $\Phi_c = (\phi_1, \phi_2, \phi_3, \phi_4)^T$ is the pressure vector at the primal cell vertex.. The system of equations is rearranged as in Chapter 4.

$$A_L^{5X5}\Phi_f + B_L^{5X4}\Phi_c = A_R^{5X5}\Phi_f + B_R^{5X4}\Phi_c \tag{B.14}$$

where A_L^{5X5}, A_R^{5X5} are 5X5 matrices and B_L^{5X4}, B_R^{5X4} 5X4 matrices as defined above.

Since we only require the four fluxes, we let A_L^{4X5} denote the first four rows of matrix A_L^{5X5} and B_L^{4X4} denote the first four rows of matrix B_L^{5X4}.

The dependence on Φ_f is thus removed by the above equations and the continuous fluxes of the families of FPS schemes are now expressed in terms of Φ_c with

$$\mathbf{F} = (A_L^{4X5}(A_L^{5X5} - A_R^{5X5})^{-1}(B_R^{5X4} - B_L^{5X4}) + B_L^{4X4})\Phi_c$$

B.2 Triangular Pressure Support Scheme in 2D quadrilateral grids

For each subcell, the flux is built using the local vertex. For the first subcell (1,s,m,w), we have:

$$\begin{aligned} F_S^1 &= a_1 * \Phi_1 + a_2 * \Phi_S + a_3 * \Phi_W \\ F_W^1 &= b_1 * \Phi_1 + b_2 * \Phi_S + b_3 * \Phi_W \end{aligned} \tag{B.15}$$

For the second subcell, namely (2,s,m,e), we have

$$\begin{aligned} F_S^2 &= c_1 * \Phi_2 + c_2 * \Phi_S + c_3 * \Phi_E \\ F_E^2 &= d_1 * \Phi_2 + d_2 * \Phi_S + d_3 * \Phi_E \end{aligned} \tag{B.16}$$

For the third subcell (3,n,m,e), we have

$$\begin{aligned} F_N^3 &= e_1 * \Phi_3 + e_2 * \Phi_E + e_3 * \Phi_N \\ F_E^3 &= f_1 * \Phi_3 + f_2 * \Phi_E + f_3 * \Phi_N \end{aligned} \tag{B.17}$$

For the fourth subcell (4,n,m,w), we have

$$\begin{aligned} F_N^4 &= g_1 * \Phi_4 + g_2 * \Phi_N + g_3 * \Phi_W \\ F_W^4 &= h_1 * \Phi_4 + h_2 * \Phi_N + h_3 * \Phi_W \end{aligned} \tag{B.18}$$

Applying the flux continuity condition:

$$\begin{aligned} F_S^1 &= F_S^2 \\ F_E^2 &= F_E^3 \\ F_N^3 &= F_N^4 \\ F_W^4 &= F_W^1 \end{aligned} \tag{B.19}$$

Then we can get the local matrix:

$$A_L = \begin{pmatrix} a_2 & 0 & 0 & a_3 \\ d_2 & d_3 & 0 & 0 \\ 0 & f_2 & f_3 & 0 \\ 0 & 0 & h_2 & h_3 \end{pmatrix} \tag{B.20}$$

$$B_L = \begin{pmatrix} a_1 & 0 & 0 & 0 \\ 0 & d_1 & 0 & 0 \\ 0 & 0 & f_1 & 0 \\ 0 & 0 & 0 & h_1 \end{pmatrix} \tag{B.21}$$

For the right hand side, we have:

$$A_R = \begin{pmatrix} c_2 & c_3 & 0 & 0 \\ 0 & e_2 & e_3 & 0 \\ 0 & 0 & g_2 & g_3 \\ b_2 & 0 & 0 & b_3 \end{pmatrix} \tag{B.22}$$

and

$$B_R = \begin{pmatrix} 0 & c_1 & 0 & 0 \\ 0 & 0 & e_1 & 0 \\ 0 & 0 & 0 & g_1 \\ b_1 & 0 & 0 & 0 \end{pmatrix} \tag{B.23}$$

$$F = A_L\Phi_f + B_L\Phi_v = A_R\Phi_f + B_R\Phi_v \tag{B.24}$$

where $F = (F_N, F_S, F_E, F_W)^T$ are the fluxes defined in the dual-cell and $\Phi_f = (\phi_N, \phi_S, \phi_E, \phi_W)^T$ are the interface pressures. Similarly $\Phi_v = (\phi_1, \phi_2, \phi_3, \phi_4)^T$ are the cell centered pressures. Thus the four interface pressures are expressed in terms of the four cell centered pressures. Using the above equation, Φ_f is now expressed in terms of Φ_v to obtain the dual-cell flux and coefficient matrix as in chapters 4 and 5:

$$F = (A_L(A_L - A_R)^{-1}(B_R - B_L) + B_L)\Phi_v \tag{B.25}$$

B.3 Full Pressure Support Scheme in 2D triangular grids

For each subcell, the flux is built using the local vertex. For the first subcell (1,s,m,n), we have:

$$\begin{aligned} F_S^1 &= a_1 * \Phi_1 + a_2 * \Phi_s + a_3 * \Phi_m + a_4 * \Phi_n \\ F_N^1 &= b_1 * \Phi_1 + b_2 * \Phi_s + b_3 * \Phi_m + b_4 * \Phi_n \end{aligned} \tag{B.26}$$

$$\begin{aligned} F_W^1 &= a_5 * \Phi_1 + a_6 * \Phi_s + a_7 * \Phi_m + a_8 * \Phi_n \\ F_E^1 &= b_5 * \Phi_1 + b_6 * \Phi_s + b_7 * \Phi_m + b_8 * \Phi_n \end{aligned} \tag{B.27}$$

For the second subcell, namely (2,s,m,e), we have

$$\begin{aligned} F_S^2 &= c_1 * \Phi_2 + c_2 * \Phi_s + c_3 * \Phi_m + c_4 * \Phi_e \\ F_E^2 &= d_1 * \Phi_2 + d_2 * \Phi_s + d_3 * \Phi_m + d_4 * \Phi_e \end{aligned} \tag{B.28}$$

$$\begin{aligned} F_W^2 &= c_5 * \Phi_2 + c_6 * \Phi_s + c_7 * \Phi_m + c_8 * \Phi_e \\ F_N^2 &= d_5 * \Phi_2 + d_6 * \Phi_s + d_7 * \Phi_m + d_8 * \Phi_e \end{aligned} \tag{B.29}$$

For the third subcell (3,e,m,n), we have

$$\begin{aligned} F_E^3 &= e_1 * \Phi_3 + e_2 * \Phi_e + e_3 * \Phi_m + e_4 * \Phi_n \\ F_N^3 &= f_1 * \Phi_3 + f_2 * \Phi_e + f_3 * \Phi_m + f_4 * \Phi_n \end{aligned} \tag{B.30}$$

$$\begin{aligned} F_S^3 &= e_5 * \Phi_3 + e_6 * \Phi_e + e_7 * \Phi_m + e_8 * \Phi_n \\ F_W^3 &= f_5 * \Phi_3 + f_6 * \Phi_e + f_7 * \Phi_m + f_8 * \Phi_n \end{aligned} \tag{B.31}$$

Applying the flux continuity condition:

$$\begin{gathered} F_S^1 = F_S^2 \\ F_E^2 = F_E^3 \\ F_N^3 = F_N^1 \\ F_E^1 + F_W^1 + F_W^3 = F_S^3 + F_S^2 + F_E^2 \end{gathered} \tag{B.32}$$

Then we can get the local matrix:

$$A_L = \begin{pmatrix} a_2 & 0 & a_4 & a_3 \\ d_2 & d_4 & 0 & d_3 \\ 0 & f_2 & f_4 & f_3 \\ a_6 + b_6 & f_6 & a_8 + b_8 + f_8 & a_7 + b_7 + f_7 \end{pmatrix} \tag{B.33}$$

$$B_L = \begin{pmatrix} a_1 & 0 & 0 \\ 0 & d_1 & 0 \\ 0 & 0 & f_1 \\ a_5 + b_5 & 0 & f_5 \end{pmatrix} \tag{B.34}$$

For the right hand side, we have:

$$A_R = \begin{pmatrix} c_2 & c_4 & 0 & c_3 \\ 0 & e_2 & e_4 & e_3 \\ b_2 & 0 & b_4 & b_3 \\ c_6 + d_6 & c_8 + d_8 + e_6 & e_8 & c_7 + d_7 + e_7 \end{pmatrix} \tag{B.35}$$

and

$$B_R = \begin{pmatrix} 0 & c_1 & 0 \\ 0 & 0 & e_1 \\ b_1 & 0 & 0 \\ 0 & c_5 + d_5 & e_5 \end{pmatrix} \tag{B.36}$$

The degrees of freedom of the five equation system above are the five interface pressures $\Phi_f = (\phi_n, \phi_s, \phi_e, \phi_m)^T$ and the four primal cell centred pressures $\Phi_c = (\phi_1, \phi_2, \phi_3)^T$ for a cell centred scheme. For cell vertex schemes, $\Phi_c = (\phi_1, \phi_2, \phi_3)^T$ is the pressure vector at the primal cell vertex.. The system of equations is rearranged as in the Chapter 4.

$$A_L^{4X4}\Phi_f + B_L^{4X3}\Phi_c = A_R^{4X4}\Phi_f + B_R^{4X3}\Phi_c \tag{B.37}$$

where A_L^{4X4}, A_R^{4X4} are 4X4 matrices and B_L^{4X3}, B_R^{4X3} 4X3 matrices as defined above. Since we only require the three fluxes, we let A_L^{3X4} denote the first three rows of matrix A_L^{4X4} and B_L^{3X3} denote the first three rows of matrix B_L^{4X3}.

The dependence on Φ_f is thus removed by the above equations and the continuous fluxes of the families of FPS schemes are now expressed in terms of Φ_c with

$$\mathbf{F} = (A_L^{3X4}(A_L^{4X4} - A_R^{4X4})^{-1}(B_R^{4X3} - B_L^{4X3}) + B_L^{3X3})\Phi_c$$

B.4 Triangular Pressure Support Scheme in 2D triangular grids

For each subcell, the flux is built using the local vertex. For the first subcell (1,s,m,w), we have:

$$\begin{aligned} F_S^1 &= a_1 * \Phi_1 + a_2 * \Phi_S + a_3 * \Phi_N \\ F_N^1 &= b_1 * \Phi_1 + b_2 * \Phi_S + b_3 * \Phi_N \end{aligned} \tag{B.38}$$

For the second subcell, namely (2,s,m,e), we have

$$\begin{aligned} F_S^2 &= c_1 * \Phi_2 + c_2 * \Phi_S + c_3 * \Phi_E \\ F_E^2 &= d_1 * \Phi_2 + d_2 * \Phi_S + d_3 * \Phi_E \end{aligned} \tag{B.39}$$

For the third subcell (3,n,m,e), we have

$$\begin{aligned} F_E^3 &= e_1 * \Phi_3 + e_2 * \Phi_E + e_3 * \Phi_N \\ F_N^3 &= f_1 * \Phi_3 + f_2 * \Phi_E + f_3 * \Phi_N \end{aligned} \tag{B.40}$$

Applying the flux continuity condition:

$$\begin{aligned} F_S^1 &= F_S^2 \\ F_E^2 &= F_E^3 \\ F_N^3 &= F_N^1 \end{aligned} \tag{B.41}$$

Then we can get the local matrix:

$$A_L = \begin{pmatrix} a_2 & 0 & a_3 \\ d_2 & d_3 & 0 \\ 0 & f_2 & f_3 \end{pmatrix} \tag{B.42}$$

$$B_L = \begin{pmatrix} a_1 & 0 & 0 \\ 0 & d_1 & 0 \\ 0 & 0 & f_1 \end{pmatrix} \tag{B.43}$$

For the right hand side, we have:

$$A_R = \begin{pmatrix} c_2 & c_3 & 0 \\ 0 & e_2 & e_3 \\ b_2 & 0 & b_3 \end{pmatrix} \tag{B.44}$$

and

$$B_R = \begin{pmatrix} 0 & c_1 & 0 \\ 0 & 0 & e_1 \\ b_1 & 0 & 0 \end{pmatrix} \tag{B.45}$$

$$F = A_L\Phi_f + B_L\Phi_v = A_R\Phi_f + B_R\Phi_v \tag{B.46}$$

where $F = (F_N, F_S, F_E)^T$ are the fluxes defined in the dual-cell and $\Phi_f = (\phi_N, \phi_S, \phi_E)^T$ are the interface pressures. Similarly $\Phi_v = (\phi_1, \phi_2, \phi_3)^T$ are the cell centered pressures. Thus the four interface pressures are expressed in terms of the four cell centered pressures. Using the above equation, Φ_f is now expressed in terms of Φ_v to obtain the dual-cell flux and coefficient matrix

$$F = (A_L(A_L - A_R)^{-1}(B_R - B_L) + B_L)\Phi_v \tag{B.47}$$

Author's Publications

Pulibcation and Papers In Refereed Journals

1. M.G. Edwards, H. Zheng, *A Quasi-Positive family of Continuous Darcy-Flux Finite Volume Schemes with Full Pressure Support*, J. Comp. Phys. 227 (2008), 9333-9364.

2. M.G. Edwards, H. Zheng, *Double-Families of Quasi-Positive Darcy-Flux Approximations with Highly Anisotropic Tensors on Structured and Unstructured Grids*, J. Comp. Phys. 229 (2010) 594-625

3. M.G. Edwards, H. Zheng, *Quasi-Positive Families of Continuous Darcy-Flux Finite Volume Schemes on Structured and Unstructured Grids*, Journal of Computational and Applied Mathematics. In presss. DOI: 10.1016/j.cam.2009.08.078

4. M. G. Edwards, Mayur Pal and Hongwen Zheng , *Quasi-Monotonic Variable Support (q1,q2)families of Continuous Darcy-Flux CVD(MPFA) Finite Volume Schemes*, SIAM Journal on Sci. Comp), Submitted 2006.

5. M.G. Edwards, H. Zheng, *Quasi-Positive Multi-Family Continuous Darcy-Flux Approximations with Full Pressure Support on Structured and Unstructured Grids in 3-D*, Submitted. 2008.

Publication In Conference Proceedings

1. H.Zheng, M.G.Edwards and Mayur Pal., *Flux-continuous finite volume schemes with full pressure continuity*, In ACME 07 Conference Proceeding, Scotland, 2nd - 3rd April 07.

2. M.G. Edwards, H. Zheng,, *Quasi-Positive families of Continuous Darcy-Flux Finite Volume Schemes on Structured and Unstructured Grids*, In Proceedings of ACOMEN 2008, University of Liege, Belgium. May 26-28, 2008

3. M.G. Edwards, H. Zheng, *Double families of quasi-positive flux-continuous finite volume schemes on structured and unstructured grids.*, 11th European Conference on the Mathematics of Oil Recovery (ECMOR XI),Bergen Norway, 7-11, Sep. 2008.

4. H. Zheng, M.G. Edwards, *Continuous Darcy-flux Approximations with Full Pressure Support for Structured and Unstructured Grids in 3D*, 11th European Conference on the Mathematics of Oil Recovery (ECMOR XI), Bergen Norway, 7-11, Sep. 2008.

5. H. Zheng, M.G. Edwards, *Quasi-Positive Multi-Family Continuous Darcy-Flux Approximations with Full Pressure Support for Structured and Unstructured Grids*, Proceedings of SPE Reservoir Simulation Symposium, paper: SPE 119186, 2nd-4th Feb. 2009, Woodlands, USA.